A METHODOLOGY FOR CAPTURING THE AERO-PROPULSIVE COUPLING CHARACTERISTICS OF BOUNDARY LAYER INGESTING AIRCRAFT IN CONCEPTUAL DESIGN

A Thesis
Presented to
The Academic Faculty

By

Jai Ahuja

In Partial Fulfillment
of the Requirements for the Degree
Doctor of Philosophy in the
School of Aerospace Engineering

Georgia Institute of Technology

December 2020

A METHODOLOGY FOR CAPTURING THE AERO-PROPULSIVE COUPLING CHARACTERISTICS OF BOUNDARY LAYER INGESTING AIRCRAFT IN CONCEPTUAL DESIGN

Approved by:

Dr. Dimitri N. Mavris, Advisor
School of Aerospace Engineering
Georgia Institute of Technology

Dr. Lakshmi N. Sankar
School of Aerospace Engineering
Georgia Institute of Technology

Dr. Jimmy C. Tai
School of Aerospace Engineering
Georgia Institute of Technology

Dr. Marilyn J. Smith
School of Aerospace Engineering
Georgia Institute of Technology

Dr. Irian Ordaz
Aeronautics Systems Analysis Branch
NASA Langley Research Center

Date Approved: October 09, 2020

To my parents

who have always supported me

every step of the way

ACKNOWLEDGEMENTS

There are a number of individuals I would like to acknowledge, without whom this effort would not be possible. First, I would like to thank my advisor, Prof. Dimitri Mavris, for having faith in me and providing an opportunity to work at ASDL. Thank you for your guidance over the years, as you calmly addressed any concerns I had, and for building a research environment where I could gain valuable experience in line with my career goals and interests.

In the same vein, I would also like to acknowledge Prof. Paul Barnhart at Case Western Reserve University, my mentor and the best professor I had during my time in undergrad. Your advice was instrumental in helping me commit to a career in aerospace engineering, and your passion and excellence in teaching some of my most interesting courses prepared me exceedingly well for my education and research in graduate school.

I am very thankful to my committee members Prof. Lakshmi Sankar, Dr. Irian Ordaz, and Prof. Marilyn Smith for taking the time out of their busy schedules to share their insights, suggestions, and general advice on my research. In particular, I would like to thank Dr. Jimmy Tai for his guidance from the very start of the process as I tried formulate a research topic covering every little thing I was interested in, for critiquing both the big picture and the minutiae of my research, and for managing my cluster submissions.

There are also a few individuals in the lab that I would like to acknowledge for their contributions to this research effort. Christian Perron, for being an ever helpful source of knowledge and advice for aerodynamics, a sounding board for half-baked ideas, and for general good suggestions that made this research process a lot easier. Jon Gladin and Luis Salas Nunez for their advice on BLI, EDS, and all things related to propulsor modeling. And lastly Steven Berguin, for patiently guiding me through

my first CFD research project and CFD learning experience, and for helping me scope my thesis topic.

Lastly, and most importantly, I am ever grateful to my parents and Crystal. Your unconditional love, support, encouragement, patience, and belief in me have helped me come this far. Thank you for sharing this journey with me.

TABLE OF CONTENTS

LIST OF TABLES

LIST OF FIGURES

NOMENCLATURE

Acronyms

ACARE	Advisory Council for Aeronautics Research in Europe
ADP	Aerodynamic Design Point
AIP	Aerodynamic Interface Plane
ANN	Artificial Neural Network
AR	Aspect Ratio
BLI	Boundary Layer Ingestion
BPR	Bypass Ratio
BWB	Blended Wing Body
CAD	Computer Aided Design
CFD	Computational Fluid Dynamics
CFL	Courant Friedrichs Lewy number
CRM	Common Research Model
CST	Class Shape Transformation
DoE	Design of Experiments
EDET	Empirical Drag Estimation Technique
EDS	Environmental Design Space
EIS	Entry Into Service
ERA	Environmentally Responsible Aviation
FFD	Free Form Deformation
FLOPS	Flight Optimization System
FPI	Fixed Point Iteration
FPR	Fan Pressure Ratio
HPCPR	High Pressure Compressor Pressure Ratio
IDF	Individual Discipline Feasible

LDGFL	Landing Field Length
LHS	Latin Hypercube Sampling
LPCPR	Low Pressure Compressor Pressure Ratio
MDA	Multidisciplinary Design Analysis
MDAO	Multidisciplinary Design Analysis and Optimization
MDF	Multidisciplinary Feasible
MDO	Multidisciplinary Design Optimization
MDP	Multi Design Point
MFE	Model Fit Error
MFRF	Mass Flow Ratio Parameter
MRE	Model Representation Error
MTOW	Maximum Takeoff Weight
N3CC	N+3 Conventional Concept
NASA	National Aeronautics and Space Administration
NOVA	Nextgen Onera Versatile Aircraft
NPSS	Numerical Propulsion System Simulation
OEW	Operating Empty Weight
OML	Outer Mold Line
OPR	Overall Pressure Ratio
PAI	Propulsion Airframe Integration
PSC	Power Saving Coefficient
RANS	Reynolds Averaged Navier Stokes
RASE	Root Average Square Error
RMSE	Root Mean Square Error
RSE	Response Surface Equation
RSM	Response Surface Model(ing)
SAX	Silent Aircraft Experimental

SLS	Sea Level Static
SLSQP	Sequential Least Squares Programming
SQP	Sequential Quadratic Programming
STARC-ABL	Single-Aisle Turboelectric Aircraft with Aft Boundary Layer Propulsor
SUGAR	Subsonic Ultra Green Aircraft Research
SWETF	Fuselage wetted area (or multiplier) in FLOPS
SWETN	Nacelle wetted area (or multiplier) in FLOPS
TASOPT	Transport Aircraft System Optimization
TeDP	Turboelectric Distributed Propulsion
TKO	Takeoff
TOC	Top of Climb
TOFL	Takeoff Field Length
TOGW	Takeoff Gross Weight
TRL	Technology Readiness Level
TSFC	Thrust Specific Fuel Consumption
VSP	Vehicle Sketch Pad
WSR	Weight to Planform Area Ratio (Wing Loading)
XDSM	Extended Design Structure Matrix

Symbols

Some symbols defined in this section relate to properties that are calculated at different engine flow stations. Examples include thermodynamic, flow, and geometrical properties. Within the text, integer subscripts are used in conjunction with the symbol to indicate the engine station at which these properties are being calculated. For brevity, these engine station subscripts are defined separately in this nomenclature, after the symbols. Also, the Conventions section of this nomenclature describes additional common subscripts and superscripts that can apply to multiple symbols.

A	Area
C_D	Drag coefficient
$C_{\dot{E}}$	Non dimensional change in wake dissipation
C_L	Lift coefficient
C_p	Pressure coefficient
$C_{P_{K_{\text{in}}}}$	Non dimensional $P_{K_{\text{in}}}$
d	Diameter
D	Drag
$\dot{E}$	Total mechanical energy flow rate out of the control volume boundary
$\dot{E}_a$	Wake streamwise kinetic energy outflow rate
$\dot{E}_p$	Wake pressure difference work rate
$\dot{E}_v$	Wake transverse kinetic energy outflow rate
$\dot{E}_w$	Mechanical energy outflow rate from control volume side boundary
F_N	Net momentum flux across propulsor (net thrust for non-BLI engine)
F_X	Net axial force on an aircraft
$\mathbf{g}$	Vector of inequality constraints in the optimization problem
$\mathbf{h}$	Vector of equality constraints in the optimization problem
h	Altitude
$\dot{h}$	Rate of change of altitude
$\mathcal{K}_{in}$	Ingested kinetic energy defect
L_{ref}	Reference length to non-dimensionalize axial location on the fuselage
L_{x}	Length of geometry in the x direction
L_{y}	Length of geometry in the y direction
L_{z}	Length of geometry in the z direction
$\dot{m}$	Mass flow rate
M	Mach number
$\hat{\mathbf{n}}$	Unit normal vector for a control volume boundary surface

p	Static pressure
P	Propulsor power
P_K	Net mechanical power added to the flow by the propulsor
$P_{K_{\text{in}}}$	P_K evaluated at the propulsor inlet
$P_{K_{\text{out}}}$	P_K evaluated at the propulsor outlet
P_S	Net propulsor shaft power
p_t	Total pressure
P_V	Mechanical power of fluid expanding against atmospheric pressure
q	Dynamic pressure
$\mathcal{R}_i$	i^{th} residual equation
R^2	R-squared metric for quality of regression
Re	Reynolds number
S	Wing planform area
$\bar{S}$	Wing planform area initial guess in vehicle sizing iteration
S_B	Control volume boundary on airframe body surface
S_O	Control volume outer boundary
S_{PO}	Propulsor outlet integration plane
S_{ref}	Reference area for non-dimensional aerodynamic coefficients
S_{TP}	Trefftz Plane
SPW_{c_2}	Specific corrected flow at fan face
$\left(\frac{t}{c}\right)_{\max}$	Maximum airfoil thickness to chord
T	Static temperature
T_t	Total temperature
u	Perturbation velocity in the x direction
v	Perturbation velocity in the y direction
$\mathbf{V}$	Velocity vector
V	Flow velocity magnitude

V_{app}	Approach speed
V_j	Jet exhaust velocity
V_r	Re-energized wake velocity
V_w	Wake velocity
w	Perturbation velocity in the z direction
W	Aircraft weight
$\mathbf{x}$	Vector of design variables
$\mathbf{x}_{\mathrm{L}}$	Vector of lower bounds on design variables
$\mathbf{x}_{\mathrm{S}}$	Vector of design variables shared among disciplines
$\mathbf{x}_{\mathrm{U}}$	Vector of upper bounds on design variables
$\mathbf{y}$	Vector of coupling variables
$\mathbf{y}^t$	Vector of coupling variable targets
y^+	Non-dimensional distance from the wall for turbulence modeling
$\mathbf{z}$	Vector of constants not perturbed by the solver or optimizer

Greek

α	Angle of attack
β	Symbol representing all BLI effects
γ	Flight path angle
Γ	Dihedral
δ	Boundary layer thickness
Δ	Change in the value of a given quantity
ϵ	Small numerical value ≈ 0
η_{PR}	Pressure recovery
θ	Circumferential (angular) location of engine on fuselage
λ	Taper ratio
$\Lambda_{c/4}$	Quarter chord sweep angle

Λ_{LE}	Leading edge sweep angle
μ	Dynamic viscosity
ρ	Static density
$\bar{\bar{\tau}}$	Shear stress tensor
τ_w	Wall shear stress
ϕ	Inlet ramp angle
Φ	Total dissipation
Φ_{afm}	Total dissipation contribution from the airframe i.e. $\Phi - \Phi_{\text{jet}}$
Φ_{jet}	Propulsor jet mixing dissipation
Φ_{surf}	Dissipation in aircraft surface boundary layers
Φ_{vortex}	Dissipation in aircraft trailing vortex sheet
Φ_{wake}	Dissipation in aircraft wake
ψ	Inlet skinning angle

Engine Station Numbers

These integer subscripts are used within the document to identify the engine flow station corresponding to any relevant quantity defined in the Symbols section above.

0	Ambient
1	Inlet highlight plane
2	Fan face
41	High pressure turbine inlet plane
17	Bypass nozzle inlet plane
7	Core nozzle inlet plane
19	Bypass nozzle exit plane
9	Core nozzle exit plane

Conventions

This section describes some other common subscripts, superscripts, and conventions used in the document that apply to multiple symbols defined above.

$(\cdot)'$	Non-BLI quantities
$(\cdot)_{\mathrm{A}}$	Quantities related to the aerodynamics discipline
$(\cdot)_{\mathrm{B}}$	Quantities related to the BLI effects model
$(\cdot)_{\mathrm{P}}$	Quantities related to the propulsion discipline
$(\cdot)_{\infty}$	Freestream quantities
A$(\cdot)$C$(\cdot)$	Axial and circumferential location of measurement station on fuselage in experiments related to research question 2

SUMMARY

Economic and environmental benefits of fuel efficient aircraft have driven research towards unconventional configurations and technologies. Boundary Layer Ingesting (BLI) concepts appear to be a promising solution, relying on a synergistic interaction between the airframe and propulsor for improved fuel efficiency. Maximizing benefits of BLI while minimizing the risks not only involves careful design of the propulsor, but also the airframe given that the embedded propulsor performance is dependent on the ingested boundary layer flow, which in turn is affected by the airframe. The highly coupled nature of the propulsion system with the airframe for BLI concepts requires a Multidisciplinary Design Analysis and Optimization (MDAO) approach.

Majority of the modeling approaches in literature, however, have treated the BLI problem in a decoupled fashion, especially at the vehicle sizing stage. On the other hand, coupled aero-propulsive methodologies proposed are better suited for point design refinement at the preliminary design stage. Decoupled methods fail to capture aero-propulsive interactions. The impacts of BLI may be overestimated or underestimated, and thus, there is a risk that the sized vehicle will not be satisfactory or even feasible. Quantifying the consequences of ignoring BLI aero-propulsive coupling at the aircraft sizing stage is the primary motivation of this research effort. To address this aspect, a parametric and coupled aero-propulsive design and analysis methodology that is appropriate for conceptual design BLI vehicle sizing and corresponding trade studies is necessary.

A MDAO methodology for BLI aircraft in conceptual design is proposed, allowing for design space exploration and simultaneous optimization of the airframe and propulsor cycle. BLI effects on vehicle performance are identified using the Power Balance formulation. Studies are devised to identify the critical airframe and propulsor design space influencing these BLI effects. Through physics based reasoning, these

studies provide rule of thumb guidelines for concept designers to focus on certain design parameters over others. High fidelity aerodynamic analysis, through CFD, is used strategically for constructing parametric semi-empirical models of the BLI effects, which are then integrated with a cycle analysis code, an aircraft sizing and mission analysis tool, and other analysis modules in a MDAO environment. A fine balance is thus achieved between high fidelity requirements for modeling complex physics and the need for expedited MDAO in conceptual design.

The proposed method is applied to the design and analysis of two tube and wing BLI configurations with different engine locations, similar to the D8 and NOVA-BLI concepts. These vehicles are also designed using a decoupled approach that is reflective of similar methods in literature. A design space exploration involving engine cycle and airframe design parameters is conducted, using the decoupled and coupled approaches, followed by optimization to find the best designs within the specified constraints. The studies show noteworthy differences in performance and design trends between the two BLI modeling approaches. Additionally, the wing influence on the ingested airflow is observed to affect the BLI aero-propulsive coupling strength. The top-mounted engine configuration like the D8 exhibits stronger coupling compared to the side-mounted engine aircraft like the NOVA-BLI. In general, the results support use of coupled and parametric methodologies for BLI concept design.

CHAPTER 1
INTRODUCTION

1.1 The Need for Improved Fuel Efficiency

In a highly competitive market, airlines are striving to capture a larger share of the growing demand for air travel. Ticket prices have a strong influence on customer demand. While lowering ticket prices through various incentives is an effective way to remain competitive, airlines are constrained by their operating costs. In particular, fuel prices have a major economic impact. In a recent study by Airlines for America (A4A), fuel expenses on average accounted for 29.5% of the total direct operating costs and 15.5% of the total operating expenses for U.S. passenger airlines, second only to labor costs [93, 1].

Mirroring the competitive nature of the airline industry, albeit with a fewer number of players, airframe and engine manufacturers are vying for dominance in the aircraft industry. Given the impact of fuel prices on airline operating costs, it should be no surprise that reduced fuel burn is one of the primary design drivers for each new generation of aircraft. As seen in Fig. 1.1 (adapted from [11]), small changes in performance parameters, like nacelle inlet pressure recovery for example, have a substantial impact on engine thrust specific fuel consumption (TSFC) and thus overall mission fuel burn. Even vehicle level block fuel burn changes as low as 0.25% can have a substantial impact, when considering fleet operations.

In addition to economic benefits, fuel burn reduction translates to reduced emissions, a motivation that is also at the forefront in current research studies. Entities like National Aeronautics and Space Administration (NASA) in the United States, and the Advisory Council for Aeronautics Research in Europe (ACARE), are spear-

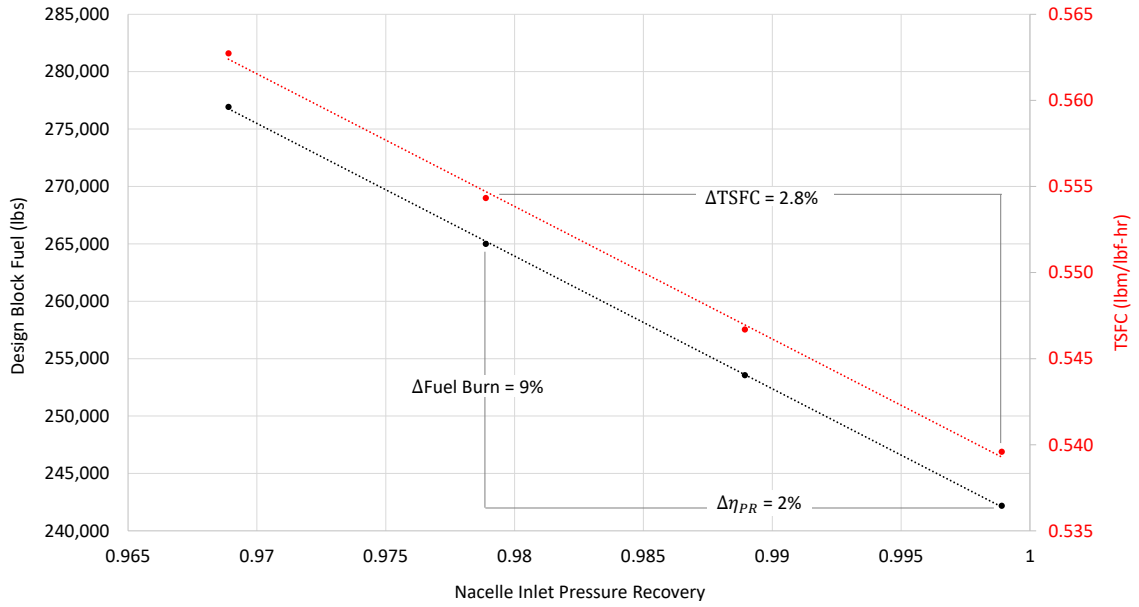

Figure 1.1: Fuel burn as a function of nacelle inlet pressure recovery for a notional 300 passenger class transport and high bypass 94,000 lbs thrust class turbofans (adapted from [11]).

heading research efforts into technologies for improved fuel efficiency [87, 68]. As part of the Environmentally Responsible Aviation (ERA) endeavor, NASA has set targets for fuel burn reduction of 50% by 2020, and 60% by 2025, relative to the Boeing 777-200 and 737-800 vehicles respectively [87]. Composite airframes, advanced propulsion systems like open rotors and ultra high bypass geared turbofan engines, advanced combustor designs, etc. are being proposed as enablers in this quest to achieve improved fuel efficiency.

However, given such aggressive targets, it is widely believed that incremental evolution in technologies, as has been the case over the past few decades, is not sufficient. We appear to be reaching a limit on performance improvements with current technologies. To meet the desired targets, more radical vehicle configurations and technologies must be considered and matured. As a consequence, several unconventional aircraft designs have been proposed that are currently under investigation. One promising set of concepts are Boundary Layer Ingesting (BLI) aircraft.

1.2 Boundary Layer Ingestion

Boundary layer ingestion implies that the propulsor ingests low momentum flow in the boundary layer over the airframe surface. This idea for aircraft applications was initially proposed in 1947 by Smith and Roberts [85]. Their initial studies, using turbojet engines, showed a fuel efficiency benefit of 5-10% per mile relative to a ram inlet jet airplane. Subsequent research over the years focused on boundary layer ingestion for maritime applications. In 1960, Wislicenus [102] found that for a submerged body with a boundary layer inlet, an increase in propulsive efficiency by around 33% relative to a non boundary layer inlet was possible. In 1967, Goldschmied [25] found that propulsive power gains around the order of 50% were possible with an integrated hull-propulsor design relative to the best conventional design. While research into BLI applications for aircraft continued over the years, interest was renewed following Leroy Smith's work in 1993 [86]. Smith quantified benefits of BLI using a new metric termed "Power Saving Coefficient (PSC)", which characterized the savings in propulsor power requirements when the boundary layer is ingested. Smith found that the power savings for a BLI propulsor was highest for propulsors with high thrust loading, and when the ingested wake form factor is high. In this instance, a maximum propulsive power reduction by almost 55% was found in the studies.

Today, there are several entities all over the world actively involved in BLI research, with a number of concepts put forward as a potential successors for the current tube and wing aircraft. Some key concepts are shown in Fig. 1.2. Liu [58] summarizes the system level benefits for BLI reported in several studies relating to the Blended Wing Body (BWB), like the N3-X shown in Fig. 1.2, and D8 concepts, noting a 3-10% reduction in fuel burn for the BWB and a 6-9% reduction in mechanical power requirements for the D8. Though there is some uncertainty in the amount of benefit that can be achieved from BLI, stemming from differences in the concepts considered,

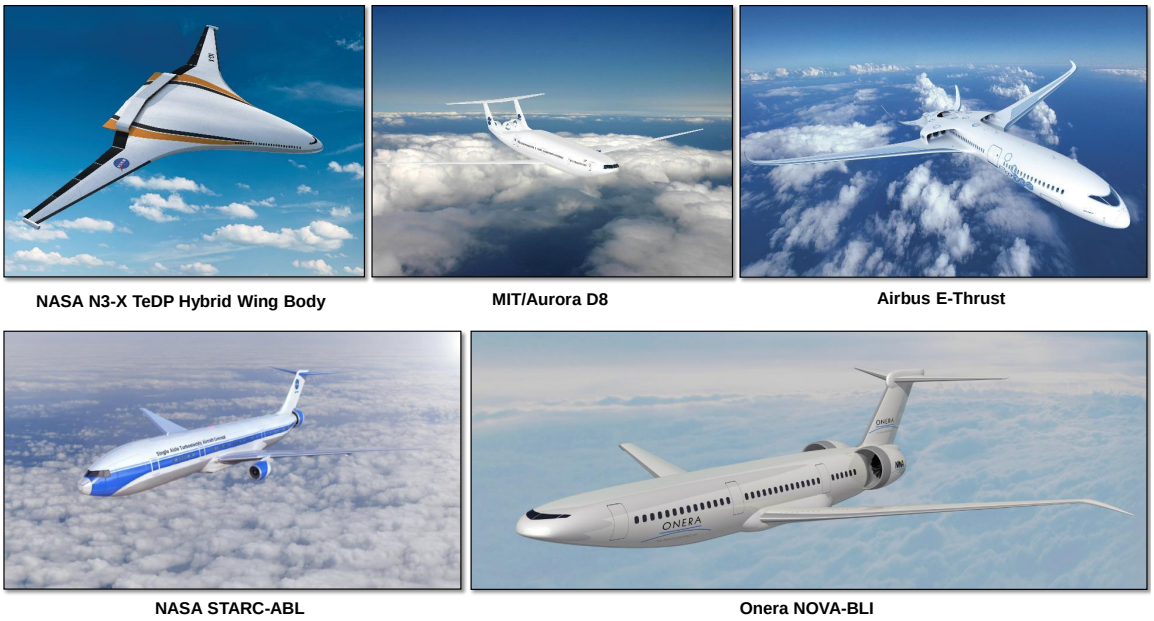

Figure 1.2: Current state of the art in BLI aircraft concepts

modeling approaches, and the baseline configurations to which the BLI vehicles are compared against, on the whole, research suggests that BLI is a promising option for fuel efficient aircraft.

Fuel burn savings going from a non-BLI to a BLI vehicle are a result of reductions in required propulsive power. There are two viewpoints that show how this power required is affected by BLI. The first, is the classical perspective posed by Betz [12], who related the decrease in propulsive power required for a given net momentum flux across the propulsor to the lower ingested flow velocity. This observation can be conveyed more easily using elementary equations in an idealized scenario [74]. Fig. 1.3 compares a podded configuration, where the engine ingests freestream flow at V_∞, to a BLI configuration, where the engine ingests boundary layer flow over the airframe with an average velocity of V_1, where $V_1 < V_\infty$ due to viscous effects. Terms with $(\cdot)'$ are used to denote quantities related to the podded configuration. The net momentum flux for the podded engine, F'_N, ingesting freestream flow with a flow rate $\dot{m}'$, is given by

$$F'_N = \dot{m}'(V'_j - V_\infty) = \dot{m}'\Delta V' \tag{1.1}$$

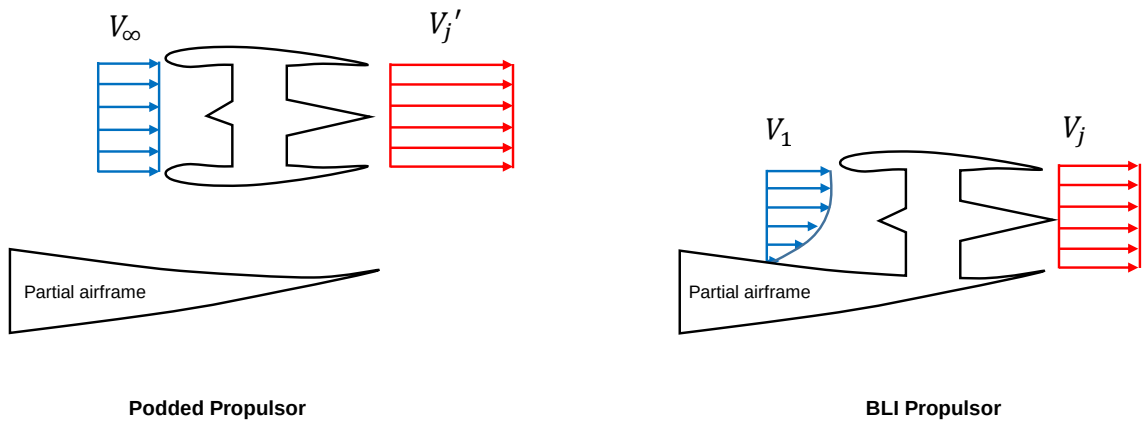

Figure 1.3: Podded propulsor vs BLI propulsor

The power, P', provided by the engine to produce this thrust is equal to the difference in the kinetic energy rate of the flow exiting and entering the propulsor, and is proportional to the net momentum flux as shown by

$$P' = \frac{\dot{m}'}{2}(V_j'^2 - V_\infty^2) = \frac{F_N'}{2}(V_j' + V_\infty) = F_N'\left(\frac{\Delta V'}{2} + V_\infty\right) \tag{1.2}$$

The net momentum flux for the BLI case, F_N, is given as

$$F_N = \dot{m}(V_j - V_1) = \dot{m}\Delta V \tag{1.3}$$

while the propulsive power requirement, P, for this case is

$$P = \frac{\dot{m}}{2}(V_j^2 - V_1^2) = \frac{F_N}{2}(V_j + V_1) = F_N\left(\frac{\Delta V}{2} + V_1\right) \tag{1.4}$$

The required net momentum flux across the propulsor for the non-BLI vehicle (thrust) is driven by the airframe aerodynamic performance, i.e., drag. In the BLI case, to produce the same net momentum flux across the propulsor ($F_N = F_N'$), assuming that the BLI propulsor is sized to ingest the same mass flow rate as the non-BLI engine ($\dot{m} = \dot{m}'$), implies that $\Delta V' = \Delta V$. The following two observations can be made:

(i) Comparing Eq. (1.1) to Eq. (1.3), one sees that due to a lower inflow velocity, the jet velocity for the BLI case must be lower than that for the non-BLI case ($V_j < V_j'$). This implies a lower gross thrust requirement since the ram drag decreases.

(ii) Comparing Eq. (1.2) to Eq. (1.4), one can clearly see that due to the lower inflow velocity, the propulsive power required for the same net momentum flux is lower for the BLI vehicle.

The second perspective relates to the global balance of power within the control volume around the vehicle [34, 81]. Excess power in the control volume is the difference between the power added to the flow by the propulsor and the power dissipated within the control volume. At cruise, both power produced and dissipated must balance. Thus, propulsive power requirements are driven by power dissipation in regions like the airframe surface, wake, jets, etc. For the BLI configuration, given that $V_j < V_j'$ as shown above, jet dissipation is lower for the BLI vehicle, compared to non-BLI, due to lower jet mixing losses. In addition, since the embedded propulsor ingests part of the flow that would have contributed to the airframe wake, and then re-energizes it, mixing losses in the wake and thus dissipation is also lower for the BLI case. This reduction in dissipation results translates to a decrease in propulsive power for a given excess power requirement. Other impacts on fuel burn savings come from a reduction in the wetted area of the nacelle and from removal of the pylon. Both result in lower airframe surface dissipation. In addition, weight savings from these configuration changes can also have a favorable impact on mission fuel burn.

1.3 Problem Statement

BLI concepts, such as those seen in Fig. 1.2, rely on a synergistic interaction between the airframe and propulsor for an improvement in the system level fuel burn relative

to conventional designs. However, such configurations pose challenges not typically faced in conventional designs with podded engines. There are certain risks associated with BLI, primarily relating to propulsor performance, which can offset some or all of the fuel burn benefits. These risks include a reduction in pressure recovery as a result of the total pressure losses in the boundary layer ingested by the engine, in addition to the total pressure loss contribution from the nacelle inlet. There are also degrading impacts on fan efficiency, stall margins, and nozzle performance as a result of ingesting distorted boundary layer flow [49, 75]. This ingested airflow is dependent on the airframe design upstream of the propulsor. Maximizing benefits of BLI while minimizing the risks not only involves careful design of the propulsor, but also the airframe given that the embedded propulsor performance is dependent on the ingested boundary layer flow, which in turn is affected by the airframe. This coupled aero-propulsive design problem requires a Multidisciplinary Design Analysis and Optimization (MDAO) architecture, such as that shown in Fig. 1.4.

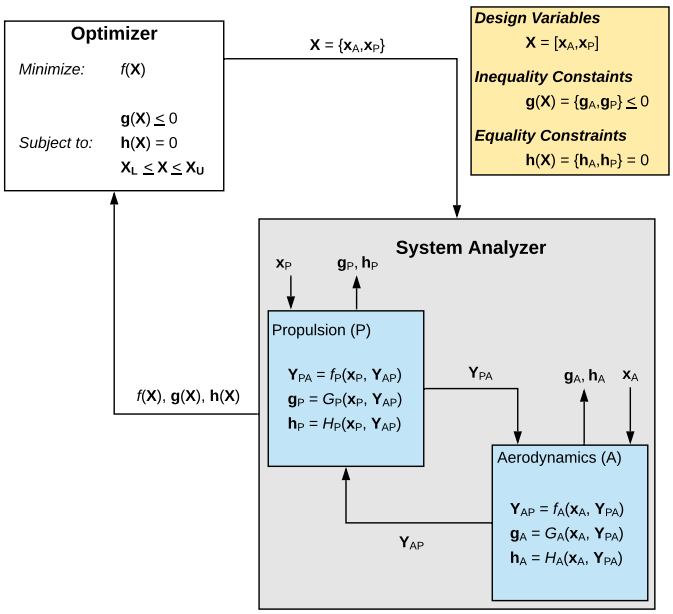

Figure 1.4: A possible MDAO architecture for capturing aero-propulsive interactions in the design and analysis of BLI concepts. The system analyzer enforces interdisciplinary compatibility, presenting a converged solution to the optimizer.

Significant interdependency between the airframe and propulsor design for BLI aircraft will require closer collaboration between engine and airframe manufacturers to obtain the best performance from the concept. Drela [21] illustrates the importance of a multidisciplinary approach, as shown in Fig. 1.5 (adapted from [21]). The red and blue bands depict the technology bounds of current engines and airframes. Aircraft over the years have been produced by incremental, isolated discipline centric optimization of the airframe and engine in a decoupled fashion by the respective entities. Rodriguez notes that due to the "unusually more substantial trade-off between propulsive and aerodynamic efficiencies ... conventional design methods are unable to properly integrate these systems and fail to realize and fully exploit the advantages of BLI"[79]. The optimum from this conventional decoupled approach is much further away from the true optimum, which can only be reached using a multidisciplinary design approach.

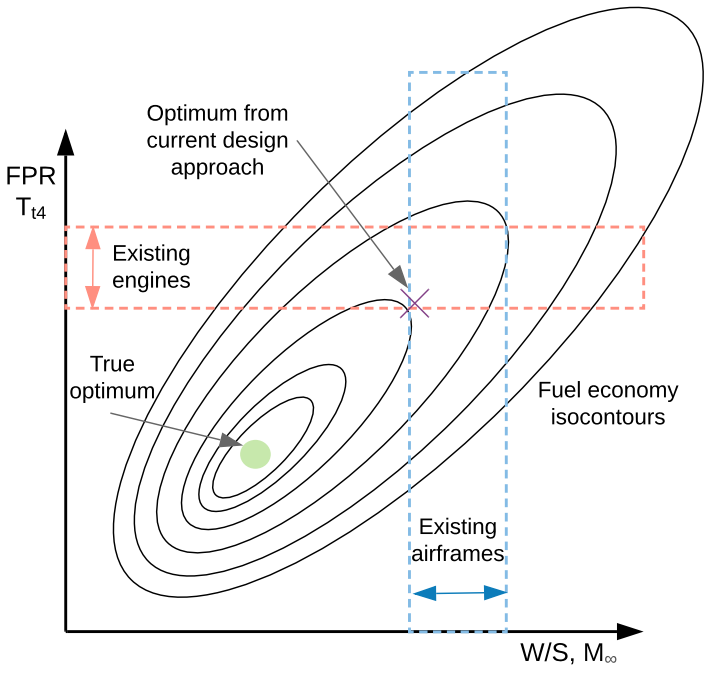

Figure 1.5: True optimum obtained from an MDAO approach vs. local optimum from isolated disciplinary optimization (adapted from [21])

As discussed in chapters 2 and 3, there are several different approaches that researchers have adopted to incorporate BLI effects in conceptual design of the airframe and engines. Coupled approaches in literature have typically been used for a single operating point, conducted after the airframe and engine have been sized, with greater emphasis on analysis of a given configuration and/or detailed shape optimization of the outer mold line (OML). The need for CFD to capture complex BLI physics, linking aerodynamics tools with propulsion codes in an integrated design environment, and the computational expense of running several iterations of CFD in MDA to reach convergence make coupled approaches somewhat challenging to implement efficiently. This aspect is particularly true at the vehicle sizing and engine cycle design stage, where efficient design space exploration at multiple flight conditions is necessary. Additionally, decoupled approaches allow researchers to focus on their areas of expertise, enabling growth in design knowledge at a faster rate. For these reasons, majority of the approaches in literature have treated the BLI problem in a decoupled fashion. The vehicle sized using a decoupled approach, however, is dependent on the validity of the assumptions used for modeling the BLI impact, imparting an additional degree of uncertainty in the performance of the proposed concept. The impacts of BLI may be mis-estimated from a decoupled approach. Consequently, there is a risk that the sized vehicle will not be satisfactory or even feasible. Given this uncertainty, the motivating question for this research effort can be posed as follows:

> **Motivating Question:** What are the consequences of ignoring the aero-propulsive coupling resulting from BLI on vehicle sizing, engine cycle design, and vehicle performance?

Given limitations of proposed approaches in literature to address this issue, which are elaborated in chapter 3, the research objective of this thesis can be stated as follows:

Research Objective: Develop a parametric methodology for the conceptual design and analysis of boundary layer ingesting aircraft that captures the interaction between airframe and propulsor design, and quantifies the consequences of ignoring aero-propulsive coupling at the vehicle sizing and cycle design stage.

In the proposed method, CFD is used strategically to generate a parametric representation of the BLI effects i.e., the impacts of BLI on performance. These semi-empirical relations are then used in sizing the airframe and engine, and determining cycle design. As part of this effort, sensitivity of BLI effects to changes in airframe and propulsor design variables is also investigated. These studies provide guidelines for which variables have to be considered at the conceptual level for BLI aircraft, and what variables can be defaulted at this stage. Impact of flight conditions on the BLI effects is also considered. While the proposed methodology is general enough to tackle any type of BLI vehicle, the scope of this thesis is restricted to tube and wing type BLI concepts. Detailed propulsor design, such as distortion tolerant turbomachinery, nozzle design in the presence of distortion, etc. is not part of the scope for this thesis. In the same vein, impacts of distortion on the propulsor performance are not considered. Similarly on the airframe side, details such as flaps and other control surface design, stability and trim considerations, and detailed structural design are not part of the scope.

1.4 Document Road Map

This section presents an overview of the material covered in the following chapters and then comments on how the reader can efficiently navigate through the content.

Chapter 2: Classification and discussion of the various BLI modeling approaches adopted in literature for the Blended Wing Body, D8, STARC-ABL and NOVA BLI concepts

Chapter 3: Organizes findings from literature based on common practices, general observations, and gaps, leveraging this information to formulate the research problem. Key requirements for the BLI vehicle sizing methodology, research questions, and hypotheses are described

Chapter 4: Provides a description of the methodology along with supporting theory. The BLI effects are formally defined in this chapter. Experimental setups to test the hypotheses are also briefly outlined

Chapter 5: Describes the experiments conducted to investigate the sensitivity of the BLI effects to flight conditions and airframe design

Chapter 6: Presents a similar effort to address the BLI effects sensitivity to the propulsor

Chapter 7: Describes implementation of the methodology on the design and analysis of BLI aircraft. Performance and design differences between the decoupled and coupled approaches are discussed.

Chapter 8: Synthesizes the research effort highlighting significant findings, contributions to literature, and recommendations for future work

Chapter 2 is intended to serve as compendium of relevant BLI literature and terminology on modeling approaches. A reader unfamiliar with this topic may wish to browse this chapter for relevant background information, since pertinent details from various studies are concisely presented in this chapter for context. More experienced readers can skip straight to the research formulation in chapter 3, followed by chapter 4. Chapters 5 to 7 can be read in any order, noting that chapter 7 addresses the primary research question. Readers merely interested in high level conclusions from the experiments can find these in chapter 8. More detailed concluding remarks can be found in sections 5.10, 6.5 and 7.4.

CHAPTER 2
LITERATURE REVIEW

This chapter discusses various modeling approaches adopted in literature for BLI aircraft. Readers who are unfamiliar with seminal works and key terminology in this domain may benefit from perusing the background material presented in this chapter. The idea is for the reader to get a feel for the different ways researchers have tackled the BLI problem, specifically focusing on the treatment of the aerodynamics and propulsion disciplines. More experienced researchers in this field may skim or complete skip this chapter, using it as a stand alone reference as needed for additional information on studies that are cited in the following chapter. This chapter is organized into two sections. The first section presents an overview on how the BLI modeling methods, pertaining to airframe and/or engine design and analysis, can be classified based on certain characteristics. Important terminology is also defined in this section. This information is helpful when evaluating the strengths and weaknesses of the methods. The second section describes and assesses examples of these approaches found in literature for the Blended Wing Body, D8, STARC-ABL, and NOVA-BLI concepts.

2.1 Classification of BLI Modeling Approaches

There are a variety of methods in literature that have been used to model BLI concepts. Hendricks [36] provides a good overview of such approaches used at NASA. In addition, he provides two schemes to categorize the different methodologies, one based on the extent of aero-propulsive coupling captured in the modeling methodology, and the other based on the fidelity level used for the aerodynamics and propulsion models. Fig. 2.1 shows a slightly modified classification scheme for the methods discussed in

this chapter. BLI modeling procedures can also be categorized based on what aspect of the problem is being tackled. Studies can focus on the design and/or analysis of the overall integrated vehicle, with consideration given to both the airframe and propulsor, or emphasis can be on one of the two disciplines. Conceptual design proposals of new concepts presented in literature typically tend to be vehicle centric, while subsequent studies seeking to refine the concept tend to focus on one of the two disciplines in more detail.

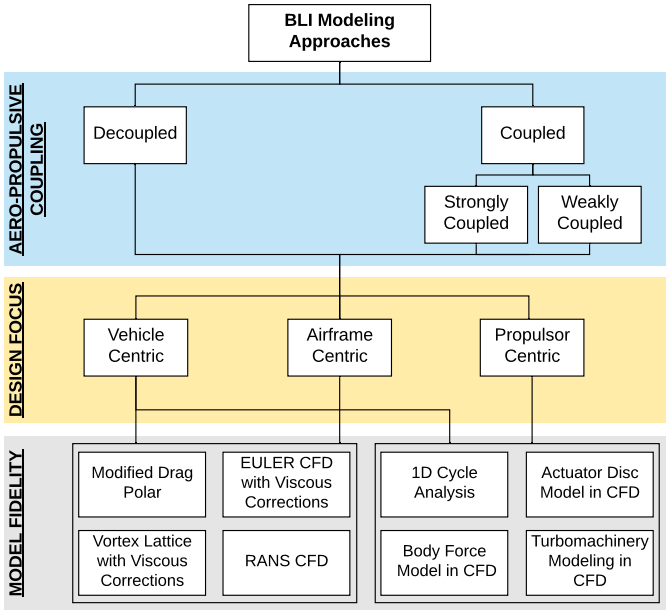

Figure 2.1: Classification of BLI modeling approaches

2.1.1 Decoupled Analyses

BLI modeling can either be decoupled or coupled. Decoupled analyses do not involve any iterative information exchange between the aerodynamics and propulsion disciplines. In airframe centric studies, emphasis is on the aerodynamic design and/or analysis of the airframe. Either the propulsor is not considered at all in the modeling domain, as shown in Fig. 2.2a, or sometimes propulsor impacts may be considered in the form of boundary conditions needed by the aerodynamics model. These values are however provided in a feed-forward fashion by the propulsion model and are not

updated based on the responses from the aerodynamics model, as shown in Fig. 2.2b. Similarly, in propulsor centric studies, either the airframe is not part of the modeling domain, with the propulsion model input requirements such as vehicle drag (thrust required) for example, estimated from prior experience (Fig. 2.2c), or the requirements are calculated from an aerodynamic model, but are not updated based on the outputs from the propulsion model (Fig. 2.2d). For decoupled vehicle centric studies, both disciplines are evaluated in isolation and any information exchange between the two is in a feed-forward fashion, as a result of which the boundary conditions between the two disciplines are not converged (Fig. 2.2e). The order of execution of the aerodynamics and propulsor disciplines can be swapped depending on the problem.

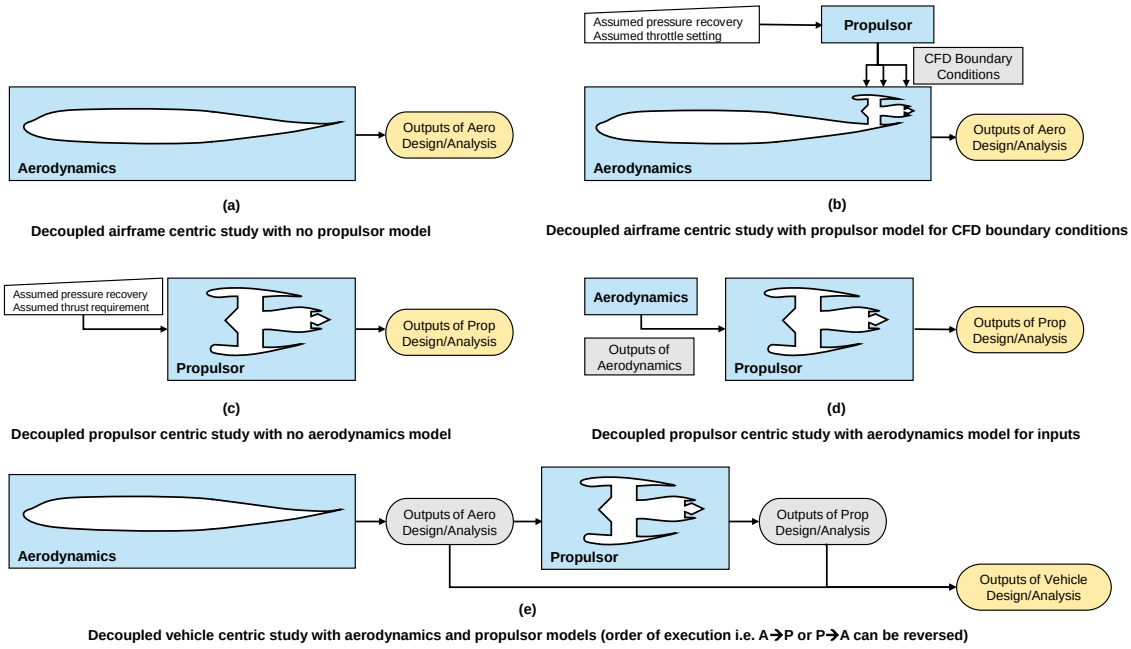

Figure 2.2: Airframe, propulsor, and vehicle centric decoupled approaches

2.1.2 Coupled Analyses

Coupled analyses involve an iterative exchange of information between the aerodynamics and propulsion disciplines till interdisciplinary compatibility is achieved (converged solution), as illustrated in Fig. 2.3. Hendricks further refines coupled ap-

proaches into weakly and strongly coupled. Weakly coupled approaches involve a few manual iterations between the two disciplines that are stopped after a defined limit is reached. While these approaches allow for some degree of interaction between the aerodynamics and propulsion disciplines, they do not necessarily reach fully converged solutions. Strongly coupled approaches on the other hand involve an automated exchange of information between the two models and are driven to fully converged solutions by non-linear solvers. Coupled analyses or multidisciplinary design analyses (MDA) can also be embedded in optimization studies in a MDAO environment as shown in Fig. 1.4. While both aerodynamics and propulsion disciplines are evaluated in coupled studies, the design and analysis focus can still be airframe, propulsor, or vehicle centric.

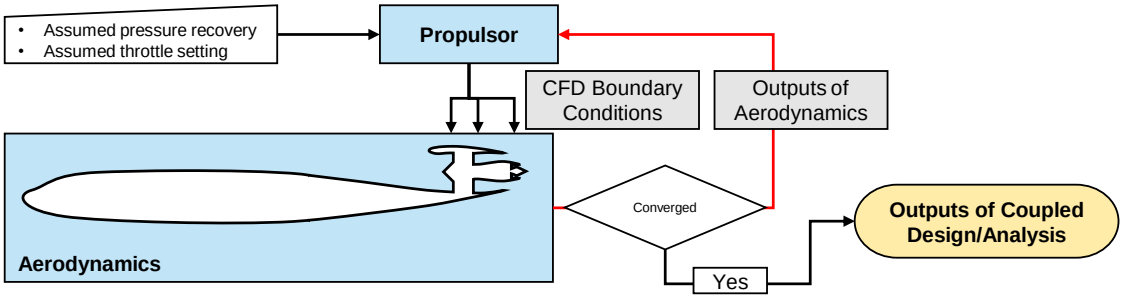

Figure 2.3: A possible coupled aero-propulsive BLI design and/or analysis approach. The feedback loop associated with coupled analyses is highlighted in red.

2.1.3 Model Fidelity

The level of fidelity used for the aerodynamics and propulsion models in various studies depends on factors such as "physics captured by the tool, assumptions made, computational cost, availability and ease of integration with other analyses" [36]. On the aerodynamics side, the lowest fidelity approach for modeling BLI impacts is by reducing the wetted area used in drag buildup approaches. A reduction in wetted area arises from configuration changes like partially embedded nacelles and the elimination of pylons. This approach is akin to modifying the vehicle drag polar.

It is also possible to estimate the BLI impacts using higher order approaches and then artificially adjust the wetted area in the lower fidelity model such that the net effect is the same. Higher fidelity approaches include vortex lattice analysis or Euler CFD, with lower order viscous estimates, for modeling airframe drag. Even higher numerical modeling fidelity can be achieved through Reynolds Averaged Navier Stokes (RANS) CFD.

The lowest fidelity option for propulsor modeling involves semi-empirical relations derived from a database of existing engines. Higher fidelity design and analysis is possible through a 1D thermodynamic cycle analysis code. Propulsor modeling in CFD also has different levels fidelity as shown in Fig 2.4. The simplest approach is a 1D powered CFD engine model, where the fan face is modeled as a pressure outlet with uniform static pressure and temperature, and the fan and core exits modeled as stagnation inlets with uniform total pressure and temperature. No details about the turbomachinery are captured, except indirectly through the boundary conditions imposed at the fan face and exit, obtained from 1D cycle analysis. The fan can be modeled more realistically as an actuator disc, where a pressure jump across the fan is specified as a function of the incoming flow conditions and fan design. Even greater fidelity can be obtained from a body force model which models the effect of the fan blades and their camber as source terms in the momentum and energy equations [6]. Some researchers are even developing approaches for direct turbomachinery modeling in CFD [51].

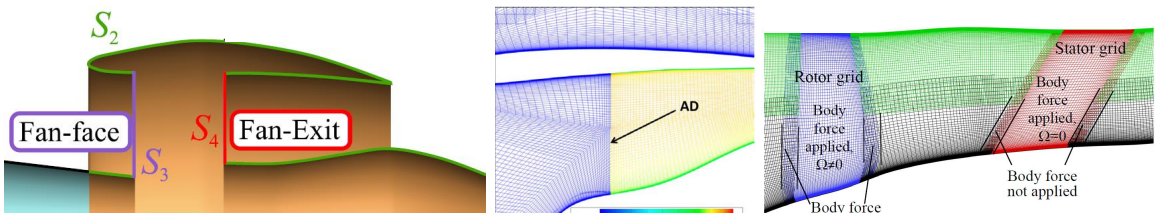

Figure 2.4: Different CFD propulsor model fidelity levels: (a) 1D powered boundary conditions (reproduced from [26]) (b) actuator disc (reproduced from [100]) (c) body force model (reproduced from [6])

2.2 Conceptual Design and Analysis of Selected BLI Concepts

The following section reviews different modeling approaches that BLI researchers have used for the conceptual design proposals and further design refinement studies for the Blended Wing Body (BWB), D8, STARC-ABL, and NOVA-BLI concepts. The focus in this section is on the way the aerodynamics and propulsion disciplines are treated in the various methodologies and how the BLI portion of the problem is considered. Additional details on other aspects of the design and methodologies can be found in the included references.

2.2.1 Blended Wing Body with BLI Propulsors

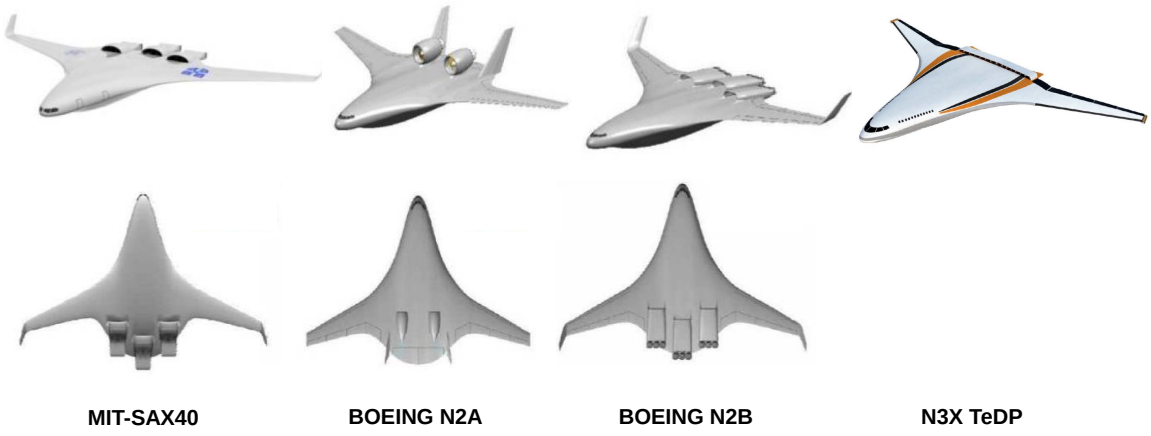

Figure 2.5: Variants of the blended wing body concept. All variants except the N2A employ BLI engines (adapted from [43, 22])

Decoupled Analysis: Liebeck et al. BWB Conceptual Design Proposal

The blended wing body concept was proposed by Liebeck et al. as part of Boeing design studies into more efficient subsonic transport configurations [56]. The BWB was initially designed as an 800 passenger class vehicle, however, subsequent studies also considered smaller concepts [54, 55]. In Liebeck's papers, emphasis is placed on the airframe design, describing the driving design requirements, constraints, and

decisions, while demonstrating the superior performance characteristics of the blended wing-body over the conventional tube and wing design. Aerodynamic analyses of the airframe were enhanced with RANS CFD simulations and NASA's CDISC inverse design method. CFD analyses allowed designers to identify shocks on the outboard wing and track its strength to the centerbody, thus enabling optimal placement of the engines away from the influence of the shocks. Designers were also able to find critical buffet regions outboard of the Yehudi break.

Different engine placements were considered and analyzed based on takeoff gross weight impacts, foreign object damage, noise, flow field quality at the fan face, etc. CFD was used to analyze engine mass flow effects, size and location, and isolated duct performance. The S duct inlets with upper surface mounted engines was deemed the best solution given all considerations, in particular avoiding the poor boundary layer characteristics at the engine face associated with the mid-bifurcated inlet design. However, for the initial preliminary design study, Boeing opted to avoid BLI engines for the 450 pax class vehicle (BWB-450) to minimize technology risk. Based on CFD studies, boundary layer diverters were found to have a large drag and inlet recovery penalty and were thus dropped in favor of the podded engine [55].

Though the impacts of engine placement and flow requirements were factored into the airframe design, discussion on engine sizing and the influence of the ingested boundary layer on the propulsor cycle design and performance, and the corresponding feedback to the airframe design (aero-propulsive coupling) was not presented. However, researchers at Stanford University, as part of this initial investigation into the BWB-BLI concept, presented a multidisciplinary optimization approach for the inlet design, which will be discussed in further detail later in the chapter.

Decoupled Analysis: BWB MDO Conceptual Design

Ko [46] presented a conceptual design based multidisciplinary optimization approach for the BWB-BLI concept, shown in Fig. 2.6. Ko used low-medium fidelity tools for the studies, with vortex panel codes used to predict induced drag, and in house codes 'wdrag' to predict wave drag, and 'friction' for viscous analyses. Ko used ModelCenter to integrate the various tools. 21 design variables including chord, thickness, quarter chord sweep, span, and center body shape were used to modify the geometry planform to minimize gross takeoff weight. 19 equality constraints relating to range, fuel volume, landing etc. were imposed. The only propulsion centric design variable was the thrust requirement per engine. While this was a multidisciplinary approach involving structures, aerodynamics, and propulsion, accurate capturing of the BLI effects was not included. The study assumed inlet performance for the BLI engines to be the same as that on pylons. Additionally, the propulsion module was only used to capture weight, thrust and specific fuel consumption using semi-empirical relations and engine models based on previously published data.

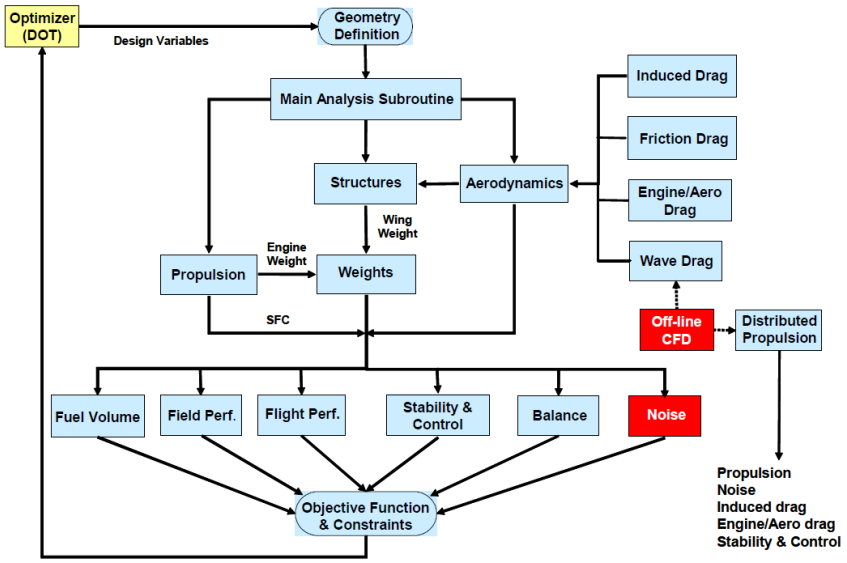

Figure 2.6: Ko's BWB MDO conceptual design framework (reproduced from [46])

Decoupled Analyses: Silent Aircraft Initiative Airframe Centric Studies

As part of the Silent Aircraft Initiative at MIT, several versions of the BWB concept designated SAX-12 [18], SAX-29 [37], and the SAX-40 [38] were developed. These concepts feature embedded BLI engines as a means for noise and fuel burn reduction. The SAX-12 vehicle was developed using low fidelity methods invoking simple physics and empirical relations. The propulsor was modeled in GasTurb, a 1D cycle analysis code, and data tables with thrust and specific fuel consumption at various flight conditions were generated to be used as lookup tables during vehicle sizing. Vortex lattice methods were used for induced drag calculations, with empirical corrections for skin friction and compressibility effects. The SAX-29 and SAX-40 were developed using higher fidelity methods in a quasi-3D design optimization approach, shown in Fig. 2.7. This methodology allowed the designers to avoid the computational expense of 3D-RANS CFD in the design space exploration and optimization routines [37, 38].

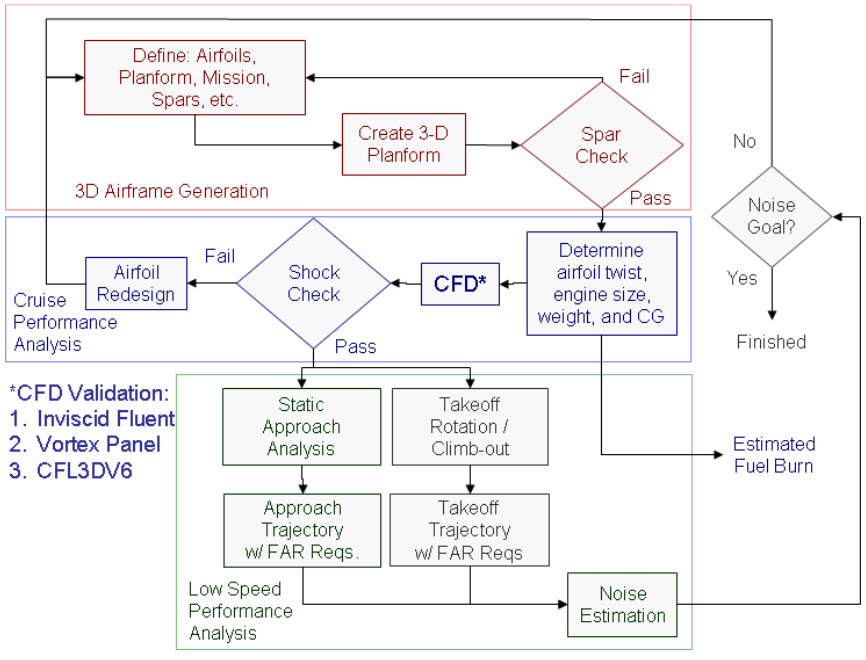

Figure 2.7: SAX-29/40 airframe design methodology (reproduced from [38])

In the quasi-3D design methodology shown in Fig. 2.7, vortex lattice methods were combined with viscous and compressible airfoil analysis, with 3D Euler CFD used sparingly. For a given initial airframe shape, represented as a stack of airfoils and a planform, a 3D model of the geometry was created. Vortex lattice codes were used for trim analysis and for determining airfoil twist distributions. MSES, a two dimensional compressible analysis code was used for determining the wave drag, and XFOIL was used for the viscous analysis. At every major design change, Euler simulations were used to assess airfoil loading and shock strengths. Validation of this method was carried out using full RANS 3D and was found to yield acceptable results. While the SAX concepts featured BLI engines, emphasis in the cited studies was on optimizing the airframe in isolation to minimize fuel burn and noise. Impacts of BLI on the airframe and engine were not explicitly tackled in these studies, though they were analyzed in other related engine centric studies, as will be discussed shortly.

Decoupled Analyses: BWB Airframe Aerodynamic Shape Optimization

There have been other studies in literature that focus on the airframe design and performance of the BWB concept. Kuntawala et al. [48] conducted single-point drag minimization of a 10 passenger BWB concept by optimizing the planform shape using an Euler CFD solver coupled to a sequential quadratic programming (SQP) optimizer. Reist and Zingg [77] extended this work to a 98 passenger BWB concept, conducting both Euler and RANS CFD based optimization and also accounted for multiple operating points in the problem formulation. Lyu and Martins [61] conducted RANS CFD based, lift, thickness and stability constrained, drag minimization of the 800 passenger BWB airframe, using a SQP optimizer and adjoint based gradients with the free form deformation method. The planform shape and details like airfoil twist, chord lengths, sweep were optimized. Both single and multiple point optimizations were considered. Studies like these provide methods that can be used for design refine-

ment after the vehicle sizing stage, highlighting the design improvement capabilities afforded by high fidelity analysis tools. Similar approaches have also been used for coupled optimization studies, as discussed later in the chapter.

Decoupled Analyses: Silent Aircraft Initiative Engine Centric Studies

In parallel to the SAX airframe design studies, researchers have looked into aspects relating to engine design and performance in the presence of distorted flow for the SAX variants. Hall and Crichton [32] discussed engine cycle and mechanical design aspects of the SAX engines. On and off design performance was considered, with the cycle optimized for compatibility with a variable exhaust system, an embedded installation in a BWB airframe, and an ultra-high bypass engine. The engine operating conditions were optimized for max thrust at top of climb, minimum fuel consumption at cruise, and reduced noise footprint at low altitude conditions. 1D thermodynamic cycle analysis was conducted using GasTurb. An airframe design tool was used to quantify thrust requirements at different points in the mission profile, based on the method presented in [18]. An S-Duct inlet was considered. Preliminary CFD studies at cruise showed flow separation at the fan face, leading to an inlet pressure recovery of 0.96. While the impact of BLI on the thrust requirements and engine performance was noted in this paper, to simplify the design and analysis, boundary layer diverters were assumed. Additionally, the previously calculated pressure recovery was assumed to still hold in this case, treating this value as a lower bound that would be improved as a result of future design refinements. The impact of distortion on the engine was also not considered in this study.

Plas et al. [74] looked into quantifying the performance of BLI propulsors while accounting for distortion impacts. Plas investigated the impacts of the following features on the BLI benefits:

- Boundary layer properties at the start of the inlet

- External and internal inlet design
- Distortion variation from inlet to fan face
- Distortion transfer across the fan
- Fan response to ingested distortion
- Distortion distribution downstream of the fan
- Duct losses

Plas found that the BLI impacts on fuel burn were very sensitive to the fan and duct losses, as well as the distortion transfer across the fan. Plas' modeling domain was restricted to the inlet and propulsor. RANS CFD coupled to a body force model of a ducted fan was the highest fidelity approach adopted to analyze distortion transfer across the fan. For the SAX-40 configuration analyses, boundary layer profiles from a CFD solution of the clean airframe were used as boundary conditions for the reduced domain viscous analyses of the ducted fan model. Consequently, there was no opportunity to investigate propulsor impacts on the upstream flow field and treat the distortion analysis as a coupled problem.

Decoupled Analysis: N3X Engine Centric Study

Liu et al. at Cranfield University proposed a decoupled design approach for the N3-X Turboelectric Distributed Propulsion (TeDP) engines [57]. To match the flow rate requirements, they defined a non dimensional mass flow ratio parameter (MFRF) , which normalized the flow rate of the fan with the product of the freestream density, velocity, and inlet duct area. CFD simulations for a geometry similar to the N3X at one flight condition were conducted to obtain pressure and velocity profiles at 4 different MFRF values, with interpolation used to extract intermediate results. Using these profiles, average total pressure and velocity values were calculated. At

on-design, the inlet and flow capture heights were assumed to be the same, with inlet duct pressure losses assumed to be 0.2%. Off-design impacts of BLI were accounted for as changes in inlet recovery, as a function of flow rate, temperature and pressure, given the absence of CFD data at other flight conditions. An in house cycle analysis tool, TURBOMATCH, was used to model the engine.

Decoupled Analyses: Inlet Design Centric

There have been several studies, decoupled and coupled, that have focused on inlet design optimization for the BWB BLI concept. Lee et al. [52] used a discrete adjoint approach to optimize the inlet entrance for minimizing distortion and maximizing pressure recovery using 3D RANS CFD. Baseline inlet geometry was obtained from Boeing. Instead of using the full airframe geometry, Lee modeled a flat plate with a circular type S-Duct inlet and defined the length of the plate to be such that the boundary layer thickness at the inlet was about 30% of the inlet height.

Florea [24] aimed to come up with a distortion tolerant propulsion system design by minimizing the distortion impacts on fan efficiency and stall margin. Boundary layer profiles obtained from Boeing's CFD analysis of the N2A BWB concept were used as inputs for this study. Various inlet parameters were optimized to minimize total pressure loss and distortion. Inlet and fan modeling were coupled to varying degrees, with high fidelity unsteady CFD analysis conducted for the fully coupled fan-inlet simulation, outside the optimization routine. However, the airframe and propulsion system were decoupled since the input boundary layer profiles were fixed. Engine sizing and cycle design were not a part of the scope, and only one flight condition was considered.

Decoupled Analysis: System Level Centric

Hardin et al. [35], conducted a system level assessment of the BLI propulsion system for the BWB concept. Cycle modeling was done using Numerical Propulsion System Simulation (NPSS) [60]. Boundary layer profiles were extracted from Boeing CFD studies of the isolated N2A airframe. Airframe impacts on the propulsion system were considered by using inlet conditions for the NPSS cycle, obtained from the Boeing CFD profiles, rather than freestream. As shown in Fig. 2.8, the "pre-solver" was used to provide NPSS with flow conditions at the inlet, primary and secondary nozzle planes. The "post solver", shown at the bottom, adjusted the pressure at these planes, as well as ram drag and spillage drag, accounting for the non-freestream pressure at these planes.

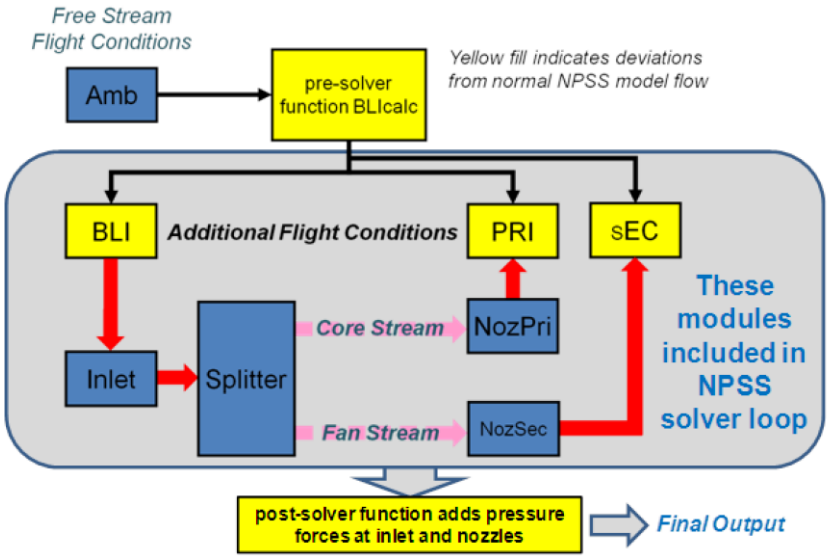

Figure 2.8: Modifications made by Hardin et al. in NPSS to account for BLI (reproduced from [35])

The engine impact on the flow fields could not be captured given the fixed input profiles. The authors assumed that for a well designed inlet at cruise, this interaction would be negligible. Changes in propulsion system drag and weight were estimated using empirical models and used in the system level fuel burn assessment. Low fidelity

estimates for inlet and fan efficiency losses were used to correct TSFC results from NPSS, and combined with the propulsor impacts on the vehicle, the mission fuel burn estimates were obtained.

Coupled Analysis: N3X Engine Centric Studies

Felder et al. looked into engine designs for the N3X TeDP concept [22, 23]. Unlike the previous BWB concepts that featured 3-4 embedded ultra high bypass turbofan engines, this concept features distributed fans, electrically driven by gas generators. The initial cycle design and analysis [22] was a decoupled approach where the propulsion system was sized at the aerodynamic design point (ADP) and a rolling take off condition at sea level. The ADP thrust requirement was based on a prior study for the N2A variant which featured podded engines on the BWB airframe. A reduction in this thrust requirement by 7% was assumed to account for the BLI benefit, a reasonable estimate based on previous studies. The inlet pressure recovery at ADP was assumed to be fixed at 0.965.

Felder recognized the importance of propulsion-airframe integration early in the design process, stating that the embedded engine inlet performance must be based on inlet conditions rather than freestream, and obtaining the correct inflow conditions is an iterative process. Using freestream properties overestimates ram drag and inlet pressure recovery, which affect TSFC predictions. In the following paper [23], CFD analyses of the N2A from Boeing were used to obtain velocity, temperature and pressure profiles. Mass averaged Mach number and total pressure profiles were calculated using the raw data. These profiles were then divided by the freestream values to obtain normalized profiles that could be used at other flight conditions. Since CFD data was only available at cruise, it was implicitly assumed that the profiles had the same shape throughout the flight envelope. A fan pressure ratio (FPR) sweep was conducted for the engine. The flow capture height was assumed to equal the inlet

throat height at the engine design point. For each FPR value, an iterative approach was adopted. The averaged Mach and total pressure values were calculated for an assumed capture height, fed to the NPSS cycle analysis to obtain a new inlet height, thereby updating the capture height given the equality assumption. This update led to a recalculation of the averaged inflow quantities. This process was repeated till convergence. For off design analysis, the capture height was varied such that the flow rate requirement stipulated by the cycle analysis was matched. As the capture height was varied, the averaged Mach and total pressure values were recalculated in an iterative fashion as before.

The importance of this coupled approach, over one that used the same representative values of averaged total pressure and Mach number for all FPR values, was highlighted in the results obtained. Propulsive efficiency for example was overestimated for a FPR of 1.15 and underestimated for FPR of 1.5. While Felder's approach did consider aero-propulsive coupling in the cycle analysis, the approach was propulsor centric given the absence of airframe aerodynamic modeling. The aerodynamic inputs from Boeing were for a fixed airframe and only at a single flight condition. Consequently, the impact of propulsor size, throttle setting, and flight condition on the boundary layer profiles could not be captured.

Coupled Analyses: Inlet Optimization

Rodriguez [79] presented a multidisciplinary inlet optimization approach for the BWB-BLI concept. RANS CFD was coupled to a 1D cycle analysis code and integrated with a nonlinear optimizer in a MDAO framework, as shown in Fig. 2.9. The objective for this MDAO approach was to minimize engine fuel burn, for a constant aircraft weight, by perturbing 16-22 design variables controlling the nacelle shape, with gradients being computed using the complex step approach. The outboard wing linear twist was included as a design variable to control pitching moment, but the

airframe center body outer mold line was fixed. Aerodynamic forces and fan face boundary conditions such as mass flow, inlet pressure recovery, and distortion, were provided by CFD to the cycle analysis. Based on these inputs, the required mass flow was re-computed from the cycle code. The inlet back pressure boundary condition in CFD was varied by the optimizer to match the CFD predicted flow rate with the cycle requirement, which was imposed as a constraint in the optimization problem. Optimized results for the BWB-BLI inlet were compared to an optimized podded baseline. Though it was found that the optimized BWB-BLI airframe drag was lower than the podded baseline case, this benefit came at the expense of deteriorated inlet performance. As a result, the optimized BWB-BLI configuration had a higher fuel burn than the podded BWB baseline. Rodriguez claims that the limited number of design variables restricted design freedom, and that opening up the design space by including more variables could lead to improved results.

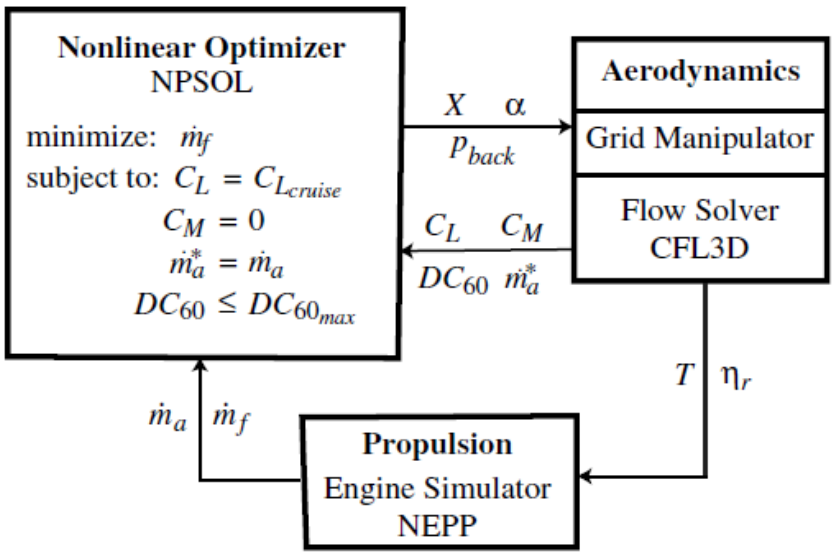

Figure 2.9: MDAO inlet design architecture used by Rodriguez (reproduced from [79])

The number of design variables was limited due to the computational expense of CFD based complex step gradient evaluations. Computational cost also restricted optimization to a single objective, single-operating point problem without airframe

center body re-design. Rodriguez also notes another limitation of this approach in his thesis stating that "while the constant weight assumption necessitates only two disciplines in the method, it does limit its ability in preliminary aircraft design. To adhere to the constant weight assumption, the aircraft size, structural layout, fuel volume, and engine must have already been frozen in the design. Clearly this is only true in detailed design work late in the aircraft design process. In other words, this method is really only practical when the aircraft design has already been mostly determined. While it may be very effective in improving a design, it is not useful in conceptual design work [78]."

Kim conducted unconstrained shape optimization of the inlet for the N2B BWB concept [43] and for the N3X TeDP concept [44]. In both these papers, inlet design was the primary focus with the rest of the airframe fixed. The N2B inlet was optimized for reducing drag and distortion using adjoint based optimization. The propulsor was based off the SAX-40 engine and was modeled in NPSS. To simplify integration of NPSS with CFD, response surface models for the engine cycle were used for providing the boundary conditions. Off design propulsor analysis at different inlet recoveries were used to generate response surfaces for the boundary conditions. These response surfaces were embedded in the CFD solver, and based on the simulation results, updated values of pressure recovery were passed back to the cycle model. The exchange of boundary conditions between the two disciplines was repeated till convergence. The mass flow rate requirement for the engine was met by varying the static pressure in CFD. For this study, a uniform back pressure boundary condition was imposed at the fan, which is not entirely representative of the fan-inlet interaction and tends to yield conservative estimates for distortion. Since distortion minimization was the primary focus, the following study [44] adopted a body force model for the N3X engine in CFD. A similar approach as before was used to optimize the mail slot inlet for this concept.

2.2.2 D8 Double Bubble

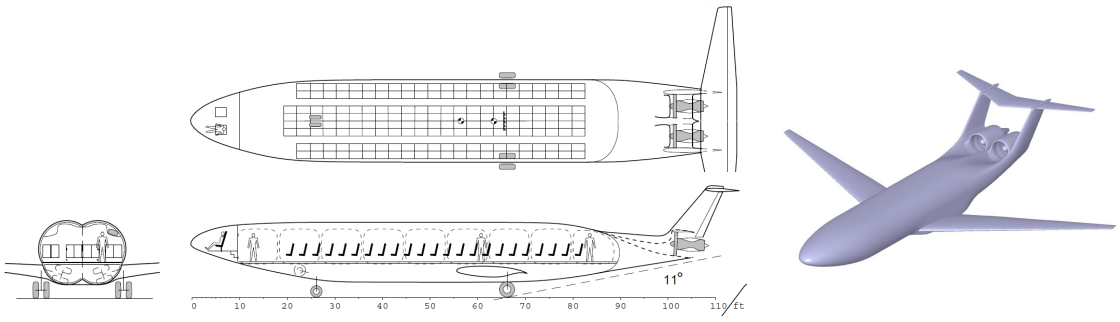

Figure 2.10: D8 Double Bubble concept (drawing view adapted from [19], CAD view reproduced from [33])

Decoupled Analyses: D8 Conceptual Design Proposal by MIT and Aurora

The D8 Double Bubble concept was proposed by MIT as part of the NASA N+3 design studies [30, 19] and is thus envisioned for the 2035 time frame. This is a 180 passenger class vehicle that features BLI turbofans embedded on the aft end of the fuselage, in between the pi-tail. The novel double bubble fuselage cross section is unique to this concept. The initial proposal [30] featured two variants of the D8, one designed with 2010 technologies and the other with 2035. The Boeing 737-800 served as a baseline, and the CFM56 class engines on the 737-800 were modified for the initial D8 BLI variants to reflect technological advancements by 2035. The following proposal [19] featured modifications to the initial variants to reflect changes in the design methodology. The D8 variants were designed using a vehicle sizing tool called Transport Aircraft System OPTimization (TASOPT), MIT's in house aircraft MDO code, similar to NASA's Flight Optimization System (FLOPS)[64]. TASOPT was used to develop the D8 by minimizing vehicle fuel burn, accounting for the mission, propulsion system, structures, aerodynamics, etc. Additonal details on the TASPOT optimization methodology can be found in [29].

Low fidelity physics based models, as opposed to empirical relations, were predominantly used for the various discipline analyses in TASOPT. The propulsion model in TASOPT is a 1D thermodynamic cycle analysis model with on-design mode for engine sizing at cruise and off-design mode for takeoff, climb, and descent performance analysis. MSES, a viscous transonic analysis code for airfoils, and vortex lattice codes like AVL and QUADPAN were the primary aerodynamic models used for the D8. The initial D8 proposals focused on airframe design and aerodynamic performance. Details concerning the treatment of the boundary layer on engine sizing and performance analysis were not presented.

Aurora Flight Sciences, in collaboration with MIT, further refined the D8 concept [104]. As before, TASOPT was used for the conceptual sizing of the vehicle. CFD was then used for maturing the design. The engine cycle was modeled using Aurora's in-house tool, comparable to NPSS, and assumed that 40% of the fuselage boundary layer was ingested by the engines. This value was supported with RANS CFD studies which assessed the engine integration with the airframe. These studies however used a flow through nacelle instead of a powered engine, thus missing out on throttle dependent effects. In the conceptual sizing stage, TASOPT used an assumed boundary layer profile to estimate the entropy of the ingested boundary layer, which was then used to calculate the total pressure and thus inlet recovery. Handbook methods were used for the drag/dissipation buildup during the sizing process, and an assumption was made that only the wake dissipation changed as a result of the BLI. To model that, a wake dissipation correction factor was used. Euler CFD was used to assess detailed aerodynamic characteristics of the airframe like airfoil camber, thickness, and wing twist distribution. Overall vehicle aerodynamics was also assessed using CFD, but without the engines.

Decoupled Analyses: D8 Power Savings Assessments

There have been a number of studies that have looked into estimating the fuel burn benefits of the D8 concept. Uranga et al. [92, 91] conducted low speed wind tunnel assessments of the D8 to quantify the aerodynamic benefit of BLI in terms of propulsor electric power savings for a measured net axial force on the vehicle. Pandya et al. [72, 73] conducted computational assessments of the D8 using the the wind-tunnel results presented by Uranga [92] as validation for the unpowered case. The unpowered case here was the airframe without any nacelles. Pandya used RANS CFD and modeled the propulsor as an actuator disc for the powered configuration. Four different stagnation pressure rises were considered across the actuator disc, representative of the expected pressure rises at cruise.

Hall et al. adopted a theoretical approach, supported with CFD analyses, to present applications of the power balance performance bookkeeping method proposed by Drela [20] to BLI configurations similar to the D8 [34]. This energy based bookkeeping method is an alternative to the conventional thrust-drag (momentum based) approach, and will be discussed in more detail in chapter 4. An axisymmetric fuselage with an actuator disc propulsor model placed at the trailing edge, ingesting the entire boundary layer, was used to demonstrate power balance based analysis and present some important findings. These findings will be elaborated on in the context of the proposed methodology in chapter 4. The D8 configuration was then assessed, and a 1D application of the power balance approach, along with the assumption of 40% fuselage boundary layer ingestion, was used to show variations of propulsor power and dissipation, with propulsor mass flow. Comparisons between a non-BLI and BLI configuration were also made. Following this, CFD simulations of the D8 fuselage with a single propulsor at the trailing edge, modeled as an actuator disc, were used to compare the flow power savings benefits of BLI vs non-BLI aircraft.

In a subsequent study [33], Hall used CFD to analyze the representative D8 geom-

etry shown in Fig. 2.10. While most of the analyses adopted a decoupled approach with flow through nacelles, motivation for a coupled study was provided, stating that "powered analysis is required to capture the details of the interactions in ultra-integrated configurations [33]" and that "powered analysis should thus be fed back iteratively into the vehicle power balance and engine cycle analyses to improve the accuracy of the power requirements and cycle performance [33]."

Decoupled Analyses: D8 System Level Assessments

Welstead [97] conducted an independent assessment of the D8 using FLOPS, comparing results to MIT's work. Welstead followed the procedure adopted by MIT [92] to morph the 737-800 into the D8 in a series of steps, and used surrogate models of the engine from TASOPT. Normalized fuel burn, maximum takeoff weight, sweep, wing loading, area and span, and component weight estimates from FLOPS and TASOPT were compared at each stage of the morphing process. Based on the differences in the results, it was observed that there was a high degree of uncertainty in areas relating to structural design and weight estimates, and low speed high angle of attack analysis. Welstead also made an important observation regarding engines, stating that "no manufacturer customizes an architecture for a single aircraft design" and that "highly integrated PAI could be an enabling technology of future commercial transports." Engine designs for the D8 have been proposed by Pratt and Whitney and are discussed in [59]. To account for the BLI benefits in the cycle, ram drag was decreased by 14% of the aircraft drag at cruise, based on recommendations from MIT.

Marien et al. at NASA [62] conducted a system level study to evaluate the vehicle level impact of a BLI propulsion system on the D8. They used ModelCenter to connect FLOPS, OpenVSP, and other custom sizing codes. FLOPS was used for the vehicle sizing, mission analysis, aerodynamics, and the engine model was devel-

oped using NPSS and WATE++ [90]. A tabular engine deck was created from the cycle model and provided to FLOPS. The engine cycle parameters were unchanged during the different sizing runs. ModelCenter was used to vary the wing area, sea level static engine thrust, and wing sweep to minimize block fuel for the given performance requirements. 40% fuselage boundary layer was assumed to be ingested by the propulsors when calculating the BLI benefits. This value was held constant during the sizing process. The reduction in wake dissipation and its subsequent impact on the profile drag was modeled as a reduction in fuselage wetted area in FLOPS. Reduction in nacelle drag as a result of partially embedding the engines was accounted for by a reduction in nacelle wetted surface area in FLOPS. Based on the assumed ingested boundary layer fraction, and fraction of fuselage dissipation occurring in the wake, an estimate for the total pressure at the inlet was obtained for the cruise flight condition. Like the ingested boundary layer fraction, the inlet recovery was not updated during the sizing process. Additionally, a fan efficiency penalty of 3.5% was assumed as a result of BLI, though a sensitivity study of fuel burn to fan efficiency was also conducted.

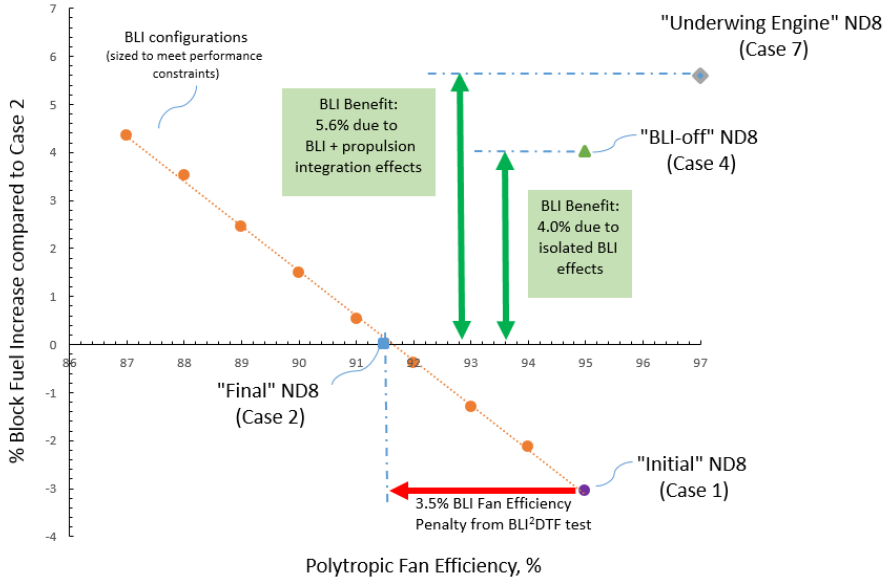

Figure 2.11: BLI system level benefits for various NASA D8 sized configurations (reproduced from [62])

Fig. 2.11 above shows the block fuel increase relative to the baseline BLI D8 version (Case 2) as a function of fan efficiency. Each point represents a configuration re-sized to meet the specified performance requirements. Case 1 represents the BLI D8 version without a fan efficiency penalty. Case 4 corresponds to a vehicle that was re-sized to meet performance requirements without BLI benefits, and showed a 4% increase in fuel requirements. This case however did not account for the propulsion-airframe integration effects needed to make a reasonable podded aircraft. Accounting for these effects in Case 7 resulted in an additional 1.6% increase. These results highlight the importance of sizing effects on the magnitude of BLI benefits. In none of these cases, however, was any mention made concerning a change in the ingested boundary layer fraction with changes in airframe and engine size. Given that the ingested fraction and all derived quantities from that were held constant, this process is a decoupled vehicle centric approach.

2.2.3 STARC-ABL

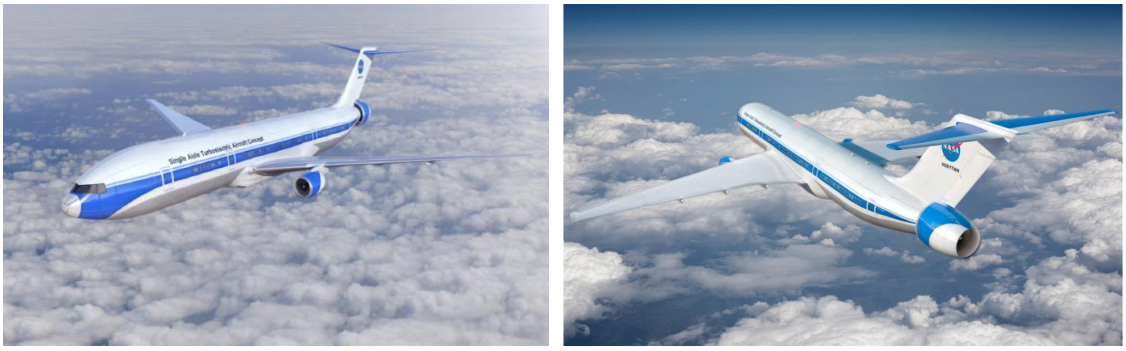

Figure 2.12: STARC-ABL concept

Decoupled Analysis: STARC-ABL Conceptual Design Proposal

The Single-Aisle Turboelectric Aircraft with Aft Boundary Layer Propulsor (STARC-ABL) is a NASA N+3 BLI concept based off a Boeing 737-800, proposed by Welstead

and Felder [98]. With a desired entry into service in 2035, this vehicle is a conventional tube and wing concept with two under-wing mounted turbofan engines and generators that extract power for an electrically driven, fuselage tail cone mounted BLI fan. The aircraft is sized for a mission similar to a notional B737-800 or A320 aircraft, with a desired 3500 nmi range. This concept was developed using FLOPS for the airframe analysis and NPSS for the engine. Specifically, aerodynamic data for the vehicle were estimated using FLOPS' Empirical Drag Technique, a low fidelity modeling approach based on wetted areas. Modifications were made to the nacelle and tail cone wetted areas to model the change in drag as a consequence of the aft propulsor integration with the fuselage. No detailed aerodynamic shaping of the tail cone geometry was conducted. The engine was based off the gFan+ model by Georgia Tech.

Boundary layer data were obtained from Boeing's viscous CFD analysis of the Subsonic Ultra Green Aircraft Research (SUGAR) fuselage and tail cone. The velocity and total pressure profiles in the boundary layer from this geometry were extracted at different axial locations at two flight conditions: Mach 0.25 at sea level, and Mach 0.7 at 42,000 ft. Following a similar approach adopted for the N3X [23], normalized versions of these profiles were then used to generate a map that could be fed to the NPSS propulsion model. Mass averaged Mach number and total pressure were calculated from the CFD profiles for each boundary layer. These mass averaged values were then normalized by the freestream conditions such that estimates at different flight conditions could be obtained from this scaling. The boundary layer height was also normalized, and was assumed to only vary with Mach number and not altitude. An interpolation scheme was used to obtain boundary layer data at flight conditions other than that obtained from the CFD results. For the specified and fixed aft fan shaft horsepower, 45% of the boundary layer height was found to be captured.

The vehicle centric approach described above used CFD sparingly to obtain boundary layer profiles. This approach allowed for quick and efficient design space explo-

ration, while incorporating some of the physics associated with the BLI, but missed a few key characteristics. First, this process could not capture the change in wake dissipation that occurred as a result of BLI, and thus a key BLI benefit was not captured. Second, viscous CFD profiles were obtained for a single fuselage at two flight conditions. Effects of the propulsor on the ingested flow field were not captured, and changes in the airframe such as wing area, as part of the sizing process, and their impact on the ingested boundary layer were also not modeled, thus missing out on the aero-propulsive coupling effects.

Decoupled Analysis: Aerodynamic Shape Optimization

Kenway and Kiris [42] conducted aerodynamic shape optimization of the fuselage diffuser and nacelle inlet for the STARC-ABL concept to minimize flow distortion at the aft fan face. Baseline geometry was provided by Welstead at NASA. RANS CFD analysis was coupled to a non-linear optimizer, and design parameters in OpenVSP controlling the aft fuselage shape and nacelle inlet were perturbed to minimize distortion. The BLI propulsor was modeled as an actuator disc in CFD. Though an actual cycle analysis wasn't conducted, thrust requirements for the propulsor at the flight conditions considered were set such that the input power required by the aft fan was 3550 hp, consistent with the system level analysis by Welstead [98]. Four optimization cases were run, two with just the fuselage and tail cone nacelle, and two with the wing-body-tail cone nacelle, but no under-wing engines or tail in either geometry. Of the two cases for a given configuration, one was a multi-point optimization (cruise, climb, takeoff) and one was single point.

Single point optimization was sufficient to minimize distortion to acceptable levels and multiple-point optimization yielded almost identical results. However, there was a clear difference in distortion for the isolated fuselage and wing-body cases. Results showed that the wing downwash had an adverse effect on the distortion, in particular

for low angle of attack cases. The authors believed that this was due to the asymmetric placement of the tail cone propulsor relative to the fuselage centerline and the asymmetric growth of the boundary layer. As a consequence of downwash effects, the optimized shapes were different for the two cases. Additionally, all optimized designs resulted in an increase in the power requirements for the fan, violating the fixed shaft horsepower specification, a constraint not explicitly defined in the optimization problem. This result highlights the necessity for conducting coupled aero-propulsive analysis to ensure consistency between the two disciplines. Impacts of BLI on the propulsion system design could not be considered given the absence of a detailed engine model in their studies.

Coupled Analyses: Gray et al.

Gray et al. conducted a series of coupled aero-propulsive studies related to the STARC-ABL concept, highlighting the importance of capturing this coupling in BLI vehicle analysis. The first study involved modeling an axisymmetric fuselage and tail cone propulsor representation of the STARC-ABL (no wings, empennage, zero angle of attack) [28]. Gray coupled RANS CFD analysis to a 1D thermodynamic cycle tool, and conducted MDA for a sweep of aft propulsor fan pressure ratios at cruise condition using the open source OpenMDAO framework as the discipline integration environment. As shown in Fig. 2.13, the total pressure p_t, temperature T_t, and mass flow $\dot{m}$ at the fan face (FF) were matched between the cycle model and CFD for each case, while the fan face static pressure, p_s, boundary condition in CFD was varied to match the flow rates at the fan face and the fan exit boundary planes in the 1D powered boundary condition representation of the engine in CFD. The propulsor diameter d_{nac} was varied to match the flow rate calculations in CFD with the requirements stipulated by the cycle code.

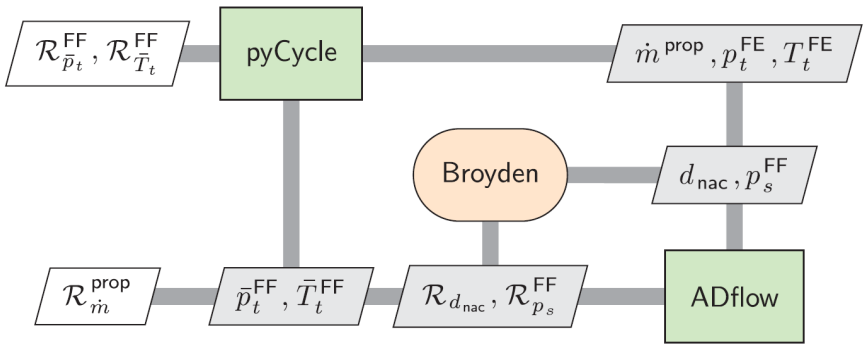

Figure 2.13: Aero-propulsive MDA by Gray et al. (reproduced from [28])

An equivalent podded configuration was also developed that was used as a baseline for comparing the BLI performance. The podded configuration consisted of analyzing the propulsor and fuselage separately, and was thus done in a decoupled manner. In addition to demonstrating the BLI benefit, Gray also showed that a decoupled approach, when used for the BLI configuration, overestimated the total pressure at the fan face, and thus inlet recovery, as shown in Fig. 2.14a. Therefore, decoupled approaches would overestimate engine performance and thus the BLI benefit. Gray also highlighted the sensitivity of the flow field over the fuselage as a result of the propulsor, for varying FPR values. Fig. 2.14b shows the aft fuselage surface pressure coefficient differences for two FPR values, relative to the podded case, while Fig. 2.14c shows the variation in boundary layer profiles. The flow field variations explain the differences in the decoupled and coupled total pressure results, and highlight the necessity for capturing the aero-propulsive interactions in the analysis.

Having demonstrated the importance of MDA for BLI, Gray extended this work to include optimization. Using a more realistic geometry with wings and empennage that was representative of the STARC-ABL configuration, Gray conducted MDAO studies by optimizing the tail cone portion of the fuselage and nacelle shape to minimize the power requirements for the aft BLI propulsor [27]. Net axial force, lift, geometric thickness, and nozzle pressure ratio constraints were imposed. The same approach as before was used to model the BLI vehicle propulsor and aerodynamics, except now

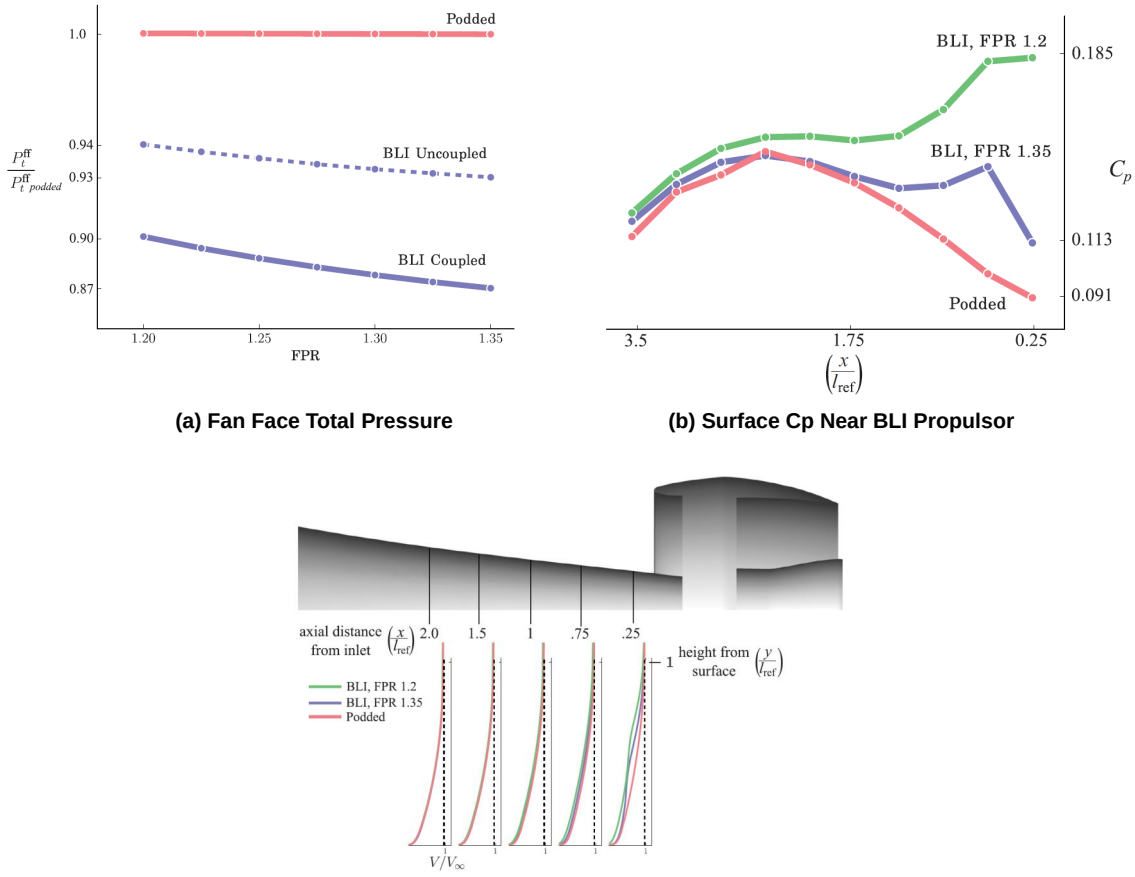

(a) Fan Face Total Pressure

(b) Surface Cp Near BLI Propulsor

(c) Boundary Layer Profiles Near BLI Propulsor

Figure 2.14: Key results from Gray et al. MDA (reproduced from [28])

the propulsor was modeled in CFD as body force actuator zone, unlike the powered 1D boundary condition approach used previously. A cycle model was still used to quantify the shaft power requirements for generating the thrust measured in CFD. Three optimization cases were conducted for three different net force requirements. Results showed differences in the optimized geometries for each case and the distortion patterns showed sensitivity to wing downwash and vertical tail, corroborating findings by Kenway and Kiris [42].

This work was extended further to include the propulsor design variable FPR as well in the optimization problem formulation [26]. FPR, fan face static pressure, and hundreds of design variables controlling the fuselage and nacelle shapes were per-

turbed to find the design that minimized the shaft power requirements for the tail cone propulsor, given a net axial force requirement. This was done for the axisymmetric fuselage and tail cone propulsor case, rather than the 3D representative STARC-ABL geometry. As shown in Fig. 2.15, aero-propulsive compatibility was enforced in the optimziation problem through constraints, shown in pink. These constraints involved matching flow rates at the fan face and fan exit in CFD, total pressure, temperature and shaft power matching between CFD and the cycle code, and a net vehicle axial force target matching.

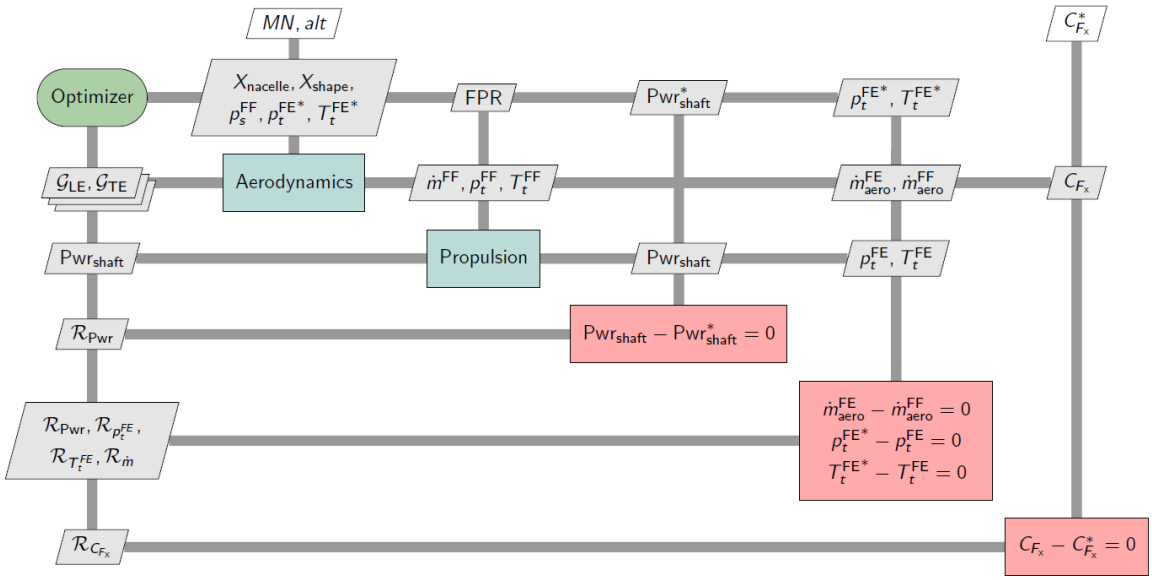

Figure 2.15: Aero-propulsive MDAO by Gray et al. (reproduced from [26])

Optimizations were conducted for both BLI and the podded baseline configurations for different values of net axial force requirements, and the power saving coefficient (PSC) from the optimized results was tracked. Results indicated that smaller BLI propulsors showed the best PSC, with PSC decreasing with an increase in propulsor size. Results also demonstrated the importance of using a fully coupled analysis. Coupling effects of the propulsor were shown to vary with the size, which resulted in a non-linear trend in the BLI benefits.

Coupled Analyses: Ordaz et al.

Ordaz et al. presented an aero-propulsive design and analysis framework that integrated OpenVSP for geometry modeling with CFD and NPSS in ModelCenter [70]. They demonstrated the framework capability on design optimization of a business jet fuselage with a tail cone propulsor to minimize distortion at the Aerodynamic Interface Plane (AIP) [71]. The optimization was achieved by modifying the inlet and fuselage section entering the inlet using an adjoint based approach. A simplified ducted fan model was sized for a fixed mass flow requirement. An iterative feedback loop involving the engine boundary conditions and pressure recovery as coupling variables was converged using an MDA solver. However, the authors made the assumption that boundary conditions at the AIP and fan exit would not change much during optimization, for small geometry changes, and were thus kept fixed after the initial MDA convergence. Additionally, only a single operating point was considered in the problem. A similar approach was adopted for the STARC-ABL geometry (without the under-wing engines) [71] to demonstrate MDA for the concept. No shape optimization was done. The results showed significant variations in the inlet pressure recovery and net thrust over the course of the MDA iterations, highlighting the importance of coupled analyses for BLI.

2.2.4 Onera NOVA-BLI

Figure 2.16: NOVA-BLI concept (reproduced from [101])

The NOVA (Nextgen Onera Versatile Aircraft) BLI concept is Onera's BLI proposal. With a desired entry into service by 2025, this is a 180 passenger vehicle designed to fly at Mach 0.82 with a design range of 3000 nmi. NOVA has a few similarities with the D8, however, it places the embedded engines on the side of the fuselage rather than on the top, thus allowing for a more conventional empennage. The conceptual design proposal for NOVA was presented in [101], however the focus was predominantly on the aerodynamic design considerations of the fuselage and wing, with some discussion on the structural aspects of those designs. The approach for vehicle sizing was conventional, using semi-empirical methods for weights, structures, aerodynamics, and propulsion, with constraints for runway length, landing speed, etc. accounted for in the sizing process. First order assumptions were used to account for BLI impacts on the design. BLI benefits relative to a podded configuration were modeled as a removal of the engine pylons (wetted area and weight reduction) and moving of the engines closer to the centerline. The impact of fan pressure ratio on the sizing process was accounted for by modeling the associated change in fan diameter, engine and nacelle weight, and specific fuel consumption from previously published data. The wing surface area and maximum thrust at ground level were adjusted for each FPR to achieve the lowest possible fuel consumption. An engine sizing tool was developed to obtain engine boundary conditions that could be used in powered CFD analyses of the airframe-engine combination. 3D RANS simulations were conducted to determine drag values for the airframe. While CFD was used to analyze the detailed aerodynamic characteristics of the wing design, fuselage, and nacelle design (with fixed engine BCs), it wasn't used to analyze the BLI effects and no high fidelity BLI related coupling between the aerodynamics and propulsion system was modeled. CFD was also used to analyze thrust vectoring effects for the non-BLI configuration, and analyze the optimum placement of the engine on the wing for the under-wing baselines. For the BLI configuration, CFD was only used

for detailed inlet design studies, where a target mass flow rate was imposed for the fan actuator disc model. Impact of the ingested boundary layer on engine sizing and performance, and its subsequent feedback to the airframe wasn't directly considered. Only the first order assumption mentioned above was made at this stage. In Ref. [100], more detailed CFD studies were conducted for the BLI configuration. The focus was on quantifying the aero-propulsive benefit of the BLI concept relative to a similar podded configuration using two different actuator disc models in 3D RANS CFD. No aero-propulsive coupling effects were considered.

CHAPTER 3
FORMULATION

In the previous chapter, a background on the diverse modeling approaches adopted for BLI concepts was presented. A few observations can be made from the reviewed literature. These observations highlight certain common practices, their benefits and limitations, and identify gaps, thus forming the basis for the BLI aircraft conceptual design method proposed in this thesis. Key requirements for this process, derived from the observations, and an informal overview of the main idea behind this methodology are presented. This preview is intended to give readers a sense of where this dissertation is headed. Research questions and associated hypotheses stemming from the gaps in literature are then discussed in this chapter.

3.1 Observations from Literature

Fig. 3.1 summarizes the literature review presented in the previous chapter. Coupled analyses are highlighted using filled markers. Studies are tagged based on the concept they relate to and the lead author for a given study. Studies involving wind tunnel testing are not shown since the focus of this thesis and most conceptual design methodologies is on computer based modeling. Certain studies used different levels of fidelity for a particular discipline, with individual markers representing each fidelity level and arrows connecting markers related to the same study. Observations 1-4 relate to model fidelity levels used for the aerodynamics and propulsion disciplines, while observations 5-7 pertain to the treatment of aero-propulsive coupling in various studies. With regards to the favored fidelity level for propulsion, the following observation can be made:

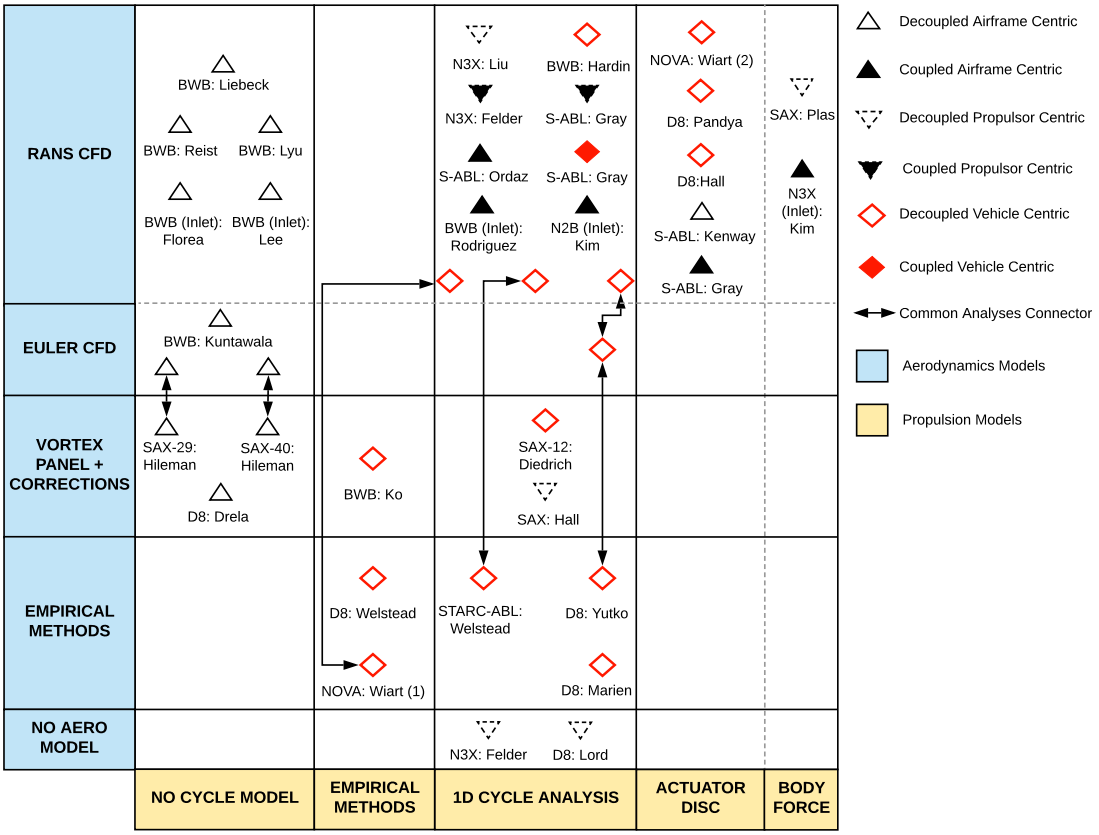

Figure 3.1: Summary of literature review

> **Observation 1:** 1D thermodynamic cycle analysis is typically used for propulsor modeling.

Majority of BLI studies that consider the propulsor use a 1D thermodynamic cycle model, with analysis conducted using industry standard tools such as NPSS, GasTurb, or equivalent in-house codes. While using empirical regressions from previously published engine data, like in Ko's MDO approach [46] for example, may be easier and quicker to implement in cases where metrics like engine weight and TSFC are needed for vehicle level mission analysis, such approaches are inadequate when a new engine has to be designed. In the case of BLI concepts, where historical data are sparse, a first-principles approach is needed for designing engines and analyzing performance. Cycle analysis is rather inexpensive, providing designers an efficient way to conduct

trade studies. Parametric investigation of the impact of key cycle design parameters and component efficiencies on the propulsor performance, and in the case of coupled analyses, airframe performance as well, is possible. Engine decks specifying thrust available and TSFC at different points in the flight envelope can easily be generated by cycle codes, that can then be used by an airframe sizing tool to conduct mission analysis, like in the case of the SAX-12 airframe [18] and Marien's D8 system level study [62] for example. Cycle analyses are also used to provide boundary conditions to the powered engine representation in CFD as seen in the coupled approaches by Rodriguez [79], Gray [28, 26], and Ordaz [71] for example. The versatility and computationally inexpensive nature of cycle analysis codes makes it a prime choice for any conceptual design level BLI vehicle study.

Observation 2: CFD is used to model complex flow physics that drive BLI vehicle design decisions such as nacelle placement, inlet shaping, etc.

Low fidelity drag buildup approaches based on wetted areas and shape factors, vortex panel methods, empirical corrections or low-medium fidelity estimations for compressibility and viscous effects have been used in conceptual design of the SAX, D8, STARC-ABL and NOVA-BLI to size the vehicle and evaluate performance. However, these studies and several others have recognized the limitations of these low fidelity models for capturing complex physics like shocks, 3D boundary layer features, flow separation, and other transonic flow effects that have a significant influence on the vehicle design, thereby using CFD to augment aerodynamic modeling at the conceptual design stage.

The BWB conceptual design proposal by Liebeck [56, 55] used CFD to optimize nacelle placement away from the influence of the outboard wing shock, as well as analyze different inlet designs and locations, with flow quality at the fan being a critical factor. The SAX-29/40 airframe design methodology [38, 37] used Euler CFD to

verify airfoil loading and shock strengths at every major design iteration, with RANS CFD used at the end to verify the overall process. Aurora [104] used RANS CFD to analyze engine integration with the D8 airframe and Euler CFD to mature the wing design, while assessing overall airframe performance. The STARC-ABL conceptual design proposal [98] used CFD generated boundary layer profiles for modeling the BLI impact, an approach that some inlet design (Florea [24]) and engine cycle design studies (Felder [23], Liu [57]) also adopted. Onera's BLI concept study [101] also used CFD to design and analyze the wing, nacelle etc. Thus, CFD is needed at conceptual design to enhance the aerodynamic analysis at this stage and drive major design decisions that would not be possible with the information available from merely using low fidelity tools. However, there are factors that limit CFD usage in BLI vehicle conceptual design:

> **Observation 3:** Computational expense of CFD limits the extent to which it can be used at the conceptual design stage.

Advances in computational resources have allowed researchers to use CFD more extensively for detailed aerodynamic analyses, however, CFD is still time consuming, both to set up and generate high quality meshes, and to run, which limits to extent to which CFD can be used for design space exploration studies in conceptual design. As of today, CFD is still not fast enough to be embedded directly in vehicle sizing tool like FLOPS as an aerodynamics module. To provide some context regarding the computational expense of CFD, consider the author's prior research into CFD analyses of over-wing nacelles for commercial transport aircraft [10]. 3D RANS CFD analysis of the wing-body-nacelle combination using an unstructured Cartesian mesh of size $\approx$ 30M with the commercially available STAR-CCM+ CFD software by Siemens, required 350 CPU-hrs, or about 14.5 hrs of wall clock time for the residuals to converge to acceptable levels, using a High Performance Computing Cluster.

Optimization of this wing-body-nacelle combination required 18 iterations of SciPy's SLSQP optimizer, and assuming 2 CFD function calls per iteration for the line search based on previous experience, 36 CFD calls for a single flight condition optimization of this configuration would have taken 522 hours (≈22 days) of wall time with the same amount of computational resources.

Given the cost of a single CFD simulation, MDA studies, aerodynamic shape optimization, or aero-propulsive coupled optimization only exacerbate the computational burden. Some of the studies reviewed used different ways to minimize this expense. For example, Gray [28, 26] used a non-representative, axisymmetric model for the STARC-ABL, thereby reducing the computational time by orders of magnitude. Ordaz [71] only conducted MDA for the baseline geometry, assuming that small geometry changes resulting from optimization would not affect the boundary conditions significantly, an assumption that is no longer valid for large geometry changes at the vehicle sizing stage. Some other studies that used CFD generated profiles, obtained them from a single simulation of a fixed airframe and flight condition (Florea [24], Liu [57], Hardin [35]), thereby ignoring the aero-propulsive interactions and making an assumption regarding the similarity of profiles at different flight conditions when needed (Felder [23], Welstead [98]).

Another challenge with using CFD in early conceptual design is the level of geometry detail that one needs to consider to obtain performance estimates for a vehicle. Metrics like drag, lift, pitching moment, etc. are rather sensitive to details like fairings, winglets, fuselage nose contours, etc. in addition to the usual candidates like airfoils, planform shape, etc. The dimensionality of the problem is thus opened up considerably when using CFD for performance analysis than when using lower fidelity aerodynamic models. It is not very practical to define detailed airframe contour parameters like spline fit coefficients and vehicle sizing parameters at the same time, since the latter require aerodynamic analysis at all points in the mission profile,

something that is too expensive with CFD, while the former cannot always be appropriately modeled using lower fidelity aerodynamic models. For this reason, low fidelity approaches have traditionally been used for vehicle sizing, with CFD used for detailed design and analysis once a few promising baselines have been established.

With BLI, as discussed before, there is a need for CFD analysis at the very early stages of design. If one restricts the modeling scope to just capturing the ingested boundary layer characteristics relevant for a given design/analysis problem, then how does the dimensionality of the problem reduce for conceptual design purposes? Guidelines on defining which geometry OML features for CFD analysis need to be considered in conceptual design and which can be tailored later in preliminary design is helpful. These guidelines will enable CFD usage for modeling BLI physics at a stage where design knowledge is limited and high dimensionality adds additional degrees of freedom which cannot be tractably addressed in conceptual design. Considering the BLI studies that have used CFD to generate boundary layer profiles that have served as inputs for a given analysis, the following observation can be made:

> **Observation 4:** Several BLI studies requiring boundary layer properties as inputs used flow profiles provided by Boeing from CFD analysis of fixed geometries.

Florea [24], Hardin [35], and Felder for the N3X [23], obtained profiles from Boeing's CFD analysis of the BWB, while Welstead [98] used Boeing's SUGAR CFD analysis to obtain representative profiles for the STARC-ABL conceptual design. Other studies like Liu [57] used profiles from a fixed geometry similar to the N3X, while Lee [52] obtained baseline inlet geometry from Boeing, but used a flat plate to model the airframe. The study by Kenway and Kiris [42] (who used baseline STARC-ABL geometry provided by Welstead at NASA) provides some insight into the impacts of geometry detail on the boundary layer characteristics. As discussed in chapter 2, they found that wing downwash had an impact on the distortion pattern at the BLI

propulsor AIP. This finding suggests that an axisymmetric model, such as that used by Gray, is not adequate for modeling the BLI characteristics for the STARC-ABL. In general, however, discussion concerning the sensitivity of CFD calculated boundary layer characteristics on the geometry features could not be found in the reviewed literature.

Having discussed the main observations concerning model fidelity in BLI studies, a few observations can now be made regarding the degree of coupling captured by the different analyses. The first observation is as follows:

> **Observation 5:** A significant number of studies relating to BLI concepts decouple the airframe and propulsion system design and/or analysis.

Decoupled approaches for BLI concepts are particularly useful when there is limited design knowledge regarding the airframe and/or the propulsor, as is usually the case in conceptual design. Conceptual proposals for the BWB, D8, STARC-ABL, and NOVA-BLI all treated the BLI problem in a decoupled fashion. Decoupled approaches are particularly amenable at this stage since, as Hendricks [36] notes, decoupled approaches do not need an integrated design environment which coordinates the execution of and the exchange of information between the aerodynamics and propulsion analysis codes. This enables a "traditional division of modeling"[36], allowing researchers to focus on their areas of expertise and use any fidelity level for modeling their disciplines, without having to incur the computational expense of ensuring compatibility with other disciplinary tools. Rapid design space exploration is thus possible early in the design stage enabling growth of design knowledge. The SAX-29 and SAX-40 concept design methodologies are prime examples of this strategy. Decoupled approaches also facilitate development of new methodologies for design refinement by restricting the modeling scope, such as the BWB airframe optimization approaches by Kuntawala [48], Reist [77], and Lyu [61]. These methodologies

can then later be embedded in coupled analyses. However, despite the advantages of a decoupled approach, studies have shown limitations of this strategy for highly integrated concepts like BLI. This observation can be formulated as follows:

> **Observation 6:** Decoupled analyses fail to capture the aero-propulsive interactions and their impact on vehicle design.

As discussed before, BLI concepts exhibit stronger interactions between the airframe aerodynamics and propulsion system relative to conventional designs with podded engines. Coupled analyses in literature, such as Felder's work with the N3X engine [23], Gray's [28, 26] and Ordaz's [71] analyses of the STARC-ABL concept have shown the significance of these interactions. Decoupled approaches fail to capture the interdependency between aerodynamics and propulsion, and the results are inconsistent between the two disciplines, given that interdisciplinary compatibility in terms of boundary conditions is not enforced. Rodriguez notes the deficiency of decoupled approaches, stating that "state-of-the-art aerodynamic design tools (such as Navier-Stokes-based shape optimization schemes) can reduce drag, but cannot predict the trade-off on engine performance. Likewise, engine simulators can predict the effects of ingesting boundary layer on propulsive efficiency, but cannot address the trade-off on aerodynamic performance.[79]" This casts a degree of uncertainty in the design and the associated performance of the vehicle. Additionally, maximizing fuel burn benefits for BLI concepts requires PAI efforts that maximize favorable and minimize detrimental interactions between the airframe and propulsor. Decoupled approaches cannot be used to optimize the integrated vehicle since they do not capture this interaction. Thus coupled methodologies for aero-propulsive design and analysis is the most appropriate way for BLI concepts. Regarding the coupled approaches reviewed in the previous chapter, the following observation can be made:

Observation 7: Coupled aero-propulsive methodologies found in literature for BLI concepts are typically suited for the preliminary design stage as a means for design refinement.

In conceptual design, when design knowledge is limited, design space exploration is essential. Parametric variations of key vehicle features like wing area, aspect ratio, sweep, etc., facilitate this process. A parametric approach coupled to computationally inexpensive analyses enable efficient evaluation of thousands of designs. For BLI concepts, there is a need to capture the aero-propulsive coupling in this parametric design environment. However, the coupled approaches presented in literature are better suited to post conceptual design stages where the vehicle has already been sized, and it is then necessary to refine the contours of the vehicle OML to minimize adverse flow features like shocks or separation that are inimical to performance.

Coupled design optimization approaches by Gray [27, 26], Ordaz [71], and Kim [43] parameterize geometry changes, rather than the geometry itself. This parametrization approach, known as Free Form Deformation (FFD) [80, 41] (see Fig. 3.2), is best suited for achieving small to medium levels of geometry changes, and is thus appropriate for the preliminary design stage where such small geometry changes, coupled with high fidelity analyses that can model complex flow physics, can have a substantial impact on vehicle performance [80]. The mesh topology is fixed during the optimization process, thus allowing for automatic deformation of grids, rather than having to re-mesh after each deformation [80]. Larger, more complex geometry changes, typically associated with the vehicle sizing process, are difficult to achieve using this approach given that negative volume cells can be generated in the mesh [41], and while mesh deformation approaches that minimize these occurrences for larger changes are being developed, achieving large variations of geometry with CFD based techniques is challenging.

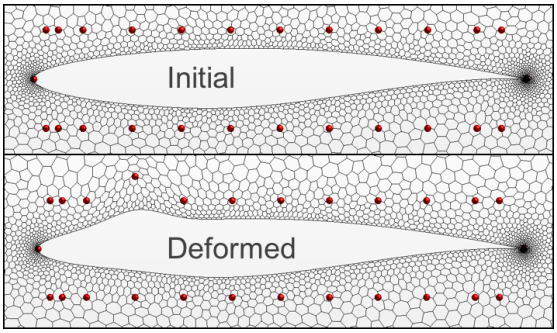

Figure 3.2: Free Form Deformation (FFD) parameterization of an airfoil. Perturbation of control points (red) deforms the mesh, thus deforming the geometry (reproduced from [10])

Restriction to small geometry changes implies that the above approaches are best suited when the aircraft layout is mostly defined, with structural considerations accounted for in conceptual design. This limitation was also noted by Rodriguez with his inlet optimization methodology. Additionally, the coupled analyses reviewed are only conducted at one flight condition. The computational expense of reaching interdisciplinary compatibility, using high fidelity analyses, at each point in the flight envelope is another major limitation of these approaches. As a result, this process is unsuitable at the conceptual design stage where multiple flight conditions at key points in the mission profile need to be considered. Felder's approach [23] for modeling the boundary layer impacts on the propulsor using fixed CFD profiles, but varying the capture height, and accounting for multiple flight conditions, is one way the aero-propulsive coupling can be captured in conceptual design of BLI propulsors. However, this approach is not fully coupled given that the profile shapes are assumed to remain the same throughout the flight envelope, and for varying propulsor sizes, the latter shown by Gray to be invalid. Additionally, for vehicle centric design studies where the airframe size is also varying, the assumption of fixed boundary layer profiles and properties is no longer appropriate.

3.2 The Need for a New Approach

Based on the presented studies and the observations above, it is apparent that there is a gap in the literature. This gap leads to the research objective introduced in chapter 1, repeated here for convenience.

> **Research Objective:** Develop a parametric methodology for the conceptual design and analysis of boundary layer ingesting aircraft that captures the interaction between airframe and propulsor design, and quantifies the consequences of ignoring aero-propulsive coupling at the vehicle sizing and cycle design stage.

There is a need for a new approach that addresses previously highlighted deficiencies, while incorporating useful aspects of proposed methodologies in literature. The following requirements need to be fulfilled:

Requirement 1: Impacts of the airframe and propulsor on the ingested boundary layer characteristics must be considered in a parametric fashion.

Rationale: Airframe design and engine cycle section in conceptual design involve trade space exploration studies. Single point analysis of an airframe in CFD to obtain estimates of the BLI effects, as conducted in several studies in literature, is not adequate to cover the entire design space. A parametric representation of the BLI effects is needed to account for BLI physics at every design point in the exploration studies.

Requirement 2: Impacts of variations in flight Mach number and altitude on the boundary layer characteristics must be considered.

Rationale: Vehicle sizing requires a mission, which involves multiple flight conditions, while the engine is also not typically de-

signed for a single operating point. Accounting for flight conditions on the measured BLI effects is thus required.

Requirement 3: The BLI effects must be updated at each iteration as the airframe and propulsor size vary in the vehicle sizing loop, till convergence is achieved i.e., the engine size matches the requirements set by the sized airframe, and the calculated boundary layer effects used in the sizing are consistent with the resulting vehicle.

Rationale: Requirement is derived from observation 6, which highlights deficiencies of decoupled approaches for BLI concepts in literature and emphasizes the need for capturing the coupling.

Requirement 4: Low to medium fidelity aerodynamic models, like drag buildup approaches for example, must be leveraged wherever suitable to enable rapid design space exploration and aerodynamic analysis at all points in the flight envelope.

Rationale: Observation 3 highlighted the computational expense of CFD and the impracticality of using it as an aerodynamic analysis module in vehicle sizing tools. CFD should only be used when required, relying on lower fidelity analyses where appropriate to ensure conceptual design of BLI vehicles is manageable.

Requirement 5: RANS CFD must be used to complement low fidelity aerodynamic analysis by obtaining estimates for the ingested boundary layer characteristics.

Rationale: Requirement can be traced to observation 2, which showed how BLI studies in literature used CFD to make design decisions not possible with just low fidelity aerodynamics modeling.

Requirement 6: 1D cycle analysis must be the minimum fidelity level used for propulsor modeling.

Rationale: Requirement is derived from observation 1 which showed the prevalence of 1D cycle modeling in literature and the deficiencies of empirical modeling techniques for BLI propulsors.

The idea behind the above requirements is to develop a BLI conceptual design methodology similar to the approach adopted for sizing conventional vehicles with non-BLI engines, but enhance that method by modeling elements that are unique to BLI concepts. These elements, which can be called the BLI effects, model changes in performance as a result of ingesting the boundary layer. Capturing these elements early in the design stage improves confidence in the baseline designs generated, and consequently high fidelity tools and computational resources can be used more efficiently only on designs that are most likely to meet the performance requirements. Failure to capture these elements early in the design process can lead to a greater degree of uncertainty, and may lead to wastage of resources on designs that upon more detailed inspection require excessive redesign to meet requirements.

Fig. 3.3 shows the extended design structure matrices (XDSM) [50] presenting a high level comparison of the conventional (non-BLI) vehicle sizing process to the proposed coupled BLI vehicle sizing method. The vehicle sizing loop can be represented in general terms as a MDA problem between aerodynamics and propulsion, as shown in Fig. 3.3. For conventional concepts with podded engines, the vehicle sizing loop begins with sizing the engine (Process 1 in Fig. 3.3a) for chosen values of cycle design parameters and other propulsor design variables, represented by the vector $\mathbf{x}_\mathrm{P}$ in the figure. The engine is sized for assumed thrust requirements (targets) at different design points, contained in the vector $\mathbf{y}_\mathrm{A}^t$. The sized engine is then used to generate engine decks, and provide values for engine weight, length, and maximum diameter, represented by the vector $\mathbf{y}_\mathrm{P}$, to the airframe sizing module (Process 2).

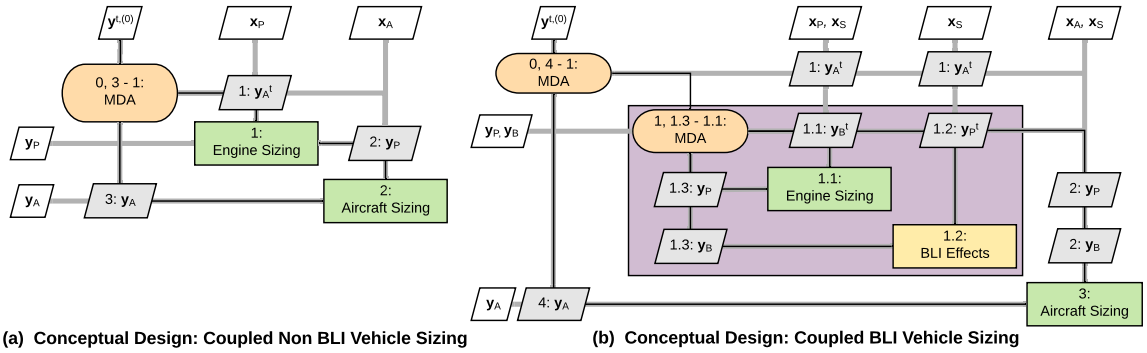

Figure 3.3: XDSMs comparing the sizing process for non BLI and BLI vehicles

For a given set of airframe design parameters such as airfoils, wing sweep, fuselage length, etc., captured by $\mathbf{x}_\mathrm{A}$, and coupling variables from the engine module, $\mathbf{y}_\mathrm{P}$, the airframe is sized, run through the mission, and the thrust requirements are compared to the thrust availability from the provided engine decks. If there is a mismatch, a thrust scaling factor, contained in $\mathbf{y}_\mathrm{A}$, is passed back to the engine module to re-size the engine for the same cycle design parameters. This process is repeated till convergence i.e., thrust available matches the thrust requirements.

The proposed BLI vehicle sizing process in Fig. 3.3b includes an additional analysis module that provides estimates for the ingested boundary layer characteristics. As discussed before, CFD is the most appropriate modeling fidelity level for capturing the BLI effects. However, MDA(O) approaches using CFD presented in literature are too expensive and not suited for vehicle sizing studies. The expense of CFD also prevents it from being used as a replacement for the empirical methods currently used in vehicle sizing tools like FLOPS. To minimize the computational expense of CFD while retaining the inexpensive nature of conceptual design models, a compromise is made. CFD can be used to formulate semi-empirical models of the BLI effects as a function of airframe and propulsor design parameters and coupling variables, $\mathbf{x}_\mathrm{S}, \mathbf{y}_\mathrm{P}, \mathbf{y}_\mathrm{A}$ at various flight conditions. This parametric representation of the BLI effects is contained in box 1.2 in Fig. 3.3b. The vectors $\mathbf{x}_\mathrm{P}$ and $\mathbf{x}_\mathrm{A}$ now represent design variables local to the propulsion and aerodynamics disciplines, while $\mathbf{x}_\mathrm{S}$ represents the airframe

and propulsor variables that influence the BLI effects. The BLI effects iteratively correct engine ambient inputs and performance within the sizing stage, represented by the sub-MDA process 1 in Fig. 3.3b. The purple box can thus be thought of as a BLI effects enhanced engine sizing stage. The rest of the process is similar to the non-BLI sizing procedure, except convergence is now achieved when the engine is sized correctly for the airframe, and the BLI effects calculated are consistent with the sized vehicle and input geometry parameters. This process still relies on lower fidelity aerodynamic analysis for airframe sizing, but uses surrogates generated from CFD to capture physics that lower fidelity tools cannot model, i.e., the boundary layer properties. This procedure allows one to efficiently size BLI vehicles, conduct trade studies, and optimize the airframe and propulsor design simultaneously in a coupled fashion in conceptual design.

A formal description of the methodology and associated theory is presented in the following chapter. Research questions that arise from gaps in the literature and associated hypotheses that will be tested, are discussed in the next section.

3.3 Research Questions and Hypotheses

Observation 5 highlighted the largely decoupled nature of BLI studies in literature, while observation 6 commented on deficiencies of these decoupled approaches, emphasizing the need for coupled aero-propulsive design and analysis, based on findings from such studies. However, observation 7 noted that these coupled approaches have been adopted for design refinement and analysis only after the vehicle has been sized. A natural question thus arises concerning the need for and impact of coupled analyses at the vehicle sizing stage, a question that cannot be answered from the reviewed literature given the absence of an appropriate parametric and coupled methodology for BLI vehicle sizing and engine cycle design. The overarching research question that this thesis answers with the proposed approach can be formulated as follows:

Research Question 1: What are the consequences of ignoring the aero-propulsive coupling resulting from BLI on vehicle sizing, engine cycle design, and vehicle performance?

Consider a hypothetical scenario illustrated in Fig. 3.4. For a given mission profile and maximum takeoff weight (MTOW) constraints, BLI and podded engine vehicles are sized for four different design FPR values, and the resulting vehicle fuel burn is tracked. A BLI benefit is assumed for this scenario, thus placing the podded engine fuel burn curve above the BLI vehicle curves. The BLI vehicles are sized using two different approaches. In the decoupled approach, the airframe and engine are sized using profiles from a CFD solution of a single fixed and representative airframe, similar to the process adopted in several studies in the literature. The profiles are not updated over the course of the sizing process. In the coupled approach, the vehicle is sized using a parametric representation of the BLI characteristics as a function of geometry, flight conditions, and propulsor variables in a MDA environment. Data points for the decoupled approach are shown with error bars, depicting error in the solution solely from the absence of a coupled aero-propulsive model. What is this

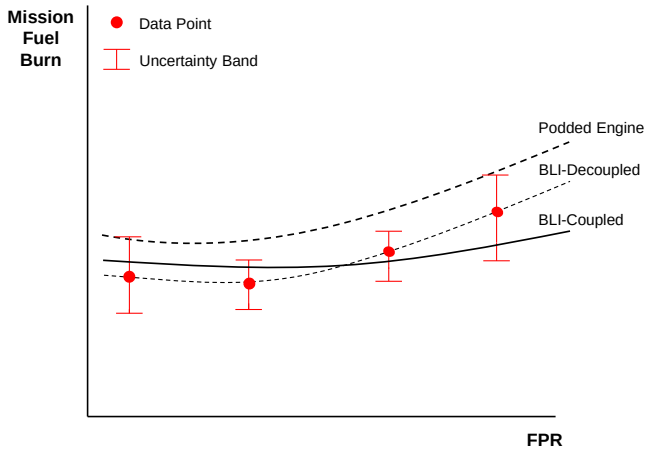

Figure 3.4: Hypothetical difference in mission fuel burn estimates using decoupled and coupled approaches

error? What does the 'BLI-Coupled' curve look like relative to the 'BLI-Decoupled', not just for FPR, but also for other sizing parameters like wing loading. How does coupling play a role if vehicle optimization is now part of the picture? What are the differences in the sized vehicle features and cycle designs between the decoupled and coupled approaches if constraints are imposed on range or fuel weight, for the same performance requirements? Determining the quantitative impact of ignoring aero-propulsive coupling at the vehicle sizing and cycle design stage is the primary objective behind research question 1. A formal hypothesis can be posed as follows:

> **Hypothesis 1:** If aero-propulsive coupling is ignored at the vehicle sizing stage, then the error introduced by neglecting throttle dependent physics and variations in airframe and engine size on the BLI effects will result in an under-sized and infeasible vehicle if the BLI benefits are overestimated. In contrast, the vehicle is over-sized if the BLI benefits are underestimated. Significance of the aero-propulsive interaction is determined by the effective contribution of the wing to the BLI effects, which is driven by the engine location. Vehicle design and performance differences between the decoupled and coupled approaches will be more severe in configurations where the wing has a more significant impact on engine inflow.

A coupled design methodology results in airframe and propulsion system size and performance that are consistent with the state of the boundary layer being ingested by the propulsor. By using fixed boundary layer profiles generated from a representative airframe geometry, interactions between the airframe and propulsor, as well as impacts of changes in their size are not captured, as discussed before in observation 6. Underestimating the BLI benefits leads to an over-sized engine, which increases engine weight and overall drag. This results in an increase in fuel burn, thus increasing fuel weight requirements for a specified range constraint. The overall aircraft weight is thus penalized, which either reduces payload carrying capability, or places more

stringent constraints on other airframe component weights if MTOW is constrained. Increase in aircraft weight is matched by a corresponding scaling in wing planform area, for the same wing loading, which in turn increases wetted area and overall airframe drag. Even if the wing loading is allowed to vary, an increase in fuel weight requirements may force designers to scale up the wing planform to accommodate the extra fuel. On the other hand, overestimating the BLI benefits will result in an undersized vehicle and would thus not be feasible.

Given the nature of the problem, there will always be some degree of interaction between the airframe and propulsion system, but factors like airframe OML definition, location of the engine relative to the wing, propulsor size, and operating conditions, play a role in defining the strength of this interaction. Thus, to address research question 1, it is also essential to determine the sensitivity of the ingested boundary layer characteristics to these factors. From the discussion relating to observation 4, it was established that the reviewed literature did not provide definitive answers concerning the sensitivity of the BLI effects to the airframe geometry definition, a question that can be formulated as follows:

> **Research Question 2:** What features of the airframe OML and external layout need to be considered when generating a parametric representation of the BLI effects using CFD in conceptual design, and what features can be defaulted?

In idealized 3D boundary layer theory, at any given point there is a zone of influence and a zone of dependence that can be identified from examining the characteristics and sub-characteristics of the governing equations [96] as shown in Fig. 3.5. As explained by McLean [66], for a column normal to the surface through a given point P, the extents of these zones are defined by the "widest range of streamline directions passing through the column"[66]. Thus, the flow at every point in this column is dependent on properties of the streamlines contained within the zone of

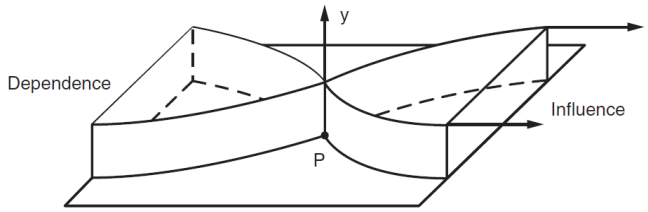

Figure 3.5: Zones of influence and dependence in 3D boundary layers (reproduced from [66])

dependence, while the flow properties along the column at P affect the streamlines contained in the zone of influence. McLean also highlights the finite influence of upstream perturbations on the downstream boundary layer flow by comparing two flows, with one subjected to a small patch of surface roughness. McLean states that "when a boundary-layer flow is perturbed in some way, it remembers the perturbation and then gradually forgets" [66]. In other words, impact of small upstream perturbations in the zone of dependence decays after a finite distance.

In idealized theory, there is no influence or dependence of the flow outside these zones on the flow properties along the column at P. Flow in the zone of influence can only have an indirect upstream impact if the flow affects the externally imposed pressure gradient. If the change is small, such as that introduced by a small bump on the surface in the zone of influence, then as McLean claims, the direct upstream influence is limited to a small distance. If however there is flow separation as a result of this disturbance, the upstream influence is more significant. Lastly, McLean explains that for real flows where the effect of lateral viscous diffusion is present, the effects of flow outside the idealized zones are only significant over distances on the order of the boundary layer thickness. The discussion above implies that viscous effects are more localized than pressure effects. The latter are predominantly driven by the inviscid flow field variations, determined by the shape of the entire airframe, while the former are more strongly influenced by the geometry that fall within the zone of dependence of the boundary layer.

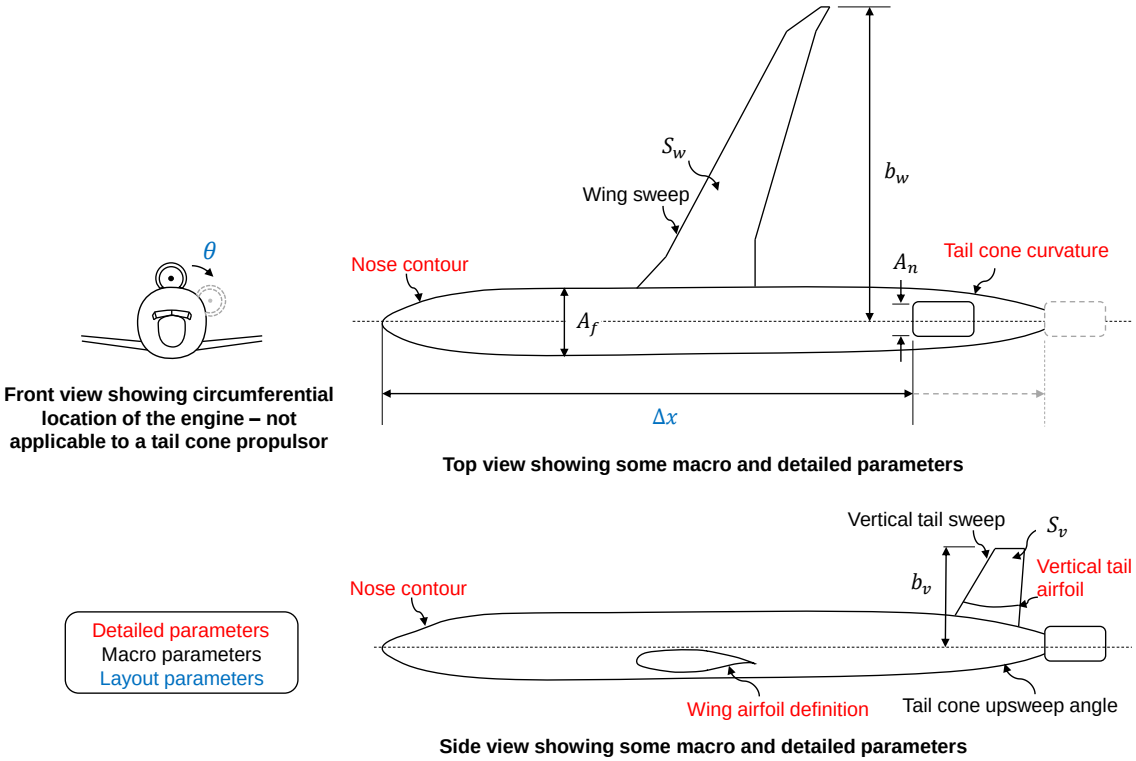

Figure 3.6: Illustration highlighting some possible airframe OML and layout parameters that affect the ingested boundary layer characteristics

The airframe geometry OML can be defined by two types of parameters: macro and detailed. At the most general level, macro parameters quantify lengths, areas, and angles, i.e., quantities that one typically associates with conceptual design of an aircraft. Detailed parameters on the other hand define geometry features like curvature radii, airfoil camber, etc. These are finer features of the geometry that add definition to the airframe shape. Typically, it is these variables that are perturbed as part of the design refinement process in preliminary design. Fig. 3.6 shows examples of a few macro and detailed parameters. With regards to modeling BLI effects, macro and detailed features that have the strongest impact on the BLI effects can be called active variables, while those that have a relatively smaller impact, and can thus be defaulted, can be called inactive variables. To clarify, this terminology is not related to the field of active subspaces. The terms 'active' and 'inactive' are merely used to highlight the importance of some design parameters over others.

When considering the impact of airframe geometry on the ingested boundary layer properties, where the boundary layer is being ingested is critical. This is determined by the position of the engine, specifically, the circumferential (θ) and axial location (Δx) on the airframe as shown in Fig. 3.6. The zones of dependence and influence for the *ingested* streamtube, and thus the geometry parameters that feature in the active and inactive variable sets, are linked to the position of the engine. Kenway and Kiris [42] found sensitivity of the distortion pattern at the STARC-ABL BLI propulsor AIP to the wing downwash, verified by Gray [27], who also found the vertical tail to have an impact. The streamtube ingested by a tail-cone mounted propulsor has a larger zone of dependence than for propulsors that are mounted on the fuselage, like on the D8 or NOVA-BLI. The zones of dependence for the D8 and NOVA-BLI are likely to be dissimilar, given the different circumferential positions of the engines. The axial location of the engine has two contributions. The first has to do with the amount of mass, momentum, and energy defect growth in the boundary layer, proportional to the length of the surface over which the boundary layer grows. The second has to do with the impact of small perturbations on the flow. Small perturbations in the zone of dependence have more time to die out before they reach the engine in instances where the distance between the engine and perturbation is long enough. This distance, thus, also determines which upstream geometry parameters affect the ingested boundary layer. Lastly, all geometry features in the zone of influence are unlikely to have impacts on the upstream properties, as discussed before. This hypothesis is valid as long as there is no excessive flow separation or shocks, i.e., no major adverse pressure gradient effects, which is also a criterion for separating small and large perturbations. The objective of research question 2 is to develop a set of guidelines defining which parameters fall under the active and inactive sets, by quantifying the sensitivity of the ingested boundary layer properties to these parameters. The following hypothesis can be made based on the above discussion:

Hypothesis 2: Parameters present in the active and inactive variable sets are determined by the axial and circumferential location of the engine on the airframe. The axial location defines the distance over which the boundary layer grows, as well as the impact of small perturbations in the zone of dependence. The circumferential location determines how much the wing contributes to the ingested boundary layer properties. Within the active set, if perturbations in detailed parameters do not result in shocks or flow separation in the ingested streamtube, then these parameters can be defaulted for conceptual design purposes since the BLI effects in this instance are more sensitive to changes in macro parameters.

Having looked at the airframe impacts on the boundary layer, it is now time to consider the other part of the picture, i.e., the impact of the propulsor, which leads to research question 3:

Research Question 3: In CFD modeling of the ingested boundary layer for a BLI propulsor, what aspects of its on-design and off-design characteristics need to be considered?

Consider the propulsor model in CFD shown in Fig. 3.7. This is a 1D powered boundary condition representation of the engine, identical to the propulsor models used by Gray [28, 26], Rodriguez [79], and Ordaz [71] for their coupled BLI studies, except for inclusion of the core. The figure is representative of the BLI propulsors on the D8 and NOVA-BLI concepts. The fan face is modeled as a pressure outlet i.e., a face where flow leaves the CFD fluid domain, while the bypass and core nozzle inlets are modeled as stagnation inlets, where flow enters the CFD fluid domain. Static properties are required for the pressure outlet face, while stagnation properties are required for the stagnation inlets as shown in Fig. 3.7. For configurations like the STARC-ABL, where the BLI propulsor is an electrically driven ducted fan, the core is absent and the fan is modeled as above.

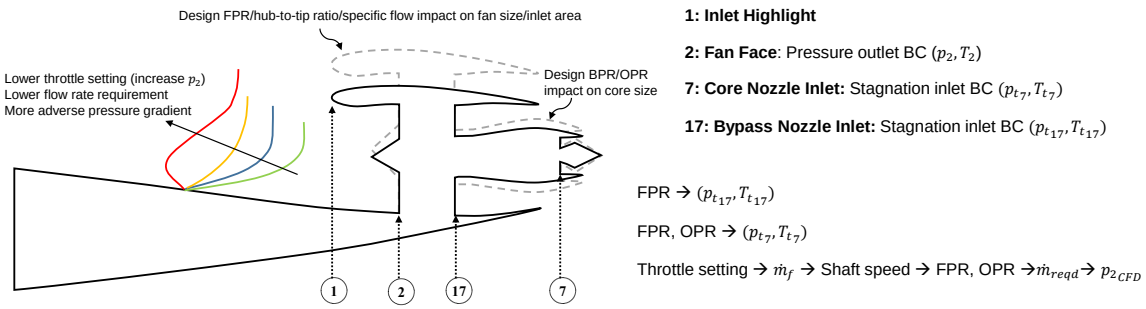

Figure 3.7: 1D powered boundary condition representation of BLI propulsor in CFD and impact on the ingested boundary layer

The specific flow rate through the fan i.e., mass flow rate per unit area, is a measure of how much air flow can be sucked in by the fan for a given annulus area. This metric, in engine on-design, is a measure of blade design technology, and is typically assumed at the conceptual design stage given current fan technology availability, or future technology readiness levels (TRLs). In engine on-design, for both ducted fans and separate flow turbofans, given a design FPR, assumed specific flow, and specified hub to tip ratio, the size of the fan is determined by the mass flow requirements at the most critical engine sizing point, typically top of climb. Thus, the annulus area at station 2, and as a consequence stations 1 and 17, in Fig. 3.7 are a fallout of the chosen design parameters and fan technology assumption. For a given thrust requirement, assumed specific flow and hub to tip ratio, a decrease in design FPR increases the fan diameter required to allow for higher mass flow. Similarly, a decrease in the assumed specific flow, for the same requirements, results in a larger fan. For turbofan engines, size of the core is determined by the design OPR, and assumed core specific flow, for a given mass flow rate set by the thrust requirement for the engine and the design BPR. For a fixed fan size, determined by the design FPR, decreasing BPR increases the flow rate requirement for the core, and thus for a given OPR and assumed core specific flow, the core size increases. For a given BPR and assumed core specific flow, as design OPR decreases, the core size increases to allow the same mass flow.

For a given mass flow rate, an increase in fan annulus area reduces the average inflow velocity and increases static pressure, while a decrease in size has the opposite effect, due to conservation of mass and momentum. The impact of fan size on the shapes of the ingested boundary layer profiles is evident from Gray's studies [28]. This influence however decays one nacelle diameter upstream, consistent with the theoretical discussions on the zones of influence and dependence for 3D boundary layers above. The fan size also affects the captured streamtube, impacting the amount of boundary layer flow ingested relative to clean flow. Total pressure is typically higher in the freestream than in the boundary layer. Ingesting a larger percentage of clean flow by increasing the fan size has a favorable impact on the averaged total pressure seen by the fan. This benefit of course is counteracted by the added penalties of larger nacelle wetted area and weight. This trade-off seems to suggest that there is an optimum fan size (and thus design FPR/design specific flow/hub-to-tip ratio) that maximizes the BLI benefits, while minimizing the adverse impacts on performance. With regards to engine size, it can be reasonably assumed that the BLI effects calculated from the ingested boundary layer are *directly* dependent only on the fan size, and not the core size. While cycle design parameters like OPR, BPR, and T_{41} for example have a direct impact on the vehicle fuel burn, these parameters only have an *indirect* influence on the ingested boundary layer properties. As the compressor and turbine design changes, the fan size and operation changes accordingly, for the same design requirements. Thus, the influence on the BLI effects due to changes in the on-design characteristics of the core, are felt through the corresponding changes in the fan design.

In engine off-design, the throttle setting is adjusted such that engine thrust matches the vehicle drag at a given point in the mission. For turbofans, this entails varying the fuel flow rate, which then adjusts the shaft speed. FPR and OPR in off-design are a fallout of the shaft speed and turbomachinery performance maps, and the flow

rate needed to match engine thrust with vehicle drag, for the sized engine, is thus determined. Thermodynamic properties at stations 17 and 7 are also a fallout. For electrically driven ducted fans like on the STARC-ABL, varying throttle amounts to changing the input shaft power, with the flow rate requirements, FPR, and fan exit conditions varying as a function of shaft power. The impact of the propulsor operation, i.e., mass flow rate requirements, on the boundary layer can be explained using standard boundary layer theory. The ingested boundary layer properties are largely dependent on the externally imposed streamwise pressure gradient. While the airframe contour entering the propulsor influences the external inviscid stream, thus affecting the pressure gradient imposed on the boundary layer, the propulsor throttle setting, i.e., amount of airflow being sucked in, also impacts this pressure gradient. Fig. 3.7 shows the impact of varying pressure gradient on the boundary layer profiles. Positive (adverse) pressure gradients slow down the flow. The velocity gradient at the wall, $\frac{du}{dy}\Big|_w$, decreases as the pressure gradient becomes more adverse, and thus the wall shear stress, $\tau_w = \mu \frac{du}{dy}\Big|_w$, decreases. If the pressure gradient is too adverse, the flow will separate as depicted by the red profile in Fig. 3.7, leading to reversed flow and significant losses in total pressure in that region. This separation bubble displaces neighboring streamlines, altering the effective shape of the airframe, thus impacting the ingested streamtube. As a reminder, changes to flow rate are not the only cause for variations in the pressure gradient. As discussed above, changes to the fan size, for a given flow rate, also affect pressure. In addition to influencing the pressure gradient and wall shear, changes to the required mass flow rate, for a given inlet area, also affect the extent of the captured streamtube. Due to mass conservation, for a given inlet area, an increase in flow rate increases the streamtube capture area.

The throttle setting is modeled in CFD as a variation in $p_2, p_{t_{17}}$ and $T_{t_{17}}$ (along with p_{t_7} and T_{t_7} for BLI turbofans). To match the flow rate requirement for the engine predicted by the cycle code with that measured in CFD, the fan face static

pressure boundary condition in CFD needs to be adjusted, as discussed in chapter 2. Boundary conditions $p_{t_{17}}$, $T_{t_{17}}$, along with p_{t_7} and T_{t_7} affect flow downstream of the engine. For this thesis, engine exit flow properties are calculated using the cycle analysis code, not CFD. Additionally, since the engine locations of interest are primarily in the fuselage aft section, the flow downstream of the fan is of no interest for this thesis. Given that the core size and flow properties have no *direct* impact on the ingested boundary layer, the core model can be omitted from the CFD domain for simplicity. The discussion above can be summarized in a general hypothesis to research question 3, shown below. After the BLI effects of interest are defined in chapter 4, a more specific hypothesis is derived from this starting point in chapter 6.

Initial Hypothesis 3: Fan size and mass flow rate requirements are the main engine on-design and off-design factors that influence the BLI effects. If the fan size is changed for a given flow rate requirement, the pressure gradient imposed on the ingested flow will exhibit a positive correlation with this change, while the inflow velocity and wall shear will exhibit a negative correlation, as dictated by the conservation laws. The ratio of clean to boundary layer flow in the ingested streamtube will also show a positive correlation with fan size. On the other hand, if the required flow rate is adjusted for a given fan size, the correlations for pressure gradient, inflow velocity, and wall shear are now opposite. In addition, the streamtube capture area will positively correlate with required inflow.

Having established the need for a new BLI vehicle sizing methodology, and providing an informal overview of what this new approach would entail, details of the proposed approach can be described in the following chapter. Additionally, the experimental setups to test the proposed hypotheses for the research questions will also be described in the next chapter.

CHAPTER 4
METHODOLOGY

This chapter presents a formal description of the proposed methodology to satisfy the research objective and answer the research questions posed in the previous chapter. In the first three chapters, the term "BLI effects" was used somewhat broadly to label the impact of ingesting the boundary layer. This chapter clearly defines these BLI effects using an energy based aircraft performance bookkeeping methodology that is gaining traction in literature for BLI applications. Following this, the experimental approach required to assess sensitivities of the BLI effects to the airframe and propulsor is briefly outlined. These experiments will test hypotheses 2 and 3, and establish a set of guidelines regarding which design variables need to be considered when generating surrogates for the BLI effects. The methodology involved in development and implementation of the BLI effects surrogates in the aircraft sizing and engine cycle design process is then introduced. Subsequently, experiments to ascertain the impacts of capturing aero-propulsive coupling on aircraft design and performance are discussed. These experiments test hypothesis 1 and justify the need for the proposed methodology over decoupled approaches presented in literature. Details on the experimental approach, results, and discussions will feature in the following chapters.

4.1 Aircraft Performance Bookkeeping

The net axial force F_X acting on an aircraft in the streamwise direction can be broken down into net thrust (gross thrust minus ram drag) and airframe drag for an aircraft with podded engines, where the propulsor jet and airframe wake do not interact downstream. Thus the airframe drag can be calculated in isolation and passed to the propulsion model as a net thrust requirement. This bookkeeping approach

is common practice for conventional tube and wing vehicles with podded engines. However for BLI vehicles, the distinction between thrust and drag becomes unclear. This ambiguity can be illustrated using a simplified control volume analysis.

Consider the control volumes shown in Fig. 4.1 for the podded and BLI vehicles. The control volume boundaries are far enough from the bodies such that the static pressure at the boundaries is at ambient condition. The net axial force, per unit depth, in the x direction acting on the body in either control volume is given as

$$F_X = \int_2 (V_1 - V_2)\, d\dot{m} \tag{4.1}$$

where V is the velocity at a given boundary. This integral is carried out over the extent of boundary 2 in the control volume, and $d\dot{m}$ is the differential mass flow contained in a streamtube. To simplify the analysis, the following assumptions are made:

- The nacelle wake contribution is negligible
- Wakes and jets can be represented as uniform velocity flows with the appropriate magnitude
- The analysis is being conducted at cruise, hence the net axial force on the vehicle is zero
- Fuel flow rate contribution from the engine to the overall mass flow is negligible

For the podded case, with the assumptions made above, one recognizes that the jet momentum excess must balance the wake momentum deficit at cruise. Eq. (4.1) results in the following expression:

$$F_X = \dot{m}_a\,(V_\infty - V_w) + \dot{m}_j\,(V_\infty - V_j) = 0 \tag{4.2}$$

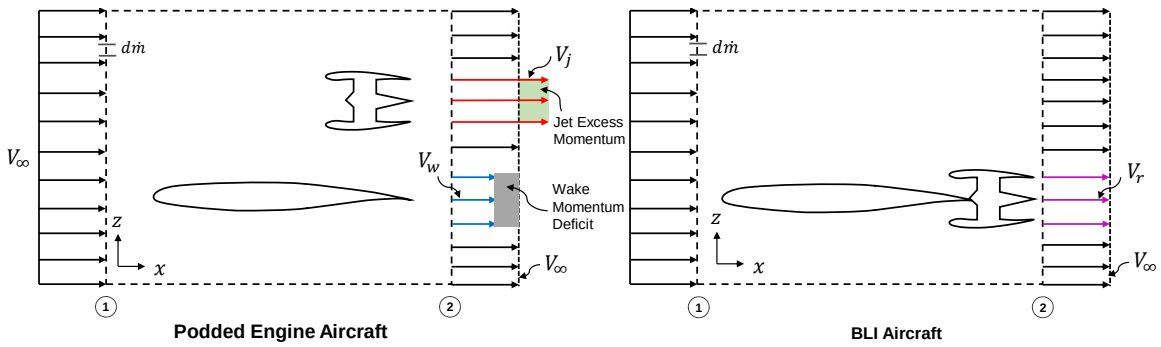

Figure 4.1: Control volume analysis for non-BLI and BLI vehicles

where $\dot{m}_a$ is the total mass flow associated with the streamtube passing over the airframe, $\dot{m}_j$ is the total mass flow in the streamtube ingested by the engine, V_w is the averaged airframe wake velocity, and V_j is the averaged propulsor jet exhaust velocity. From Eq. (4.2), one can clearly see that $\dot{m}_a\,(V_\infty - V_w)$ corresponds to the airframe drag, while $\dot{m}_j\,(V_\infty - V_j)$ is the net thrust provided by the propulsor, and thus Eq. (4.2) reduces to $D - F_N = 0$. For the BLI case, Eq. (4.1) results in the following expression:

$$F_X = \dot{m}_a\,(V_\infty - V_r) = 0 \tag{4.3}$$

Since this analysis is being done at cruise, V_r must equal V_∞ for the net axial force to equal zero. V_r is the re-energized wake velocity. The portion of the boundary layer that would have contributed to the airframe wake in the podded case is now ingested by the propulsor and re-energized. Thus the airframe boundary layer flow ingested by the propulsor contributes to both thrust and drag, and while the net axial force for both the BLI and podded cases is the same, separating the contributions as thrust and drag is now ambiguous for the BLI case.

Recognizing deficiencies of the thrust-drag bookkeeping approach for highly integrated aircraft concepts, alternative bookkeeping approaches have been proposed in literature. One such approach is the power balance formulation proposed by Drela [20] and extended by Sato [81] and Hall [34]. This approach involves a mechanical en-

ergy balance, as opposed to the traditional momentum balance. Another bookkeeping approach involves an exergy analysis, developed by Arntz [7], which takes into account both aircraft thermal and mechanical energy. This method is more global than the power balance approach. Since aircraft thermal analysis is not considered in this thesis, the power balance bookkeeping approach is adequate, and as will be shown later, can be easily adapted to work with tools that rely on thrust-drag bookkeeping.

4.2 Power Balance Formulation

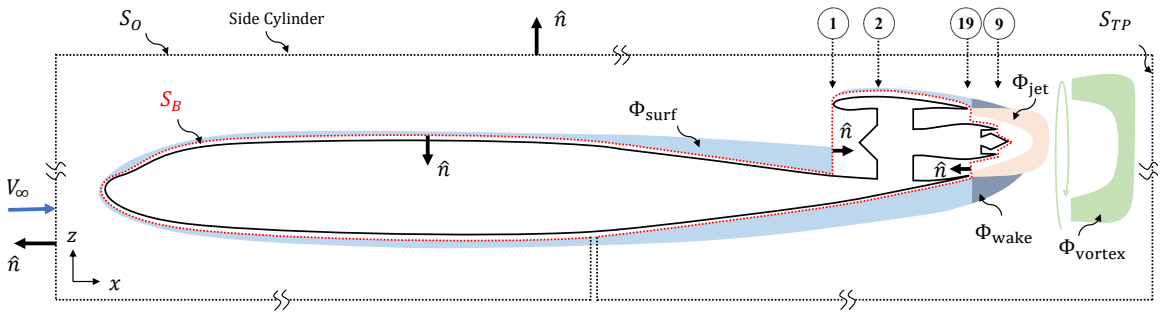

Figure 4.2: Control volume for power balance based BLI analysis

The control volume used for developing the power balance approach can be seen in Fig. 4.2. Though the vehicle shown is similar to a notional D8, the methodology is valid for all BLI concepts considered in this thesis. The control volume is cylindrical with the upstream and downstream (Trefftz Plane - S_{TP}) boundaries normal to the freestream flow, and the side boundaries parallel to the freestream. The side boundaries are assumed to be sufficiently far from the body and thus flow there is at ambient conditions. An infinitesimal cut in the control volume links the outer boundary, S_O, with the inner boundary, S_B, which wraps over the surface of the body and around the propulsor inlet and exit planes, shown in red in the figure. While the propulsor itself is not part of the control volume, the planes at stations 1, 19, (and 9 for BLI propulsors with a core) represent boundaries where flow exits and enters the control volume. Contributions from the nacelle can be included by shifting S_B inwards from

station 1 to 2. S_B is represented by an inward pointing normal $\hat{\mathbf{n}}$, which is outward pointing for S_O. The general power balance equation can be expressed in the form

$$P_S + P_K + P_V = W\dot{h} + \dot{E}_a + \dot{E}_v + \dot{E}_p + \dot{E}_w + \Phi \tag{4.4}$$

All terms on the left-hand side of Eq. (4.4) represent power sources, while terms on the right-hand side represent power sinks, i.e., power losses, outflows, and consumption.

4.2.1 Power Sources

The term P_S is the net propulsor shaft power and characterizes contributions from all surfaces moving relative to the control volume, such as turbomachinery components, propellers, flapping wings, etc. Since the control volume shown in Fig. 4.2 does not include any of these components, P_S is zero.

The net mechanical power added to the flow by the propulsor across the surface S_B is represented by P_K. This term represents the net pressure-work and kinetic energy flux rate, and captures the contributions from turbomachinery and combustors not included in the control volume boundary S_B. This quantity is calculated as follows

$$P_K = \oiint - \left[(p - p_\infty) + \frac{1}{2}\rho\left(V^2 - V_\infty^2\right)\right] \mathbf{V} \cdot \hat{\mathbf{n}} dS_B \tag{4.5}$$

where $V^2 = \mathbf{V} \cdot \mathbf{V}$ is the square of the magnitude of the local velocity vector $\mathbf{V}$, p is the static pressure, and ρ is the static density, at a given location. Freestream quantities are denoted by $(\cdot)_\infty$. Since the flow is tangent to the control volume boundary S_B everywhere over the airframe except the propulsor inlet and outlet planes i.e., stations 1, 19 and 9 in Fig. 4.2, the contributions to P_K from these surfaces is zero since $\mathbf{V} \cdot \hat{\mathbf{n}} = 0$. Therefore, P_K can be expressed as follows:

$$P_K = P_{K_{\text{in}}} + P_{K_{\text{out}}} \tag{4.6}$$

where $P_{K_{\text{in}}}$ and $P_{K_{\text{out}}}$ are the non-zero P_K contributions evaluated at the propulsor inlet (station 1 or 2 depending on where S_B is defined) and exit areas (station 19 for a ducted fan, and both 19 and 9 for a BLI turbofan) respectively. Since the state of the flow exiting the propulsor can be estimated in conceptual design using a 1D thermodynamic cycle analysis tool, which assumes uniform axial flow, $P_{K_{\text{out}}}$ for a turbofan can thus be calculated rather easily as follows

$$\begin{aligned} P_{K_{\text{out}}} = &\left[(p_{19} - p_\infty) + \frac{1}{2}\rho_{19}\left(V_{19}^2 - V_\infty^2\right)\right] V_{19}A_{19} \\ &+ \left[(p_9 - p_\infty) + \frac{1}{2}\rho_9\left(V_9^2 - V_\infty^2\right)\right] V_9 A_9 \end{aligned} \tag{4.7}$$

Recognizing that the flow rate $\dot{m} = \rho A V$, for a given flow area A, one obtains

$$\begin{aligned} P_{K_{\text{out}}} = &\left(p_{19} - p_\infty\right) V_{19}A_{19} + \frac{1}{2}\dot{m}_{19}\left(V_{19}^2 - V_\infty^2\right) \\ &+ \left(p_9 - p_\infty\right) V_9 A_9 + \frac{1}{2}\dot{m}_9\left(V_9^2 - V_\infty^2\right) \end{aligned} \tag{4.8}$$

Note that the flow exiting the propulsor is in a direction opposite to the unit normal vector at that plane, which cancels the negative sign outside the integrand in Eq. (4.5). Significant variations in the thermodynamic properties in the ingested boundary layer invalidate the uniform flow assumption, and thus the integral equation must be used to calculate $P_{K_{\text{in}}}$ from CFD as shown

$$P_{K_{\text{in}}} = \iint -\left[(p_1 - p_\infty) + \frac{1}{2}\rho_1\left(V_1^2 - V_\infty^2\right)\right] \mathbf{V_1} \cdot \hat{\mathbf{n}} dS_1 \tag{4.9}$$

This term is related to the thermodynamic properties of the ingested boundary layer and is a measure of the ingested profile drag power [33]. It is thus directly dependent on the airframe geometry and indirectly on the propulsor through fan size and throttle setting. In the case of a podded propulsor, $V_1 = V_\infty$ and $p_1 = p_\infty$ for an isentropic streamtube and hence $P_{K_{\text{in}}} = 0$ for the non-BLI case. On the other hand, $P_{K_{\text{out}}}$ is

dependent on the propulsor jet exhaust velocities, pressures, and densities, which are dependent on the shaft power, component efficiencies, and thermal efficiency, and can thus be mapped to the engine fuel burn. $P_{K_{\text{out}}}$ is indirectly dependent on the airframe geometry through the propulsive power requirements set by the airframe.

The symbol P_V denotes the mechanical power of the fluid expanding against atmospheric pressure. It can be calculated from the expression

$$P_V = \iiint (p - p_\infty) \nabla \cdot \mathbf{V} d\mathcal{V} \tag{4.10}$$

For incompressible flow, this term is zero since $\nabla \cdot \mathbf{V} = 0$. For compressible flow, there are significant nonzero contributions from regions where there is isentropic expansion or compression of the fluid, and in regions where heat is added to the flow at a static pressure different from freestream, such as in cases where the combustor is included in the control volume [20]. For the control volume shown in Fig. 4.2, integration of the Gibbs equation for isentropic streamtubes that start and end at ambient pressure results in P_V for that streamtube to be exactly zero [91]. Thus, there are no contributions from the (shock-free) streamtubes outside the boundary layers. Contributions of the propulsor jet exhaust to P_V are also negligible as long as the jet exhaust is not severely under-expanded, or over-expanded, as is typically the case for commercial transport aircraft [91]. Contributions to P_V from the compressible boundary layers over the airframe are also small. Sato [81] showed that the total contribution of P_V is about 5% compared to the other contributions in the power balance formulation. Uranga [91] suggests that this contribution can be bookkept as a correction to the surface dissipation, but that since this contribution is virtually unchanged between BLI and non-BLI contributions, it has no impact on the measured BLI benefit relative to the non-BLI case, and can thus be neglected.

4.2.2 Power Sinks

The rate of change of potential energy of the aircraft, which is a power requirement for climb, and a source for descent, is captured by $W\dot{h}$. The aircraft weight is denoted by W and $\dot{h}$ is the rate of change of altitude. For a coordinate system where the x axis is aligned with the flight path that is at a climb angle γ, at steady flight, $W\dot{h}$ can be related to the net streamwise force F_X and flight velocity V_∞ as follows

$$W\dot{h} = -F_X V_\infty = W V_\infty \sin\gamma \tag{4.11}$$

The total mechanical energy flow rate, $\dot{E}$, out of the control volume boundary S_O is given by

$$\dot{E} = \dot{E}_a + \dot{E}_v + \dot{E}_p + \dot{E}_w \tag{4.12}$$

This term quantifies the dissipation that occurs downstream of the control volume for the instance where S_O is close to S_B [34]. The wake streamwise kinetic energy outflow rate, $\dot{E}_a$, is given by

$$\dot{E}_a = \iint \frac{1}{2}\rho u^2 \left(V_\infty + u\right) dS_{TP} \tag{4.13}$$

where u is the perturbation velocity in the x direction. The wake transverse kinetic energy outflow rate, $\dot{E}_v$, is computed from

$$\dot{E}_v = \iint \frac{1}{2}\rho \left(v^2 + w^2\right) \left(V_\infty + u\right) dS_{TP} \tag{4.14}$$

where v and w are the perturbation velocities in the y and z directions respectively. The wake pressure difference work rate, $\dot{E}_p$, is found from

$$\dot{E}_p = \iint \left(p - p_\infty\right) u dS_{TP} \tag{4.15}$$

All these expressions are evaluated at the Trefftz plane and assume that the normal of this plane is parallel to the x axis. The pressure work and kinetic energy outflow through the side cylinder boundary, $\dot{E}_w$, is only significant in supersonic flows due to the presence of oblique shock waves. For subsonic flows, this expression decays as $1/r^4$ and thus can be neglected as long as the outer side boundaries are sufficiently far away from S_B [20]. Plugging in Eqs. 4.13, 4.14 and 4.15 into 4.12 and neglecting $\dot{E}_w$, one obtains the following expression for the total mechanical energy flow rate

$$\dot{E} = \iint \left[\frac{1}{2}\rho \left(u^2 + v^2 + w^2\right)(V_\infty + u) + (p - p_\infty)\, u \right] dS_{TP} \tag{4.16}$$

The final power sink in the power balance equation is the viscous dissipation inside the control volume, where the flow kinetic energy is converted to thermal energy. The total viscous dissipation inside the control volume can be calculated as

$$\Phi = \iiint (\bar{\bar{\tau}} \cdot \nabla) \cdot \mathbf{V} d\mathcal{V} \tag{4.17}$$

where $\bar{\bar{\tau}}$ is the shear stress tensor. Dissipation in the control volume occurs predominantly in the boundary layers on the airframe surface, followed by the propulsor jet, wake, trailing vortex sheet, and in any shocks on the body. Thus, the total dissipation Φ can be decomposed into distinct contributions as shown by

$$\Phi = \underbrace{\Phi_{\text{surf}} + \Phi_{\text{wake}} + \Phi_{\text{vortex}} + \Phi_{\text{shock}}}_{\Phi_{\text{afm}}} + \Phi_{\text{jet}} \tag{4.18}$$

where Φ_{afm} denotes the dissipation contributions from the airframe and Φ_{jet} represents the jet mixing dissipation from the propulsor exhaust. The latter is equal to the excess mechanical energy deposition rate at the propulsor outlet [34] and can be calculated using Eq. (4.16) evaluated at the propulsor outlet area, assuming $v = w = 0$, which

also implies $\dot{E}_v = 0$, as follows:

$$\Phi_{\text{jet}} = \iint \left[\frac{1}{2}\rho \left(V - V_\infty\right)^2 V + \left(p - p_\infty\right)\left(V - V_\infty\right) \right] dS_{PO} \tag{4.19}$$

where S_{PO} is the propulsor outlet area. For the control volume shown in Fig. 4.2, Eq. (4.19) is evaluated over the core and bypass nozzle exit areas, i.e., at stations 9 and 19 respectively, and then summed. If in addition to the 1D flow assumption, one assumes no variations in the axial flow over the propulsor exit areas, then Φ_{jet} can be calculated using a cycle analysis tool, like in the case of $P_{K_{\text{out}}}$, as follows:

$$\begin{aligned} \Phi_{\text{jet}} = &\left(p_{19} - p_\infty\right)\left(V_{19} - V_\infty\right) A_{19} + \frac{1}{2}\dot{m}_{19}\left(V_{19} - V_\infty\right)^2 \\ &+ \left(p_9 - p_\infty\right)\left(V_9 - V_\infty\right) A_9 + \frac{1}{2}\dot{m}_9\left(V_9 - V_\infty\right)^2 \end{aligned} \tag{4.20}$$

It is important to note that for a given analysis, the sum of Φ and $\dot{E}$ is independent of the Trefftz plane location relative to the body [20]. Only the contributions from Φ and $\dot{E}$ to the sum vary based on the Trefftz plane location. In the limit as S_O tends to infinity, $\dot{E}$ tends to zero since all perturbations in the flow have had a chance to dissipate and the flow returns to freestream conditions. Thus, for a sufficiently far outer boundary, $\dot{E}$ can be bookkept as dissipation. However, the relation between $\dot{E}$ and Φ is useful in that certain contributions to Φ can be easily estimated from Eq. (4.16), like in the case of Φ_{jet}.

4.3 Implementation of Power Balance in Conceptual Design

Based on the discussion in the previous section, Eq. (4.4) can be written for a control volume with the boundary S_O far away from the body surface S_B as follows

$$P_{K_{\text{out}}} - \Phi_{\text{jet}} = \Phi_{\text{surf}} + \Phi_{\text{wake}} + \Phi_{\text{vortex}} + \Phi_{\text{shock}} - F_X V_\infty - P_{K_{\text{in}}} \tag{4.21}$$

Eq. (4.21) is thus the power balance equation for a BLI configuration. For a non-BLI configuration, $P_{K_{\text{in}}}$ is zero, and Eq. (4.21) can be written for the non-BLI [1] case as

$$P'_{K_{\text{out}}} - \Phi'_{\text{jet}} = \Phi'_{\text{surf}} + \Phi'_{\text{wake}} + \Phi'_{\text{vortex}} + \Phi'_{\text{shock}} - F'_X V_\infty \tag{4.22}$$

Eqs. (4.21) and (4.22) are written in a manner where terms in the power balance equation that depend only on the propulsor exhaust jet are expressed on the left-hand side, while terms related to the airframe and ingested boundary layer are expressed on the right-hand side. Thus, the left-hand side terms can be calculated from a simple 1D engine cycle model with uniform flow assumptions, while the right-hand side terms can be obtained from the aerodynamics model. The right-hand side terms can be thought of as a requirement for the propulsion model, analogous to the situation where airframe drag is a thrust requirement for a non-BLI propulsor.

For a net axial force requirement, i.e., where $F_X = F'_X = \mathcal{F}_X$, the propulsor requirement in Eq. (4.21) for the BLI configuration can be expressed in terms of dissipation components in the non-BLI case and changes in dissipation that occur as a result of the engines ingesting the boundary layer, as

$$\begin{aligned} P_{K_{\text{out}}} - \Phi_{\text{jet}} = \Phi'_{\text{surf}} + \Phi'_{\text{wake}} + \Phi'_{\text{vortex}} + \Phi'_{\text{shock}} - \mathcal{F}_X V_\infty \\ - (P_{K_{\text{in}}} + \Delta\Phi_{\text{surf}} + \Delta\Phi_{\text{wake}} + \Delta\Phi_{\text{vortex}} + \Delta\Phi_{\text{shock}}) \end{aligned} \tag{4.23}$$

where the Δ terms in the above expression are defined by

$$\Delta\Phi_{\text{component}} = \Phi'_{\text{component}} - \Phi_{\text{component}} \tag{4.24}$$

The advantage of expressing power balance in the form shown in Eq. (4.23) is not

[1] To be consistent with literature, the notation $(\cdot)'$ is used to represent quantities that are obtained with reference to non-BLI configurations, while un-primed terms represent quantities calculated for the BLI case. The same notation was used in chapter 1.

immediately apparent at this point. However, it will be shown subsequently how the power balance formulation can be mapped to the more familiar thrust and drag terms. Expressing power balance in this fashion allows one to use a combination of low and high fidelity aerodynamic models to obtain reasonable estimates for the propulsor requirements.

4.3.1 Relating Power Balance to Thrust and Drag

The main challenge with adopting power balance in conceptual design is that current industry standard engine and airframe sizing tools like NPSS and FLOPS function in the thrust-drag bookkeeping domain. It is possible however to translate power balance into an equivalent thrust-drag formulation, under certain reasonable assumptions, which can then be used with existing tools. Consider the power balance expression for a non-BLI configuration as shown in Eq. (4.22). Using the definitions for $P_{K_{\text{out}}}$ and Φ_{jet} in Eqs. (4.8) and (4.20) respectively, one sees that $P'_{K_{\text{out}}} - \Phi'_{\text{jet}}$ evaluates to

$$\begin{aligned} P'_{K_{\text{out}}} - \Phi'_{\text{jet}} = &\left[\dot{m}_{19}V_{19} + \dot{m}_9 V_9 - (\dot{m}_{19} + \dot{m}_9)\, V_\infty\right] V_\infty \\ &+ \left[(p_{19} - p_\infty)\, A_{19} + (p_9 - p_\infty)\, A_9\right] V_\infty \end{aligned} \tag{4.25}$$

Assuming $\dot{m}_{19} + \dot{m}_9 = \dot{m}_1$, it can clearly be seen that the above expression is equal to $F'_N V_\infty$, where F'_N is the net thrust (gross thrust minus *freestream* ram drag) for a separate flow turbofan engine without BLI. The assumption of mass continuity above ignores contributions from fuel flow and customer bleed extractions on the propulsor exit mass flow. These contributions are however usually small, compared to the total flow rate, and thus it is acceptable to neglect them in early conceptual design. Eq. (4.25) can also be used for a ducted fan, like that on a STARC-ABL, by ignoring terms related to the core (9). In this situation, since there is no bleed or fuel flow, the mass continuity assumption above is exactly valid. It should be emphasized that while the expression for $P_{K_{\text{out}}} - \Phi_{\text{jet}}$ is identical for BLI and non-BLI cases, labeling it

as net thrust times freestream velocity is only appropriate for non-BLI aircraft since the notion of thrust and drag for BLI aircraft is ambiguous as discussed before. Using the above observation and dividing each term in Eq. (4.22) by V_∞, one sees that Eq. (4.22) can now be written as

$$F'_N - \left(\frac{\Phi'_{\text{surf}} + \Phi'_{\text{wake}} + \Phi'_{\text{vortex}} + \Phi'_{\text{shock}}}{V_\infty} \right) = -F'_X \tag{4.26}$$

As shown in Sec. 4.1, $F'_X = D' - F'_N$ for the podded case. Therefore, it must follow that

$$\Phi'_{\text{surf}} + \Phi'_{\text{wake}} + \Phi'_{\text{vortex}} + \Phi'_{\text{shock}} = \Phi'_{\text{afm}} = D'V_\infty \tag{4.27}$$

Finally, one can express the power balance formulation for a BLI vehicle by substituting Eq. (4.27) in Eq. (4.23) to obtain

$$\underbrace{P_{K_{\text{out}}} - \Phi_{\text{jet}}}_{\approx F'_N V_\infty} = D'V_\infty - \underbrace{F_X V_\infty}_{P_{\text{ex}}} - \underbrace{\beta}_{\approx \Delta D' V_\infty} \tag{4.28}$$

where P_{ex} is the excess power requirement and $\beta \equiv P_{K_{\text{in}}} + \Delta\Phi_{\text{surf}} + \Delta\Phi_{\text{wake}} + \Delta\Phi_{\text{vortex}} + \Delta\Phi_{\text{shock}}$. Eq. (4.28) expresses the power balance in terms of quantities that are well defined and understood for non-BLI vehicles (net thrust, drag, and excess power requirements) and identifies the additional elements needed to account for the BLI impacts, thus sidestepping the thrust-drag ambiguity issue with BLI aircraft. The terms represented by β are the BLI effects. These terms capture the changes to the propulsive power requirements as a result of placing the engines in a manner that results in the partial or complete ingestion of the airframe boundary layer. By definition, these are zero for a non-BLI aircraft.

Expressing the power balance equation in this form has certain advantages. The quantity $P_{K_{\text{out}}} - \Phi_{\text{jet}}$ can easily be calculated in an engine cycle analysis tool given the definition in Eq. (4.25). The total drag of the *un-powered and non-BLI airframe*, D',

can be estimated using empirical drag buildup approaches, such as the Empirical Drag Estimation Technique (EDET) in FLOPS for example. These calculations can be augmented with a vortex panel code and other corrections if desired. While there is no fidelity requirement for calculating D', the choice of using lower fidelity aerodynamic models to estimate overall airframe drag arises from requirement 4 described in the previous chapter. Since most BLI configurations are a tube and wing type, estimating the drag for this type of airframe using empirical approaches is not as inaccurate as one may think, given the vast amounts of historical data available for similar geometries. Most of the BLI effects however cannot be estimated using empirical approaches, and hence CFD is required to estimate these terms, based on requirement 5.

4.3.2 BLI Effects

The analysis in the preceding subsection identified certain terms that are related only to BLI. Calculating these terms allows one to determine the impact of BLI on the vehicle design and performance.

$\Delta\Phi_{\text{surf}}$ This term represents the change in total surface dissipation of the airframe as a result of placing the propulsors in the boundary layer flow. Sato [81] and Hall [34] showed that the surface dissipation for a body is relatively insensitive to pressure changes due to throttle effects. Therefore, this term quantifies the impact of configuration changes going from a podded variant of the airframe, to the BLI variant. Since the surface dissipation is strongly dependent on wetted area, the change in surface dissipation can be modeled by the change in wetted area going from the podded to the BLI configuration. Elimination of the pylons and partial embedding of the engines in the airframe, for example, contribute to reductions in wetted area. However, addition of a third nacelle, like in the STARC-ABL, contributes to an increase in surface dissipation.

$\Delta\Phi_{\text{shock}}$ This term represents the change in dissipation as result of changes to the shock strengths on the airframe, going from the non-BLI to BLI configurations. A well designed transonic airplane will minimize interference effects and adverse contributions from shocks, whether it is a podded or a BLI configuration. Even if shocks are present, it can be assumed that the contributions for the BLI and non-BLI cases are similar, and thus the difference is negligible.

$\Delta\Phi_{\text{vortex}}$ This term represents the change in dissipation of the trailing vortex system for the wing as a result of the engines ingesting the boundary layer. Hall initially assumes that this term is negligible [34]. While this assumption sounds reasonable for fuselage mounted BLI engines that are far away from the wing, this assumption is unnecessary if Hall's approach to calculating wake dissipation, presented in [33], is adopted.

$\Delta\Phi_{\text{wake}}$ Hall proposes two methods for estimating the change in wake dissipation. In the first approach discussed in [34], the change in wake dissipation due to BLI is estimated as follows

$$\Delta\Phi_{\text{wake}} = \frac{\mathcal{K}_{in}}{\Phi'_{\text{surf}}}\Phi'_{\text{wake}} \tag{4.29}$$

where $\mathcal{K}_{in}$ is the ingested kinetic energy defect, as defined in standard boundary layer theory. In this approach, only the change in fuselage wake dissipation is calculated. The wing wake, comprising of shed vortices, is not included. This approach also requires estimating the terms Φ'_{surf} and Φ'_{wake}, which are challenging to calculate. For example, accurate estimation of Φ'_{wake} requires wake mesh refinement in CFD, which increases computational requirements, making it somewhat impractical for parametric studies that require multiple CFD evaluations.

The second method suggested by Hall in [33] approximates the change in overall airframe wake dissipation as the reduction in amount of mechanical flow energy being deposited off the airframe due to ingestion by the propulsor. Hall estimates $\Delta\Phi_{\text{wake}}$ by using Eq. (4.16), but evaluates it at the nozzle outlet plane for an un-powered configuration. The vector form of Eq. (4.16) is shown below

$$\dot{E} = \iint \left[\frac{1}{2}\rho|\mathbf{V} - \mathbf{V}_\infty|^2 \mathbf{V} \cdot \hat{\mathbf{n}} + (p - p_\infty)(\mathbf{V} - \mathbf{V}_\infty) \cdot \hat{\mathbf{n}} \right] dS_{PO} \quad (4.30)$$

Unlike the first method, this approach accounts for the pressure defect work rate and potential contributions from wing vortex wake ingestion, making it the preferred method for this thesis. In addition, the single equation formulation simplifies the calculation process.

It is important to highlight that $\Delta\Phi_{\text{wake}}$ is estimated from an un-powered configuration. Recall, Eq. (4.16) quantifies of the perturbation kinetic energy rate and pressure defect work rate at a given location in the boundary layer. Integrating this equation at the propulsor outlet plane to calculate $\Delta\Phi_{\text{wake}}$ implies the following reasoning: by placing a propulsor at that location, these perturbations in the flow are ingested and thus will not dissipate in the airframe wake. With a powered engine jet, this reasoning is not valid given that perturbations in the flow arise primarily from the jet, and not from the ingested wake. Thus, an un-powered configuration needs to be defined to calculate $\Delta\Phi_{\text{wake}}$.

This un-powered configuration is the same as the BLI aircraft, with two possible ways for dealing with the engine. The first way, as done by Hall, uses a through-flow nacelle. An integration area is defined at the nozzle exit plane on which Eq. (4.30) is calculated. The alternative

is to eliminate the through-flow nacelle geometry altogether and just leave the appropriately sized integration area on which $\Delta\Phi_{\text{wake}}$ can be evaluated. The latter approach has two advantages. First, the effect of nacelle diameter on $\Delta\Phi_{\text{wake}}$ can be captured quite easily by changing the radius of the integration area within a CFD run, without having to run additional cases. Second, based on test cases with an axisymmetric fuselage geometry and tail-cone propulsor, through-flow nacelles may produce separation bubbles in regions where such flow would not exist if a powered nacelle was present, or if no nacelle was modeled. This kind of flow skews the results. Removing the through-flow nacelle geometry ensures that the airframe and flight conditions are the primary drivers behind the solution, and not artificial propulsion integration effects due to a semi-unrealistic engine model.

$P_{K_{\text{in}}}$ This term captures the mechanical energy defect of the ingested boundary layer flow, which affects the propulsive power requirements. This term can be calculated from Eq. (4.9) as described before.

η_{PR} The pressure recovery seen by the engine is another factor that shows appreciable differences between BLI and non-BLI engines, even though it does not explicitly feature in the power balance equation. For non-BLI configurations, the biggest source of pressure loss in the flow ingested by the propulsor is due to the inlet. Typically, the pressure recovery, η'_{PR}, for non-BLI propulsors is defined as:

$$\eta'_{PR} = \frac{p_{t_2}}{p_{t_1}} \tag{4.31}$$

with the assumption that $p_{t_1} = p_{t_0}$. However, for BLI configurations, there are additional losses in the ingested boundary layer flow that are

a function of the airframe geometry. Thus for BLI configurations, it is more appropriate to define the pressure recovery as:

$$\eta_{PR} = \frac{p_{t_2}}{p_{t_1}} \frac{p_{t_1}}{p_{t_0}} = \frac{p_{t_2}}{p_{t_0}} \tag{4.32}$$

4.4 Sensitivity of BLI Effects to Airframe and Propulsor

To answer research questions 2 and 3, a series of experiments have to be designed to test the supporting hypotheses. Specifically, the experiments must enable understanding of the following aspects of the problem:

(i) The role of engine axial and circumferential location on the fuselage in determining the design features that fall under the active and inactive variable sets

(ii) Impacts of changes in macro airframe design parameters relative to the influence of changes in detailed parameters on the BLI effects

(iii) Consequences of fan size and engine flow rate requirement on the BLI effects

This section briefly alludes to the experimental plan for research questions 2 and 3, with more detailed information on the experimental setups presented in chapters 5 and 6. These experiments are visually summarized in Fig. 4.3. For research question 2, a simple fuselage geometry is used as a baseline. This baseline is systematically modified, as shown by the highlighted regions in Fig. 4.3a, to shed light on point (ii) above. To address point (i), the BLI effects are measured at different locations along the fuselage for each experiment. The results are compared to some established baseline, and the changes in the results, relative to the baseline, indicate the impact of the geometry perturbation on the BLI effects. Experiment 3 addresses point (iii) above, at two different engine locations, as shown in Fig. 4.3b. The circumferential and radial extent of BLI is different for the two engine locations. This difference is

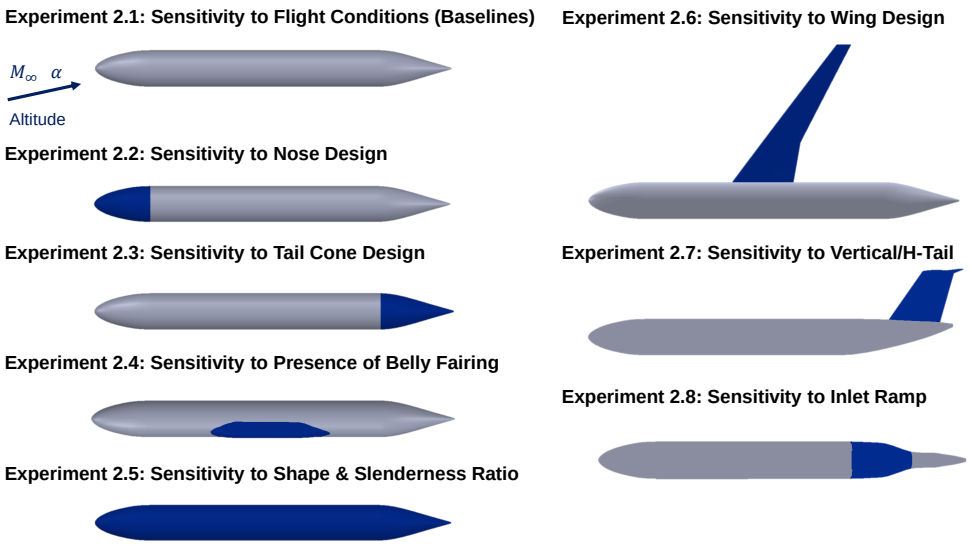

(a) Experiments for research question 2

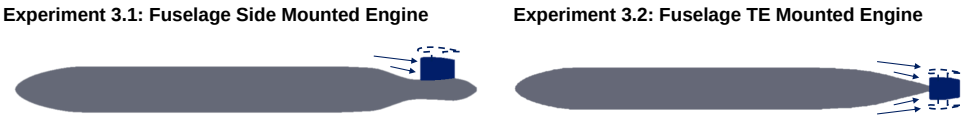

(b) Experiments for research question 3

Figure 4.3: Overview of experiments to evaluate BLI effects sensitivities

likely to affect the BLI effects trends. In each experiment, the fan diameter is varied, and a series of target mass flow rates is imposed for a given diameter.

4.5 Airframe and Engine Conceptual Design with BLI Effects

In chapter 3, an informal overview of the vehicle sizing loop with BLI effects was presented and compared to the approach currently adopted for conventional non-BLI concepts. This MDA problem can be repeated for each combination of airframe and propulsor design variables in a trade space exploration study. Optionally, the MDA problem can be extended to include *simultaneous optimization* of the cycle and airframe, to minimize some system level metric like fuel burn for example. This MDAO problem is concisely shown as an XDSM diagram in Fig. 4.4, an extension to the XDSM shown in Fig. 3.3b.

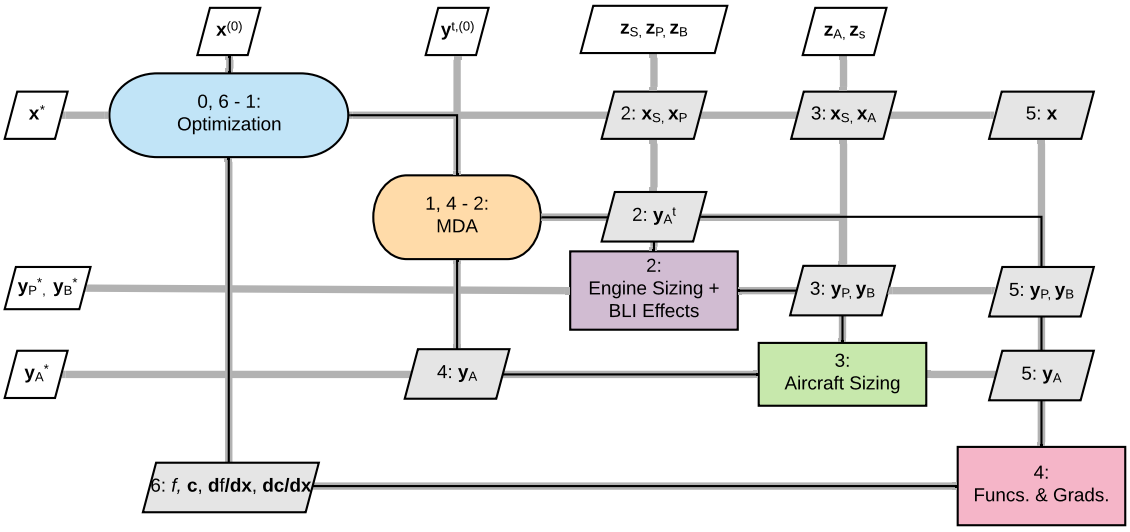

Figure 4.4: XDSM showing a Multidisciplinary Feasible (MDF) MDAO architecture for simultaneous BLI airframe and engine cycle optimization

The Multidisciplinary Feasible (MDF) MDAO architecture [15] in Fig. 4.4 is a monolithic architecture that links an optimization algorithm to an MDA solver. The MDA problem can be represented as a series of n residual equations that are a function of the system (e.g. airframe and propulsor) design variables $\mathbf{x}$, constants (e.g. flight conditions) $\mathbf{z}$, the interdisciplinary coupling variables $\mathbf{y}$, and the MDA solver defined targets for the coupling variables $\mathbf{y}^t$. The MDA solver is essentially a root finding algorithm, such as Gauss Seidel Iteration (a.k.a. Fixed Point Iteration), or a Newton Solver, responsible for enforcing interdisciplinary compatibility among the disciplines by perturbing $\mathbf{y}^t$ and driving the residuals to zero [31], as shown below:

$$\mathcal{R}_i(\mathbf{x}, \mathbf{z}, \mathbf{y}, \mathbf{y}^t) = 0 \quad \forall i \in \{1, ..., n\} \tag{4.33}$$

As a result, the optimizer sees a disciplinary consistent solution for every function call. The optimization problem can thus be formulated for the three discipline XDSM shown in Fig. 4.4 as:

$$
\begin{aligned}
&\textit{minimize:} && f(\mathbf{x}, \mathbf{y}(\mathbf{x}, \mathbf{y}), \mathbf{z}) \\
&\textit{with respect to:} && \mathbf{x} = \{\mathbf{x}_\mathrm{A}, \mathbf{x}_\mathrm{P}, \mathbf{x}_\mathrm{S}\} \\
&\textit{where:} && \mathbf{y} = \{\mathbf{y}_\mathrm{A}, \mathbf{y}_\mathrm{P}, \mathbf{y}_\mathrm{B}\} \\
&\textit{subject to:} && \mathbf{g}(\mathbf{x}, \mathbf{y}(\mathbf{x}, \mathbf{y}), \mathbf{z}) \geq 0 \\
& && \mathbf{h}(\mathbf{x}, \mathbf{y}(\mathbf{x}, \mathbf{y}), \mathbf{z}) = 0 \\
& && \mathbf{x}_\mathrm{L} \leq \mathbf{x} \leq \mathbf{x}_\mathrm{U}
\end{aligned}
$$

Since the MDF architecture treats the MDA problem as a single black-box function, it makes no difference to the optimizer whether the function values and gradients are being provided directly by the disciplinary analysis codes, or by a surrogate model. Factors like the design space dimensionality, significance of interdisciplinary coupling, and ease of interfacing several analysis codes determine the appropriate course of action. There are two potential advantages to the surrogate approach. First, it is typically easier to establish an interface between a surrogate model and an optimizer. Second, and more importantly, a surrogate model approach aids parallelization. Optimization is a sequential process and if each function call involves several iterations to converge a highly coupled MDA problem, the overall design time can be long. Instead, with a surrogate model approach, several MDA problems can be evaluated offline and in parallel for different values of the design variables. A surrogate model of the relevant system level objectives and constraints can then be formulated from these converged solutions. If however the design space is too large to efficiently sample, or the interdisciplinary coupling is weak, then a surrogate based approach may not be as advantageous.

Another popular monolithic MDAO architecture is Individual Discipline Feasible (IDF) [15] in which the residual equations are posed as constraints to the optimization problem, and thus the optimizer is now in charge of minimizing the objective function and enforcing interdisciplinary compatibility. There are also several distributed architectures proposed in literature that decompose the overall problem into smaller

sub-problems, based on the disciplines. These options are more amenable to applications in industry given that discipline autonomy is retained, unlike in the case of monolithic architectures. A survey of the various architectures and their pros and cons can be found in references [9, 63, 103]. While it may be possible to formulate the BLI aircraft optimization problem to fit some of these architectures, it is this author's opinion that given the nature of the vehicle sizing process alluded to in Sec. 3.2 and described in more detail shortly, the MDF architecture is the most intuitive and practical option for tackling simultaneous optimization of the airframe and engine for BLI vehicles.

Fig. 4.5 shows a flowchart that expands on the process and data flows summarized in Fig. 4.4. Borrowing XDSM style elements, process flows are shown with black arrows and also imply data flows. Data flows are shown with gray lines and are highlighted in situations where there is no explicit process flow, but there is a transfer information between two processes.

4.5.1 Pre-Vehicle Sizing Stage

This is the first stage in the BLI aircraft design process. It starts with a requirements definition, where the functional and performance requirements for the aircraft are defined, and any constraints are identified. The aircraft design mission profile is also specified. At this point, a conventional (non-BLI) baseline airframe design can be defined, along with the engine architecture, and initial cycle design variables. The idea is to take a reasonable non-BLI aircraft as a starting point, and then morph it into the final BLI vehicle by accounting for the BLI effects, the aero-propulsive coupling, and the resulting changes to the airframe and engine design as a result of BLI. For example, a notional 737-8 can be a reasonable baseline on which the BLI-equivalent version (similar to the D8 and NOVA-BLI concepts) can be developed, or the N2A-BWB baseline for the N2B (see chapter 2). Basically, BLI is treated as a

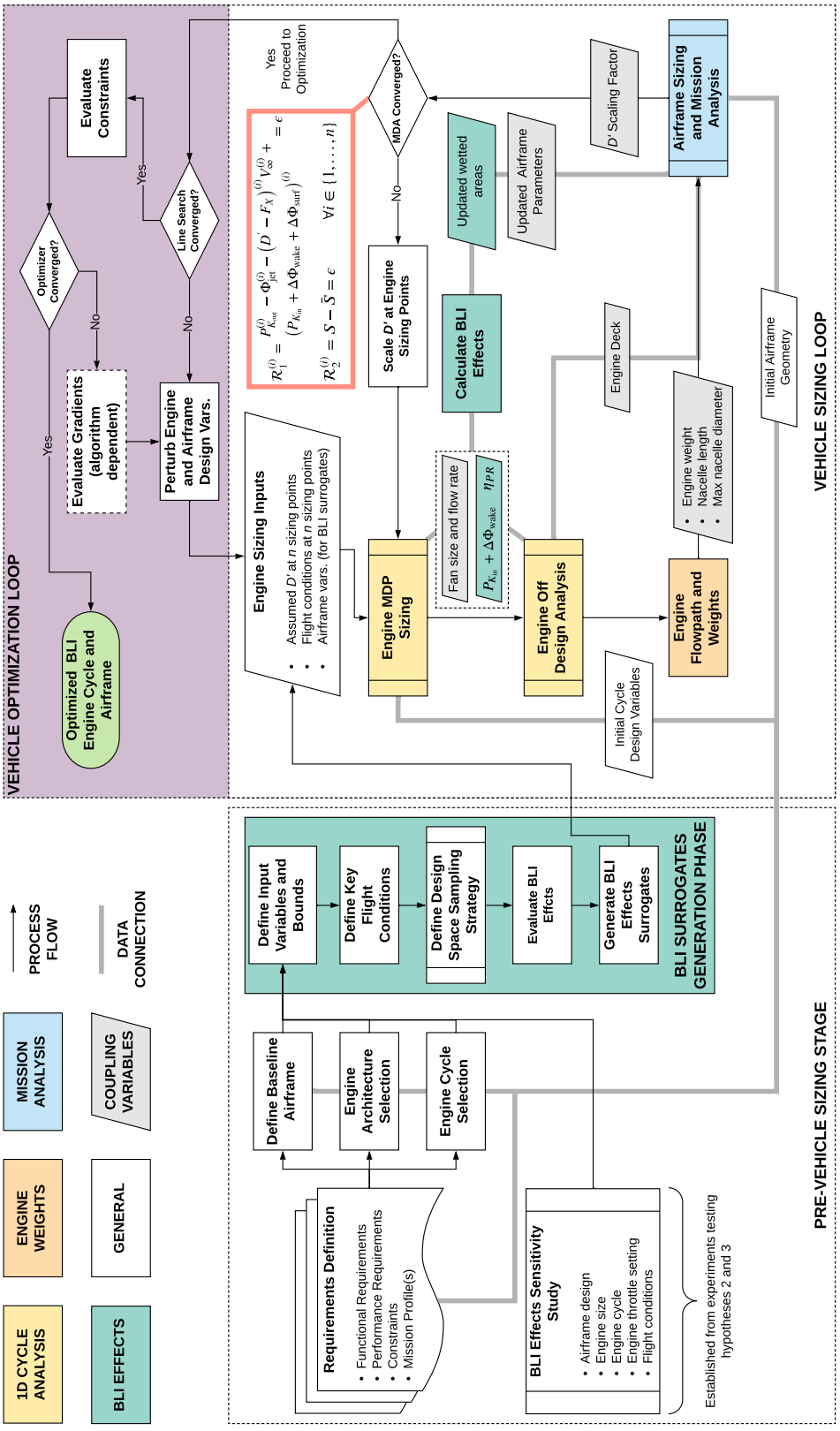

Figure 4.5: Coupled Aero-Propulsive BLI Aircraft Conceptual Design

technology that can be 'added on' to a non-BLI aircraft, and the proposed methodology in this thesis accounts for this 'BLI technology' in an appropriate manner.

In parallel, sensitivity studies to assess the most significant airframe and propulsor variables impacting the BLI effects are conducted, as described in the experimental methodology in the previous section. The sensitivity studies filter the overall design space to establish the set of variables that will feature as inputs to the surrogates of the BLI effects. Reasonable bounds are imposed on these variables to capture expected variations that occur as part of the vehicle sizing, design space exploration, and optimization routines. The baseline non-BLI aircraft developed previously serves as a reasonable initial point around which the extents of the design space can be defined.

Once the input space and flight conditions are known, a design space sampling strategy must be formulated. The number of samples is determined by the desire to maximize prediction accuracy of the surrogate model, accounting for the dimensionality of the input space, the number of CFD function calls that can be afforded, and the aircraft design objectives. If global accuracy of the surrogates is desired, then Design of Experiments (DoE) techniques such as the widely used Latin Hypercube Sampling (LHS) [65] are appropriate. Constraints on the input variables can be imposed to avoid sampling in infeasible design regions. An example of such a constraint would be one relating the minimum and maximum permissible Mach number of the aircraft as a function of altitude. Such a constraint can be formulated by looking at a typical flight envelope. If the design space is not cubical as a result of the constraints, then computer generated custom space filling designs are needed. Traditional DoEs are inappropriate for such irregular design spaces.

If however the input space dimensionality is too large to sample adequately given computational cost constraints, then dimensionality reduction techniques can be considered. Alternatively, a smaller DoE can be used in conjunction with an adaptive

sampling approach. This process allows one to obtain local accuracy (rather than global accuracy over the entire design space) in regions where maximum improvement in a metric like fuel burn is expected. The need for such approaches is ultimately determined by the results of the BLI effects sensitivity studies, and the variables of interest for the aircraft designer. Based on the results that will be presented in chapters 5 and 6, it is found that the critical design space is small enough to develop global surrogate models for the BLI effects.

Once the sample points are known, it is merely a question of running CFD for each design sample, tracking the BLI effects, and then generating surrogate models of these responses. These surrogates can be simple polynomial response surface equations (RSEs) [69], or something more advanced like Kriging [16] can be used. The latter technique also provides estimates for prediction uncertainty, useful when paired with an adaptive sampling strategy [39, 53]. Non-linear models such as Artificial Neural Networks (ANN) have also been used in aircraft design and optimization [40, 84], when standard linear regression models are inadequate. The methodology treats the surrogate models as a black box, so barring implementation challenges, any of the above approaches can be used. In this thesis, polynomial RSEs are used for modeling the BLI effects. As discussed in chapter 7, this type of model provides a good estimate for the BLI effects over the design space.

4.5.2 Vehicle Sizing Loop

Once the BLI effects surrogates are obtained, it is possible to proceed with the vehicle sizing stage. This stage can be broken down into four sub-stages as follows

(i) Engine on-design analysis

(ii) Engine off-design analysis

(iii) Engine weight and flow path analysis

(iv) Airframe sizing and mission analysis

Engine on-design begins by providing the propulsion model with estimates for the non-BLI baseline vehicle drag (thrust required), D', and the flight conditions at each of the n engine sizing points. The thrust requirements at this stage are merely initial guesses, which will be updated over the course of the sizing process. The initial cycle design is also known from the previous stage. A subset of the airframe design parameters from the baseline are also provided for the BLI effects surrogates. The engine is sized using the Multi-Design Point (MDP) approach [82, 83]. Within this sub-stage, multiple calls are made to the BLI effects surrogates for $P_{K_{\text{in}}}$, $\Delta\Phi_{\text{wake}}$, and η_{PR} to correct engine performance as a function of the changing engine size and operation. These surrogates are embedded within the engine analysis code, rather than as a separate external process. Thus, gray lines are used to depict data connections between the engine stages and the BLI effects surrogates in Fig. 4.5.

Once the engine has been sized, off-design analysis can then generate an engine deck. Again, for each point in this deck, engine performance is corrected by the BLI effects surrogates. Note that the fan size is fixed at this sub-stage. The sized engine weights and dimensions can then be estimated and values for the overall engine weight, max nacelle diameter, and nacelle length are also obtained. These results, along with the engine deck, are used in the airframe sizing process. In addition, the BLI effects surrogates also provide estimates for changes in the fuselage and nacelle wetted areas, compared to the non-BLI baseline, as a result of going to a partially embedded nacelle for the BLI configuration. These wetted area corrections are used to modify D', calculated by the airframe sizing code, thereby accounting for $\Delta\Phi_{\text{surf}}$ effects on performance.

Based on the requirements definition, airframe design parameters, and engine design and performance, the aircraft is sized and run through the specified mission. The airframe sizing code determines whether the engine performance is adequate for

the sized airframe, and if not, calculates a scaling factor that updates the thrust requirements at the sizing points. Additionally, for aircraft sized using a fixed wing loading, the wing planform area is also scaled based on the final aircraft MTOW. The engine-aircraft design loop is said to converge when the following residuals defining the MDA problem are satisfied

$$\mathcal{R}_1^{(i)} = P_{K_{\text{out}}}^{(i)} - \Phi_{\text{jet}}^{(i)} - \left(D' - F_X\right)^{(i)} V_\infty^{(i)} + \left(P_{K_{\text{in}}} + \Delta\Phi_{\text{wake}} + \Delta\Phi_{\text{surf}}\right)^{(i)} \leq \epsilon \quad \text{(4.34a)}$$

$$\mathcal{R}_2 = S - \bar{S} \leq \epsilon \quad \text{(4.34b)}$$

$$\forall i \in \{1, ..., n\}$$

In Eq. (4.34), ϵ is a user defined threshold value. The residual $\mathcal{R}_1$ is defined for each engine sizing point i. In $\mathcal{R}_2$, $\bar{S}$ is the guessed wing planform area provided to the BLI effects surrogate model at the start of the iteration and S is the value obtained from the airframe sizing code based on the calculated MTOW and the user specified wing loading. If convergence is not achieved at a given iteration, the updated planform area and propulsor power requirements are passed back to the engine MDP sizing and this Fixed Point Iteration (FPI) repeats till convergence.

4.5.3 Vehicle Optimization Loop

Given that the BLI aircraft is developed from a non-BLI starting point, it is possible that the initial engine cycle and/or airframe design parameters are not optimal. Therefore, the vehicle sizing loop can be repeated multiple times for a sweep of cycle design parameters and key airframe geometry variables in a design space exploration study. If simultaneous engine and airframe optimization is conducted, each function call corresponds to one vehicle sizing FPI. If the line search in the optimization algorithm has converged, based on algorithm dependent convergence criteria, the constraints imposed on the problem can be evaluated. If the chosen point satisfies the

constraints, and the optimization convergence criteria, then the optimum solution is obtained. If not, the cycle and airframe design variables need to be perturbed and process repeats as shown in Fig. 4.5.

4.6 Determining Consequences of Ignoring Aero-Propulsive Coupling

This section briefly outlines the experiments that will leverage the methodology described above to answer research question 1. Details can be found in chapter 7. To answer research question 1 and test the associated hypothesis, the following high-level objectives must be satisfied:

Objective 1: Implement the proposed BLI conceptual design methodology on the sizing, airframe and propulsor design, and mission analysis of a BLI aircraft.

Objective 2: Develop the same BLI aircraft with a decoupled approach, where the BLI effects are estimated from a point design, and the aero-propulsive feedback loop is not converged.

Objective 3: Compare the performance and design of the BLI concepts developed using the coupled and decoupled approaches to quantify the impacts of aero-propulsive coupling.

Objective 4: Repeat the design methodology comparison for the same class of BLI aircraft, but with a different engine location relative to the wing to determine if the strength of aero-propulsive coupling is configuration dependent.

The scope of the effort to satisfy objective 1 is restricted to the design and analysis of a 150-180 passenger, single-aisle class, BLI equivalent of the Boeing 737-8, with an E.I.S. by 2040. The STARC-ABL, NOVA-BLI, and the D8 all fit this general

description. Given differences in the engine location relative to the wing on these aircraft, objective 4 can be satisfied by comparing any of these two concepts. To clarify, there is no need to re-design the exact D8, NOVA-BLI or the STARC-ABL. Objective 4 can be met by comparing two similar aircraft, designed for the same requirements, but with engine locations similar to that on the above mentioned concepts. As such, for this effort, aircraft with a 'top-mounted' engine like on the D8 and a 'side-mounted' engine, like on the NOVA-BLI are compared, as shown in Fig. 4.6. Unlike the STARC-ABL, where the BLI propulsor is a ducted fan, both the D8 and the NOVA-BLI feature two BLI turbofans. With a similar airframe design, these two concepts share a lot of common characteristics, with the exception of the engine location. Thus, these two concepts serve as ideal baselines from which two generic BLI aircraft can be developed and compared for objective 4.

Figure 4.6: Two different configurations examined in experiment 1

To satisfy objectives 3 and 4, two sets of studies are conducted for each configuration, with a common set of requirements such as range, payload, design mission, etc.

Experiment 1.1: MDA Sweeps

In this experiment, both design wing loading and FPR are swept independently within a reasonable range. For each design point, the required fuel weight is tracked. This metric is recorded for the non-BLI configuration, the BLI configuration obtained using a decoupled approach, and the BLI aircraft with the proposed coupled methodology.

The percentage difference in fuel weight requirements between the decoupled and coupled approaches is calculated and compared for the two configurations. No additional experiments will be needed to support hypothesis 1 if a significant difference in the fuel burn estimate is observed between the coupled and decoupled approaches, and between configurations, relative to the predicted BLI benefit.

Experiment 1.2: Optimization

In experiment 1.1, most airframe and propulsor cycle parameters are kept fixed. Experiment 1.1 intends to show that there are differences in performance depending on the BLI modeling approach and configuration considered. However, experiment 1.2 intends to show that there are differences in optimum vehicle design characteristics as well. This experiment extends the previous set of trials by allowing for variations in key airframe and engine cycle design parameters. These variables will be optimized simultaneously using a decoupled and coupled approach to minimize fuel weight requirements. The architecture for conducting coupled optimization is shown in Fig. 4.4. The optimized airframe and engine design characteristics between decoupled and coupled approaches will be compared between each configuration.

CHAPTER 5
BLI EFFECTS SENSITIVITY TO AIRFRAME

This chapter describes the experiments conducted to answer research question 2 by testing the related hypothesis. A systematic experimental approach is designed to maximize information gained from a small set of trials. This endeavor is constrained to tube and wing BLI aircraft, predominantly in 150-180 passenger class. The results provide a physics based insight into the relation between engine position and the sensitivity of BLI effects at this location to a limited set of airframe design features. The active and inactive variable spaces, within this design scope, are thus identified. Rule of thumb guidelines for defaulting geometry detail, as part of the proposed BLI concept design methodology, are discussed. These suggestions are based on the relative sensitivity of the BLI effects to the macro and detailed parameters, gleaned from the results. Consequently, these experiments are an important step in the overall methodology. This chapter is organized as follows: first, a description of the experimental apparatus is provided, including comments on setting up the CFD simulations and establishing a condition for flagging significant changes in the BLI effects due to changes in airframe design. Then, experiment specific overviews and results are described. The chapter concludes with a summary of key takeaways and assesses whether the proposed hypothesis is supported by the results.

5.1 Experimental Notes

5.1.1 Software Tools

The main software tool requirements include CAD and CFD capability for generating and analyzing the aircraft geometries respectively. The commercially available CFD

code STAR-CCM+, by Siemens, is used for the aerodynamics analysis. STAR is a well validated code, used extensively in industry and academia, including boundary layer ingestion modeling studies in [104, 33] for example. STAR's RANS modeling capability with unstructured grids, ease of use, availability, and access to resources with extensive documentation and guidelines on best practices make this tool a suitable choice for this thesis. Geometry generation and modification capability is provided by OpenVSP, SolidWorks, and STAR-CCM+ CAD tools. OpenVSP facilitates creating wings and other complex shapes that would be difficult to build from scratch in CAD. SolidWorks and STAR-CCM+ on the other hand are primarily used for obtaining watertight geometry. Engine performance analysis, as required for defining the significant difference threshold, is conducted using the industry standard 1D thermodynamic cycle code NPSS.

5.1.2 Comments on CFD Model Setup

All CFD runs leverage STAR-CCM+ built-in capability for surface and volume mesh generation. An unstructured Cartesian mesh is used with prism layers for near wall refinement to capture the boundary layer. The near wall spacing is calculated such that a wall $y^+ \leq 1$ is achieved over the entire surface. All results are obtained under the assumption of steady state conditions, by solving the Reynolds Averaged Navier Stokes equations. The solver uses an implicit time integration scheme with second order upwind spatial discretization. Fully turbulent conditions are assumed, and the SST k-ω turbulence model [67] is chosen. This model is commonly adopted in the aerospace industry, and is also robust under conditions of adverse pressure gradients and separation. A small CFL sensitivity study is conducted and value of 20 is chosen for all cases without a wing, and 10 for trials with a wing. These values ensure quick and reliable solver convergence. A multi-grid initialization strategy is employed to improve solver convergence. A spherical freestream boundary with a

radius approximately 30 times the fuselage length is defined and symmetry about the x-z plane in all cases allows for half the domain to be modeled. Standard atmosphere properties [94] are assumed for all experiments.

5.1.3 Baseline Airframe Geometry

A schematic of the baseline geometry and experimental setup in CFD is shown in Fig. 5.1. The baseline geometry consists of an axisymmetric fuselage only, with a cylindrical center-body, an elliptical nose, and a conical aft section. This simplified representation of the aircraft enables a ground-up approach to assess the sensitivities, gradually building up to more complex geometry over the course of the experiments. As a result, key features that influence the BLI effects can be identified more easily than in the case where a complex geometry is used as a starting point and then parameterized.

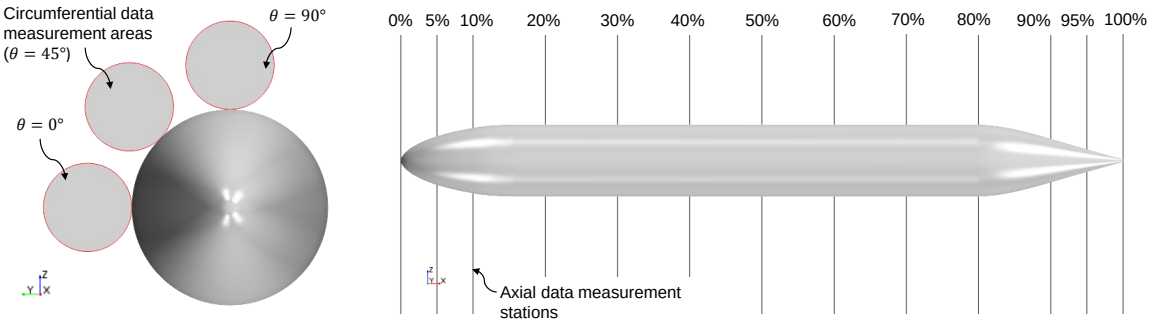

Figure 5.1: Schematic showing baseline geometry and measurement stations for experiments testing hypothesis 2. Axial stations are spaced at regular intervals along the fuselage (x/L_{ref}) where $L_{\text{ref}} = 39.12\text{m}$

The transition between the nose and center-body, and center-body and tail is smooth and gradual to avoid shocks and flow separation at high Mach numbers. Subsequent modifications to the geometry that may produce shocks or separation can thus be assessed against a relatively ideal baseline. The length of the fuselage is 39.12m. This length is similar to the Boeing 737-8 [14] and is thus also comparable

to the NOVA-BLI, D8, and STARC-ABL concepts that have been sized for 150-180 passengers. The diameter of the baseline center-body is 3.89m, defined such that the area of the cylindrical center-body cross section matches the area of the elliptical Boeing 737-8 center-body cross section [14]. The baseline features a blunt trailing edge with an arbitrarily set radius of 0.15m to avoid meshing issues around a sharp point trailing edge.

Along the axial direction, a series of planes are defined on which surface integrals for non-dimensional BLI effects $C_{P_{K_{\text{in}}}}$, $C_{\dot{E}}$ (change in wake dissipation), and η_{PR} are calculated on pre-defined circular areas, shown with red outlines in Fig. 5.1. Non-dimensionalization of the BLI effects is done by dividing the dimensional quantities by $\frac{1}{2}\rho_\infty V_\infty^3 S_{\text{ref}}$ [34], where S_{ref} is a reference area, set to 1 for these experiments. These integration areas represent a fictitious propulsor inlet and outlet at different circumferential locations. A nacelle is introduced in the experiments for research question 3, when the propulsor impacts on the BLI effects are assessed. At each axial plane, except at the trailing edge, these integration areas are tangent to the fuselage surface, and are located at 0°, 45°, and 90° relative to a coordinate system whose origin coincides with the centroid of the cross sectional area at a given axial location. Defining the measurement locations in such a fashion allows for the experiments to establish a relation between engine axial and circumferential location on the fuselage, and the sets of active and inactive design variables, as discussed in chapter 3. The axial station at the nose is shown in Fig. 5.1 for completeness, but no quantities are calculated at this station. For the axial station at the trailing edge, the center of the integration area is coincident with the centroid of the trailing edge, thus representing a fictitious tail cone propulsor like the STARC-ABL. The diameter of these integration areas is defined as 1.75m, which is approximately the fan diameter of the LEAP-1B engines on the Boeing 737-8 [89]. This diameter is fixed for all experiments related to research question 2.

5.1.4 Mesh Sensitivity Study

The first step before running any case is to establish a good quality mesh, where 'goodness' is defined by the ability of the chosen mesh to satisfy two key requirements:

1. Mesh must have sufficient resolution such that good solver convergence is achieved and accurate solutions can be obtained

2. Minimize computational requirements, i.e., mesh size must be such that the memory and CPU-time requirements are within the bounds set by the available computational resources.

Requirement 2 stems from the scenario where available computational resources are shared with other researchers and as such, it is not practical to pick meshes that require a significant percentage of the available resources to generate and run. Additionally, wall clock time concerns for such large meshes, especially when several cases need to be run, is another limiting factor. However, this requirement conflicts with requirement 1 which emphasizes the need for accurate solutions, which are usually achieved with well refined meshes. Thus, the goal of this mesh sensitivity study is to find the mesh settings that provide an adequate compromise between the requirements. Since STAR-CCM+ is an extensively validated code, the objective is not to validate the solver itself.

Sixteen cases with different combinations of mesh settings and CFL numbers are generated. These cases are run at the baseline flight condition of $M_\infty = 0.8$ at 35,000 ft, since most of the experiments for hypotheses 2 and 3 are conducted at this condition. The baseline fuselage is used as the geometry. The mesh quality is evaluated on the following criteria:

1. Sensitivity of the BLI effects to the mesh settings, specifically mesh size

2. Whether the axisymmetric nature of the flow is maintained. An axisymmetric fuselage at zero incidence to the flow and no side-slip should theoretically have axisymmetric flow. A half domain 3D solution should reflect this property.

3. Solver convergence - determined by looking at residual history and convergence plots of BLI quantities at different locations on the fuselage

Within these 16 cases, factors such as mesh type (Cartesian vs. Polyhedral), CFL number (5, 10, 20), surface and volume growth rates, number of prism layers, target cell size, etc. are tested, and factors like CPU-time, wall-time, memory requirements, etc. are tracked in addition to the results of the simulations. The mesh sizes range from 1M - 7M cells. Fig. 5.2 compares a few meshes from the 16 cases to illustrate the mesh quality with respect to criterion 1. For clarity, these results are only shown at the zero degree circumferential station. All cases shown here are run at the same CFL number of 20.

From Fig. 5.2, one can see that the trends for all three BLI effects are consistent across meshes, however, there are small numerical differences between the meshes in the tail cone region, i.e., $x/L_{ref} \geq 0.8$. These differences are critical as most BLI engines are typically mounted in this region. The best quality mesh is shown with a yellow outline to the markers (mesh 13), while the final mesh chosen (mesh 8) is shown with a black outline. The differences between these two meshes are small enough to favor the coarser mesh for computational efficiency. Evident from the plots, one can see that the coarsest mesh (mesh 2) tends to over-predict $C_{P_{K_{\text{in}}}}$ in the fuselage aft section, while the values for mesh 16 are inconsistent with other meshes at the trailing edge measurement station. An explanation of the physics behind the BLI effects trends is provided in section 5.2.

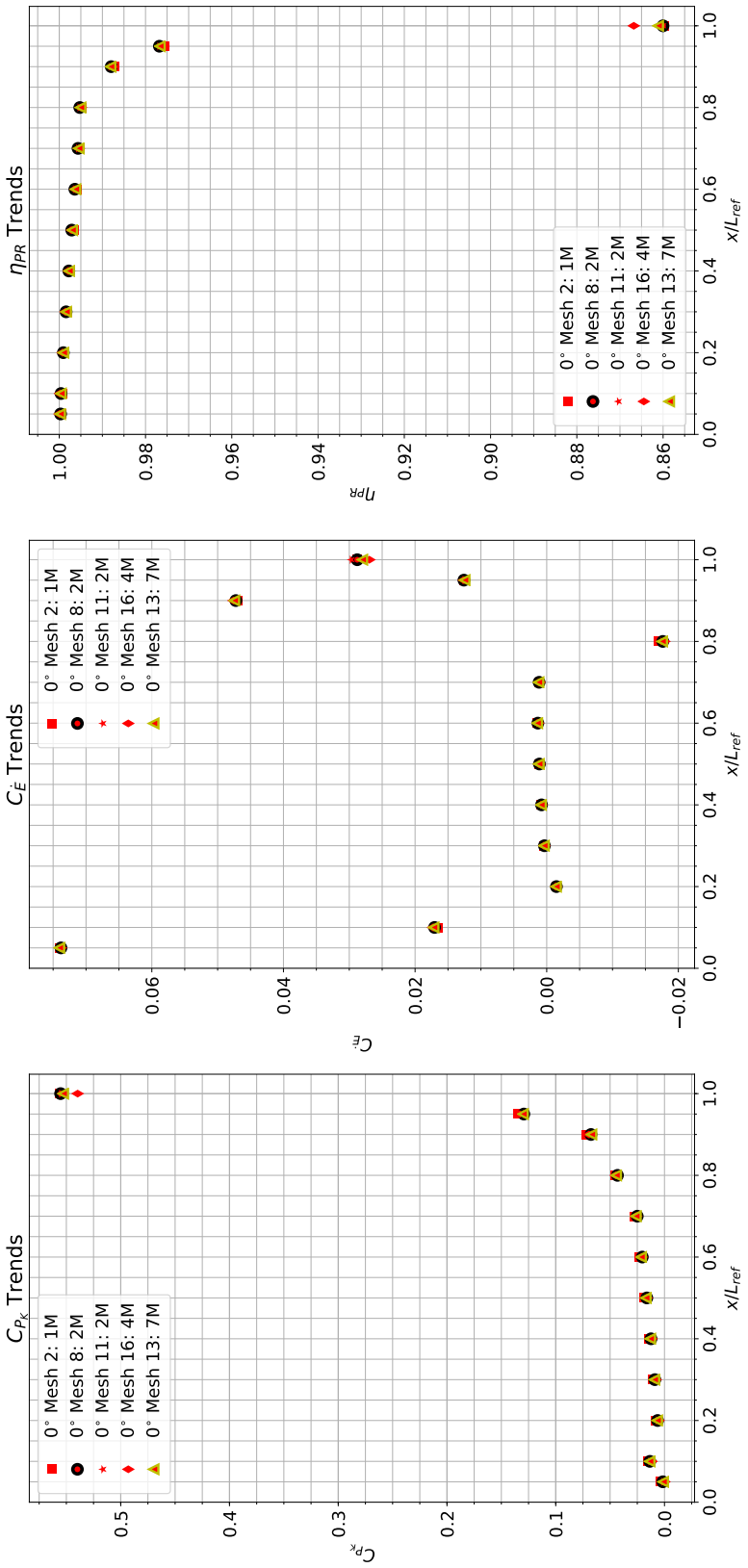

Figure 5.2: Comparison of BLI effects trends from selected meshes generated in the mesh sensitivity study, shown at the 0° circumferential station

The overall mesh size is not the only factor affecting the quality of the mesh. Both mesh 8 and 11 have a size that is roughly 2M cells, but mesh 8 is chosen because it retains the axisymmetric nature of the flow better than mesh 11, as shown in Fig. 5.3. Red, blue, and green squares are used to denote values at the 0°, 45°, and 90° stations respectively. In axisymmetric flow, these points should overlap.

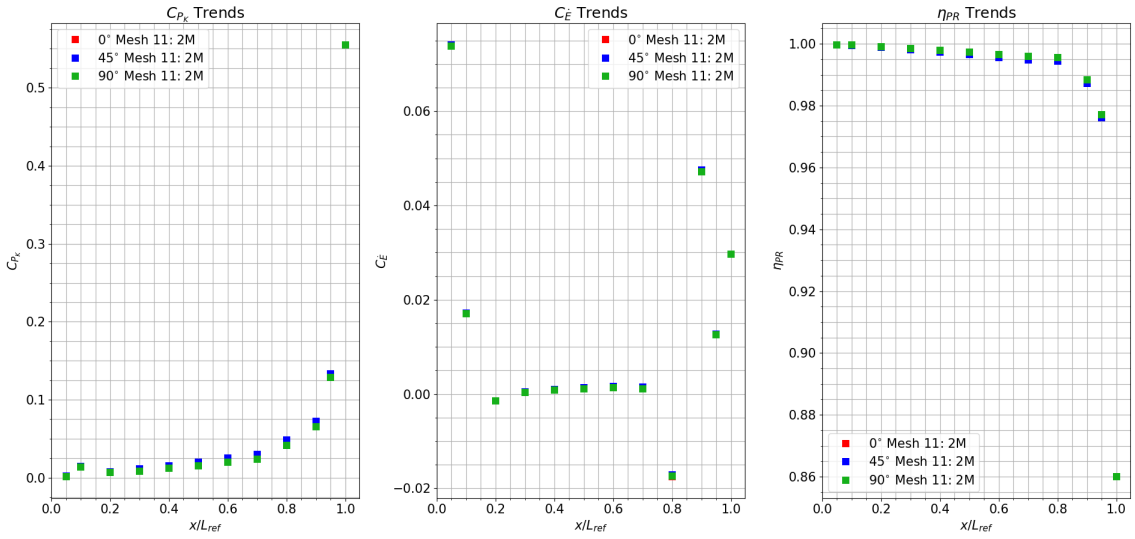

(a) Mesh 11

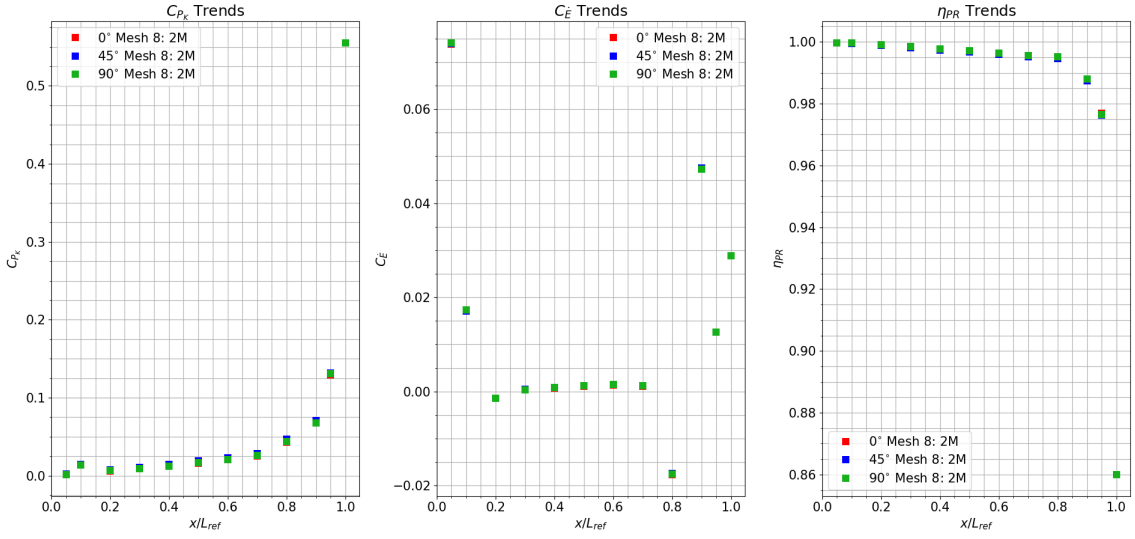

(b) Mesh 8

Figure 5.3: Comparison of mesh 11 and 8 - ability of mesh to capture axisymmetric nature of flow

In mesh 11, the 45° station $C_{P_{K_{\text{in}}}}$ and η_{PR} results are slightly offset from the 0° and 90° values. In mesh 8, however, these differences are minimized considerably. Defining a volumetric control over the fuselage, thus ensuring an almost uniform volume mesh size in that region, for a given radial extent, enables the flow solver to capture axisymmetric flow to a better degree.

Fig. 5.4 shows the final volume mesh on the symmetry plane for the baseline geometry. There is additional refinement in regions of high curvature, i.e., near the tail and nose to ensure good resolution of the geometry. For this baseline mesh, the residuals drop by three to four orders of magnitude for y and z momentum, and almost five orders of magnitude for continuity, x momentum, and energy. To save time and computational resources, the same mesh settings are used over the course of all the fuselage only experiments. Only the prism layer near wall thickness and total thickness are changed (to maintain wall $y^+ \leq 1$) when the fuselage length is

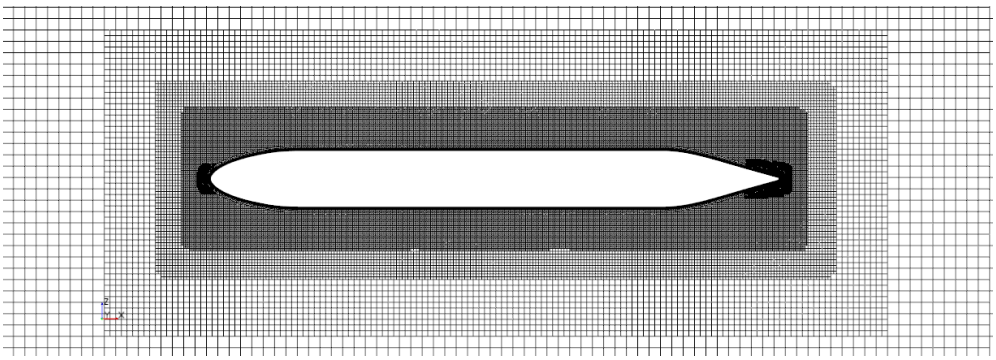

Baseline Volume Mesh (Symmetry Plane) – Near View

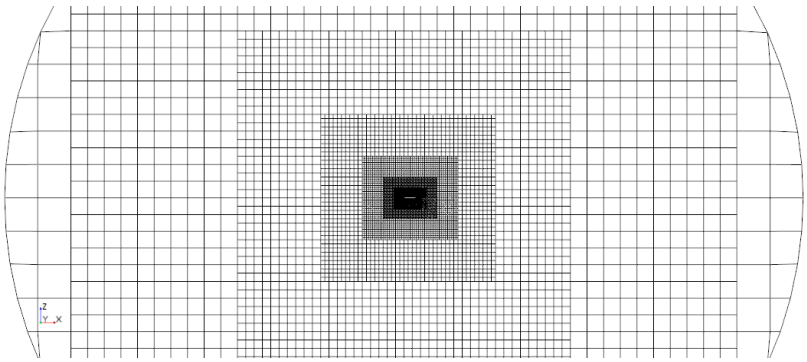

Baseline Volume Mesh (Symmetry Plane) – Far View

Figure 5.4: Baseline mesh viewed at symmetry plane

altered in experiment 2.5. For trials where the wing or empennage are added to the geometry, the mesh settings for the fuselage are kept the same. The settings for the additional component are assessed over two to three trials against the criteria stipulated previously. Similar (or sometimes even better) solver convergence behavior is noticed for all the experiments.

5.1.5 Significant Difference Criterion

Sensitivity of the BLI effects to the airframe is determined by comparing the numerical results from the modified geometry to the established baseline. To assess whether these differences are significant, some sort of threshold must be established. Since the primary objective of BLI is to minimize fuel burn, a simple condition for identifying significant changes can be obtained by comparing differences in fuel flow rate at a single operating point due to changes in thrust required and inlet pressure recovery.

A notional engine for a generic 150-pax vehicle (similar to the LEAP-1B for the 737-8) is modeled in NPSS using the MDP approach, with five design points: Sea Level Static (SLS), takeoff (TKO), hot day takeoff, Top of Climb (TOC), and ADP. The TOC and ADP points are at $M_\infty = 0.8$ at 35,000 ft. As shown in Fig. 5.5, the baseline cruise fuel flow rate is shown with an orange marker. Subsequently, the design thrust requirement at TOC is varied between $\pm$200 lbf ($\pm$3.12%) relative to the baseline and the corresponding percent change in fuel flow rate is tracked, shown with black markers in Fig. 5.5. To avoid lapse rate effects, the ratio of TOC/SLS and TOC/TKO thrust requirement is kept the same for each case regardless of the TOC thrust value. A similar exercise is conducted for the situation where the inlet pressure recovery is reduced by 1% relative to the baseline, shown with red markers.

The blue lines correspond to a $\pm$0.5% change in fuel flow rate relative to the baseline, and are defined as critical thresholds beyond which this change is significant. These thresholds map to a 35 lbf change in thrust required (0.55% of baseline TOC

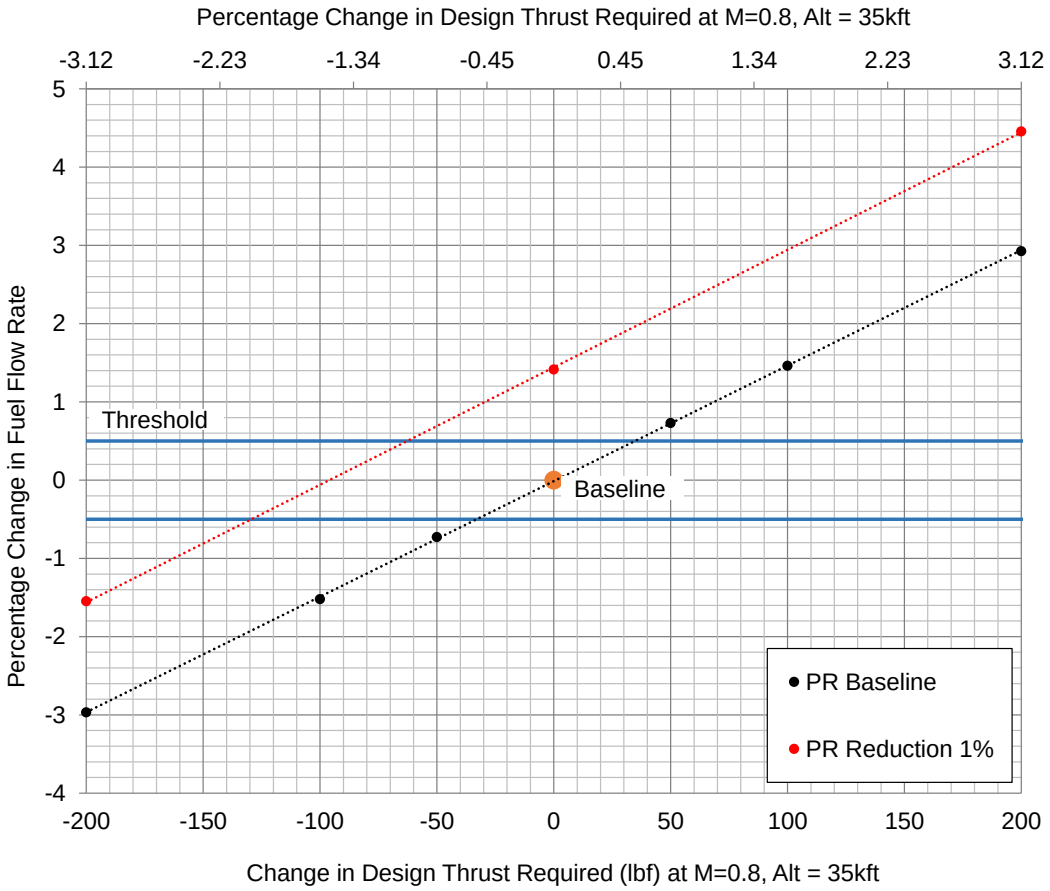

Figure 5.5: Variation of fuel flow rate at $M_\infty = 0.8$ at 35,000 ft as a function of change in design thrust required and inlet pressure recovery for an engine on a generic 150-pax aircraft

requirements) and a 0.35% change in pressure recovery. It is important to note that the objective of the experiments for research question 2 is not so much to quantify the BLI benefit, but rather, quantify the *difference in the estimate for the BLI effects* due to changes in airframe design. As such, the *change* in the estimate for the BLI effects between two trials, translated to an equivalent change in force, is compared against the threshold values derived above, in situations where the flight conditions are the same for both cases. In other situations, percentage differences, and relative differences in power counts ($\Delta(\cdot) \times 10^4$) between the non-dimensional BLI effects are shown.

5.2 Experiment 2.1: Sensitivity to Flight Conditions

5.2.1 Experimental Overview

The objective of this initial set of experiments is to assess the sensitivity of the BLI effects to flight conditions i.e., Mach number, altitude, and aircraft angle of attack. Engine performance and aircraft mission profiles are typically specified as a function of Mach and altitude, rather than Mach and Reynolds number. Subsequently, the following set of experiments treats altitude as an independent variable, with Reynolds number as a fall out. Table 5.1 below presents the five cases that are run on the baseline aircraft geometry. The Reynolds number, based on the fuselage length, corresponding to the Mach/altitude combinations is also included for clarity.

Table 5.1: Experiment 2.1 - Overview of Cases

Experiment	Mach	Altitude (ft)	α (°)	$Re_{L_{\text{fuse}}}$	Comments
2.1-1	0.8	35000	0	2.44×10^8	0° Baseline
2.1-2	0.4	35000	0	1.22×10^8	
2.1-3	0.8	17500	0	4.34×10^8	
2.1-4	0.4	17500	0	2.17×10^8	
2.1-5	0.8	35000	2	2.44×10^8	2° Baseline

Cases 2.1-1 and 2.1-5 are at a typical cruise flight condition, which is also a common TOC and ADP engine design point flight condition. For this reason, cases 2.1-1 and 2.1-5 are defined as baselines. Results from other experiments are compared to the reference case results from 2.1-1 or 2.1-5, depending on the angle of attack, unless otherwise specified. Cases 2.1-2 and 2.1-3 aim to quantify the differences in BLI effects if the Mach number and altitude are halved independently. Since cases 2.1-2 and 2.1-3 are not necessarily common points in a typical mission profile, case 2.1-4 is run to show the differences at a more realistic flight condition. The results from 2.1-2 and 2.1-3 are then used to explain the differences seen between 2.1-1 and 2.1-4.

5.2.2 Results and Discussion

Sensitivity to Mach Number

Fig. 5.6a compares the axial and circumferential trends in BLI effects for case 1 ($\alpha = 0°$ baseline), shown with squares, and case 2, shown with circular markers. Red, blue, and green colored markers are used to denote quantities at the 0°, 45°, and

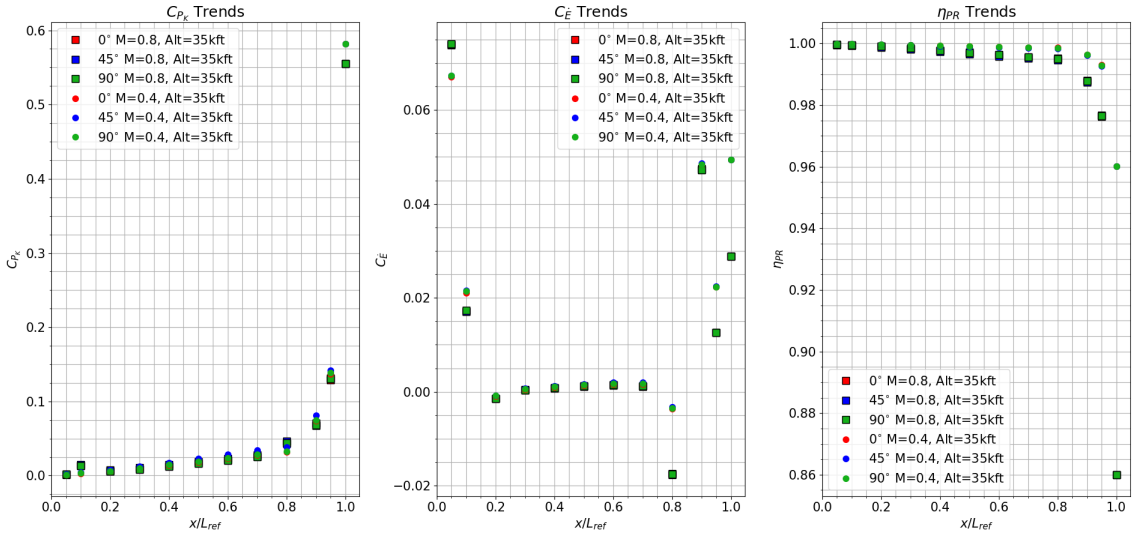

(a) Axial and circumferential trends in BLI effects

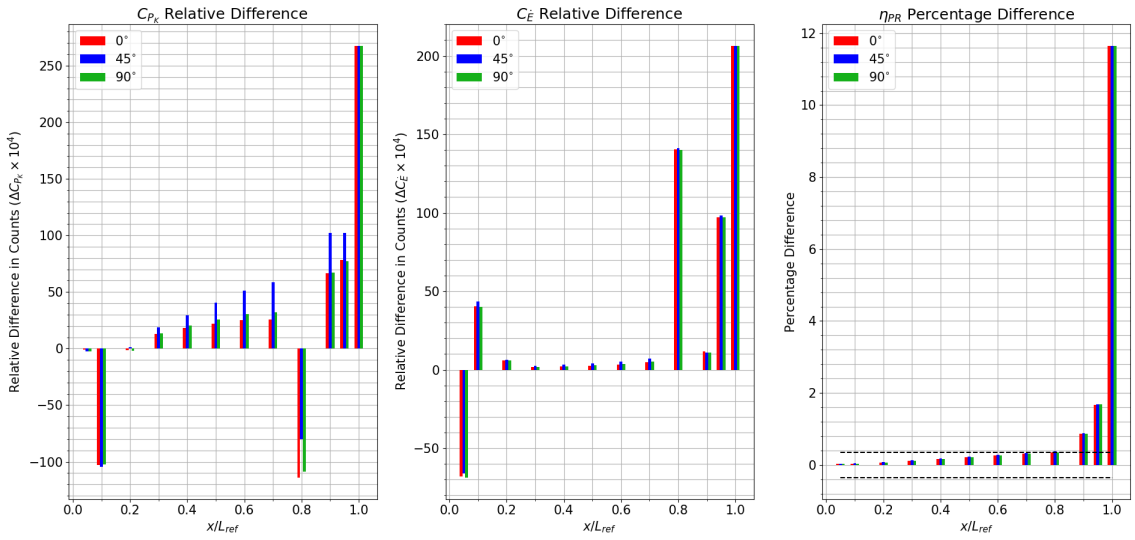

(b) Relative and percentage differences in BLI effects

Figure 5.6: Experiment 2.1 case 2 vs. 1 - sensitivity to Mach number

90° circumferential stations respectively. The relative difference in counts for $C_{P_{K_{\text{in}}}}$ and $C_{\dot{E}}$, and the percentage difference for η_{PR} is shown in Fig. 5.6b[1]. The critical difference threshold for η_{PR} is shown with dashed black lines.

Trends for $C_{P_{K_{in}}}$ and η_{PR}

Positive values of $C_{P_{K_{\text{in}}}}$ at all stations imply reductions in propulsive power requirements relative to the non-BLI case, with the greatest propulsive benefit achieved at the 100% axial station (A1.00) propulsor. However, this benefit is somewhat offset by a considerable drop in η_{PR}. The trends for $C_{P_{K_{\text{in}}}}$ and η_{PR} with axial location are opposite to each other, evident in Fig. 5.6a. The counteracting trends of $C_{P_{K_{\text{in}}}}$ and η_{PR} with axial distance highlight a challenge in designing BLI vehicles. To maximize the lower inflow momentum benefit (higher $C_{P_{K_{\text{in}}}}$), a thicker boundary layer is desired. However, a thicker ingested viscous layer comes at the cost of low pressure recovery and high distortion, which penalizes engine performance. A feasible design must have a favorable net impact.

The relatively gradual change in both $C_{P_{K_{\text{in}}}}$ and η_{PR} up to 80% of the fuselage length can be attributed to boundary layer growth along axial distance, where the boundary layer thickness, $\delta \propto x^{0.8}$, from simple turbulent flat plate boundary layer relations. As the boundary layer grows, the increasing viscous losses manifest as lower averaged total pressure at the integration planes normal to the boundary layer, which results in a drop in η_{PR} with axial location. However, the thickening boundary layer also presents a larger region of low velocity flow i.e., a larger kinetic energy defect, which translates to an increase in $C_{P_{K_{\text{in}}}}$ with axial distance.

The rapid change at the aft end is driven by the tapering of the fuselage and the

[1]In all figures that compare case j vs. case i, the relative difference between case j and i is calculated as $\Delta_{ji} = (\cdot)_j - (\cdot)_i$. This relative difference is either expressed as counts ($\Delta_{ji} \times 10^4$) when the flight conditions are not the same, or in terms of power ($\Delta_{ji} \times q_\infty V_\infty S_{\text{ref}}$) and an equivalent force ($\Delta_{ji} \times q_\infty S_{\text{ref}}$). The percentage difference for η_{PR} is given by $\frac{\Delta_{ji}}{(\cdot)_i} \times 100\%$.

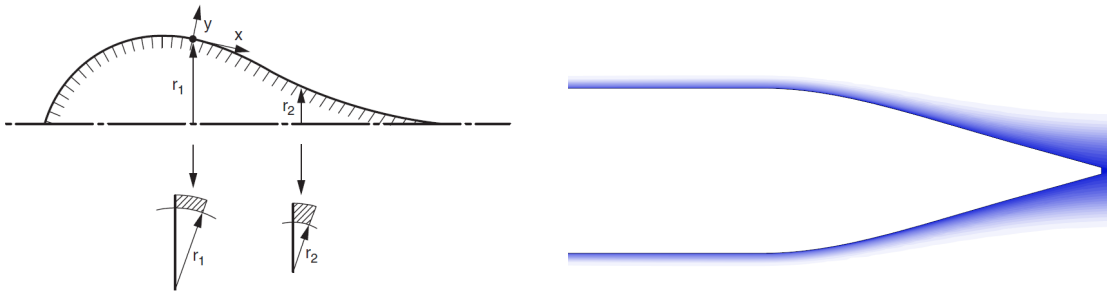

(a) Effects of axisymmetric body radius on boundary layer thickness (reproduced from [66])

(b) Boundary layer growth in aft region for baseline geometry

Figure 5.7: Effects of axisymmetric body radius on boundary layer growth

adverse pressure gradient effects on the boundary layer. According to McLean, the variation in the body radius, from the symmetry axis, affects the stretching of the boundary layer circumferentially, as illustrated in Fig. 5.7a. In this figure, the side cross sectional view is shown on top, while the illustrations below show the front cross sectional view and the circumferential stretching of the boundary layer. A smaller radius, i.e., in the tapering region of the fuselage, (indicated by r_2 in Fig. 5.7a) increases the boundary layer growth rate relative to a planar flow with the same pressure gradient [66]. The taper, in conjunction with the adverse pressure gradient, contributes to the thicker boundary layer seen in Fig. 5.7b for the baseline geometry aft region. The A1.00 plane shows the largest $C_{P_{K_{\text{in}}}}$ and the smallest η_{PR} since this location ingests the entire circumferential extent of the boundary layer, unlike the upstream stations that only ingest a sliver.

In order to explain the effects of Mach number on $C_{P_{K_{\text{in}}}}$, Eq. (4.9) needs to be manipulated to a more convenient form. Eq. (4.9) is divided by $\frac{1}{2}\rho_\infty V_\infty^3 S_{\text{ref}}$ to non-dimensionalize the quantity, and then upon rearranging terms, the following expression for $C_{P_{K_{\text{in}}}}$ at a given measurement station i is obtained:

$$C_{P_{K_{\text{in}}}} = \iint \left[\frac{\rho_i V_i}{\rho_\infty V_\infty} \left(1 - \frac{V_i^2}{V_\infty^2} \right) - C_{p_i} \frac{V_i}{V_\infty} \right] \frac{dS_i}{S_{\text{ref}}} \tag{5.1}$$

Here, $C_{p_i} = \frac{p_i - p_\infty}{\frac{1}{2}\rho_\infty V_\infty^2}$ is the pressure coefficient and V_i is the axial velocity magnitude at a given station. The first term in Eq. (5.1) is like an ingested kinetic energy thickness. The second term captures the direct contribution of the inviscid flow pressure at a given axial location on $C_{P_{K_{\text{in}}}}$. The indirect contribution of the pressure field arises through the impacts of the pressure gradient on the ingested boundary layer energy defect. The role of Mach number can be assessed by looking the two components of $C_{P_{K_{\text{in}}}}$ individually.

Fig. 5.8 compares the C_p distribution over the fuselage for the first three trials. The contours of $-C_{p_i}\frac{V_i}{V_\infty}$ are compared between the first two trials in Fig. 5.9.

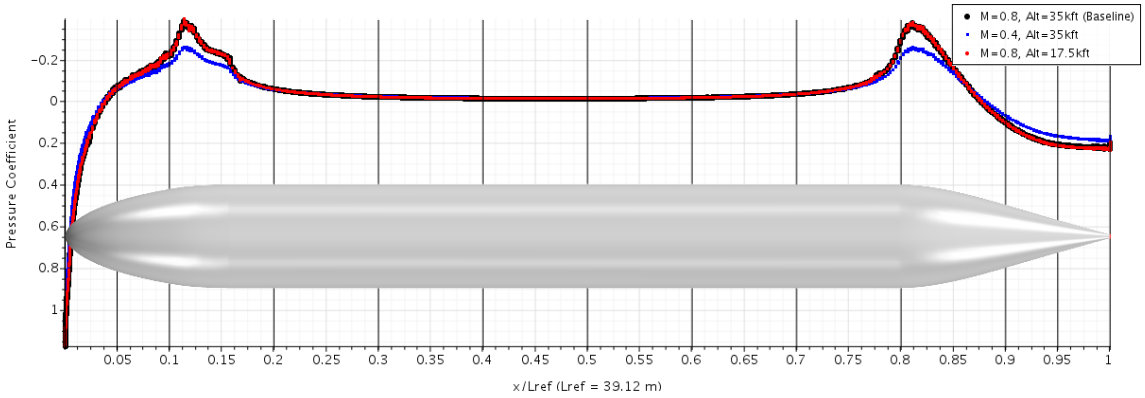

Figure 5.8: Experiment 2.1 cases 1 to 3 - pressure coefficient distribution on fuselage

The suction peaks for $M_\infty = 0.4$ are lower in magnitude than at $M_\infty = 0.8$, as one would expect based on the Prandlt-Glauert compressibility rule, which primarily accounts for the lower $C_{P_{K_{\text{in}}}}$ at the 10% and 80% axial stations for case 2. On stations along the center-body and especially the aft section, $C_{P_{K_{\text{in}}}}$ is higher for case 2. From Fig. 5.9, one can see that halving the Mach number has a more significant impact on the flow quantities at the transition regions between the nose and center-body, the center-body and tail cone, and in the tail cone region itself. The smaller magnitude of $-C_{p_i}\frac{V_i}{V_\infty}$, in the aft region for the lower Mach number case, offsets the reduction in energy thickness. The net result is an increase in $C_{P_{K_{\text{in}}}}$ with this decrease in Mach number

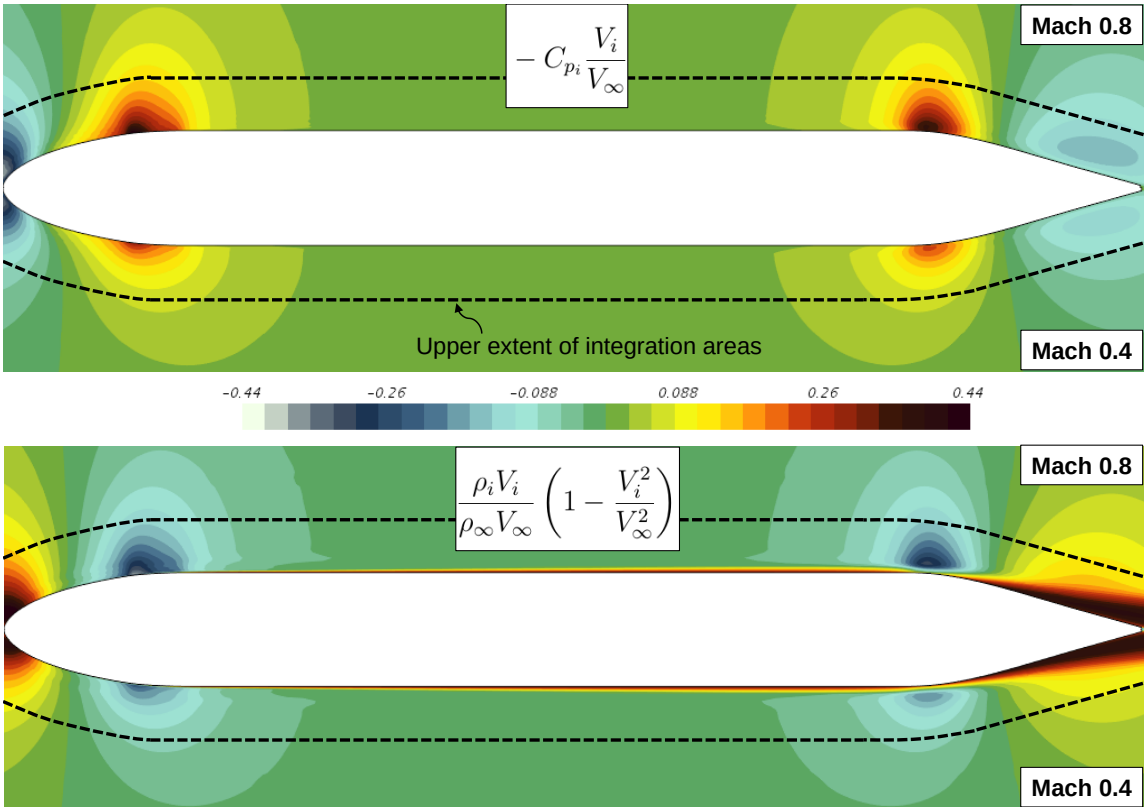

Figure 5.9: Contours comparing the pressure and energy defect contributions to $C_{P_{K_{\text{in}}}}$ at $M_\infty = 0.8$ and $M_\infty = 0.4$ at an altitude of 35,000 ft

With respect to η_{PR}, this quantity, unlike $C_{P_{K_{\text{in}}}}$ is less strongly dependent on the inviscid flow pressure. The influence of pressure is only indirect, through the effects of the pressure gradient on the boundary layer thickness, as long as there are no shocks or flow separation. The smaller energy defect in the boundary layer for case 2 is indicative of lower viscous losses relative to the baseline case. As a consequence, a higher pressure recovery is observed for a lower Mach number at all axial stations. The differences are more noticeable at the aft region where the boundary layer is thicker and a larger percentage of this flow is ingested. For regions upstream, a very small fraction of the overall ingested flow is coming from the boundary layer, and thus, the changes in the viscous losses have a much smaller effect on η_{PR} at the upstream stations.

Trends for $C_{\dot{E}}$

The change in wake dissipation, $C_{\dot{E}}$, is comprised of two contributing sources. The first, $\frac{1}{2}\rho\left(u^2+v^2+w^2\right)\left(V_\infty+u\right)$, is like a perturbation kinetic energy rate term, quantifying the dissipation contributions due to non-uniformity in the flow velocity. Any significant differences with respect to freestream flow will result in mixing losses, and thus, this term is positive, or zero in situations where the flow is at freestream conditions. In regions of reversed flow, this term is negative. The other term, $\left(p-p_\infty\right)u$, is the pressure defect work rate due to pressure differences in the flow relative to freestream [20]. This term is usually negative since $p < p_\infty$ typically implies $u > 0$ since $V > V_\infty$, while $p > p_\infty$ suggests $u < 0$. In situations where the pressure coefficient is large and negative (e.g. at the 80% axial station) the pressure work term dominates and the net result is a negative value for $C_{\dot{E}}$, as seen in Fig. 5.6a. Positive values for $C_{\dot{E}}$ imply a net reduction in propulsive power requirements for the BLI case, relative to the non-BLI aircraft. Negative values on the other hand suggest a detrimental effect, or an increase in the propulsive power requirements for the BLI case. Like $C_{P_{K_{\text{in}}}}$, $C_{\dot{E}}$ also shows both a direct and indirect dependence on the pressure field. As a result, the trends of $C_{\dot{E}}$ with Mach number are similar to $C_{P_{K_{\text{in}}}}$, given the impact of Mach number on the C_p distribution and boundary layer, as discussed previously.

The idea of estimating the change in wake dissipation at a given axial location, by calculating $C_{\dot{E}}$ on each integration area, is an engineering approximation. This approach is an extension to the one adopted by Hall [33], who calculated this quantity for a flow through nacelle placed at the end of the D8. While the notion of calculating $C_{P_{K_{\text{in}}}}$ and η_{PR} at different axial stations makes sense from a physics perspective, as these are 'local' quantities, the same is not quite as valid for $C_{\dot{E}}$. The wake starts at the trailing edge of the fuselage (or any other body like the wing for example), and thus, only the measurement at the A1.00 is valid from both the physics and the

engineering approximation viewpoints. Keeping this in mind, the $C_{\dot{E}}$ trends should be considered in the sense that these values represent an *engineering approximation* of what the wake dissipation benefit would be, if the fuselage was truncated at that axial station and an engine was placed at that location to ingest part of the wake.

Sensitivity to Altitude

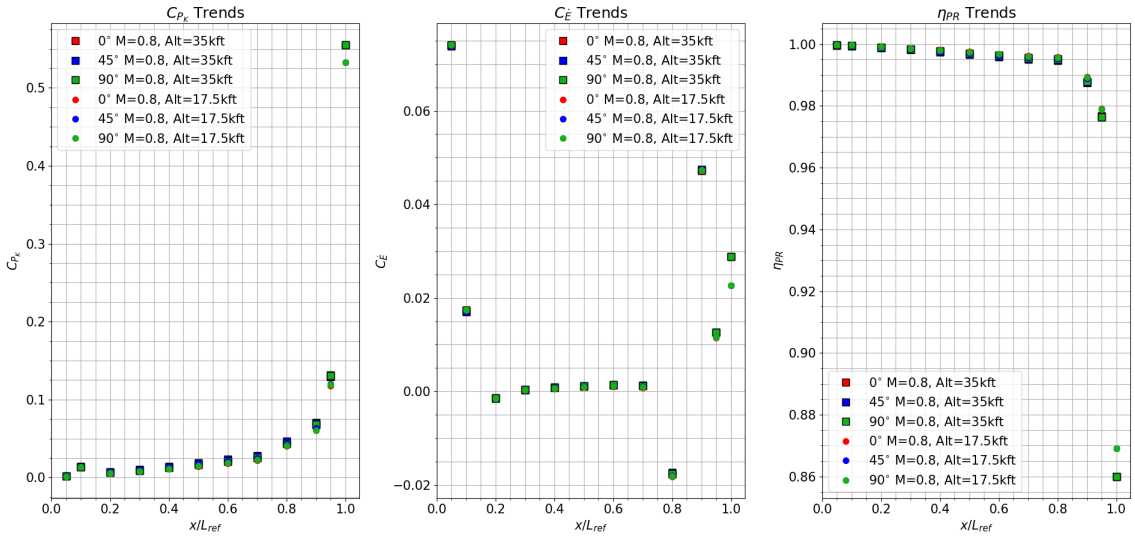

(a) Axial and circumferential trends in BLI effects

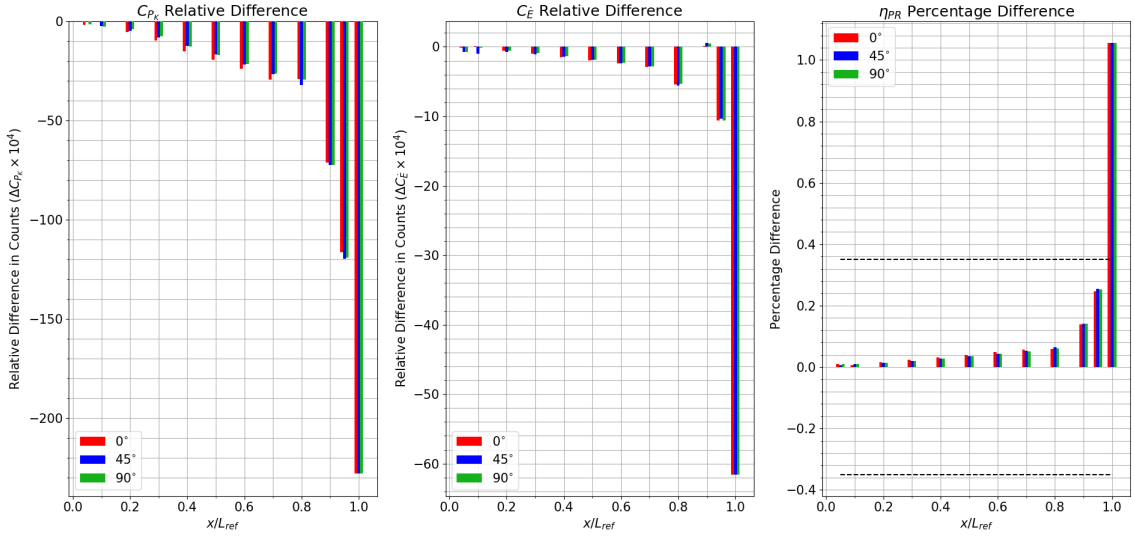

(b) Relative and percentage differences in BLI effects

Figure 5.10: Experiment 2.1 case 3 vs. 1 - sensitivity to altitude

Fig. 5.10 compares the axial and circumferential trends in BLI effects for case 1 and case 3. The Reynolds number based on fuselage length is increased by a factor of 1.78, upon halving the altitude relative to the baseline case, but the Mach number is the same. This increase in Reynolds number results in a thinner boundary layer, which accounts for the decrease in both $C_{P_{K_{\text{in}}}}$ and $C_{\dot{E}}$, noting that altitude does not affect the C_p distribution, as seen in Fig. 5.8. Pressure recovery increases relative to the baseline as a consequence of the thinner ingested boundary layer.

Sensitivity to Mach and Altitude

The results from case 4 are shown in Fig. 5.11, where both the Mach number and altitude are halved relative to the baseline. In this situation, since a decrease in Mach number and altitude both have favorable impacts on η_{PR}, the net result is an increase relative to the baseline. With respect to $C_{P_{K_{\text{in}}}}$ and $C_{\dot{E}}$, variations in flight conditions either complement or offset each other, based on axial location. As stated before, BLI effects are dependent on the thickness of the ingested boundary layer and the flow pressure. A semi-empirical equation for the compressible laminar flat plate boundary layer thickness shows that $\frac{\delta}{x} \propto \frac{M^2}{\sqrt{Re}}$ [99], highlighting the greater sensitivity of the boundary layer thickness to Mach number than to Reynolds number. This observation is supported by comparing the magnitude of the pressure recovery differences shown in Fig. 5.10b to those in Fig. 5.6b. In case 2, halving the Mach number at the same altitude halves the Reynolds number too, but the increase in pressure recovery suggests that the net effect is a thinner boundary layer. However, the favorable impacts of C_p variation with Mach number on $C_{P_{K_{\text{in}}}}$ and $C_{\dot{E}}$ offset boundary layer thickness effects, which is not observed in trial 3. The net influence of pressure and boundary layer thickness variations are seen in the results of trial 4. One can clearly conclude, based on the above results, that Mach and altitude effects need to be accounted for when formulating surrogates of the BLI effects.

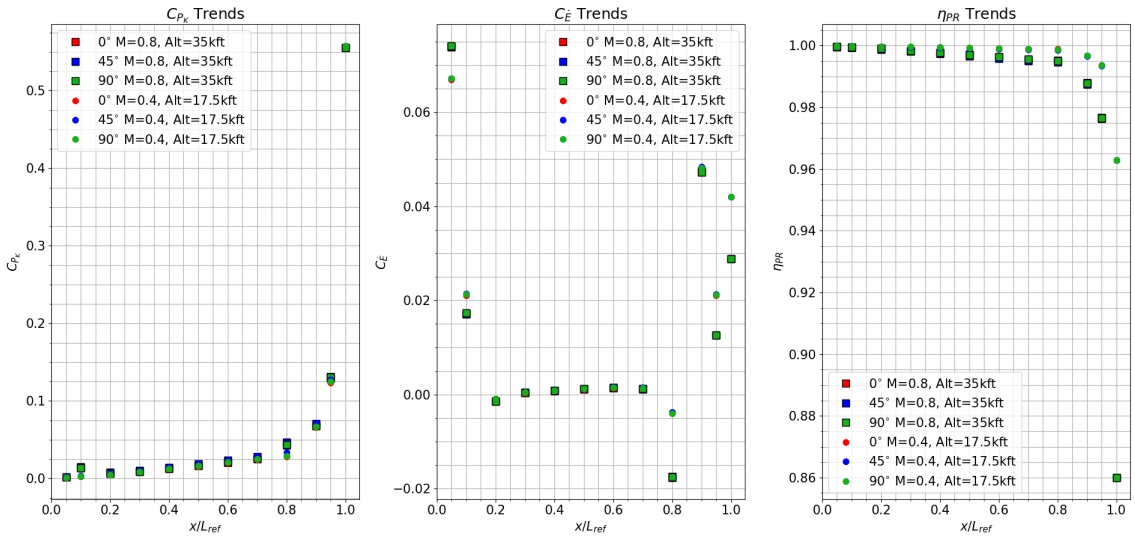

(a) Axial and circumferential trends in BLI effects

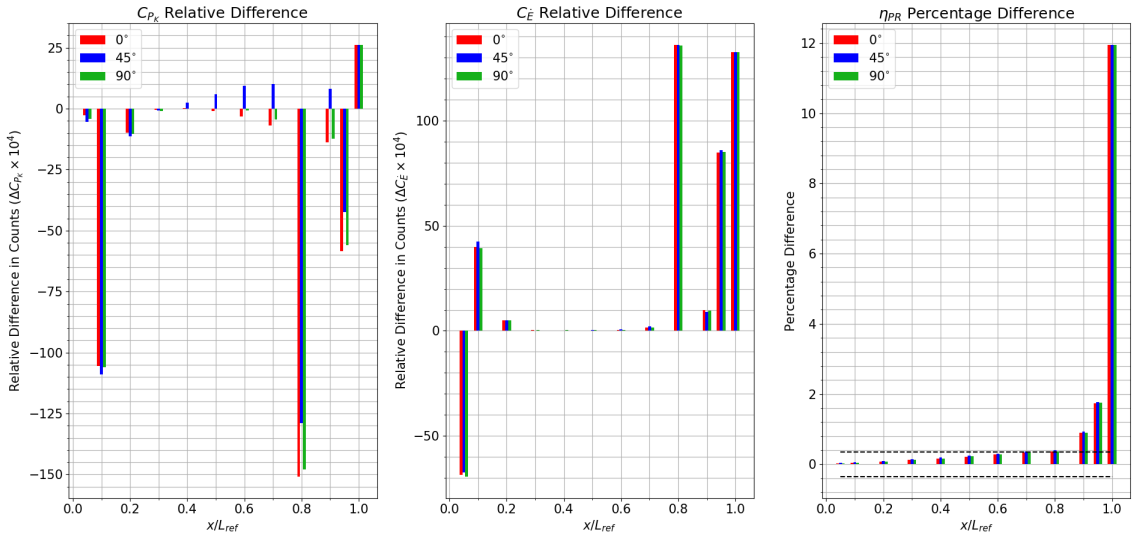

(b) Relative and percentage differences in BLI effects

Figure 5.11: Experiment 2.1 case 4 vs. 1 - sensitivity to Mach and altitude

Sensitivity to Aircraft Angle of Attack

Running the baseline geometry at $\alpha = 2°$ changes the inviscid flow field, as shown by the streamline patterns in Fig. 5.13. The boundary layer growth over the fuselage surface is no longer axisymmetric, with a thicker boundary layer seen at the 90° stations in Fig. 5.13. This difference in the boundary layer thickness accounts for the increase in $C_{P_{K_{\text{in}}}}$ and decrease in η_{PR} relative to case 1, seen in Fig. 5.12. The A1.00

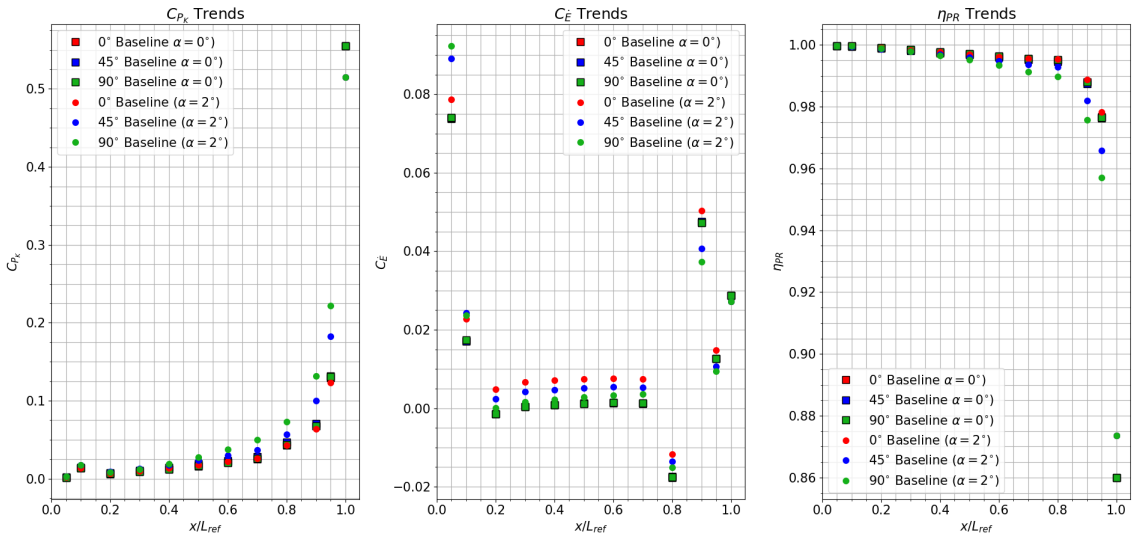

(a) Axial and circumferential trends in BLI effects

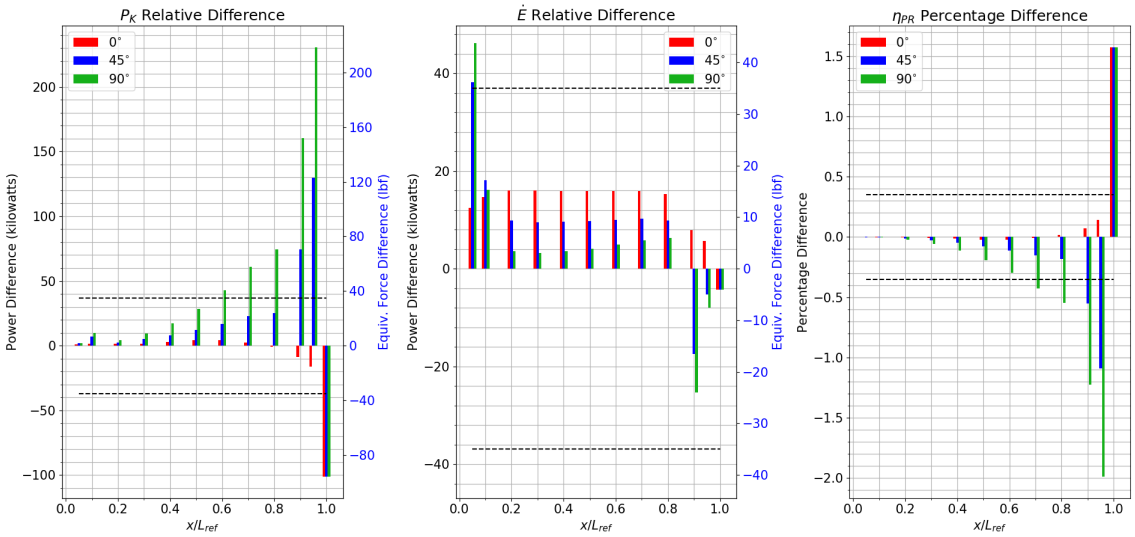

(b) Relative and percentage differences in BLI effects

Figure 5.12: Experiment 2.1 case 5 vs. 1 - sensitivity to aircraft angle of attack

station shows opposite trends to the other stations due to the overall upward shift in the boundary layer at a positive angle of attack. This flow feature is identified in Fig. 5.13 and more clearly illustrated in Fig. 5.14, which shows the η_{PR} contours at the A1.00 station for both case 1 and 5. In this figure, one can see that the integration area captures a larger portion of high total pressure flow at $\alpha = 2°$ than at $\alpha = 0°$.

The trends for $C_{\dot{E}}$ are flipped relative to the other two BLI effects, where the 0°

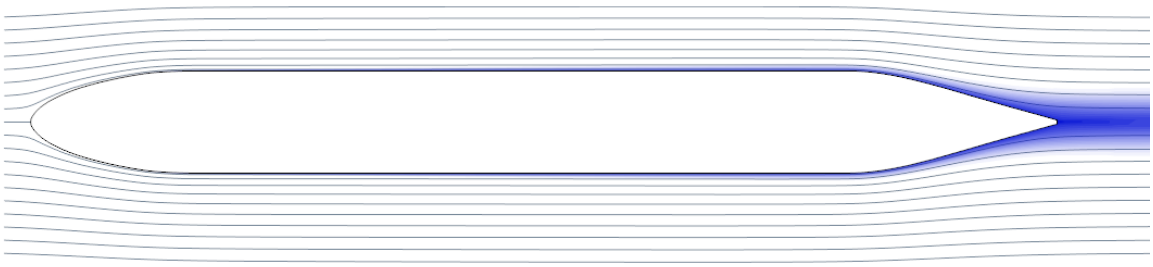

(a) E2.1-1 $\alpha = 0°$

(b) E2.1-5 $\alpha = 2°$

Figure 5.13: Experiment 2.1 case 1 vs. 5 - boundary layer and streamlines at the $x - z$ plane

stations show more change rather than the 90° stations. This observation can be attributed to the significant change in the w velocity component at the 0° stations, thereby favoring the perturbation kinetic energy component of $C_{\dot{E}}$.

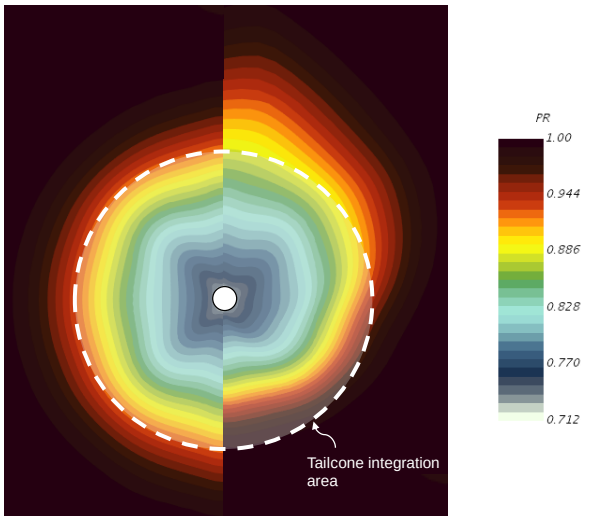

Figure 5.14: Effects of angle of attack on the boundary layer at the A1.00 station, visualized through η_{PR} contours, for $\alpha = 0\,\text{deg}$ on the left and $\alpha = 2\,\text{deg}$ on the right

5.3 Experiment 2.2: Sensitivity to Fuselage Nose Design

5.3.1 Experimental Overview

One of the key aspects of hypothesis 2 is the suggestion that perturbations in detailed airframe design parameters will produce local changes in the BLI effects, as long as these changes do not cause shocks or flow separation. If the BLI effects are measured at axial stations far away from these perturbations, it was hypothesized that the results at these locations will be insensitive to the design changes. The following set of experiments aims to assess whether this notion is valid for changes to the fuselage nose shape. Rather than defining a few detailed parameters for the nose and systematically varying them, the sensitivity of the BLI effects to the nose can be efficiently assessed using two distinct geometries. The first one modifies the nose shape and ensures that such a modification does not generate a shock, just like the baseline geometry. The second one aims to generate a shock on the fuselage as a result of this modification. The length of the fuselage, and cross sectional area of the center-body and aft section (macro parameters) are held at the baseline geometry values such that a fair comparison can be made to the results from experiment 1. The magnitude of the disturbances, measured in terms of changes to the BLI effects relative to the baseline over the axial distance, for each circumferential location, are calculated for each trial. The differences measured at the tail cone stations are of particular interest given that many existing BLI concepts feature aft-mounted engines. Table 5.2 below presents the trials conducted for this experiment.

Table 5.2: Experiment 2.2 - Overview of Cases

Experiment	Nose Shape	α (°)	Shocks
2.2-1	Notional 737-8 Nose	0	No
2.2-2	Hemispherical	0	Yes
2.2-3	Notional 737-8 Nose	2	No

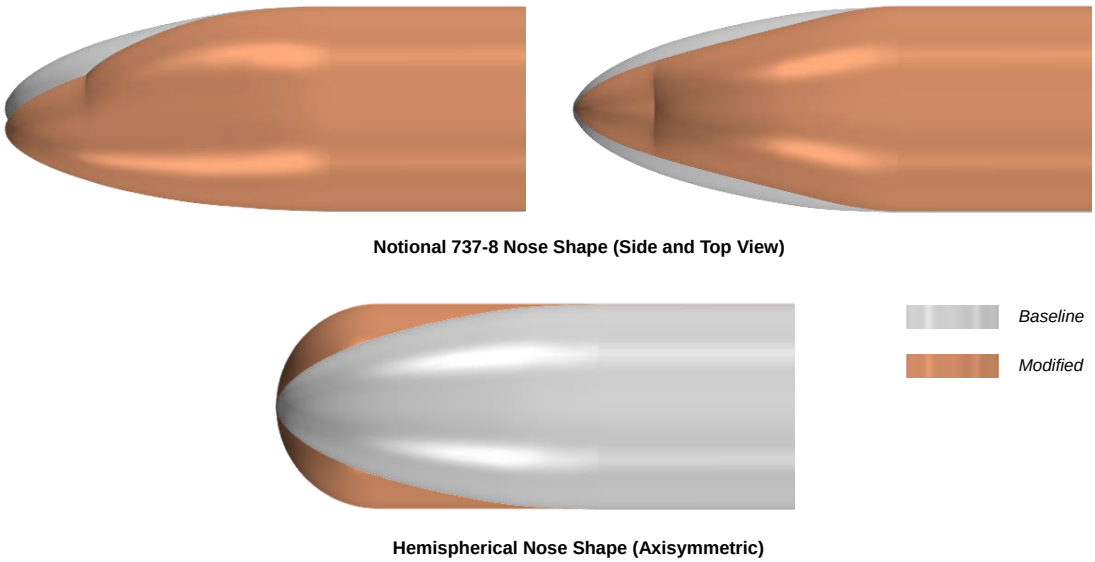

Figure 5.15: Experiment 2.2 - fuselage nose shapes

The baseline geometry has a smooth elliptical (and axisymmetric) nose shape. Most existing passenger aircraft, however, do not have axisymmetric noses. The first case aims to compare a typical nose shape to the existing baseline. OpenVSP and three-view drawings of the 737-8 from [14] are used to recreate this nose shape, modified slightly to match the baseline geometry center-body diameter. The geometry change does not produce any significant pressure effects like shocks or separation and is thus a 'small' perturbation to the nose. If the influence of this modification is indeed local, then any shock free perturbations should also be limited, which avoids the need for running additional cases if the propulsor stations of interest are outside this localized influence. Case 2 on the other hand represents the nose shape as a hemisphere. This shape is the simplest representation of the nose, however, the less gradual change in curvature produces a shock at high subsonic Mach numbers and is thus a 'large' perturbation. Case 3 is conducted to assess whether the results from case 1 also hold for a typical cruise angle of attack. Fig. 5.15 shows the different geometries used for the nose shape (orange), relative to the baseline in gray.

5.3.2 Results and Discussion

Fig. 5.16 shows the variance in the calculated BLI effects for trials 1, 2 and 3 relative to the baseline. These trends are expressed in dimensional power and equivalent force relative differences for $C_{P_{K_{\text{in}}}}$ and $C_{\dot{E}}$, while the pressure recovery changes are expressed as percentage differences like before. The thresholds for significant changes are shown with black lines. A comparison of the BLI effects axial and circumferential trends is shown in Fig. A.1 in Appendix A.

From Fig. 5.16a, it is apparent that significant changes in the BLI effects are limited to the first 10% of the fuselage, i.e., in the region of the nose. The change in $C_{\dot{E}}$ is more pronounced than the change in $C_{P_{K_{\text{in}}}}$, while the change in pressure recovery is insignificant. Pressure recovery is solely dependent on the viscous losses in the boundary layer, given the absence of shocks, and thus this result is indicative of minimal changes to the boundary layer itself as a result of the nose shape perturbation. Propagation of the disturbances downstream decays quickly. The differences in the BLI effects are well below the thresholds and are thus insignificant, supporting the theoretical reasoning behind hypothesis 2. Similar results are obtained at $\alpha = 2°$, shown in Fig. 5.16c.

Now consider case two. The relative differences in the BLI effects seen in Fig. 5.16b all exceed the critical threshold, except for $C_{\dot{E}}$ in the center-body region. This trend is due to the presence of a shock just behind the 5% station, shown in Fig. 5.17. The adverse pressure gradient across the shock, and the subsequent thickening of the boundary layer have a favorable impact on $C_{P_{K_{\text{in}}}}$, but are naturally detrimental to η_{PR}. The favorable pressure gradient in the nose region and high flow acceleration increase the pressure defect work rate magnitude, which accounts for the significant $C_{\dot{E}}$ change at the nose. The pressure distribution downstream is similar to the baseline, but the thicker boundary layer increases the perturbation kinetic energy rate, resulting in a small, but net positive impact on $C_{\dot{E}}$.

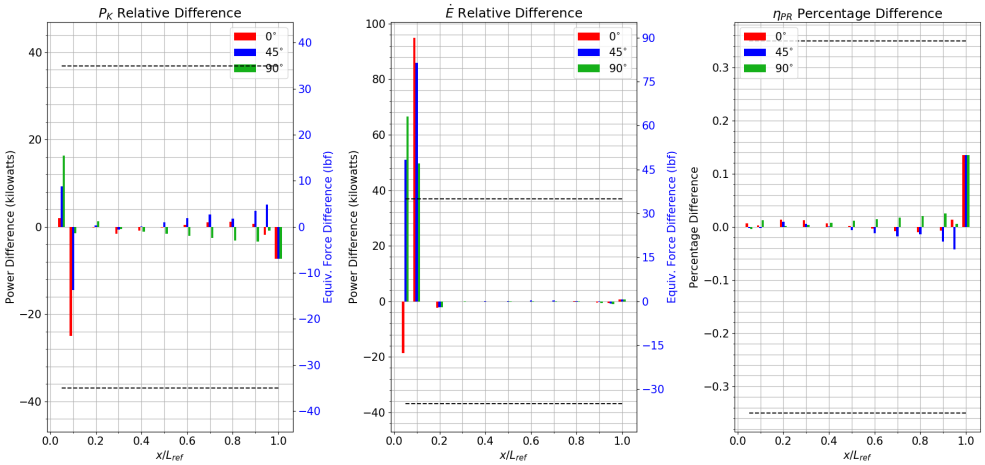

(a) E2.2-1 vs. E2.1-1 (Baseline)

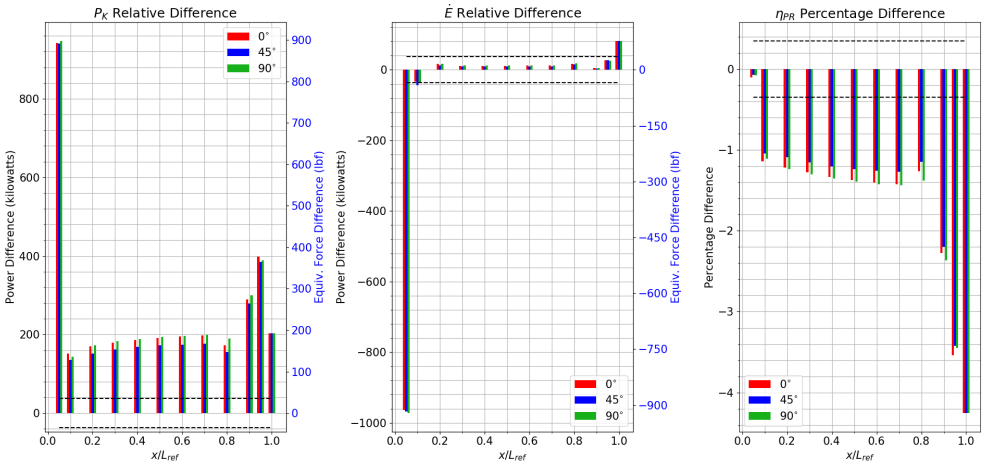

(b) E2.2-2 vs. E2.1-1 (Baseline)

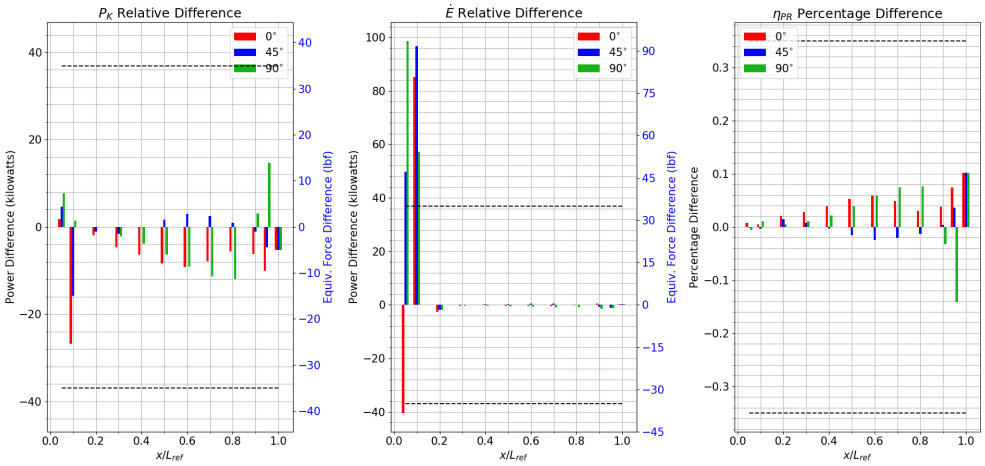

(c) E2.2-3 vs. E2.1-5 ($\alpha = 2°$ Baseline)

Figure 5.16: Experiment 2.2 - differences in estimates of the BLI effects, relative to the baseline, due to changes in fuselage nose shape

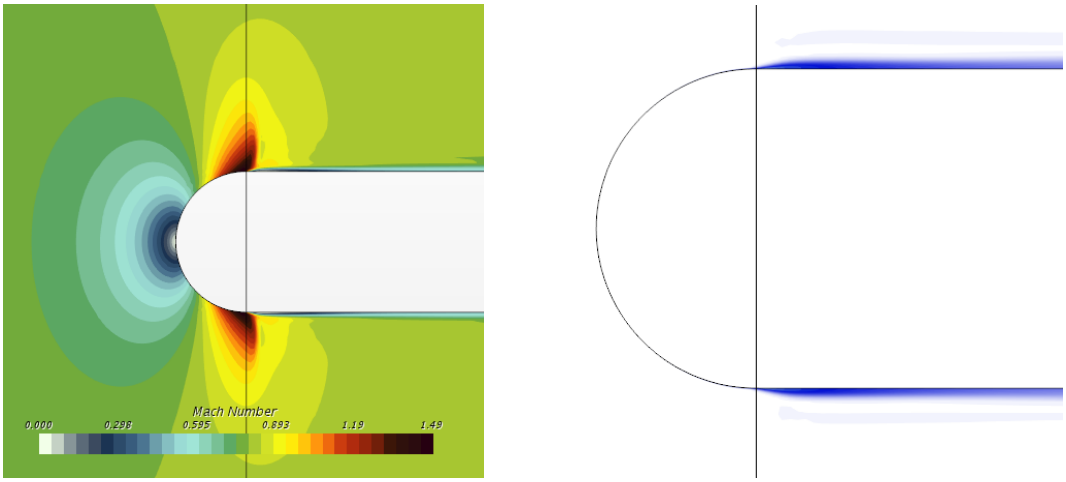

(a) Presence of a shock aft of the 5% span station (black line)

(b) Thickening of boundary layer post shock

Figure 5.17: Presence and effects of a shock on the hemispherical nose geometry

The observations above support hypothesis 2. A nose geometry change that causes a shock cannot be treated as a 'small' perturbation, since the impacts of this change are felt downstream across the entire length of the fuselage. Thus, one cannot arbitrarily default the nose geometry shape when generating surrogates of the BLI effects, if such a setting produces a shock. However, if the nose shape is defaulted to a shock free state, then the above results suggest that any shock-free perturbations to this shape will only show a localized impact on the BLI effects. As a consequence, for any engine location downstream of the nose, the detailed design variables defining the nose shape fall within the inactive variable set, given their negligible impact on the BLI effects. Thus, in the absence of design knowledge required to define the nose OML, a simplified (and shock free) representation of the nose can be used when generating surrogate models of the BLI effects.

5.4 Experiment 2.3: Sensitivity to Fuselage Aft Section Design

5.4.1 Experimental Overview

This experiment focuses on the impacts of the fuselage aft section design on the BLI effects. Experiment 2.2 highlighted the localized impact of geometry changes on the BLI effects, consistent with the theoretical reasoning behind hypothesis 2. Similar observations are expected here as well, however, given that BLI engines are typically mounted on the aft section, any changes in the BLI estimates due to geometry definition are now more critical. The significance of tail cone design on BLI concept performance is emphasized by the number of tail cone shape optimization studies that have been conducted, such as those by Gray [27, 26], Ordaz [71], and Kenway [42], discussed previously in chapter 2. Recognizing the importance of tail cone design and the impracticality of detailed shape optimization in early concept design, the objective of this experiment is to assess whether the BLI effects are more sensitive to the macro parameter changes, rather than the detailed parameters, as hypothesized previously. In doing so, the goal is also to establish a set of guidelines in determining the simplest representation of the tail cone geometry that can be used for generating surrogates of the BLI effects using CFD.

The axisymmetric conical representation of the fuselage aft section is perhaps the simplest geometry model, but is not realistic compared to existing aircraft designs. The first trial therefore aims to quantify the discrepancy in the BLI effects calculated along the fuselage as a result of replacing this simple baseline aft section with an up-swept tail cone commonly seen on aircraft. In doing so, both macro parameters like fuselage closure angle and upsweep angle are varied in addition to detailed parameters defining the OML curvature. This up-swept tail cone is created in OpenVSP using three view drawings of the 737-8 from [14]. This geometry shown in orange in Fig. 5.18.

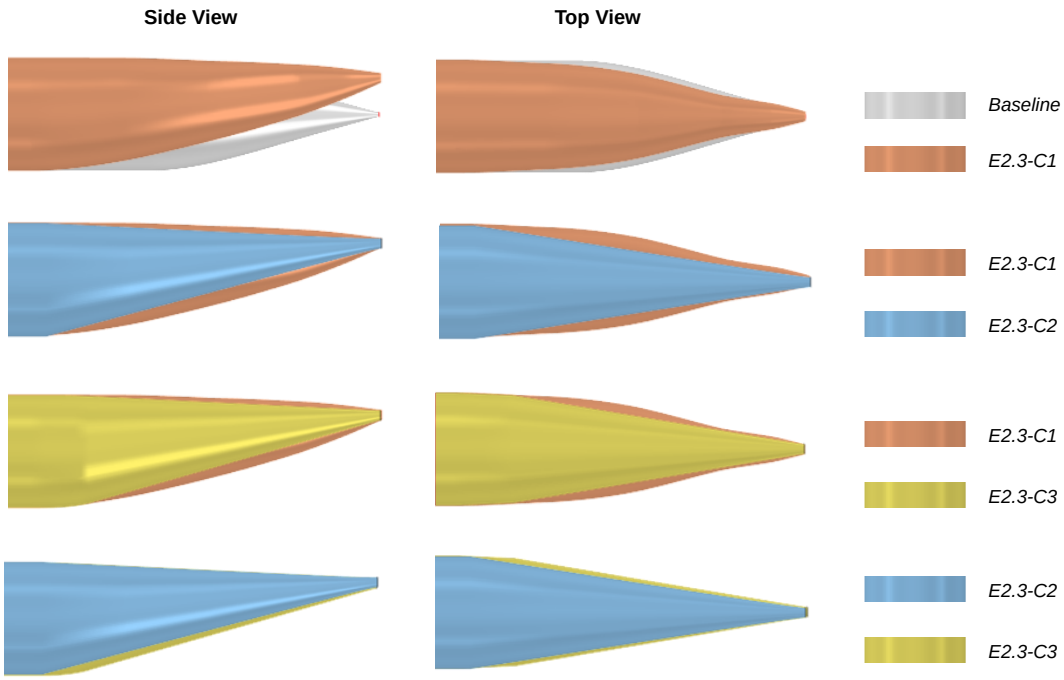

Figure 5.18: Experiment 2.3 - fuselage tail shapes

Then, to isolate the impacts of the detailed parameters defining the aft end, the second trial replaces the notional 737-8 tail cone with a simple lofted cone that approximately matches the upsweep and closure angles of the notional 737-8 geometry, shown in blue in Fig. 5.18. The transition between the fuselage cylindrical center-body and the conical upswept tail cone is sharp. A comparison between trial 1 and the baseline geometry quantifies the differences in the BLI effects largely due to a change in the aft end macro parameters. A comparison between trial 2 and trial 1 on the other hand quantifies the impact of the differences in the detailed design parameters of the tail cone. In the third trial, the transition between the center-body and tail cone is arbitrarily smoothened out (a change in detailed design parameters), to assess whether the discrepancies in the BLI effects can be minimized. This geometry is shown in yellow in Fig. 5.18, and this case is also compared to case 1. Table 5.3 summarizes the three cases that are run for this experiment.

Table 5.3: Experiment 2.3 - Overview of Cases

Experiment	Tail Cone Shape	Comments
2.3-1	Notional 737-8	Shock/Separation Free
2.3-2	Conical Upswept	Sharp Transition to Center-body
2.3-3	Modified Conical Upswept	Smoother Transition to Center-body

5.4.2 Results and Discussion

Fig. 5.19 presents the differences in the BLI effects for the three comparison sets. A comparison of the BLI effects axial and circumferential trends is shown in Fig. A.2 in Appendix A. Comparing trial 1 with the baseline geometry (Fig. 5.19a), one can see that the upstream influence of the tail cone shape change is negligible, consistent with the theoretical reasoning behind hypothesis 2. The differences are localized to the aft stations as expected, but exceed the critical thresholds quite significantly. Unsurprisingly, this finding indicates that an axisymmetric tail cone is an inadequate representation of a typical fuselage aft section.

The differences in $C_{P_{K_{\text{in}}}}$ and η_{PR} relative to the baseline, at the 45° and 90° stations, are much larger than those at the 0° circumferential station. Given the differences in slope of the geometry at the 90° stations, and to a lesser extent at the 45° stations, evident in Fig. 5.18, the boundary layer sees a less adverse pressure gradient in trial 1 than it does for the baseline tail cone. As a result, the boundary layer is thinner at these stations, as seen in Fig. 5.20, which shows a $y-z$ cross section view at the 90% axial station. The thinner boundary layer results in a smaller $C_{P_{K_{\text{in}}}}$ and larger η_{PR}.

To ascertain the likelihood of the closure and up-sweep angles being the driving factors, case 2 is compared to case 1, shown in Fig. 5.19b. It is immediately obvious that by just roughly matching the closure and upsweep angles, the differences in the BLI effects are reduced by an order of magnitude, compared to the previous comparison. The differences in η_{PR} are below the threshold for all aft stations and

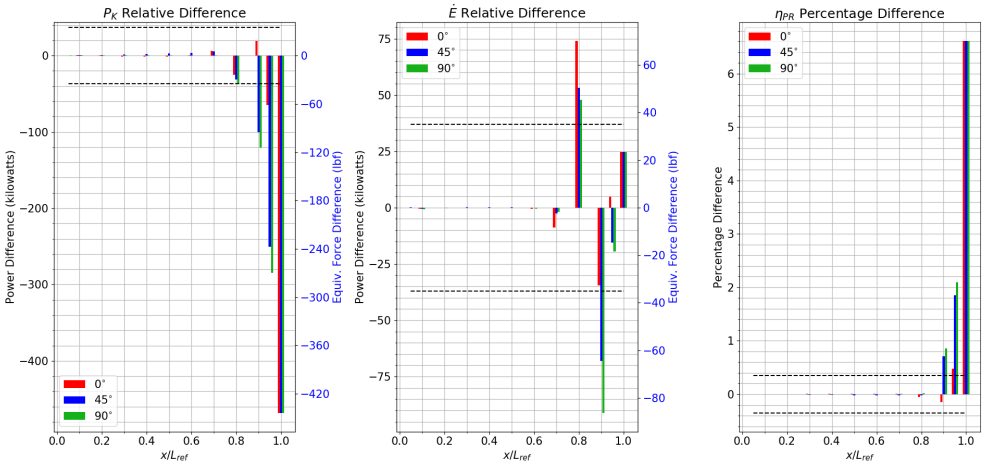

(a) E2.3-1 vs. E2.1-1 (Baseline)

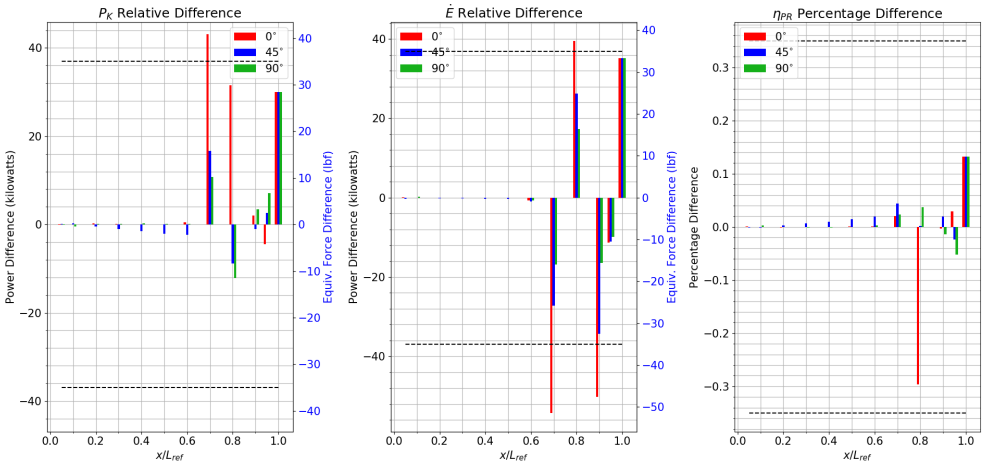

(b) E2.3-2 vs. E2.3-1

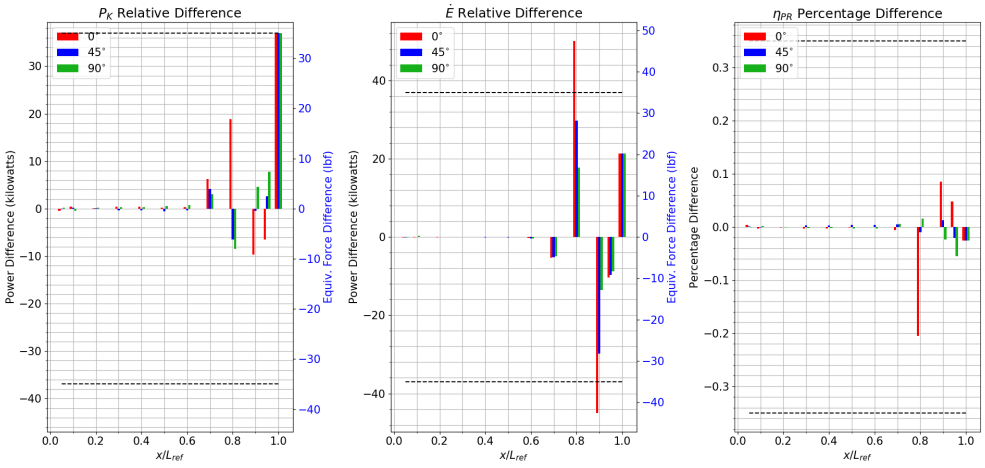

(c) E2.3-3 vs. E2.3-1

Figure 5.19: Experiment 2.3 - differences in estimates of the BLI effects due to changes in fuselage aft section shape

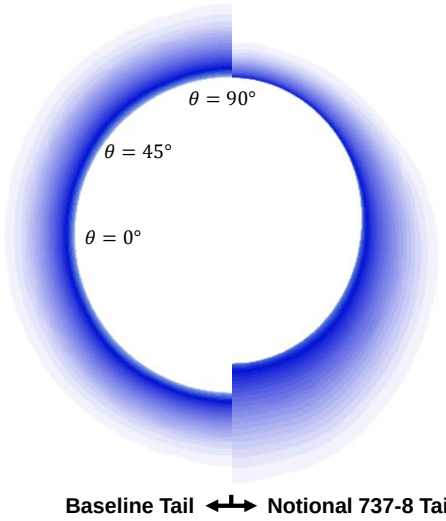

Figure 5.20: Effects of fuselage aft end slope - boundary layer thickness comparison between notional 737-8 and baseline tail cone geometries at A0.90 (images shifted such that the fuselage top aligns)

while there are still some locations that exhibit higher than critical values for $C_{P_{K_{\text{in}}}}$ and $C_{\dot{E}}$, the extent to which these values exceed the threshold is much smaller than before.

A consequence of having a sharp transition between the center-body and the tail cone is excessive flow acceleration at the corner, followed by a small separation bubble on the underside, This phenomena is illustrated in Fig. 5.21, which shows the axial velocity contours at the symmetry plane. This separation bubble creates a region of slow moving flow behind it, which most significantly affects the flow at the 0° circumferential station. The large differences in the BLI effects at the 70% and 80% span stations are a result of this flow behavior. To minimize this effect, an arbitrary curvature is applied to the transition region between the center-body and tail cone to smooth it out. As seen from the axial velocity contours at the symmetry plane in Fig. 5.22, the resulting geometry minimizes flow acceleration and eliminates the separation bubble seen previously. A comparison of the BLI effects between case 3 and 1 is shown in Fig. 5.19c. The differences in $C_{P_{K_{\text{in}}}}$ are now all below the thresholds, like η_{PR}, and the differences at the 70% and 80% span stations are also minimized.

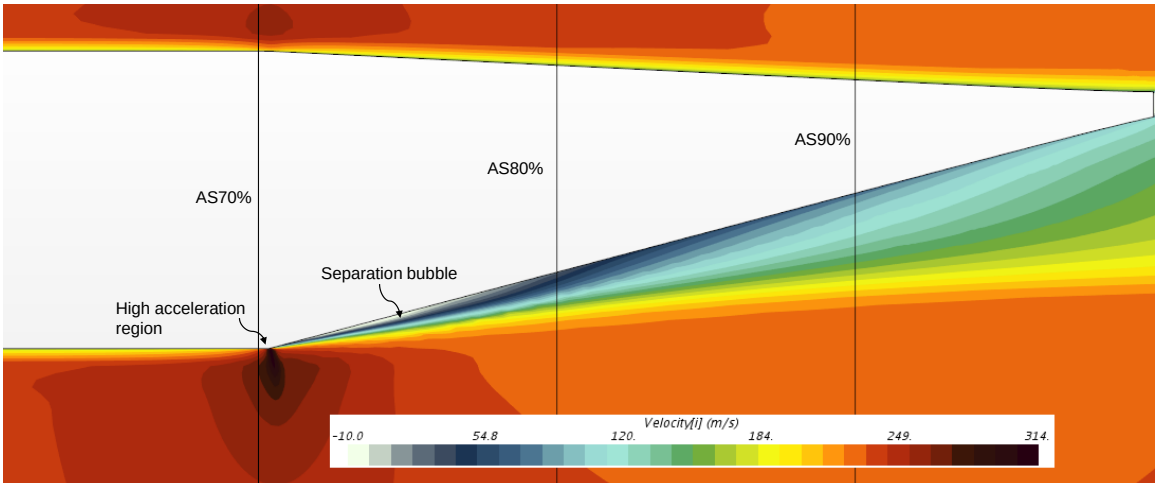

Figure 5.21: Experiment 2.3 case 2 - strong acceleration and flow separation around geometry transition corner (symmetry plane view, $V_\infty = 237\text{m/s}$)

The net difference of $C_{P_{K_{\text{in}}}} + C_{\dot{E}}$ at the A1.00 station is also smaller than before.

Based on these results, it can be concluded that the macro parameters: upsweep and closure angles, indeed have a stronger influence on the BLI effects than the more detailed curvature. Given this relative influence, it is sufficient for BLI concept design to default the curvature to a setting that avoids adverse flow features, even though this setting may not be optimal. The discrepancy in the BLI effects between

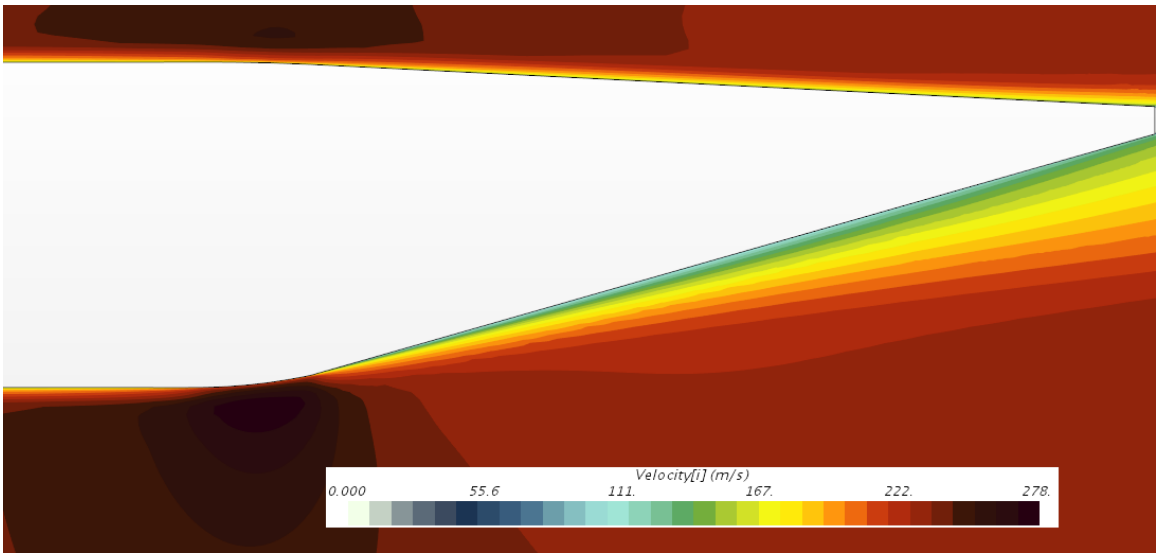

Figure 5.22: Experiment 2.3 case 3 - minimized acceleration and eliminated separation bubble on fuselage aft end underside (symmetry plane view, $V_\infty = 237\text{m/s}$)

the optimized curvature geometry at the end of preliminary design and the default geometry used in concept design for generating the BLI effects surrogates will mostly be seen in the estimates for $C_{P_{K_{\text{in}}}}$ and $C_{\dot{E}}$, while the difference in pressure recovery will be minimal. The discrepancy due to defaulting the detailed parameters however will be smaller than the discrepancy caused by a mismatch in the macro parameters. The BLI concept designer must therefore keep track of the upsweep and closure angles even at the early stages of design. Design knowledge in the form of constraints (such as on the upsweep angle for tail strike avoidance) or previous experience, can help lock down values for these macro parameters. However, if this knowledge is unavailable and a fixed value for each parameter cannot be established, then the designer must include these variables as part of the BLI effects surrogate model generation process.

5.5 Experiment 2.4: Sensitivity to Presence of Belly Fairing

5.5.1 Experimental Overview

This experiment determines the significance of the upstream and downstream perturbations to the BLI effects due to the inclusion of a belly fairing on the fuselage center-body. The objective is to assess whether the impacts of adding such detail to the geometry are small enough to neglect. This fairing, shown in Fig. 5.23, is also used in experiment 2.6 with a wing, and thus serves as a baseline reference for those trials. The size of the fairing geometry is estimated based on an approximated wing root chord length for a 180 pax class vehicle. Two cases are run for this experiment, at different angles of attack, shown in Table 5.4.

Figure 5.23: Experiment 2.4 - belly fairing geometry

Table 5.4: Experiment 2.4 - Overview of Cases

Experiment	Geometry	Aircraft α (°)
2.4-1	Baseline + Fairing	0
2.4-2	Baseline + Fairing	2

5.5.2 Results and Discussion

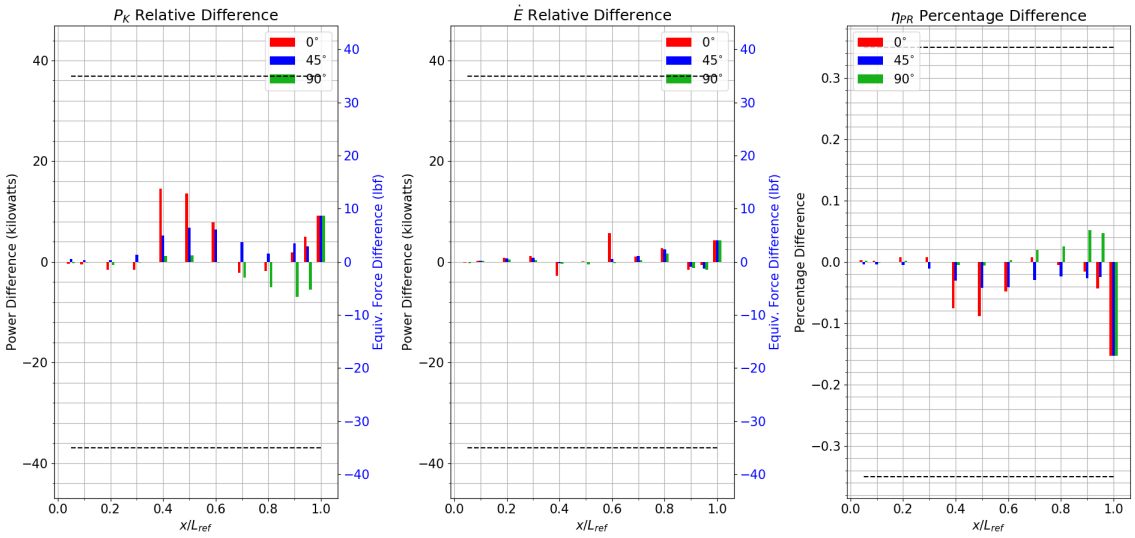

(a) E2.4-1 vs. E2.1-1 ($\alpha = 0°$ Baseline)

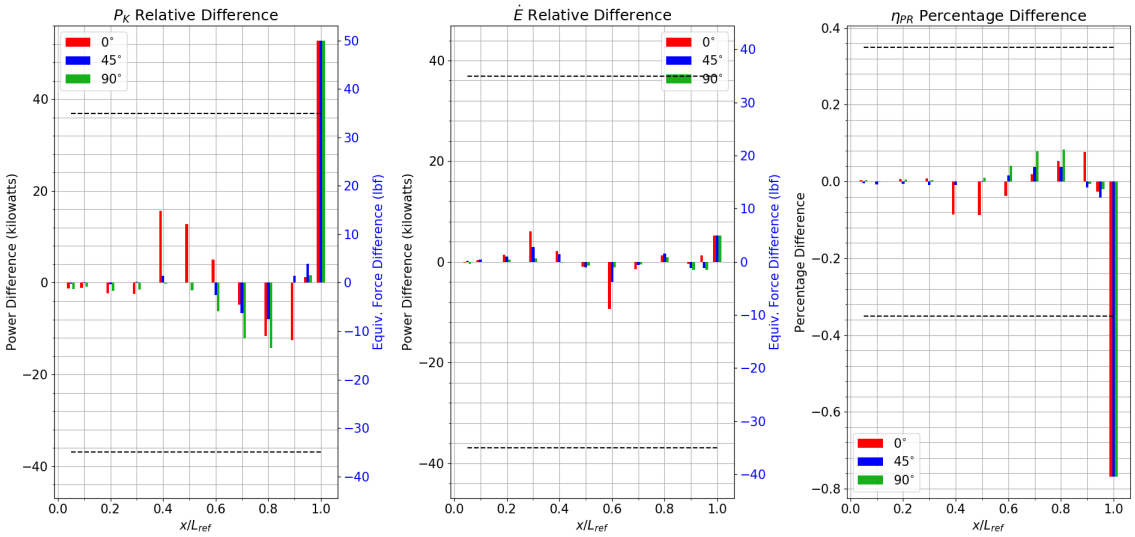

(b) E2.4-2 vs. E2.1-5 ($\alpha = 2°$ Baseline)

Figure 5.24: Experiment 2.4 - differences in estimates of the BLI effects, relative to the baseline, due to addition of a belly fairing

Fig. 5.24 shows the differences between cases 1 and 2, and the baseline at the two aircraft angles of attack. A comparison of the trends is shown in Fig. A.3 in Appendix A. For the $\alpha = 0°$ case (Fig. 5.24a), the differences between the modified geometry and baseline are well below the critical threshold. The 0° circumferential stations at 40% - 60% show the most sensitivity to the changes, given the proximity of the geometry perturbation to these measurement stations. The A1.00 station also exhibits some noticeable differences, given that it ingests the entire circumferential extent of the aft boundary layer, with fairing falling within the zone of dependence at this location. The fairing deflects flow in the z direction, as seen in Fig. 5.25a. Here, streamlines emanating from the same source are compared across cases, with the baseline streamlines shown in black, and the fairing streamlines shown in red. The change in $z-$momentum results in a thicker boundary layer at the fuselage trailing edge, which accounts for the increase in $C_{P_{K_{\text{in}}}}$ and decrease in η_{PR} seen in Fig. 5.24. These differences are magnified at $\alpha = 2°$ (Fig. 5.24b), where the streamline deflection, relative to the 2° baseline, is more significant. This observation is also highlighted in Fig. 5.25b, which compares η_{PR} contours for the belly fairing geometry to the baseline at the A1.00 station. Note the region of low η_{PR} within the integration area at A1.00, for $\alpha = 2°$, that is not present in the baseline.

The results indicate that the belly fairing has a relatively negligible impact on the BLI effects, except at the fuselage trailing edge station for a typical cruise angle of attack. While these results suggest that the fairing can be omitted from the geometry model, this conclusion is erroneous when the entire vehicle configuration is considered. As will be discussed in experiment 2.6, the fairing is necessary when including the wing in the geometry model. The fairing has an indirect impact on the BLI effects by mitigating significant flow separation that arises at wing-fuselage junction, and its downstream impact. As a consequence, the fairing minimizes the contribution of the wing at the 0° circumferential stations aft of it.

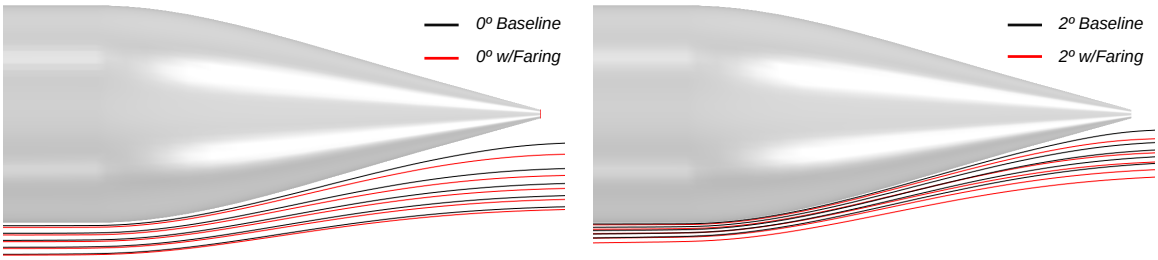

(a) Comparison of streamline deflections

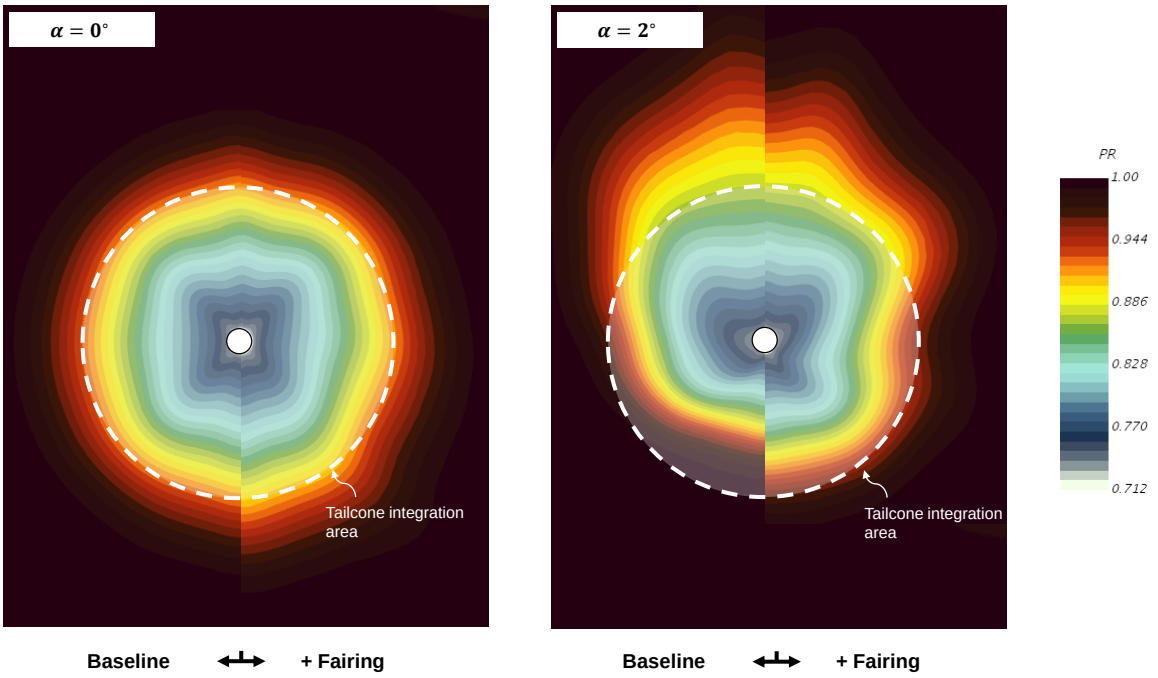

(b) Comparison of pressure recovery contours at A1.00

Figure 5.25: Experiment 2.4 - effects of belly fairing on flow field at the fuselage trailing edge station

5.6 Experiment 2.5: Fuselage Shape and Slenderness Ratio Studies

5.6.1 Experimental Overview

In the following experiment, the fuselage as a whole is considered. The relative significance of the fuselage cross sectional shape (detailed parameter) vs. the fuselage cross sectional area and length (macro parameters), on the BLI effects, is compared. The objective is to determine whether perturbations in the detailed parameters yield

changes to the BLI effects that are less significant than those caused by changes to the macro parameters, thereby supporting hypothesis 2. The baseline geometry is scaled in the x, y and z directions to vary the cross sectional shape, area, and length for a given case. While these parameters can be arbitrarily set, the scope of this experiment is restricted to reasonable geometry perturbations, bounded by existing tube and wing aircraft designs. As such, the upper bounds on the center-body cross sectional area and overall fuselage length are from the Airbus A350 (a large twin-aisle aircraft), with approximate dimensions obtained from the airport planning document [5]. The lower bound is the baseline geometry, modeled on the Boeing 737-8. The variability in cross section shape is obtained from the B737-8 and A350, but the D8 cross sectional shape is also considered in these experiments. This shape, common to both the D8 and the NOVA-BLI, is representative of an unconventional cross section given its highly elliptical definition. Table 5.5 presents the eight geometry cases considered in this experiment. Recall, the baseline fuselage length, $L_x = 39.12$m and the center-body diameter $L_y = L_z = 3.89$m. Elliptical cross-sectional shapes are obtained by scaling the entire geometry in the y and z directions. A total of eight comparisons are made, illustrated in Fig. 5.26.

Comparisons 1-4 assess the significance of the detailed fuselage shape parameters

Table 5.5: Experiment 2.5 - Overview of Cases

Experiment	L_x (m)	L_y (m)	L_z (m)	Center-body	Notional Source
2.5-1	39.12	3.76	4.01	Elliptical	B737-8 Cross Section
2.5-2	39.12	5.96	6.09	Elliptical	A350 Cross Section (CS)
2.5-3	39.12	6.03	6.03	Circular	A350 Avg. CS
2.5-4	72.25	5.96	6.09	Elliptical	A350 CS & Length
2.5-5	72.25	6.03	6.03	Circular	A350 Avg. CS & Length
2.5-6	72.25	3.89	3.89	Circular	A350 Length
2.5-7	39.12	5.36	3.95	Elliptical	D8 CS
2.5-8	39.12	4.60	4.60	Circular	Avg. D8 CS

on the BLI effects. The simplest representation of the fuselage is a circle, which is defined by a single parameter i.e. the diameter. Most conventional aircraft, however, have elliptical cross sections, as illustrated in Fig. 5.26. Elliptical shapes require two parameters, which adds a degree of uncertainty in early conceptual design. The cross sectional area is an important parameter for transonic aircraft and defining the area sets the diameter for a circular approximation of the fuselage. However, in the case of an elliptical cross section, different combinations of the major and minor axes lengths can generate the same cross sectional area. While other design constraints eventually help define the values of these detailed parameters, this design knowledge may not be available in the early stages. Thus, when generating surrogate models of the BLI

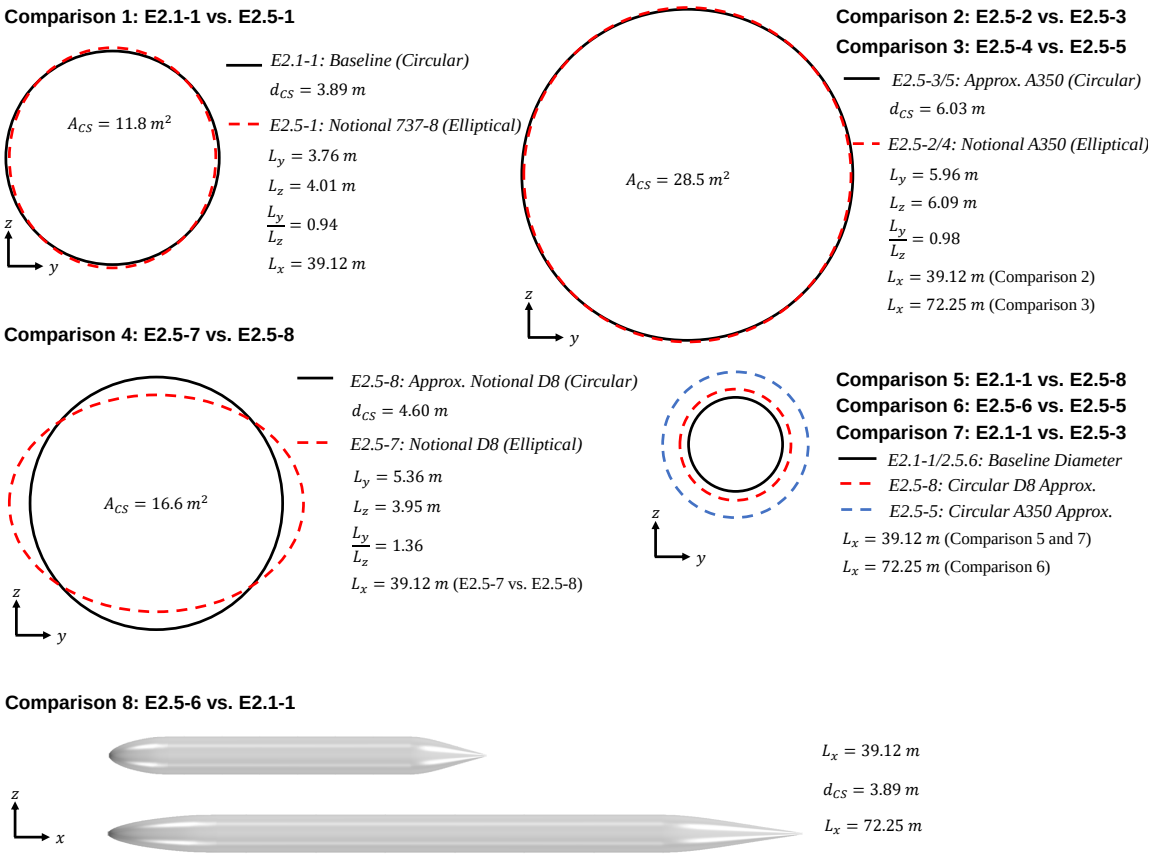

Figure 5.26: Experiment 2.5 - overview of comparisons. Comparisons 1-4 assess the impacts of detailed fuselage shape parameters, while comparisons 5-8 establish the significance of the macro parameters: cross sectional area and overall fuselage length

effects using CFD, the question arises whether this shape even matters. By comparing the BLI effects for the elliptical cross section to the circular approximation, one can assess the significance of the fuselage shape on the results. If the differences are negligible, then one can get away with the simpler geometry model with minimal loss in accuracy. As shown in Fig. 5.26, the length of the fuselage, L_x and cross sectional area, A_{CS}, are held constant for a given comparison. Comparisons 5-8 assess the significance of varying the macro parameters on the BLI effects. For each of these cases, the circular approximation of the fuselage shape is used. The relative size of the cross section and the fuselage length for these cases is shown at the bottom of Fig. 5.26.

5.6.2 Results and Discussion

Fig. 5.27 presents the relative differences in the BLI effects for comparisons 1-4. Looking at the plots for comparisons 1-3, i.e., for conventional cross section shapes vs. circular approximations, the differences in the BLI effects are well below the critical thresholds. In comparisons 1 and 3, the slenderness ratio of the fuselage is large enough to not cause a shock. However, by increasing the cross sectional area and keeping the length constant, the slenderness ratio decreases in comparison 2, causing a shock just aft of the nose. Even in this scenario, the difference between a circular and elliptical cross section is negligible. Thus, one can conclude that for conventional elliptical configurations where the final cross section shape parameters are expected to fall within a range of $0.94 \leq \frac{L_y}{L_z} \leq 1.00$, the additional parameter needed to create an elliptical shape is not necessary for modeling the BLI effects in early conceptual design. One can safely use a circular cross section geometry model since the error in doing so is negligible.

However, when considering an unconventional configuration like the D8 or the NOVA-BLI, this simplification is challenged as the differences between a circular

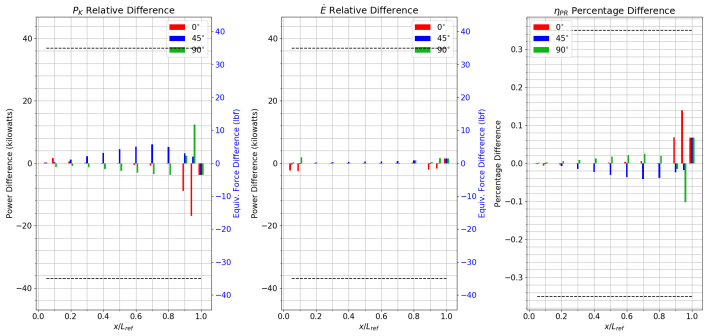

(a) Comparison 1: E2.5-1 vs. E2.1-1 (Baseline)

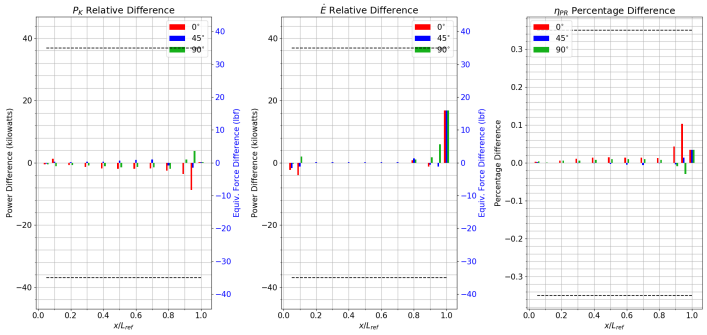

(b) Comparison 2: E2.5-2 vs. E2.5-3

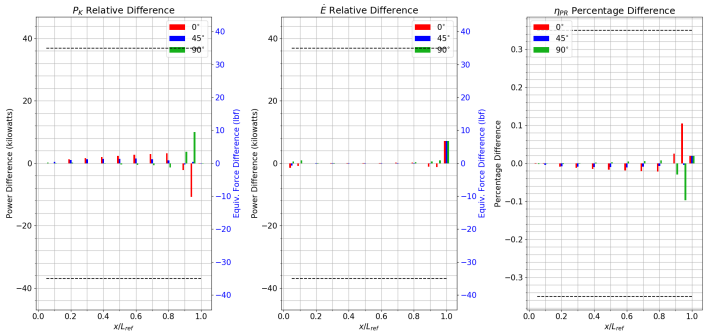

(c) Comparison 3: E2.5-4 vs. E2.5-5

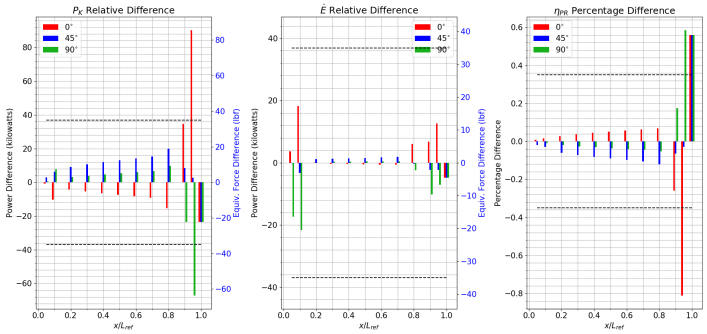

(d) Comparison 4: E2.5-7 vs. E2.5-8

Figure 5.27: Experiment 2.5 - differences in estimates of the BLI effects, due to changes in fuselage cross sectional shape representation (elliptical vs circular)

approximation and the elliptical shape are more pronounced, as seen in Fig. 5.27d. Despite the relatively exaggerated results, it is interesting to note that most the differences still fall within the critical thresholds, with only the values at the A0.95 and A1.00 stations showing differences that exceed the thresholds. The differences at the A0.90 station, though within the thresholds, are still appreciable. In short, the results at the tail cone stations are the most sensitive to the fuselage shape. This is no surprise, as the results from experiment 2.3 indicated as much. Fig. 5.28 compares the tail cone geometries in comparison 4, with the elliptical representation shown in gray, and the circular approximation shown in orange.

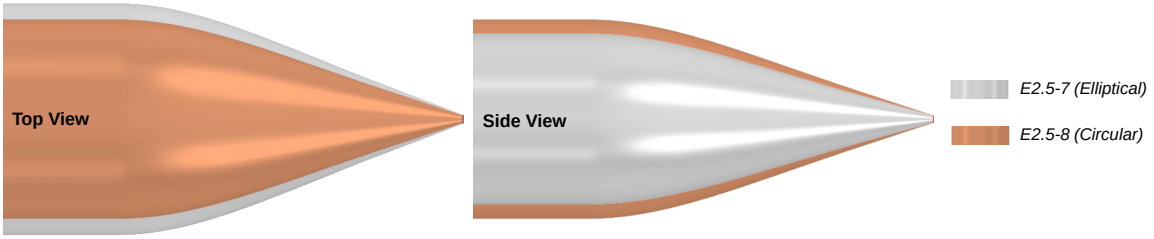

Figure 5.28: Experiment 2.5 - comparison of case 7 and case 8 tail cone geometries

Evident from the geometries in Fig. 5.28, the fuselage closure, upsweep, and upper surface angles for the circular and elliptical geometries are not the same. In changing the fuselage shape, the macro parameters defining the tail cone design were not held the same, accounting for the differences seen in this region in Fig. 5.27d. Given this result, the designer has a two options to consider when coming up with a simplified geometry model for a highly elliptical configuration in early concept design:

(i) Use an elliptical shape for the entire cross section. If the values for L_y and L_z are unknown, it is sufficient to define an *appropriate* range on these parameters (constrained by the cross sectional area requirements), and then set one term to the center point value and calculate the other based on the cross sectional area requirement. Based on the results from comparisons 1-3, the variation in

the BLI effects due to a difference in the values set for L_y and L_z, within the previously defined range, is likely to be minimal.

(ii) Use a circular cross section shape for the fore-body, but gradually loft to an elliptical cross section for the tail cone.

In both the options above, it is necessary to account for the effects of the tail cone and fuselage macro parameters. Either these parameters need to be set to the correct values in the CFD geometry model, or, varied as part of the surrogate model generation process. The first option is ideal for configurations like the D8 where it may be difficult, or impossible, to capture the closure and upsweep angles, and obtain the correct cross sectional area of the tail cone using a simple circular cross section.

The impacts of varying the fuselage cross sectional area and the length are shown in Fig. 5.29. Comparisons 5 and 6 are for shock free cases, where the reference case cross sectional area is at the baseline value of 11.8m^2 and the comparison geometries' areas are at 16.6m^2 and 28.5m^2 respectively. Increasing the area increases the magnitude of the differences in the BLI effects at most stations. These differences are even more pronounced in the presence of a shock, seen in comparison 7. This shock is caused by a reduction in the slenderness ratio going from the baseline diameter to the diameter of the circular approximation for the notional A350, for the baseline geometry length. In comparisons 5 and 6, η_{PR} variations upstream of the tail cone stations are negligible. This is because changes to fuselage diameter upstream have a more direct impact on the inviscid flow field than on the boundary layer. If there is no shock, the pressure recovery changes upstream are minimal. In comparison 7, the shock presents another source of losses, resulting in a decrease in η_{PR}. Even though the differences upstream are below the critical threshold, the magnitude of these differences in comparison 7 is much larger than those in comparisons 5 and 6. The large differences in the tail cone region for all three comparisons are due to variations in the closure and upsweep angles of the tail cone due to changes in the fuselage area, and for the A1.00 station,

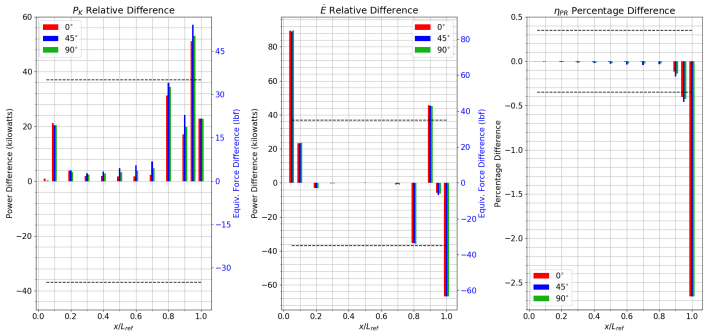

(a) Comparison 5: E2.5-8 vs. E2.1-1 (Baseline)

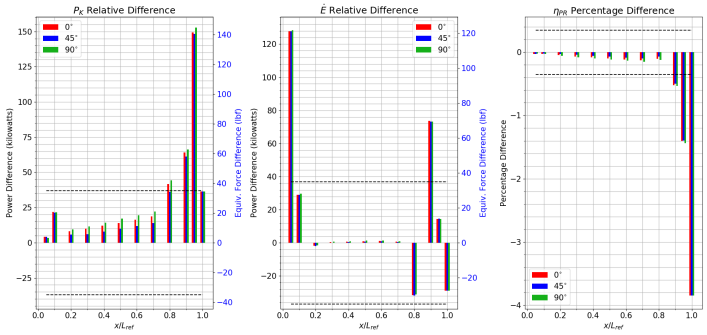

(b) Comparison 6: E2.5-6 vs. E2.5-5

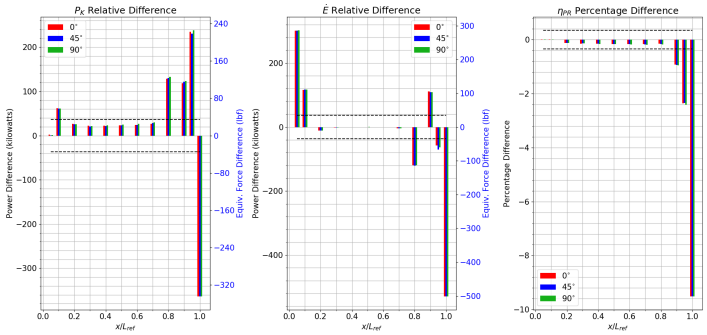

(c) Comparison 7: E2.5-3 vs. E2.1-1 (Baseline)

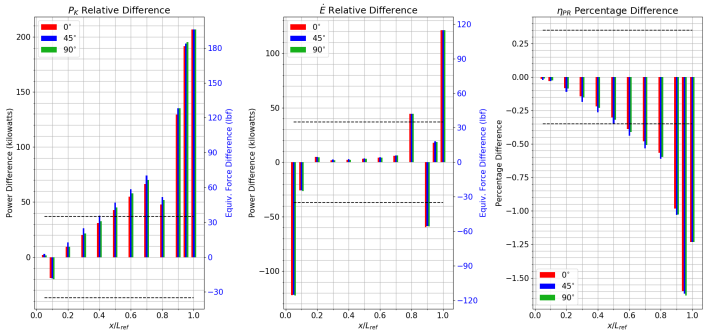

(d) Comparison 8: E2.5-6 vs. E2.1-1 (Baseline)

Figure 5.29: Experiment 2.5 - differences in estimates of the BLI effects, due to changes in fuselage cross sectional area and length

due to changes in the fuselage trailing edge area (hub area). Comparison 8, shown in Fig. 5.29d, highlights the impacts of fuselage length on the BLI effects at a given axial station. A longer fuselage implies a thicker boundary layer at the same non dimensional axial station, accounting for the increase in $C_{P_{K_{\text{in}}}}$ and decrease in η_{PR}.

The results from the above experiments provide some guidelines regarding the requirements for the geometry model from which surrogates of the BLI effects using CFD are generated. It can be seen that the macro parameters of the fuselage i.e. length and cross sectional area need to be defined correctly, or varied in the surrogate models given the sensitivity of the BLI effects to these parameters. The significance of the macro parameters of the tail are also emphasized in these trials, supporting the findings from experiment 2.3. With regards to the shape of the fuselage, it was found that the significance of such detailed parameters was minimal for conventional cross sectional fuselages, and that a circular approximation could be used. For unconventional highly elliptical cross sections, even though most of the errors are below the critical thresholds, it is recommended that an elliptical cross sectional shape be used. A circular approximation in this case may not be adequate to set the correct values of the tail cone angles and could compound the errors in the BLI effects estimates. Ranges on the values for the major and minor axes lengths of this elliptical shape will be constrained by the ranges on cross sectional area, tail cone closure, and upsweep angles.

5.7 Experiment 2.6: Sensitivity to Wing Design

5.7.1 Experimental Overview

As discussed in chapter 2, studies in literature detected the impact of wing downwash on the distortion profile at the aerodynamic interface plane of the STARC-ABL BLI propulsor [42, 27]. These findings emphasized the need to include the wing in the vehicle model for that concept. This experiment aims to corroborate those findings

and also generalizes the approach by considering other propulsor locations. This generalization allows one to draw conclusions regarding the importance of the wing on the BLI effects for concepts similar to the D8 and the NOVA-BLI. Specifically, the objective is to verify that the axial and circumferential location of the engine determines the contribution of the wing to the ingested boundary layer properties, as stated in hypothesis 2. A secondary goal of this experiment is to quantify the relative sensitivity of the BLI effects to key macro and detailed parameters of the wing. Doing so would allow the designer to default potentially inactive wing design variables, thus reducing the dimensionality of the problem when generating surrogates of the BLI effects.

The primary objective of this experiment can be achieved by comparing the differences in the BLI effects at all measurement stations between a fuselage only baseline, and the same geometry with a reference wing. For this experiment, a scaled version of the Common Research Model (CRM) wing [95] is used. This design is open source, extensively studied, and is developed specifically to provide a common and well designed geometry for CFD, making it an ideal choice as a reference wing. The original CRM wing is scaled down to a planform area of 1399ft^2, which is roughly comparable to the wing on the 737-8. The secondary objective of this experiment can be achieved by changing key wing design variables one at a time and comparing the measurements of the BLI effects for each perturbation to the reference wing case. Table 5.6 shows the main wing design variables considered as part of the scope for this experiment, the reference wing values, and the settings for the perturbed geometries.

The macro parameters are those defining the wing planform and location, while the detailed parameters considered are the airfoil thickness and camber. These variables are chosen primarily because they represent major design parameters for aerodynamic performance and stability, with the planform variables in particular featuring as part of vehicle concept design studies. The planform area for this experiment is defined

Table 5.6: Experiment 2.6 - Design Variable Settings

Variable	Reference Wing	Perturbed Wing
Planform Area: S	1399 ft^2	1722 ft^2
Aspect Ratio: AR	9	7
Taper Ratio: λ	0.20	0.28
Leading Edge Sweep: Λ_{LE}	37°	20°
Dihedral: Γ	CRM	+5°
Axial Location (Wing Root LE): $\frac{x_{\text{LE}}}{L_{\text{ref}}}$	35%	30%
Max Thickness to Chord: $\left(\frac{t}{c}\right)_{\text{max}}$	CRM	+2%
Airfoil Camber	CRM	Modified CRM

as the trapezoidal area enclosed between the wing tip and the symmetry plane. This is the only variable of the reference wing that is different from the original CRM. The taper ratio in this study is defined as the ratio of the wing tip chord to the root chord at the symmetry plane, with the length of the tip and root chords matching the CRM. The airfoils, dihedral, and sweep at all span stations are the same as the original CRM. The axial location of the wing root leading edge at the symmetry plane is estimated from the airport planning document of the 737-8 [14].

A total of 10 cases are run, one for the reference wing, and one for each perturbation of the design variables. The last case applies all perturbations, except the camber, at once. Most of the perturbed values are chosen such that they fall on or within the bounds of a reasonable design space. Using the wing area for a conventional (non-BLI) 150-180 pax aircraft, a variation of ±25% in this value can be reasonably expected as part of the sizing process with BLI and other technologies. As such, the perturbed wing area chosen is a 23% increase over the reference area. For context, the STARC-ABL concept proposed in 2016 featured a 38% increase in wing area relative to the N+3 Conventional Configuration (N3CC) [98]. The aspect ratio ranges obtained from [88] show that most aircraft fall within a range of 7-11. While current design trends favor high aspect ratios, a value of 7 for the perturbed

case provides an estimate for the highest impact this variable can have on the BLI effects, given the stronger influence of the tip vortices on the flow around the fuselage.

The perturbations for λ, Λ_{LE}, Γ and $\left(\frac{t}{c}\right)_{\text{max}}$ are based on common values for transport aircraft found in Raymer [76]. For λ, a typical range is 0.25 to 0.45. The middle point of 0.35 is a 40% increase from the lower bound. Since the baseline CRM λ is below this range, a 40% increase is applied to the reference value to obtain 0.28. The typical average Γ range is 0° to 10°. The average Γ for the reference wing is 4.5°. Thus, 5° is added to the dihedral values at each span station as a perturbation. The sweep angles for most transonic wings fall between 20° to 40°. Given that the CRM is near 40°, the perturbed wing is set to 20°. For the airfoil $\left(\frac{t}{c}\right)_{\text{max}}$, the reference wing average maximum thickness is 10.7%. The typical average values found in Raymer are between 10-14%. Thus, a positive delta of 2% is applied to each airfoil station to obtain the perturbed geometry. The airfoil camber is altered by changing two CST coefficients [47] on the lower surface of each airfoil. The upper surface and fore section of the lower surface are unchanged, as seen in Fig. 5.30.

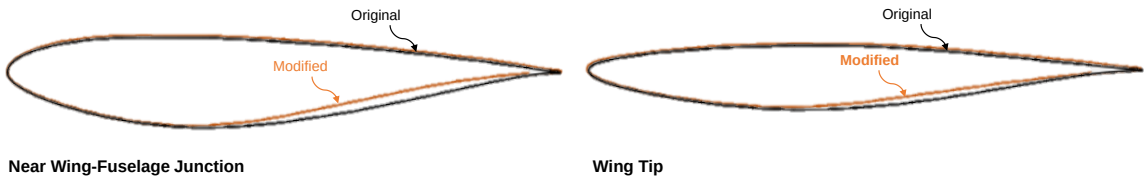

Figure 5.30: Camber variations for the wing geometry, shown for airfoils near the wing-fuselage junction and the wing tip

5.7.2 Results and Discussion

Initially, the reference wing was analyzed with the baseline fuselage without a fairing. Absence of the fairing, however, caused undesirable flow features, as shown in Fig. 5.31. Significant flow separation at the fuselage-wing junction is observed, at $\alpha = 0°$, as seen from the skin friction and x velocity contours. There is a region of slow moving flow behind the separation bubble, which appears to alter the effective body

shape. This disturbed flow propagates to the trailing edge of the fuselage and beyond, highlighted in the pressure recovery contours at the 95% station in Fig. 5.31. A consequence of this flow feature is a significant favorable impact on $C_{P_{K_{\text{in}}}}$ and large decrease in η_{PR}, as seen in Fig. 5.32. In this figure, BLI effects trends from the baseline fuselage with a wing are compared to the fuselage only trends at $\alpha = 0°$. Results at the 40% and 50% stations are omitted since the integration areas intersect with the wing geometry, leading to erroneous measurements.

Given that these flow phenomena would likely bias the results, the belly fairing was subsequently included in all analyses. Doing so eliminated the excessive separation and downstream influence at both $\alpha = 0°$ and 2°. Fig. 5.33 compares the reference wing BLI effects at both 0° (Fig. 5.33a) and 2° (Fig. 5.33b) to the geometry from experiment 2.4. As shown previously, the fairing's impact is only significant at $\alpha = 2°$ at the A1.00 station. Thus, the trends shown are primarily driven by the presence of the wing. It is immediately apparent that the significant changes at the 0° circumferential stations are no longer seen. A more interesting observation is the larger difference at the 45° and 90° stations, particularly along the tail cone.

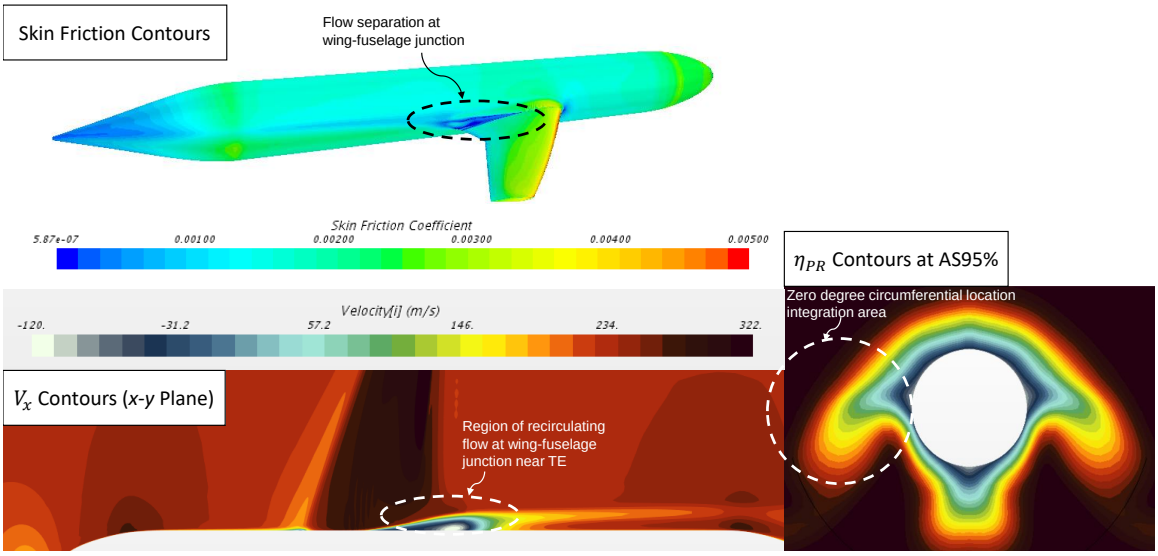

Figure 5.31: Flow separation at wing-fuselage junction in the absence of a belly fairing

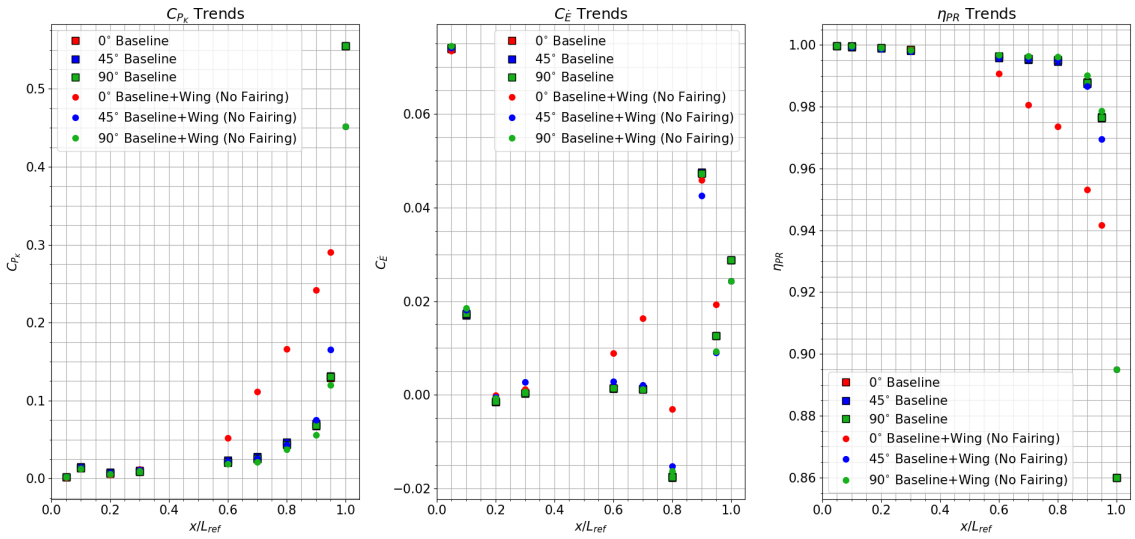

Figure 5.32: Impact of the fuselage-wing separation on the BLI effects in the absence of a belly fairing

Though initially counterintuitive, this observation highlights global influence of the wing on the flow field. In the absence of excessive separation, given the size of the integration areas and their relative location to the reference wing, the local influence of the reference wing wake is not as significant as the global effect through the induced downwash.

In Figs. 5.34a and 5.34b streamlines emanating from the same source, shown at the symmetry plane, are compared between the fuselage only (black) and wing case (red) for two angles of attack. The wing induced deflection of streamlines in the negative z direction is evident from both these plots. A scalar view of the w velocity contours at the A0.95 plane in Figs. 5.34c and 5.34d illustrates the downwash variation in the $y - z$ plane in the vicinity of the fuselage. The integration areas at the 0° and 90° stations are shown in black. Notice the larger region of $-w$ flow at the 90 degree stations for the wing case compared to the baseline fuselage. Differences in w velocity are also observed at the 0° station, but the magnitude and thus the net effect on the BLI effects is smaller relative to the other circumferential stations. A thinner boundary layer at the 90° station is observed, evident from the η_{PR} contours

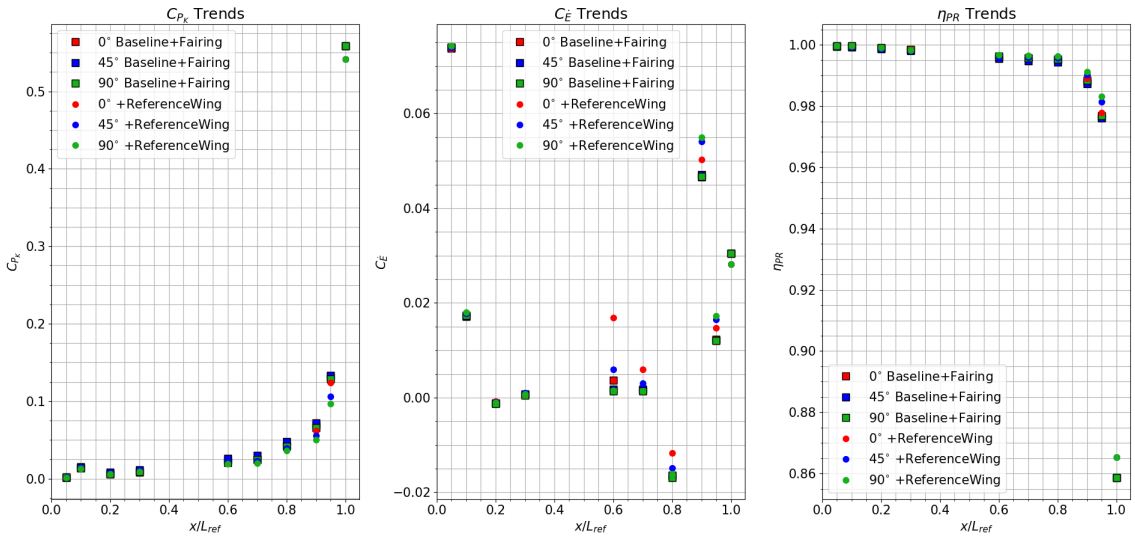

(a) E2.6-1v1 vs. E2.4-1 ($\alpha = 0°$ Baseline + Fairing)

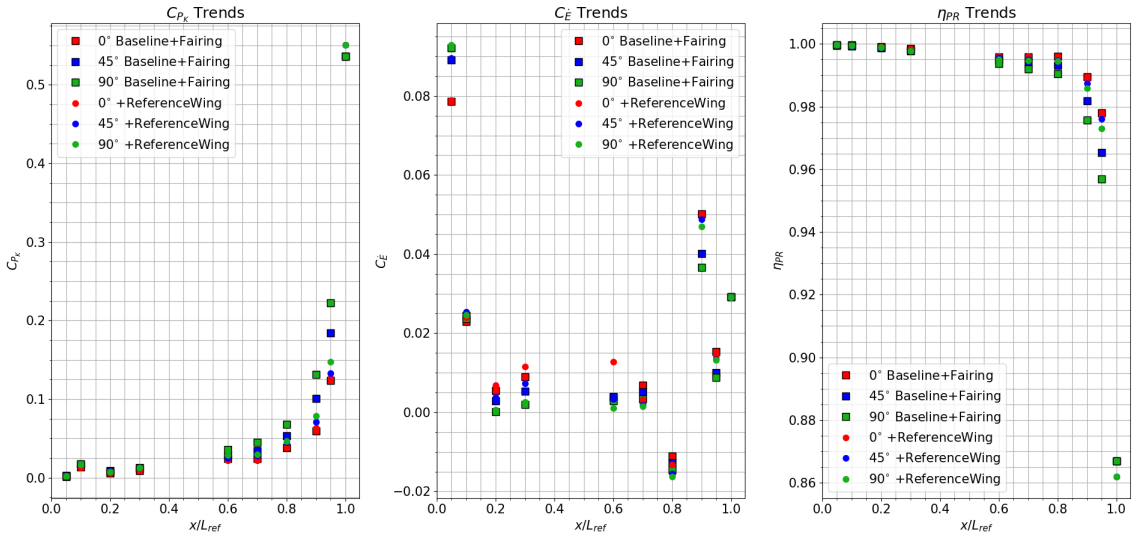

(b) E2.6-1v2 vs. E2.4-2 ($\alpha = 2°$ Baseline + Fairing)

Figure 5.33: Experiment 2.6 - influence of the reference wing on the BLI effects with the belly fairing

in Figs. 5.34e and 5.34f, which explains the lower value of $C_{P_{K_{\text{in}}}}$ and higher value of η_{PR}, relative to the no wing case, seen in Fig. 5.33.

Relation between Wing Contribution to BLI Effects and Engine Location

Fig. 5.35 summarizes the results for all 10 wing cases, run at a typical cruise $\alpha = 2°$. In Fig. 5.35a, differences in the net BLI effect, $C_{P_{K_{\text{in}}}} + C_{\dot{E}}$, relative to the fuselage only

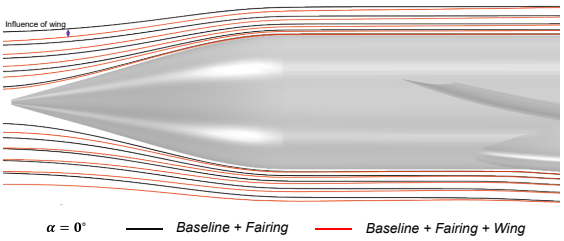

(a) Streamlines at symmetry plane aft of wing ($\alpha = 0°$)

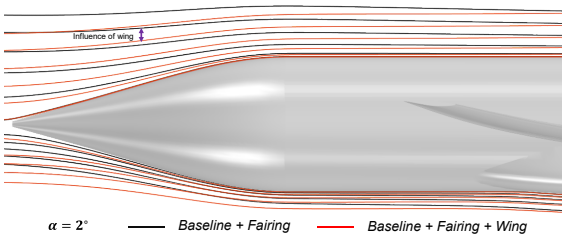

(b) Streamlines at symmetry plane aft of wing ($\alpha = 2°$)

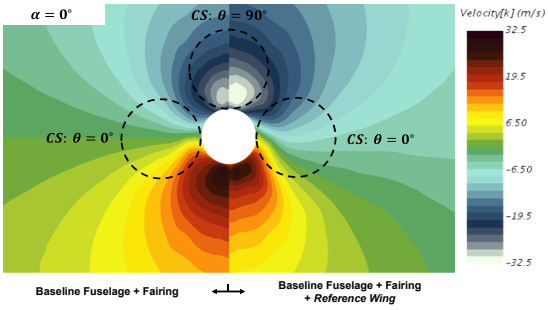

(c) w Velocity component at A0.95 ($\alpha = 0°$)

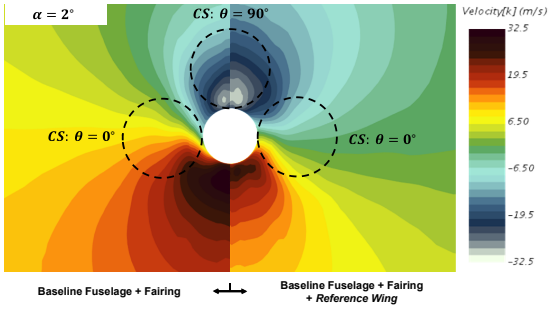

(d) w Velocity component at A0.95 ($\alpha = 2°$)

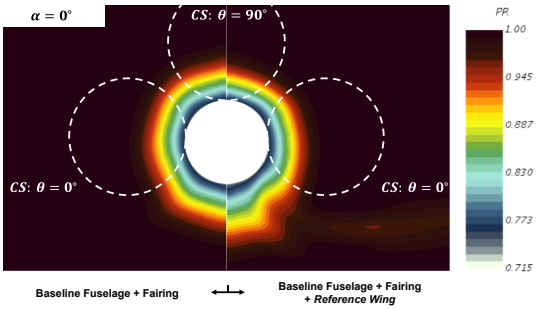

(e) η_{PR} contours at A0.95 ($\alpha = 0°$)

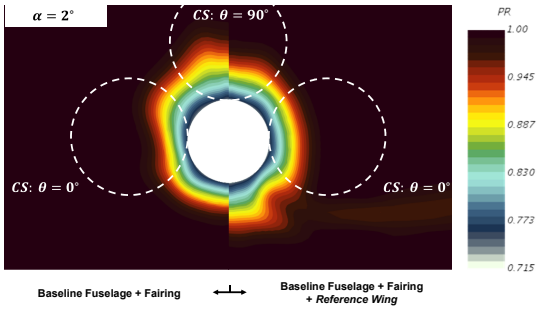

(f) η_{PR} contours at A0.95 ($\alpha = 2°$)

Figure 5.34: Experiment 2.6 - influence of the reference wing on the flow streamlines, w velocity, and boundary layer

case are shown in terms of an equivalent force. In Fig. 5.35b, the percent differences in η_{PR} relative to the no-wing baseline are presented. Similar plots for the individual components, $C_{P_{K_{\text{in}}}}$ and $C_{\dot{E}}$, are included in Fig. A.6 in Appendix A. These figures compare the BLI effects aft of the wing, given that upstream differences due to the presence of the wing are negligible. The bars in each plot, for a given measurement station, are shown in the same order as described in the legend.

Results shown in these plots clearly support the hypothesis that the wing contri-

bution to the BLI effects varies based on circumferential (and axial) location of the engine relative to the wing. The most significant influence of the wing is observed at the 90° stations, followed by the 45° and 0° stations. The magnitude of these differences grows along the axial distance for the 45° and 90° locations. Based on these results, it can be concluded that for concepts like the D8 that feature engines mounted on top in the last 10% of the fuselage, the wing must be included in the geometry model used for generating surrogates of the BLI effects. The discrepancy in the BLI effects estimates by omitting the wing is approximately 3-6 times the critical threshold for both $C_{P_{K_{\text{in}}}} + C_{\dot{E}}$ and η_{PR}, based on results at the A0.90C90 and A0.95C90 stations. The differences in BLI effects also exceed the critical thresholds at the A1.00 station, albeit to a lesser degree. Recall, the baseline geometry against which these differences are calculated includes the fairing. As seen in the results at

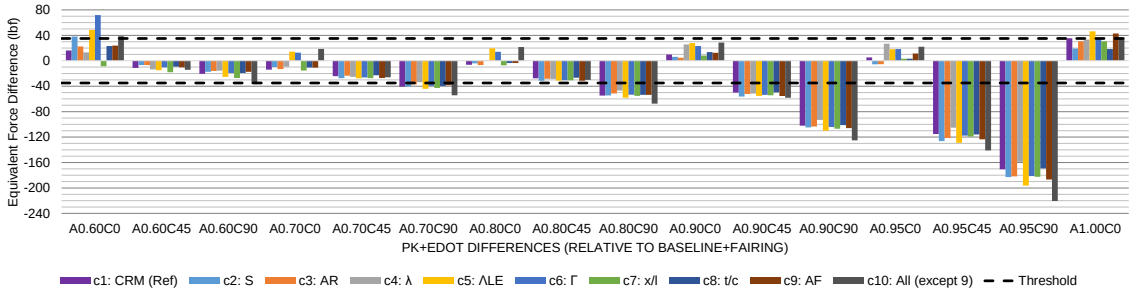

(a) $C_{P_{K_{\text{in}}}} + C_{\dot{E}}$

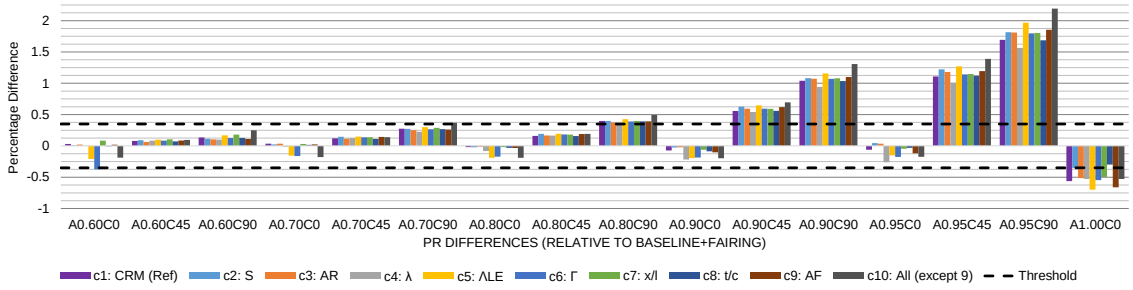

(b) η_{PR}

Figure 5.35: Experiment 2.6 - influence of the wing on the BLI effects at measurement stations aft of the wing at $\alpha = 2°$. Differences are against the results from fuselage/fairing case 2 in experiment 2.4

A1.00 from experiment 2.4, the fairing itself has a positive contribution to $C_{P_{K_{\text{in}}}} + C_{\dot{E}}$ by about 55lbf and a negative impact on η_{PR} by about 0.76%, relative to the baseline fuselage geometry used in experiment 2.1 at $\alpha = 2°$. The wing contribution compounds the influence of the fairing at $\alpha = 2°$ for A1.00, such that the net difference between the wing/fairing/fuselage case relative to baseline fuselage is even larger. For the reference wing case, these differences are approximately 90lbf for $C_{P_{K_{\text{in}}}} + C_{\dot{E}}$ and -1.3% for η_{PR}. In summary, the results presented here also support findings in literature regarding the inclusion of the wing for concepts like the STARC-ABL.

For engines mounted at the 0° locations, trends show that the wing's contribution is below the defined critical thresholds, even for case 10 where all variables are set to their perturbed values. The outlier is at the 0° circumferential station for the 60% location (A0.6C0), where differences in the BLI effects are strongly influenced by the local flow characteristics in the vicinity of the wing trailing edge. While the results suggest that the wing can be omitted from the geometry model for concepts like the NOVA-BLI, where the engine location falls close to the A0.90C0 and A0.95C0 stations, one must consider this conclusion with caution. There are a few considerations that must be kept in mind when interpreting the obtained results. First, these results are only valid within the design space considered. There is uncertainty in the results if any parameter is set outside the bounds considered in this experiment. Second, even within the perturbation bounds, not all possible combinations of design variables have been tested. Case 10 was run to provide an estimate for how much the result can change when multiple variables are altered at the same time. From these results, it can be inferred that other design combinations should produce comparable results. One cannot guarantee, however, that the BLI effects differences for other design combinations will not exceed the thresholds, especially given how close the maximum difference of 30lbf (at A0.9C0 and A0.95C0) is to the defined threshold of 35lbf. The definition of the threshold itself is dependent on the designer. If the

designer wishes to reduce this critical threshold by even 10lbf, the wing then must be included. Lastly, one must not forget about the effects of excessive flow separation on the downstream 0° stations. Conclusions from the results obtained above are only reasonable if the design perturbations stay within this domain of relativity clean flow off the trailing edge. Variations in the airfoil camber and/or thickness, or even sweep, for example, could produce adverse flow features that enhance the significance of the wing contribution to the BLI effects at the 0° stations. These designs, however, are likely to be screened out as part of the system level optimization given the expected detrimental impact of such features on the overall performance.

Another consideration is the practical aspect of including the wing geometry. The proposed BLI concept design methodology leverages CFD generated surrogates of the BLI effects. Availability of computational resources and overall run time of CFD with a wing as part of the vehicle geometry model are also important factors to consider. Limited resources may preclude the incorporation of a wing in the CFD geometry model for concepts with an engine position like that on the NOVA-BLI, especially if the differences in the estimates of the BLI effects are too small (based on the designer defined threshold) to justify this additional expense and time. Therefore, it is recommended that inclusion of the wing in the geometry model for such concepts should be left to the discretion of the designer. The experimental results indicate that the discrepancy in the BLI effects by neglecting the wing for such engine locations is relatively smaller than the error at other engine locations, such as on the D8 and the STARC-ABL, where the wing contribution is large enough to warrant its inclusion.

Relative Sensitivity of BLI Effects to Wing Design Parameters

Fig. 5.36 compares the differences in the BLI effects for cases 2-10 relative to the reference wing trial 1. These results indicate the relative sensitivity of the BLI effects to the variations in the macro and detailed design parameters. Like before, the bars in

the plot are ordered in the same manner as presented in the legend. A clear pattern is observed at the 60-90% stations where perturbations in the geometry produce noticeable changes at the 0° stations, given that these locations are more sensitive to changes in the wing wake. Just aft of the wing at the A0.6C0 station, Γ and Λ_{LE} have the strongest impact on both $C_{P_{K_{\mathrm{in}}}} + C_{\dot{E}}$ and η_{PR}. For the given engine placement, increasing the dihedral increases the amount of ingested wing wake, as seen in Fig. 5.37, which shows the $C_{P_{K_{\mathrm{in}}}}$ contours at the different measurement stations. The planform area and $\frac{x_{\mathrm{LE}}}{L_{\mathrm{ref}}}$ also have a noticeable effect on $C_{P_{K_{\mathrm{in}}}} + C_{\dot{E}}$ at this location. The influence of Γ and Λ_{LE} persists downstream at the 0° stations up to the 90% fuselage span station and thus the parameters feature in the active variable space for any engine mounted at these locations.

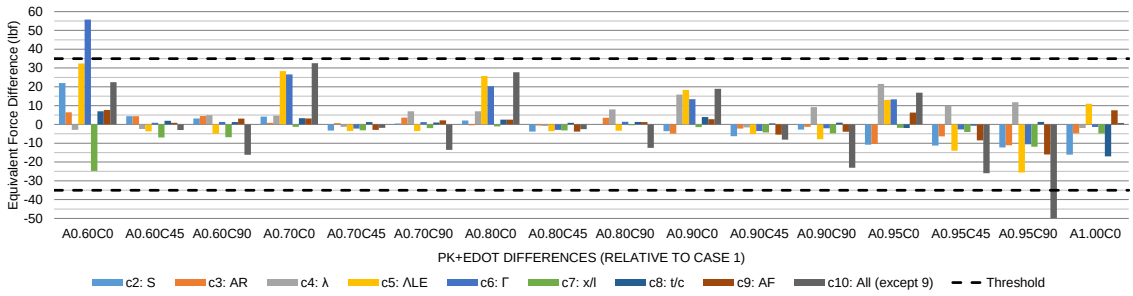

(a) $C_{P_{K_{\mathrm{in}}}} + C_{\dot{E}}$

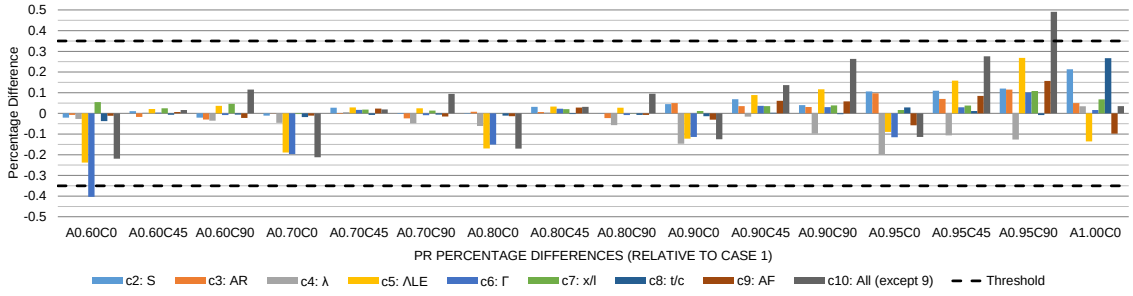

(b) η_{PR}

Figure 5.36: Experiment 2.6 - relative sensitivity of the BLI effects to the macro and detailed parameters of the wing at $\alpha = 2°$. Differences are relative to the reference wing case (E2.6-1)

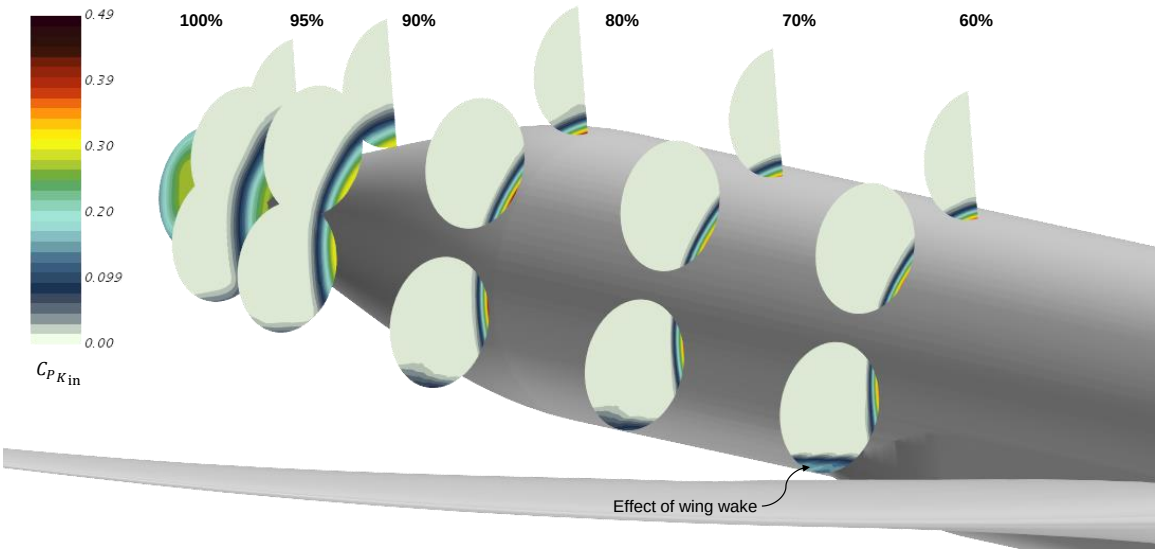

Figure 5.37: Experiment 2.6 - effects of wing wake on the 0° stations aft of the wing due to a change in wing dihedral (case 6). Visualized through $C_{P_{K_{\text{in}}}}$ contours

At the 90% span station and aft, the impact of other variables is relatively stronger and determining a dominant parameter is challenging for certain engine locations. At the A0.9C90 station, Λ_{LE} and λ produce differences that are almost double of those produced by other perturbations, except case 10 which is the largest, but the absolute differences relative to the reference wing are just under 10lbf for $C_{P_{K_{\text{in}}}} + C_{\dot{E}}$ and around 0.1% for η_{PR}. At the A0.95C90 station, the differences relative to the reference wing for most perturbations are larger, but the differences due to Λ_{LE} are still twice as large. At the A1.00 station, the wing $\left(\frac{t}{c}\right)_{\text{max}}$, S, Λ_{LE}, and to a certain extent the airfoil camber are the dominating terms. The significance of the detailed parameters at the A1.00 location is in contrast to the trends observed at other engine locations, where a macro parameter usually had a larger impact. Given the placement and extent of the measurement station at A1.00, this location is influenced strongly by the flow in the vicinity of the wing-fuselage junction. Changes to the wing $\left(\frac{t}{c}\right)_{\text{max}}$ affect the root chord thickness more prominently (given the larger chord length), which in turn affects the flow properties at the A1.00 station. Similar reasoning can be applied to explain the effects of S at A1.00.

At first glance, the results may suggest that since perturbations in the wing design produce differences that are below the critical threshold in most cases, these variations do not need to be kept track of when generating surrogates of the BLI effects. However, this view is misleading. It is important to note that these differences shown in Fig. 5.36 are with respect to some reference wing. Changing the reference wing will change the magnitude of the differences. Consider the A0.95C90 station for example. If the wing geometry from case 4 was set as the reference wing, then the sweep variation in case 5 would exceed the threshold given that there is a 37lbf difference between the two cases. Therefore, it is also important to look at the range of the differences in the BLI effects for each station, given that there is no unique basis for obtaining this reference wing. Calculating the ranges for $C_{P_{K_{\text{in}}}} + C_{\dot{E}}$ and η_{PR} yields values of about 25lbf/0.2% for A0.90C0, 32lbf/0.36% for A0.90C90, 32lbf/0.31% for A0.95C0, 62lbf/0.60% for A0.95C90, and 28lbf/0.40% for A1.00 from just the 10 experimental trials. These ranges indicate that the variability in the BLI effects is significant for top mounted engine locations, like on the D8, and for a fuselage trailing edge propulsor, like on the STARC-ABL.

The main takeaway from this experiment is that when designing vehicles with engine locations similar to the D8 and STARC-ABL, not only must the wing be present in the geometry model for the BLI effects surrogate generation, but also, the variability in the wing design parameters must be included. While the BLI effects are more strongly influenced by the the macro parameters of the wing at most engine locations, the impact of detailed parameters like the airfoil camber and thickness is comparable, or even larger, for certain stations such as at A1.00.

5.8 Experiment 2.7: Sensitivity to Empennage

5.8.1 Experimental Overview

The objective of this experiment is to assess which macro and detailed parameters of the vertical tail are significant contributors to the BLI effects. The scope of this experiment is restricted to a conventional vertical tail, common to existing aircraft. However, one trial does analyze a t-tail configuration, which is adopted on concepts like the STARC-ABL and the NOVA-BLI, to assess the significance of the horizontal stabilizer. Unlike previous studies, this experiment focuses on the BLI effects calculated at A1.00, since it is directly influenced by the vertical tail. While the BLI version of the CRM [13] places the horizontal tail in front of the A1.00 propulsor, such a configuration is not considered in this experiment for a few reasons. Primarily, it is expected that the interaction between the horizontal tail and propulsor, its effect on the ingested boundary layer, propulsor performance, and aerodynamic efficiency of the stabilizer, will warrant additional design studies to avoid adverse effects. It is thus assumed that concepts featuring a fuselage trailing edge propulsor will place the stabilizer outside the influence of the engine, leading to the t-tail configuration. Additionally, given the similarity between the vertical and horizontal tail, conclusions regarding the objective of this experiment for the conventional horizontal tail placement can be inferred from the results of the vertical tail studies.

As observed in experiment 2.3, the shape of the tail cone does have an impact on the BLI effects. To avoid any bias that may occur by integrating a vertical tail on the baseline axisymmetric tail, where, as shown previously, the boundary layer is thicker on the upper side, the tail cone geometry from experiment 2.3 is used. This tail cone is mated to the baseline fuselage fore section. In the absence of available geometry for a 737-8 like vehicle, the CRM vertical tail designed by Onera [8] is used as a reference geometry. This tail is then scaled down to an area of 223.6ft^2 based on an assumed

Table 5.7: Experiment 2.7 - Design Variable Settings

Variable	Baseline	Perturbed
Planform Area: S_v	223.6ft^2	269.1ft^2
Aspect Ratio: AR_v	1.98	1.2
Taper Ratio: λ_v	0.28	0.60
Leading Edge Sweep: Λ_{LE_v}	44.5°	35°
Avg. Max Thickness to Chord: $\left(\frac{t}{c}\right)_{\max}$	13.42%	11.42%
Airfoil Type	NACA 64A013	NACA 0013

tail volume coefficient of 0.09 (from Raymer [76]) and values of the reference wing area and span in experiment 2.6. Table 5.7 shows the main design variables considered, their baseline values, and the perturbed values. Ranges for S_v are driven by the values of the wing planform area considered in experiment 2.6, for the previously assumed tail volume coefficient. Estimates for the other ranges are obtained from [76]. The detailed design aspects of vertical tail, like in the previous experiment, are the airfoil definitions governed by the airfoil type and thickness $\left(\frac{t}{c}\right)_{\max}$. The other planform variables are the macro parameters. As illustrated in Fig. 5.38, the first trial is the baseline vertical tail geometry, while the following five trials perturb each variable one at a time, keeping the rest at the baseline values. Case 7 represents a vertical tail designed for a t-tail configuration, and is a result of setting the variables at their perturbed values all at once. Case 8 uses the vertical tail from case 7 and adds a horizontal stabilizer, while case 9 is the baseline vertical tail planform with NACA 0013 airfoils instead of those used in the scaled CRM vertical tail. All cases are run at $\alpha = 0°$.

5.8.2 Results and Discussion

Fig. 5.39 presents the differences in the BLI effect estimates at the A1.00 station for each of the nine cases, relative to the no vertical tail baseline geometry from experiment 2.3-1. Fig. 5.40 compares the η_{PR} contours between the no tail baseline

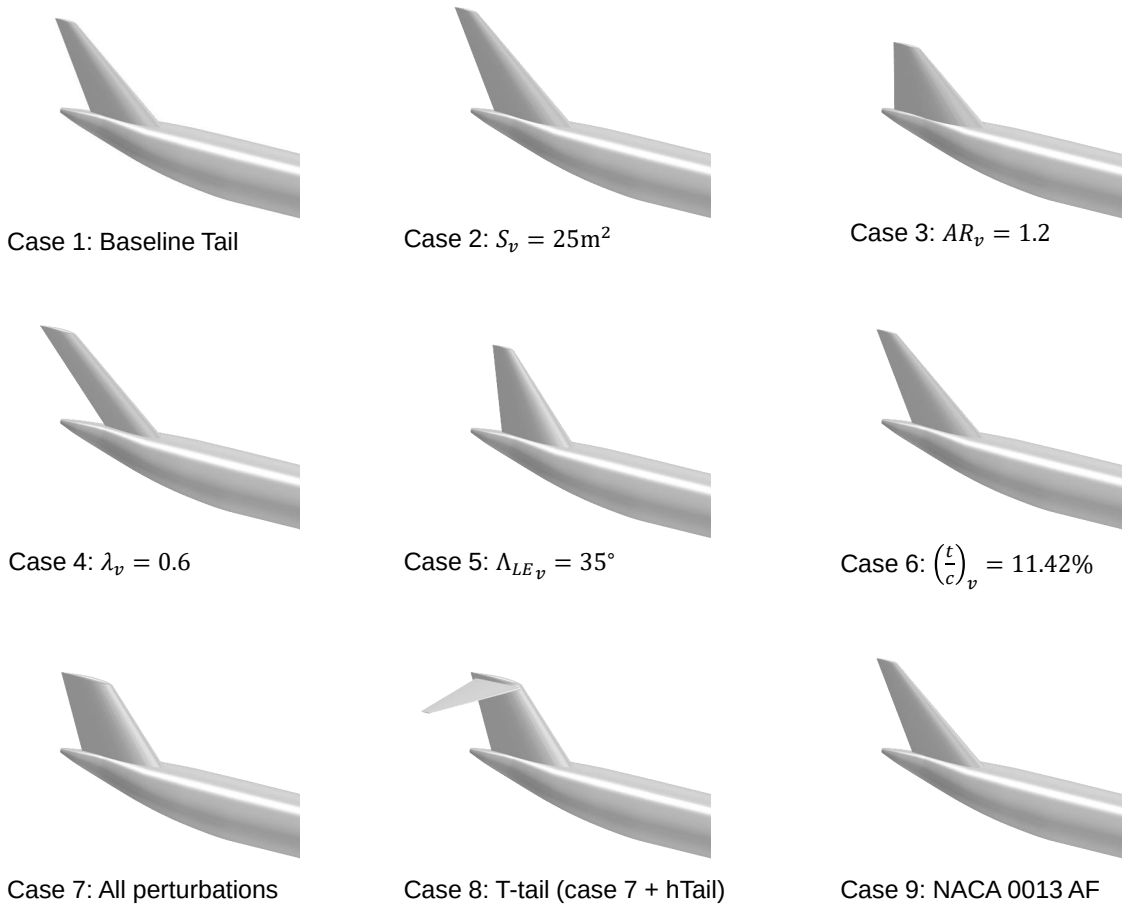

Figure 5.38: Experiment 2.7 cases

and the reference tail (E2.7-1) at the A1.00 station, highlighting the fuselage boundary layer and vertical tail wake. As evident from Fig. 5.40, the wake of the vertical tail and the outward deflection of the boundary layer in y direction help increase $C_{P_{K_{\text{in}}}}$ and decrease $C_{\dot{E}}$ and η_{PR} relative to the no tail baseline. The higher static pressure aft of the tail, relative to the no-tail case, increases the magnitude of the pressure defect work rate component of $C_{\dot{E}}$, effectively offsetting the kinetic energy defect rate benefit in the vertical tail wake, resulting in a net decrease in $C_{\dot{E}}$. While the differences in $C_{\dot{E}}$ are smaller than the critical threshold, the net effect of $C_{P_{K_{\text{in}}}} + C_{\dot{E}}$ still exceeds the threshold given the stronger favorable impact of the wake on $C_{P_{K_{\text{in}}}}$, as seen in Fig. 5.39. The differences in η_{PR} also exceed the threshold. The main

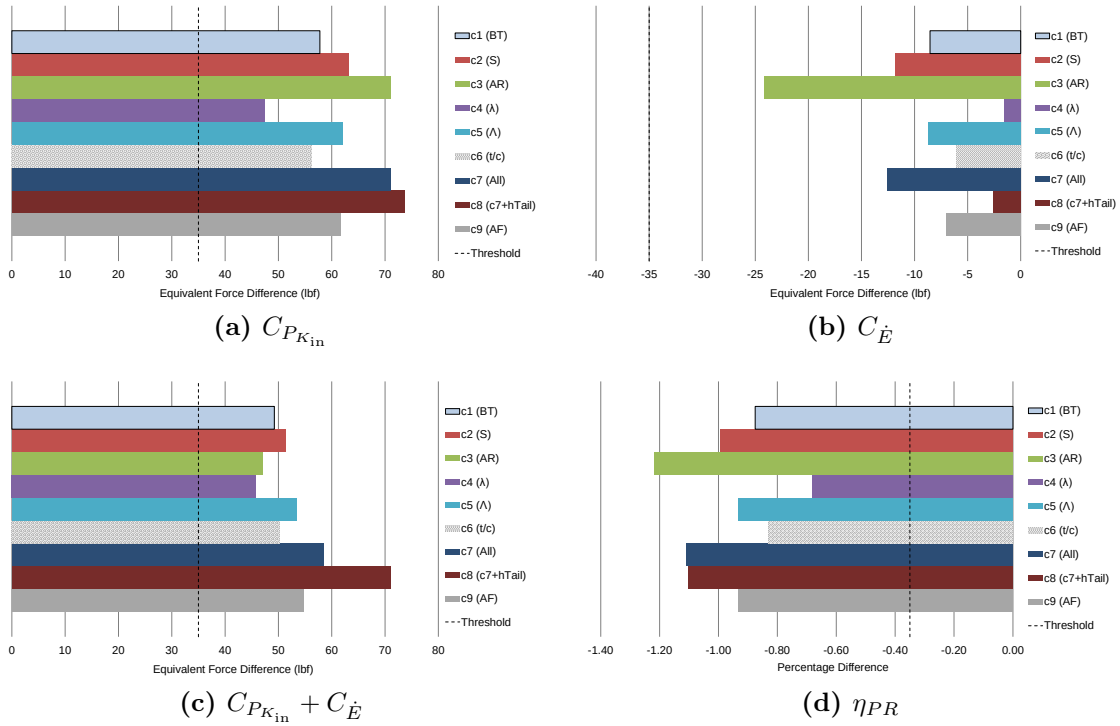

(a) $C_{P_{K_{\text{in}}}}$ **(b)** $C_{\dot{E}}$

(c) $C_{P_{K_{\text{in}}}} + C_{\dot{E}}$ **(d)** η_{PR}

Figure 5.39: Experiment 2.7 - differences in estimates of the BLI effects at the A1.00 station, due to changes in vertical tail design, relative to experiment 2.3-1.

conclusion from Fig. 5.39 is that a vertical tail must be present in the CFD geometry model when calculating the BLI effects for a STARC-ABL like concept.

To assess the significance of the design changes on the BLI effects, Fig. 5.41 ranks the differences between cases 2-9 relative to the reference tail in case 1. It is observed that all differences relative to the baseline vertical tail are below the critical threshold, for the given variable ranges. Even case 7, where all parameters (except airfoil type) are set at the perturbed values, falls below the critical threshold for all BLI effects. Variations in the pressure recovery are more significant for cases 3, 4, 7, and 8 and follow expected trends given the behavior of the vertical wake extent based on the geometry. Any configuration that tends to produce a thicker wake, such as a low aspect ratio tail, will have a lower pressure recovery. Reducing the tail $\left(\frac{t}{c}\right)_{\text{max}}$ and increasing λ_v both decrease the overall thickness of the wing in the region just in front of the A1.00 integration area, producing a thinner wake and thus improving η_{PR}.

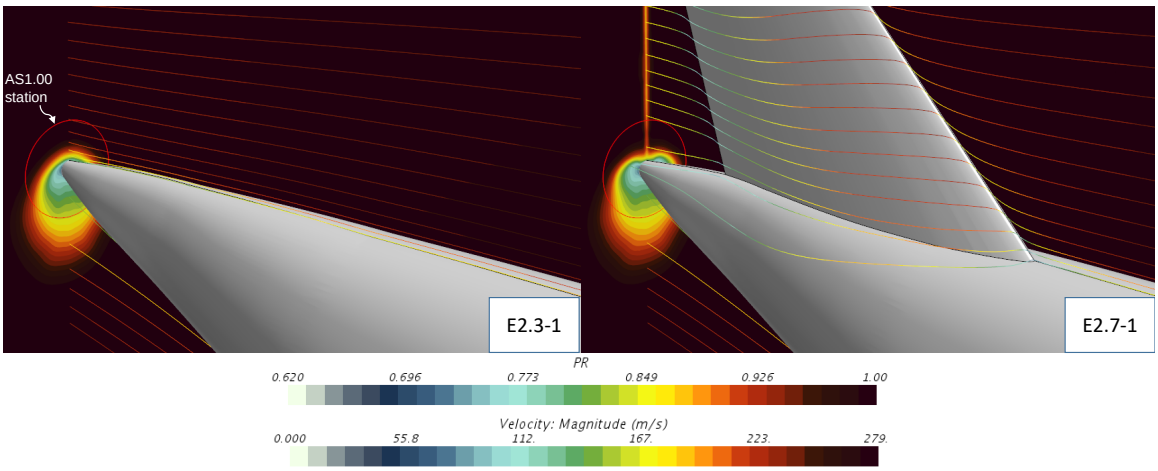

Figure 5.40: Experiment 2.7 - effects of the vertical tail on the flow streamlines (at symmetry plane) and the A1.00 boundary layer. The streamlines are colored based on the velocity magnitude

With regards to the relative significance of the parameters, it can be observed from the BLI effects plots in Figs. 5.41a, 5.41b, and 5.41d that the detailed parameters like airfoil type and $\left(\frac{t}{c}\right)_{\max}$ have a smaller impact on the BLI effects than the macro parameters, within the defined ranges, supporting hypothesis 2. Also, comparing case 7 and case 8, noting that both have the same vertical tail, the effective contribution of the horizontal stabilizer on $C_{P_{K_{\text{in}}}}$ is approximately 2.6 lbf, and 0.008% on η_{PR}. The impact on $C_{\dot{E}}$ is larger, and the net effect on $C_{P_{K_{\text{in}}}} + C_{\dot{E}}$ is around 12.6 lbf. On the individual BLI effects, AR_v, λ_v, and S_v are the most significant macro parameters. The range in $C_{P_{K_{\text{in}}}} + C_{\dot{E}}$ differences is only about 12lbf for just the vertical tail. However, the largest variation seen in the η_{PR} differences is about 0.54%, when comparing case 3 to case 4, which exceeds the critical threshold. Recall that the range in η_{PR} variation due to wing parameter changes for the A1.00 station was 0.40%. The combined effect of the wing and the tail geometry variations can have a substantial impact on the BLI effects estimates. Thus, it is recommended that the vertical tail design variables be included in the BLI effects surrogate models. A computational cost effective option is to only vary the most significant macro parameters, i.e., AR_v, λ_v, and S_v, defaulting the airfoil to a reasonable type and thickness. Doing so would

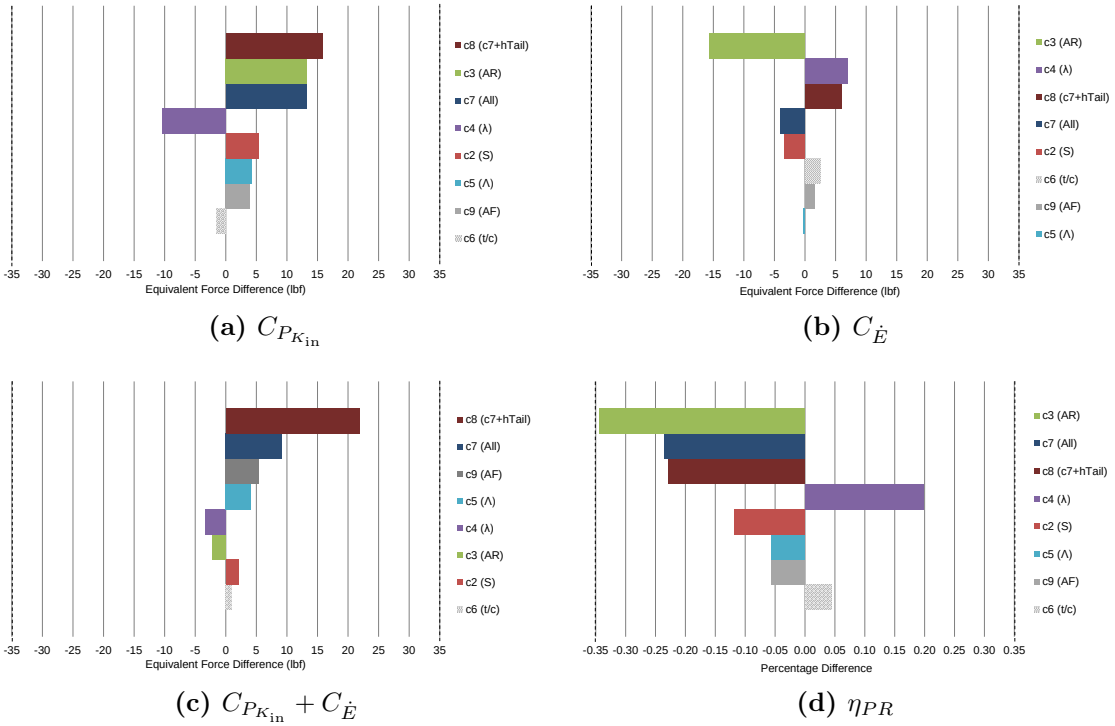

(a) $C_{P_{K_{\text{in}}}}$ **(b)** $C_{\dot{E}}$

(c) $C_{P_{K_{\text{in}}}} + C_{\dot{E}}$ **(d)** η_{PR}

Figure 5.41: Experiment 2.7 - differences in estimates of the BLI effects at the A1.00 station, due to changes in vertical tail design, relative to the reference vertical tail (Case 1)

minimize the number of runs required to cover the sample space. While the impact of the horizontal tail on the flow is expected to be more significant if it is lowered, for the location tested, the stabilizer can be neglected.

5.9 Experiment 2.8: Sensitivity to Inlet Ramp

5.9.1 Experimental Overview

Most BLI concepts feature an S-shaped inlet feeding into the propulsor. This shape can be crudely parameterized by one macro parameter and two detailed parameters, as illustrated in Fig. 5.42. In this figure, the inlet ramp is defined between two fuselage cross sectional stations, shown in gray. The end station corresponds to the nacelle highlight plane of the fictitious propulsor. The inlet ramp angle (macro parameter) is the angle created by the cross sectional area change between the start and end station.

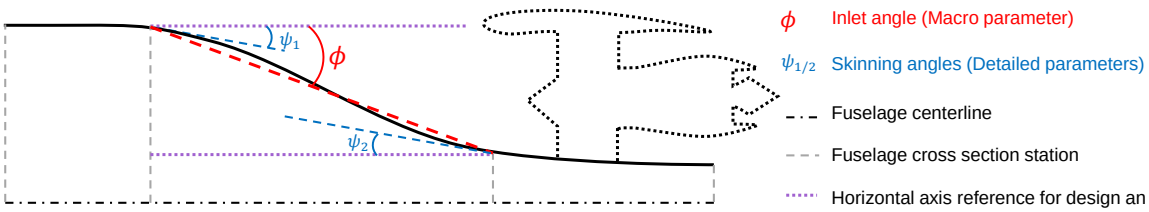

Figure 5.42: Parameterization of an S-shaped BLI inlet geometry

The detailed skinning angles, shown in blue, control the slopes of the spline curve connecting the start and end points of the inlet. The inlet and skinning angles are defined with reference to the horizontal axis shown in purple. The simplest geometry is a linear ramp, where $\psi_i = \phi$, resulting in sharp corners at the start and end points. By controlling the values of ψ_i, the designer can alter the curvature at these locations, thereby changing the shape of the S curve from a linear to a non-linear ramp.

The design variables chosen allow for an efficient experimentation process to assess the sensitivity of the BLI effects to the major design aspects of the inlet. In particular, this experiment aims to determine the relative sensitivity of the BLI effects to the changes in the inlet angle and the skinning angles. Like with the tail cone, inlet optimization studies are common in literature, as discussed previously, indicating the importance of this feature in BLI concept performance. The goal of these experiments is to assess whether hypothesis 2 holds true and that the BLI effects are indeed more sensitive to the macro parameter. In doing so, the experiments also aim to establish guidelines for handling this geometry when developing surrogates of the BLI effects for conceptual design.

The starting geometry used for this experiment is the one from E2.3-1, where the notional 737-8 tail cone was used in conjunction with the baseline fore-body. The measurements for the BLI effects are obtained at the 85% axial, 0° circumferential station, and is thus a notional model of the NOVA-BLI concept. The baseline values for the macro and detailed parameters are: $\phi = 6.71°$, $\psi_1 = 2.00°$, $\psi_2 = 11.74°$, where

the angles are defined as shown in Fig. 5.42. This geometry is modified to create four different inlet shapes. Table 5.8 presents the four cases that are run.

Table 5.8: Experiment 2.8 - Overview of Cases

Experiment	ϕ (°)	ψ_1 (°)	ψ_2 (°)	Comments
2.8-1	12	2.00	11.74	
2.8-2	16	2.00	11.74	$\Delta\phi = 4°$
2.8-3	12	12	12	Linear ramp
2.8-4	16	16	16	Linear ramp

Cases 1 and 2 are compared to quantify the differences in the BLI effects due to a four degree change in the inlet angle. Cases 3 and 4 are linear ramp approximations of cases 1 and 2, attempting to quantify the impact this simplest representation has on the BLI effects, by comparing the results to cases 1 and 2 respectively. From basic aerodynamics knowledge, and the results of experiment 2.3, the adverse characteristics of sharp corners in subsonic flows is well established. However, these cases can be considered as a reasonable lower bound in the scale of design detail, where any curvature enhances the level of detail. Cases 3 and 4 thus serve to establish how much a designer can get away with by making this crude approximation. If small, the need for determining the curvature is unnecessary in concept design, as this can be left as an OML refinement exercise in preliminary design. If large, a suitable middle ground needs to be found where defaulting such curvature has a minimal impact on the results. Fig. 5.43 compares the inlet geometries for each case.

5.9.2 Results and Discussion

Fig. 5.44 presents the differences in the BLI effects due to changes in the macro and detailed parameters. Blue bars denote changes due to the macro parameter, while gray bars depict the impact of perturbations to the detailed parameters. It is evident that the differences in all three BLI effects due to the change in the macro

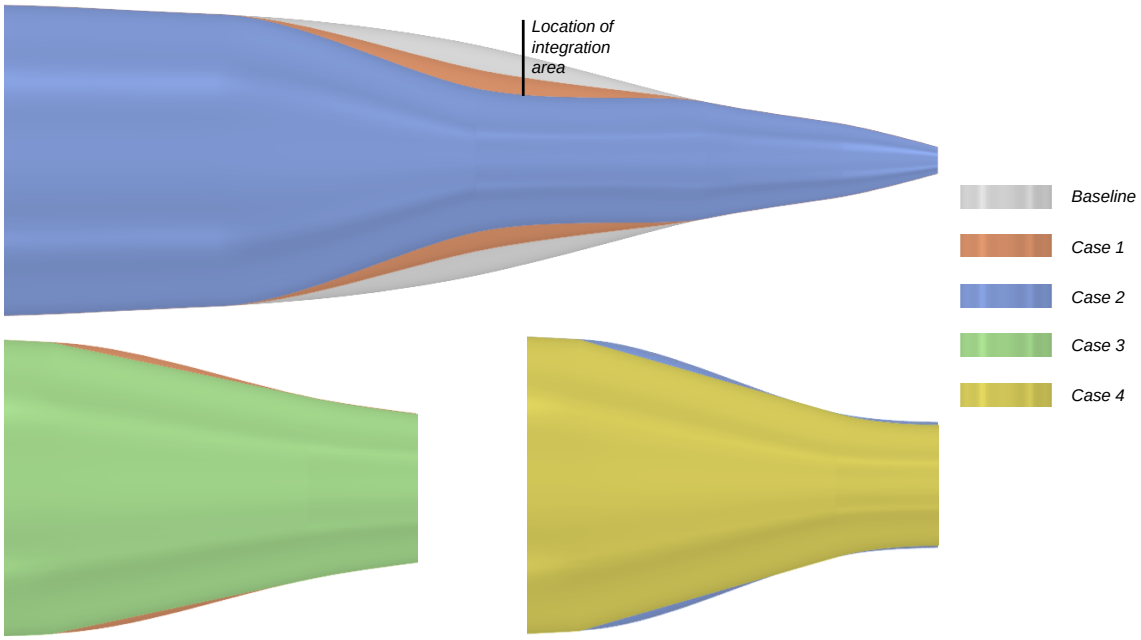

Figure 5.43: Experiment 2.8 - top view of inlet shapes. Integration area is located at the 0° circumferential station at 85% axial distance along the fuselage

parameter, $\Delta(\cdot)_{\mathrm{B}}^{\phi}$, are much larger than the differences due to the changes in the detailed parameters, $\Delta(\cdot)_{\mathrm{B}}^{\psi}$. The impact of the macro parameter change exceeds the critical thresholds, while the influence of the detailed parameters is below the critical thresholds. Table 5.9 highlights the relative impact of the macro parameters to the detailed parameters on the BLI effects by presenting values for $\frac{\Delta(\cdot)_{\mathrm{B}}^{\phi}}{\Delta(\cdot)_{\mathrm{B}}^{\psi}}$, based on the results shown in Fig. 5.44.

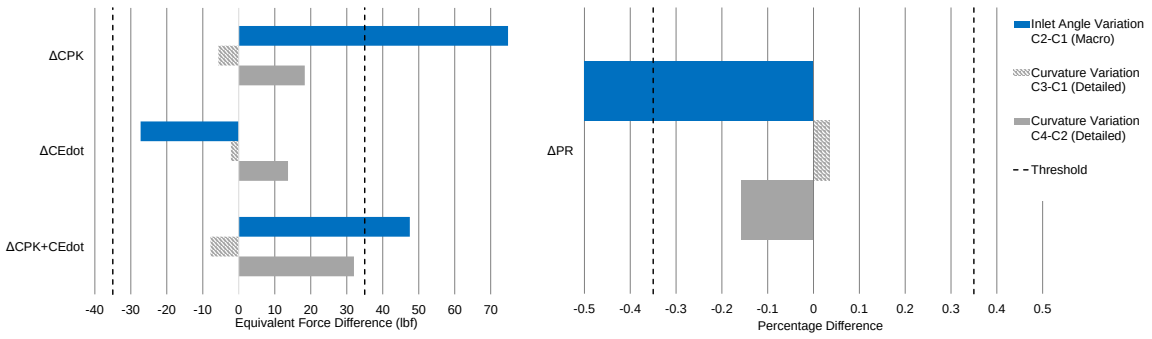

(a) Relative differences in $C_{P_{K_{\mathrm{in}}}}$ and $C_{\dot{E}}$ **(b)** Percentage difference in η_{PR}

Figure 5.44: Experiment 2.8 - differences in BLI effects from changes in inlet design

Table 5.9: Experiment 2.8 - Significance of Inlet Angle over Curvature

BLI Effect	$\frac{\Delta(\cdot)_B^\phi}{\Delta(\cdot)_B^\psi}$ Case 3-Case 1	$\frac{\Delta(\cdot)_B^\phi}{\Delta(\cdot)_B^\psi}$ Case 4-Case 2
$C_{P_{K_{in}}}$	13.1	4.1
$C_{\dot{E}}$	12.4	2.0
$C_{P_{K_{in}}} + C_{\dot{E}}$	6.0	1.5
η_{PR}	15.2	3.5

From the results, it appears that the significance of the inlet ramp curvature is dependent on the setting for the inlet ramp angle. For the ramp angle of 12°, the impact of curvature change (C3-C1) is minimal. For a steeper inlet ramp angle, the curvature influence on the BLI effects is more pronounced, albeit within the critical thresholds. Fig. 5.45 compares the Mach contours for each of the cases. Comparing case 1 to 3, one case see that switching to a sharp corner produces localized flow acceleration, consistent with observations from experiment 2.3. In this instance however, the impact on the boundary layer downstream is minimal, as seen in Fig. 5.46. Given the flow acceleration over the corner, the resulting boundary layer downstream

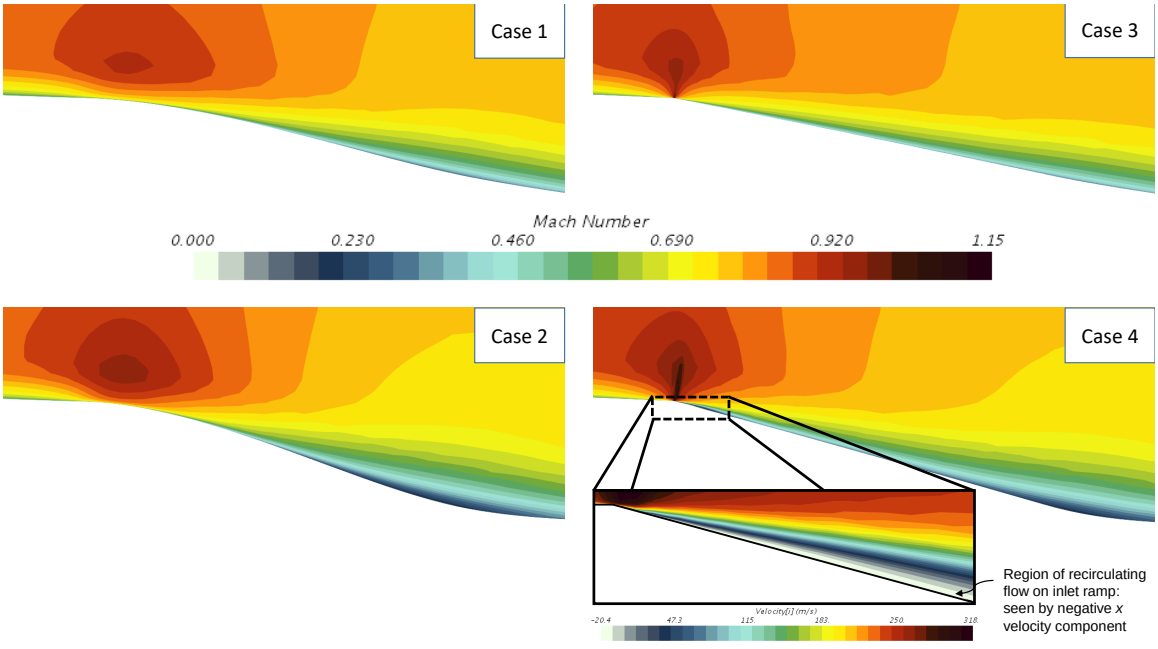

Figure 5.45: Experiment 2.8 - Mach contours at the inlet center-plane

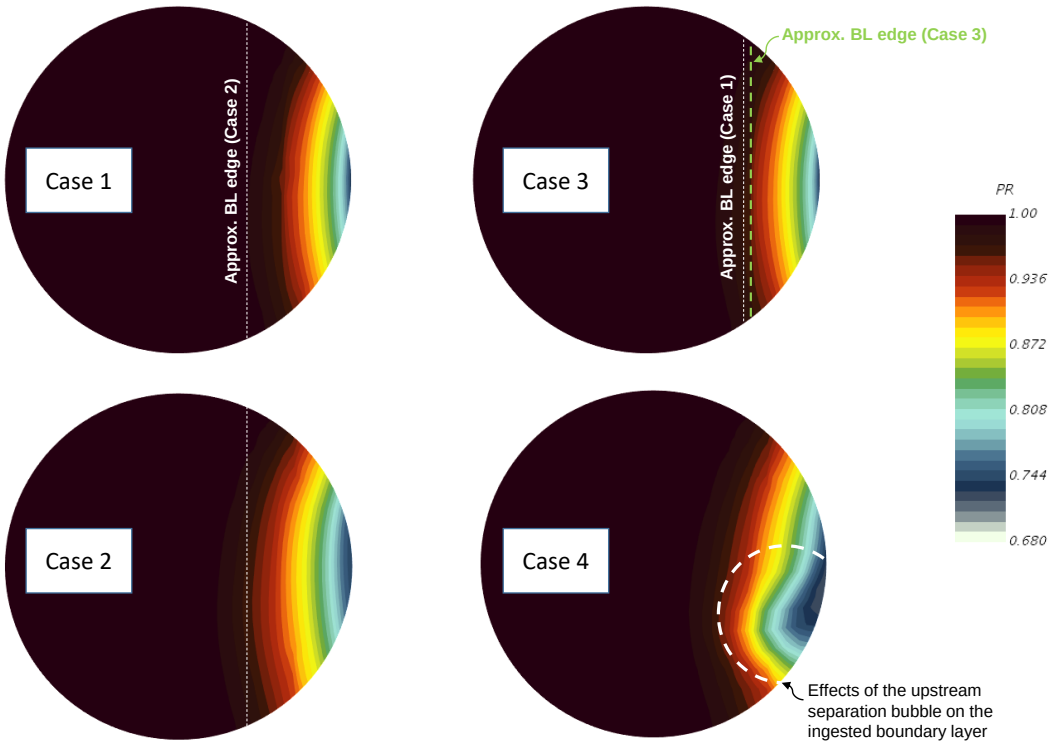

Figure 5.46: Experiment 2.8 - η_{PR} contours for the ingested boundary layer at 85% axial distance along the fuselage

is slightly thinner in case 3, accounting for the decrease in $C_{P_{K_{\text{in}}}}$ and $C_{\dot{E}}$ and increase in η_{PR} seen in Fig. 5.44. However, in case 4, a small separation bubble is formed just after the corner, highlighted in Fig. 5.45. This bubble alters the effective body shape seen by the flow and thus has a more noticeable impact on the ingested boundary layer downstream, as seen by the bulge in the η_{PR} contours for case 4 in Fig. 5.46. Also evident from the Mach and η_{PR} contours in Figs. 5.45 and 5.46 is the thicker boundary layer as a result of increasing the inlet ramp angle, which explains the increase in $C_{P_{K_{\text{in}}}}$ and decrease in η_{PR} in case 2 relative to case 1.

The results above support hypothesis 2, highlighting that as long as the detailed parameters do not cause adverse flow features like separation, these parameters can be defaulted to reasonable values for conceptual design. In this instance, the macro parameters play a more significant role. However, the importance of the detailed variables is not diminished, given that arbitrary settings can cause adverse flow effects.

These values need to be defined based on the macro parameter setting. For smaller inlet angles, the concept designer can likely get away with a simple linear ramp in the CFD geometry model. For larger ramp angles, however, this approximation may result in more substantial discrepancies in the BLI effects estimates relative to the results that are expected at the end of the preliminary design stage refinement. Recognizing that the inlet ramp OML will be subject to optimization in the later stages of design, it is recommended that the concept designer focus on the inlet ramp angle. The skinning angles should be set to some reasonable value such that no excessive separation is observed at the design conditions at which the BLI effects surrogate models will be generated. While this curvature may not be optimal, the results above suggest that the discrepancy between the concept design model and the optimized design will be small, as long as the macro parameter is the same. If the inlet ramp angle is not known, it is recommended that this value be varied within an expected range as part of the surrogate model generation process.

5.10 Concluding Remarks

An integral part of the proposed BLI concept design methodology is the formulation of surrogate models of the BLI effects as a function of airframe geometry. However, as discussed in chapter 3, general comments on the sensitivity of the boundary layer properties to the airframe design could not be found in the reviewed literature. As such, the second research question was posed regarding what features of the airframe design needed to be considered as part of this surrogate modeling process and which ones could be defaulted. Based on theoretical considerations covered in chapter 3, a hypothesis was formed, which can be broken down into three main points:

(1) The engine axial and circumferential location on the fuselage plays a role in determining how much a given design feature contributes to the BLI effects measured at that location. To elaborate:

(i) Small perturbations to the flow (no shocks/separation), as a result of modifications to the geometry, decay along the axial distance in the zone of influence. In other words, small flow perturbations are local effects.

(ii) The wing impact on the BLI effects varies based on the circumferential location of the engine

(2) The BLI effects are more sensitive to changes in the macro parameters of airframe, in general, than to changes in the detailed parameters. This aspect is tied to the condition that no shocks or flow separation results from these changes in detailed variables. Such adverse flow characteristics have a global influence on the BLI effects.

(3) Any variable present in the inactive variable space need not be considered in the surrogate model formulation. Additionally, detailed parameters that fall in the active variable space may also be defaulted to reasonable settings in concept design, under certain guidelines. The resulting difference in BLI effects estimates is smaller than the discrepancy caused by defaulting an active macro variable, under the assumption that point 2 above is true.

A series of experiments was designed to test the different aspects of hypothesis 2. Selected results from these experiments are summarized in Figs. 5.47, 5.48, and 5.49, highlighting visually how the results support the hypothesis. These figures show the absolute values of the differences in the BLI effects for a given experiment, against the appropriate baseline defined for that case. The engine locations A0.90C0/90, A0.95C0/90 and A1.00, at which these results are presented, correspond to likely positions of a BLI propulsor. Colored bars are used to depict the active variable sets, while gray bars represent the inactive variables, determined based on the critical threshold. Detailed parameters (D) are shown using red bars, while macro parameters (M) are in black. The wing and vertical tail cases only show the reference wing/tail

results, for brevity, and are thus colored both red and black. Any case that produces an adverse flow feature is highlighted with an asterisk (D*/M*).

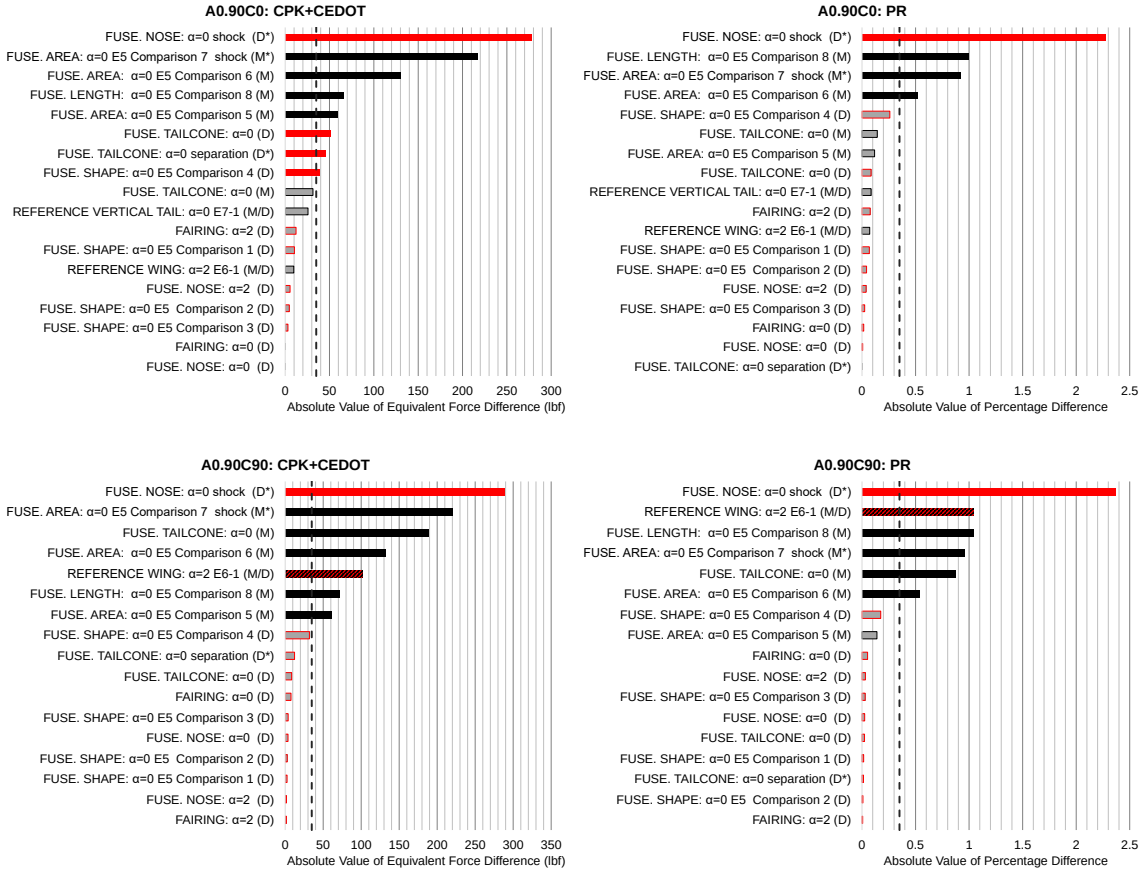

Figure 5.47: Summary of selected results at the A0.90C0 and A0.90C90 stations

Results from experiment 2.2 support points 1.i, 2 and 3. The nose geometry parameters feature in the inactive variable set for a shock free perturbation of the nose. However, when the detailed parameters are defaulted to values that produced a shock, the impact of this large perturbation is felt at all axial stations. Experiment 2.3 verifies points 2 and 3. The tail closure and upsweep angles have a stronger impact on the BLI effects than the changes in curvature between the tail cone and center-body. Point 1.i is largely supported by the results from experiment 2.4, with the exception of the case at $\alpha = 2°$, where the results at A1.00 exceeded the threshold.

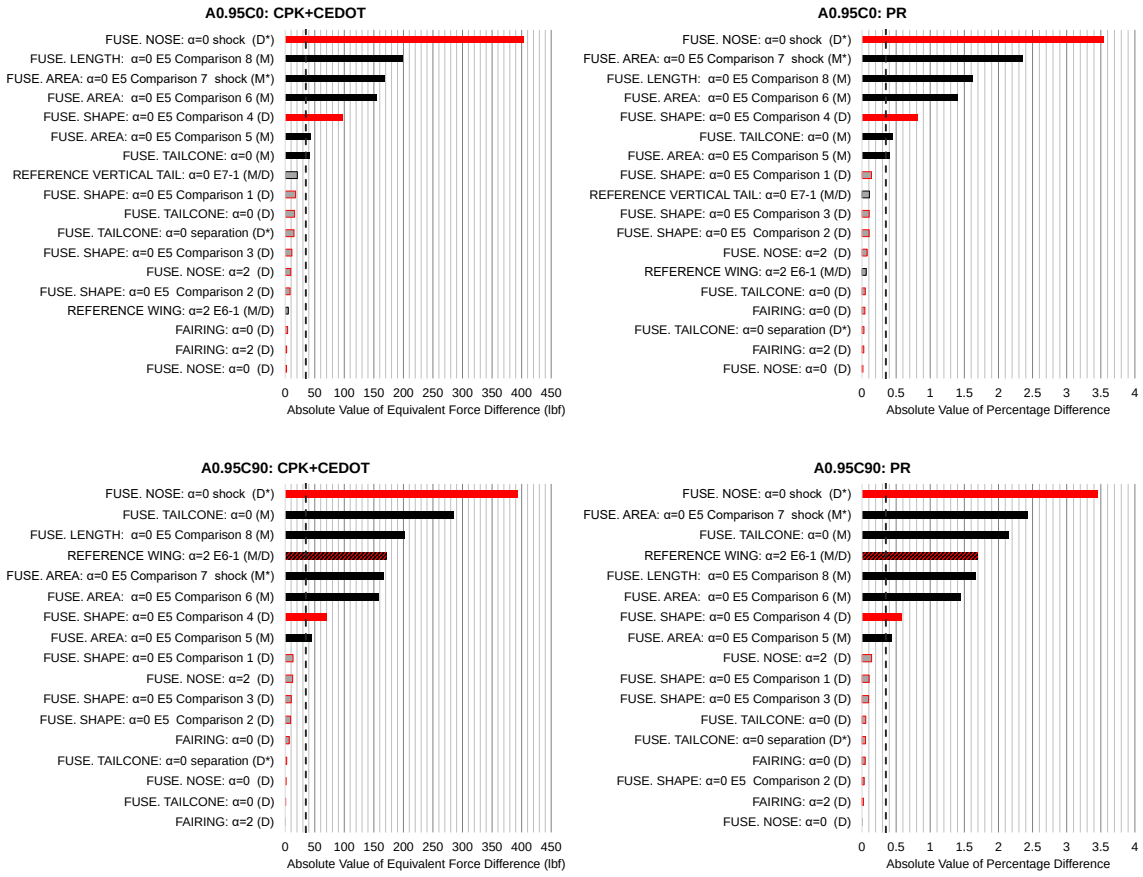

Figure 5.48: Summary of selected results at the A0.95C0 and A0.95C90 stations

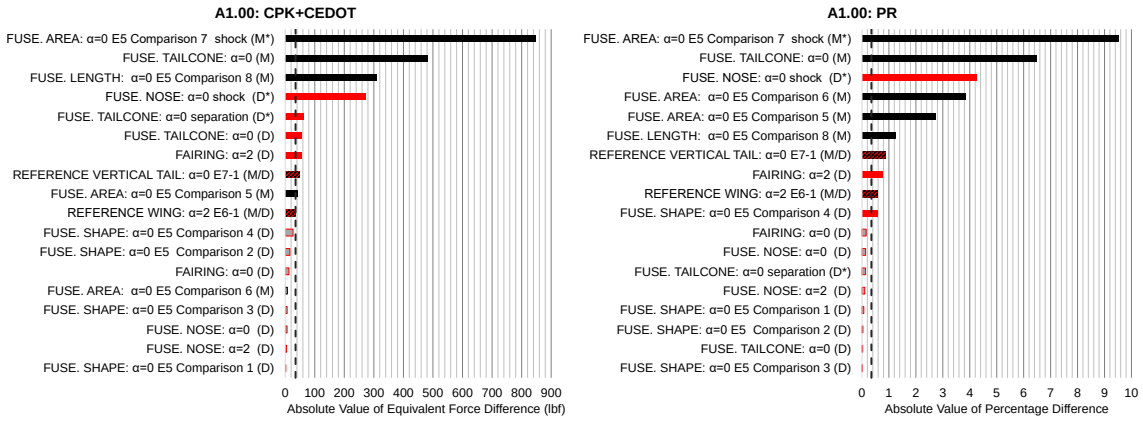

Figure 5.49: Summary of selected results at the A1.00 station

Changes to the fuselage shape, in experiment 2.5, are found to have a smaller impact in general, than modifications to the fuselage length and cross sectional area, supporting

points 2 and 3. The circular approximation for the D8 cross section is an example of when the fuselage shape variables fall under the active space, however, the differences observed, as explained before, are actually related to the macro parameters of the tail cone. Results from experiment 2.6 clearly highlight point 1.ii, where a distinct variation in the BLI effects is noticed based on engine location. A consequence of this trend is that when designing concepts with side mounted engines, the penalty of neglecting the wing in the geometry model is much smaller than for concepts with engine locations similar to the D8 and the STARC-ABL. With regards to the detailed and macro parameters of the wing, results at some engine locations support point 2, but for others such as at A1.00, sensitivity of the BLI effects to the two variable classes is comparable. For vertical tail, the results support points 2 and 3, highlighting that variations in the airfoil definition are less significant than the changes in other macro parameters. Thus, the airfoils can be defaulted for a smaller design space. Lastly, results from experiment 2.8 show that the inlet angle has a more significant impact than the detailed skinning angles, verifying points 2 and 3. In summary, the experiments answer research question 2, filling the void in literature by identifying the critical airframe design space and showing how it changes based on the engine location, for tube and wing BLI concepts.

CHAPTER 6
BLI EFFECTS SENSITIVITY TO PROPULSOR

Continuing in the same vein as the previous experiments, this chapter focuses on the impacts of propulsor on-design and off-design characteristics on the BLI effects. Specifically, the influence of changes to the fan size and mass flow rate requirements on the BLI effects is investigated. Significant variations in the BLI effects due to changes in fan size places greater emphasis on the optimal selection of engine variables like fan hub to tip ratio, fan blade technology captured in terms of design specific flow, and design FPR, relative to conventional podded engine design. These variables influence the BLI effects through their impact on fan size, which in turn affects the fuel requirements and thus airframe sizing for a given mission. Unlike conventional aircraft with podded engines, where these design parameters can be set independently from the airframe, for embedded engine concepts where the BLI effects show significant sensitivity to fan size, this decoupled approach is no longer feasible. Sensitivity of the BLI effects to engine mass flow rate requirements, on the other hand, also affects fuel weight requirements given variations in engine fuel burn at different points in the mission profile. As such, throttle dependency now needs to be considered as part of the surrogate model input variable space for the BLI effects.

Quantifying the sensitivity of the BLI effects to the propulsor establishes the extent of the engine's contribution to the aero-propulsive coupling, and thus to the overall vehicle design and performance. The experiments presented in this chapter shed light on the sensitivities, highlighting the physics behind the trends observed. The experimental results are used to evaluate the validity of hypothesis 3, which is expanded on in the following section. After this, some comments on the experimental setup are provided, and then the experimental procedure and results are discussed.

6.1 Revisiting Hypothesis 3

For the experiments relating to research question 3, the BLI effects considered are the main performance drivers: $C_{P_{K_{\text{in}}}}$ and η_{PR}. As discussed in chapters 4 and 5, the proposed approach for estimating the change in wake dissipation is an engineering approximation based on analysis of an un-powered configuration in CFD. Thus, $C_{\dot{E}}$ trends are not considered for this set of experiments, where a powered engine is modeled. In chapter 3, an initial hypothesis was posed that related ingested streamtube properties like pressure, velocity, wall shear, and capture area to changes in fan size and required flow rate. This hypothesis is repeated below for convenience:

> **Initial Hypothesis 3:** Fan size and mass flow rate requirements are the main engine on-design and off-design factors that influence the BLI effects. If the fan size is changed for a given flow rate requirement, the pressure gradient imposed on the ingested flow will exhibit a positive correlation with this change, while the inflow velocity and wall shear will exhibit a negative correlation, as dictated by the conservation laws. The ratio of clean to boundary layer flow in the ingested streamtube will also show a positive correlation with fan size. On the other hand, if the required flow rate is adjusted for a given fan size, the correlations for pressure gradient, inflow velocity, and wall shear are now opposite. In addition, the streamtube capture area will positively correlate with required inflow.

The purpose of this section is to map the hypothesized trends in flow properties to trends in the BLI effects with propulsor design and operation.

6.1.1 Trends in η_{PR}

Pressure recovery is a metric quantifying the total pressure losses in the ingested flow. An increase in wall shear stress, or sources of high vorticity like shocks or recirculating flow in separation bubbles, result in a loss in total pressure and thus η_{PR}.

The total pressure in the flow increases moving further away from the wall, and is thus typically lower in the boundary layer than in the freestream, assuming no shocks. Since an increase in flow rate ($\dot{m}$), for a given fan annulus area (A_2), increases the wall shear as discussed before, it can be hypothesized that η_{PR} negatively correlates with $\dot{m}$, assuming no flow separation at the measurement plane at which this metric is evaluated. With A_2, for a fixed $\dot{m}$ requirement, given that a larger propulsor ingests a bigger fraction of flow at a high total pressure, and that the inflow velocity is slower (lower wall shear stress), the averaged total pressure is expected to be higher. Thus, it is expected that η_{PR} shows a positive correlation with A_2.

6.1.2 Trends in $C_{P_{K_{\text{in}}}}$

To understand how $C_{P_{K_{\text{in}}}}$ behaves, it is instructive to consider the two contributing sources to $C_{P_{K_{\text{in}}}}$. Recall from chapter 5 that $C_{P_{K_{\text{in}}}}$ quantifies the ingested kinetic energy thickness and the pressure-velocity component of the ingested flow. These terms are highlighted in Eq. (5.1) in chapter 5, repeated here for convenience:

$$C_{P_{K_{\text{in}}}} = \iint \left[\frac{\rho_i V_i}{\rho_\infty V_\infty} \left(1 - \frac{V_i^2}{V_\infty^2} \right) - C_{p_i} \frac{V_i}{V_\infty} \right] \frac{dS_i}{S_{\text{ref}}} \tag{5.1}$$

where i is the measurement station number at which this integral is evaluated, which for the following experiments is 1 for the inlet highlight or 2 for the fan face. The $C_{P_{K_{\text{in}}}}$ integrand has the form of a polynomial as follows:

$$Ax(1-x^2) - Bx \;\text{ where }\; x \equiv \frac{V_i}{V_\infty};\;\; A \equiv \frac{\rho_i}{\rho_\infty} = f(x) \;\text{ and }\; B \equiv C_{p_i} \tag{6.1}$$

Eq. (6.1) is a non-monotonic function in the domain $0 \leq x \leq \mathcal{C}$ where $\mathcal{C}$ is a value typically $\mathcal{O}(10^{-1})$. This function is shown notionally in Fig. 6.1. Low values of x correspond to points closer to a wall, within the ingested boundary layer, while higher values of x are typically found away from a wall. The highest velocity ratio at some

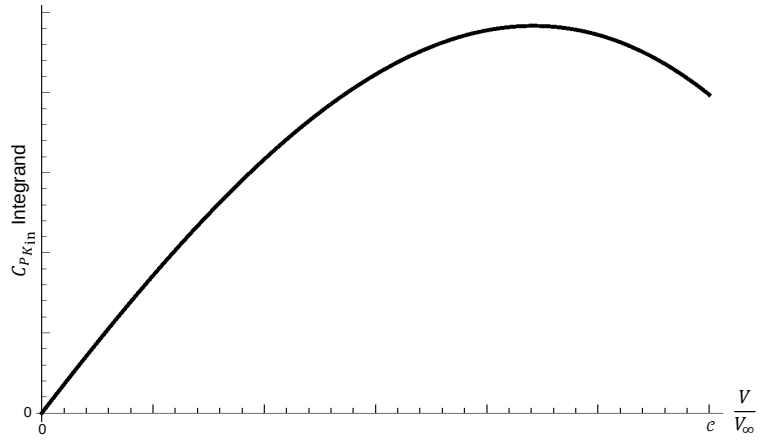

Figure 6.1: Notional plot showing how $C_{P_{K_{\text{in}}}}$ varies with $\frac{V_i}{V_\infty}$

point on the integration surface can be $\mathcal{O}(1)$ outside the ingested boundary layer, for very high required $\dot{m}$. Note that for a uniform boundary condition propulsor model in CFD, the pressure coefficient (C_{p_2}) is at the same value at all points on the fan annulus, for a given $\dot{m}$. How $C_{P_{K_{\text{in}}}}$ varies depends on the rate at which the ingested KE-thickness changes with $\dot{m}$ and A_2, relative to the pressure-velocity component. Given that the ingested KE-thickness component is proportional to $\left(\frac{V_i}{V_\infty}\right)^3$ (not including the density dependence on velocity), it is expected that this term dominates in most instances. Pressure effects would have a stronger influence on $C_{P_{K_{\text{in}}}}$ trends for very low or very high $\dot{m}$, where flow separation or shocks are likely to occur in the ingested streamtube.

If there is significant BLI with a large portion of the boundary layer falling within the linear region of Fig. 6.1, then it can be hypothesized based on the functional form of $C_{P_{K_{\text{in}}}}$, the hypothesized significance of the ingested KE-thickness component, and the correlations of pressure, velocity, and mass flux (ρV) with $\dot{m}$, that an increase in $\dot{m}$ will result in an increase in $C_{P_{K_{\text{in}}}}$. However, if the ingested boundary layer covers only a small fraction of the integration plane, then most of the integration plane sees a relatively higher $\frac{V_i}{V_\infty}$. Given the higher order effects of velocity on $C_{P_{K_{\text{in}}}}$, it is expected that for cases with low BLI, an increase in $\dot{m}$ will result in a decrease in $C_{P_{K_{\text{in}}}}$, driven

by the decrease in the ingested KE-thickness component. With respect to A_2, for a given $\dot{m}$, an increase in A_2 is expected to shift most points on the integration area further to the left in Fig. 6.1, from conservation of mass, which is expected to have a favorable impact on the KE-thickness and thus $C_{P_{K_{\text{in}}}}$. Note, this discussion assumes no shocks or separation in the ingested streamtube.

6.1.3 Synthesis

The discussions above can be synthesized into a refined hypothesis, *contingent upon the absence of shocks and separation in the ingested streamtube*, as follows:

> **Hypothesis 3:** Fan size and mass flow rate requirements are the main engine on-design and off-design factors that influence the BLI effects. Due to expected changes in inflow velocity, wall shear, and ingested boundary layer fraction with a change in A_2 or $\dot{m}$, η_{PR} will exhibit a negative correlation with $\dot{m}$, and with $C_{P_{K_{\text{in}}}}$, will positively correlate with A_2. If the ingested boundary layer fraction is small, $C_{P_{K_{\text{in}}}}$ will correlate negatively with $\dot{m}$, otherwise, a positive correlation is expected. These differences are due to non-linear dependence of $C_{P_{K_{\text{in}}}}$ on velocity.

6.2 Experimental Notes

6.2.1 General Comments

Two types of propulsor locations are considered for these experiments based on the circumferential extent of ingested boundary layer flow. For both the D8 and the NOVA BLI, the ingested boundary layer extent is similar to that shown in Fig. 6.2a, even though the position and orientation of the engine relative to the fuselage is different between the concepts. Here, the lower portion of the fan ingests the airframe boundary layer, in addition to the boundary layer formed on the nacelle wall and spinner. While the side mounted engine geometry is used in Experiment 3.1, it is

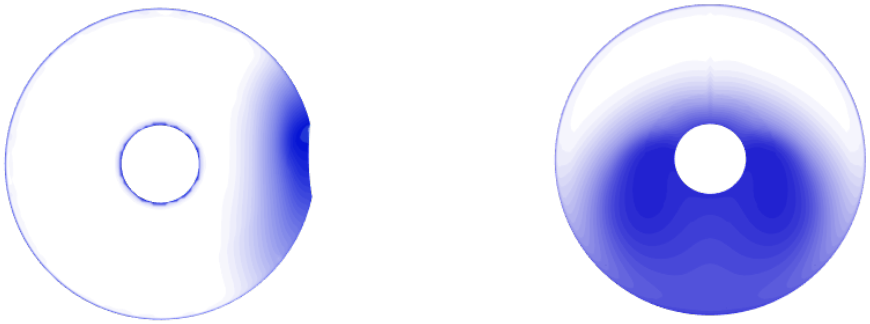

(a) CASE A BLI: Ingested boundary layer extent similar to the NOVA-BLI (as shown) and D8 (rotate clockwise 90°)

(b) CASE B BLI: Ingested boundary layer extent similar to the STARC-ABL

Figure 6.2: Engine locations considered for experiment 3 based on circumferential extent of ingested boundary layer

expected that the trends observed are also valid for a top mounted engine like on the D8. In experiment 3.2, a fuselage trailing edge mounted propulsor like on the STARC-ABL is considered. As shown in Fig. 6.2b, the entire circumferential boundary layer extent on the fan annulus is primarily due to the airframe boundary layer (excluding the nacelle wall boundary layer). The objective behind considering these two distinct cases is to assess whether the trends observed for one are consistent with the other, or whether the extent of ingested boundary layer plays a role in affecting the sensitivities as hypothesized.

Note that the scope of this study, like before, is restricted to analysis of engines on concepts similar to the D8, NOVA-BLI, and the STARC-ABL. The fuselage geometries used in experiment 3.1 and 3.2 are slightly modified versions of those used in experiments 2.8 and 2.3 respectively, sized similar to the 737-8 in the 150-180 pax class. All experiments are conducted at the cruise condition of $M_\infty = 0.8$, altitude = 35,000ft, and $\alpha = 0°$, except two trials for experiment 3.1, which are conducted at takeoff conditions. The BLI effects, $C_{P_{K_{\text{in}}}}$ and η_{PR}, are evaluated at both the fan face (station 2) and the inlet highlight plane (station 1) such that contributions from the airframe and nacelle can be isolated. The reference area S_{ref} is set to 1.

6.2.2 Development of Propulsor Model

The propulsor geometries used in the experiments are derived from the same initial geometry. The performance and design of this reference engine is obtained from NPSS and WATE++ respectively. This reference propulsor is a modified version of a notional LEAP-1B engine that was used for generating the significance difference criterion data in Fig. 5.5. The thrust required and pressure recovery are modified for the engine, based on estimates of the BLI effects obtained from experiment 2.8-2. The dimensions of the reference engine are shown in Fig. 6.3. When changing the area of the propulsor in the experiments, only the fan tip and hub diameters are varied, keeping the same hub to tip ratio of 0.25. The inlet and total nacelle length, and the contouring of the nacelle is unchanged. Note the absence of a core or plug model in the geometry.

In this study, the flow downstream of the fan is of no interest because metrics like fan exit mass flow, or net axial force for example are not being computed in CFD. The BLI effects are only dependent on the ingested flow, which does not depend on the geometry and boundary conditions downstream of the fan face *in the CFD*

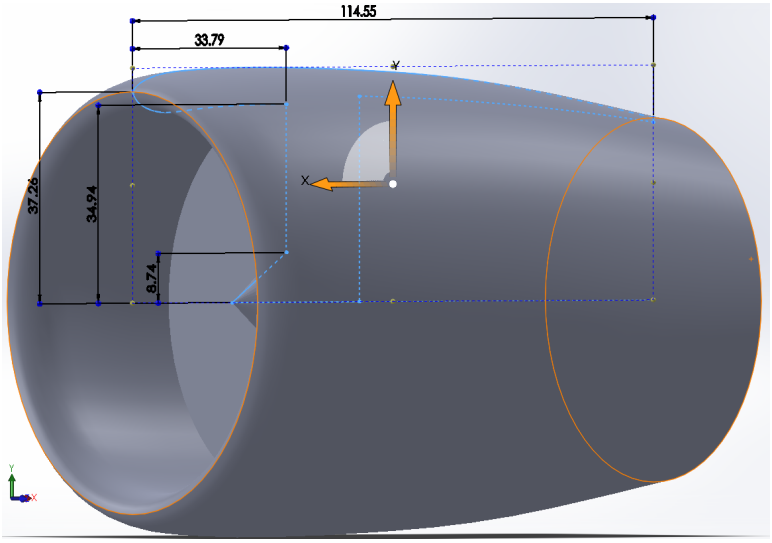

Figure 6.3: Reference engine geometry (dimensions in inches)

domain. Thus, the core and plug geometries can be excluded from the CFD model of the propulsor, thereby eliminating the need to carefully design these components, while also reducing the mesh size and overall computational expense. Recall, a 1D powered boundary condition representation of the engine is used in CFD. Uniform static pressure and temperature boundary conditions are applied to the fan face, and the static pressure is varied in CFD till the desired mass flow rate target is achieved.

6.2.3 Mesh Sensitivity Study

A mesh sensitivity study is conducted to find an appropriately sized grid for the experiments. The aircraft configuration tested in experiment 3.1, shown in Fig. 6.5, is used for this study. The propulsor is sized as shown in Fig. 6.3 while the fuselage geometry from experiment 2.8-2 is modified downstream of the 90% axial station to embed the nacelle. The optimal mesh settings found from this study are used for all cases in experiments 3.1 and 3.2. An unstructured Cartesian mesh is used like before, and the boundary conditions at the fan face and exit are kept the same for each case. Steady state conditions are assumed. The BLI effects and mass flow rate measured at the fan face are tracked across the cases. Results for $C_{P_{K_{\text{in}}}}$ and η_{PR} are shown in Fig. 6.4a, and for $\dot{m}_2$ in Fig. 6.4b. The final mesh chosen is indicated by a filled marker and contains approximately 6 million cells.

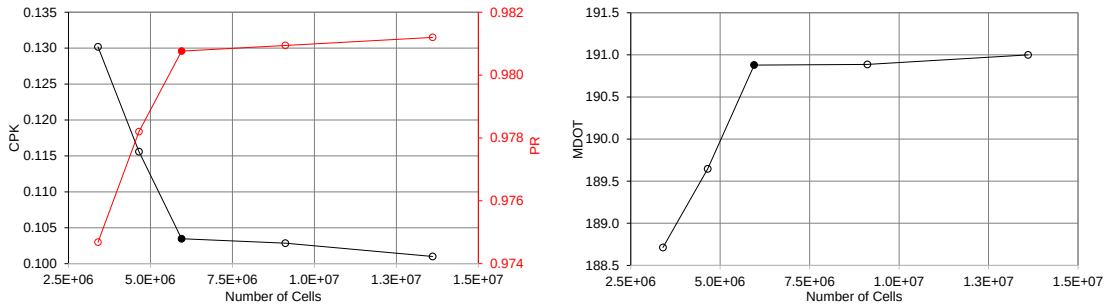

(a) $C_{P_{K_{\text{in}}}}$ and η_{PR} **(b)** $\dot{m}$

Figure 6.4: Summary of results from mesh sensitivity trials

6.3 Experiment 3.1: Case A Boundary Layer Ingestion

6.3.1 Experimental Overview

This set of experiments is conducted for an engine ingesting a boundary layer with a pattern similar to that shown in Fig. 6.2a. The engine is mounted to the side of the airframe, as shown in Fig. 6.5, with the fan face located at the 90% axial station along the fuselage. A structured design of experiments is created, where the same sweep in mass flow rate is considered for three fan diameters. A variation in fan diameter accounts for engine on-design impacts on the BLI effects. A change in mass flow rate required, for a fixed fan diameter, accounts for throttle effects in engine off-design conditions. An overview of the cases run is presented in Table 6.1.

Figure 6.5: Experiment 3.1 - engine location

As part of this propulsor size and operation exploration study, a wide enough, yet reasonable range is considered for the fan diameter and flow rate. The smallest propulsor size is obtained as discussed in the previous section. The largest fan di-

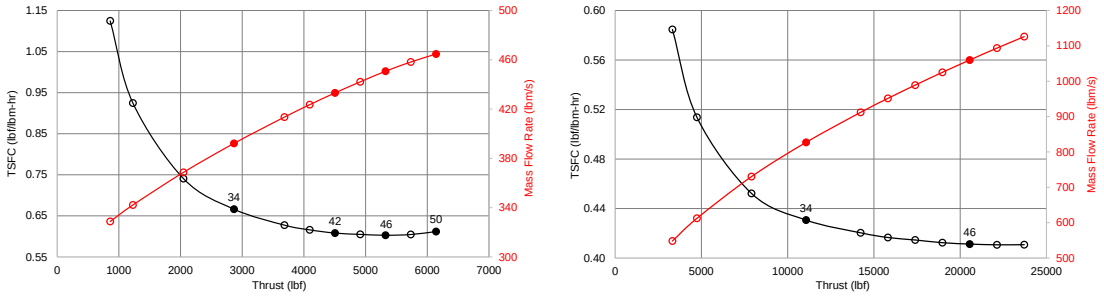

(a) At cruise conditions **(b)** At takeoff conditions

Figure 6.6: Powerhooks for the reference propulsor at cruise and takeoff conditions

Table 6.1: Experiment 3.1 - Overview of Cases

Experiment	d_2 (in)	A_2 (ft^2)	Target $\dot{m}_2$ (lbm/s)
3.1-1	69.9	24.97	452
3.1-2	69.9	24.97	434
3.1-3	69.9	24.97	393
3.1-4	77	30.32	466
3.1-5	77	30.32	452
3.1-6	77	30.32	434
3.1-7	77	30.32	393
3.1-8	85	36.94	466
3.1-9	85	36.94	452
3.1-10	85	36.94	434
3.1-11	85	36.94	393
3.1-12*	85	36.94	1060
3.1-13*	85	36.94	827

*Conducted at $M_\infty = 0.25$ Alt = SL

ameter is modeled off the NOVA-BLI [101]. The 77in fan diameter is considered as a center point case. Note that the fan sizes proposed for the D8, at 72in [59], and the STARC-ABL at 81in [98] are within this range. The required mass flow rates are obtained from the powerhooks generated by NPSS for the reference propulsor model, shown in Fig. 6.6a, with the selected points shown using filled markers. The numbers above the points represent the power code corresponding to that operating point, and are included for reference. These flow rates cover potential points that are expected to be encountered in typical cruise conditions, with a small buffer. Low throttle and flight idle settings are ignored since insufficient power is produced for cruise. In addition to the cases considered at cruise, two additional data points are investigated for the largest fan at takeoff conditions, shown in Fig. 6.6b. These points were analyzed after the cruise condition results were obtained to determine whether the observed trends changed at a different flight and engine operating condition.

6.3.2 Results and Discussion

Variation of $C_{P_{K_{\text{in}}}}$ with A_2 and $\dot{m}_2$

Fig. 6.7a shows how $C_{P_{K_{\text{in}}}}$, measured at the fan face, varies as a function of the fan annulus area A_2 for a constant $\dot{m}_2$ requirement. The $\dot{m}_2$ curves are colored blue to red indicating different values of the flow rate. The same data are plotted in Fig. 6.7b

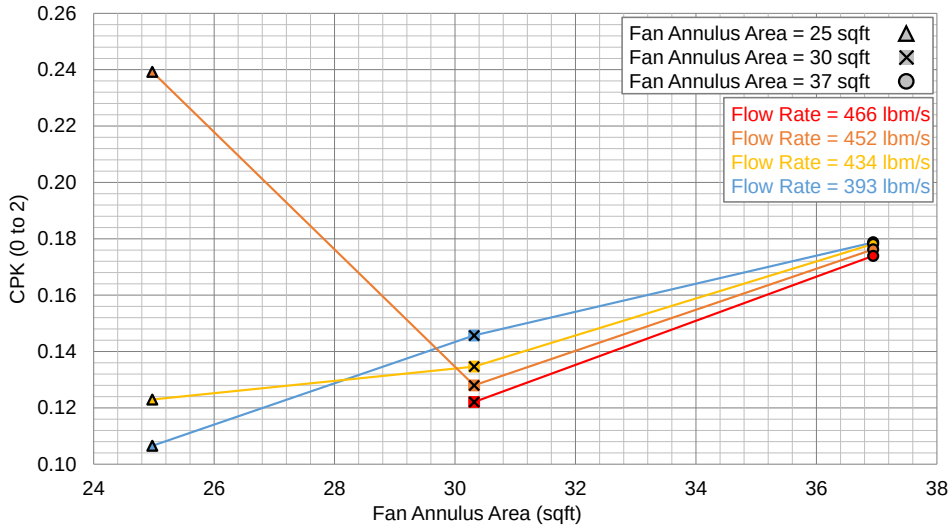

(a) $C_{P_{K_{\text{in}}}}$ variation with A_2 for different $\dot{m}_2$

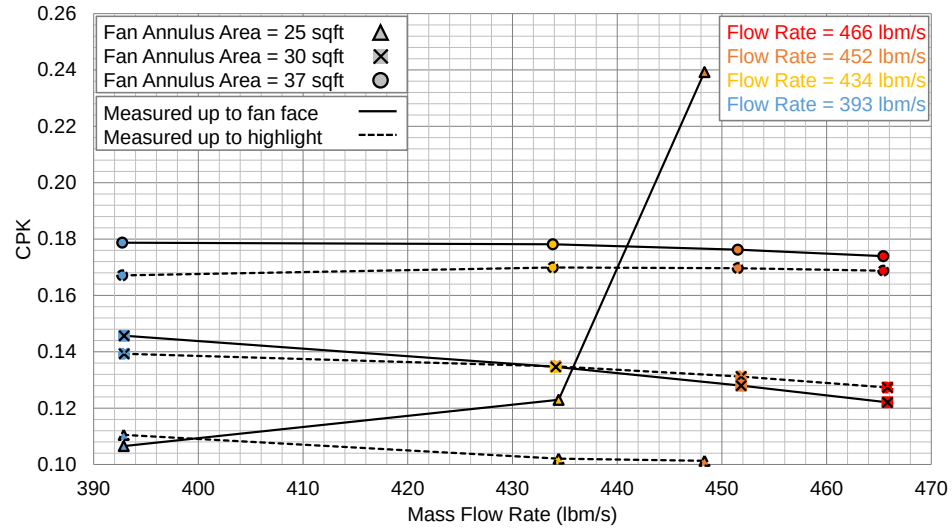

(b) $C_{P_{K_{\text{in}}}}$ variation with $\dot{m}_2$ for different A_2

Figure 6.7: Experiment 3.1 - variation of $C_{P_{K_{\text{in}}}}$ as a function of A_2 and $\dot{m}_2$

to clearly illustrate how $C_{P_{K_{\text{in}}}}$ trends with $\dot{m}_2$ for a fixed A_2. In this figure, different marker shapes are used to denote the three propulsor sizes considered. Solid lines denote trends for $C_{P_{K_{\text{in}}}}$ measured at the fan face, while dashed lines represent trends of $C_{P_{K_{\text{in}}}}$ measured at a plane slightly offset from the inlet highlight (not shown in Fig. 6.7a). The latter results quantify the airframe contribution to $C_{P_{K_{\text{in}}}}$ and how that varies with propulsor operation. The difference between the solid and dashed curves indicates the effective contribution of the inlet to $C_{P_{K_{\text{in}}}}$. In general, $C_{P_{K_{\text{in}}}}$ exhibits a positive correlation with respect to A_2 and negative with $\dot{m}_2$, as hypothesized, with two exceptions where shocks are seen in the inlet, which will be discussed shortly.

The contributions to $C_{P_{K_{\text{in}}}}$ are plotted in Figs. 6.8a and 6.8b corresponding to the perspectives shown in Figs. 6.7a and 6.7b respectively. Solid bars are used to represent the KE-thickness component, while hatched bars denote the pressure-velocity contribution. The net result is a subtraction of the pressure-velocity contribution from the KE-thickness as shown in Eq. (5.1). As the fan size increases, for a given $\dot{m}_2$ requirement, the ingested KE-thickness component increases given that the inflow velocity reduces, and thus the difference between the ingested velocity and freestream increases. There is a negative correlation between static pressure and velocity such that $C_{p_i} = \frac{p_i - p_\infty}{\frac{1}{2}\rho_\infty V_\infty^2}$ in Eq. (5.1) increases with a decrease in inflow velocity (Fig. B.2 in Appendix B). Note, for most cases, the static pressure at the fan face is higher than ambient ($p_2 > p_\infty$). Thus, C_{p_i} is usually positive and $C_{p_i}\frac{V_i}{V_\infty}$ *offsets* the kinetic energy defect component when subtracted from it in Eq. (5.1). But, as C_{p_i} increases, the value of $\frac{V_i}{V_\infty}$ decreases such that the rate of increase in $C_{p_i}\frac{V_i}{V_\infty}$ is smaller than the rate of increase in the KE-thickness component. Given the dominance of the latter term, the net effect is an increase in $C_{P_{K_{\text{in}}}}$ with A_2 as hypothesized. Similar reasoning that relates changes in C_{p_i} and KE-thickness to $\frac{V_i}{V_\infty}$ can be applied to explain the trends with $\dot{m}_2$, recognizing that the average velocity ratio must increase with $\dot{m}_2$, for a fixed A_2. These trends are also consistent with hypothesis 3.

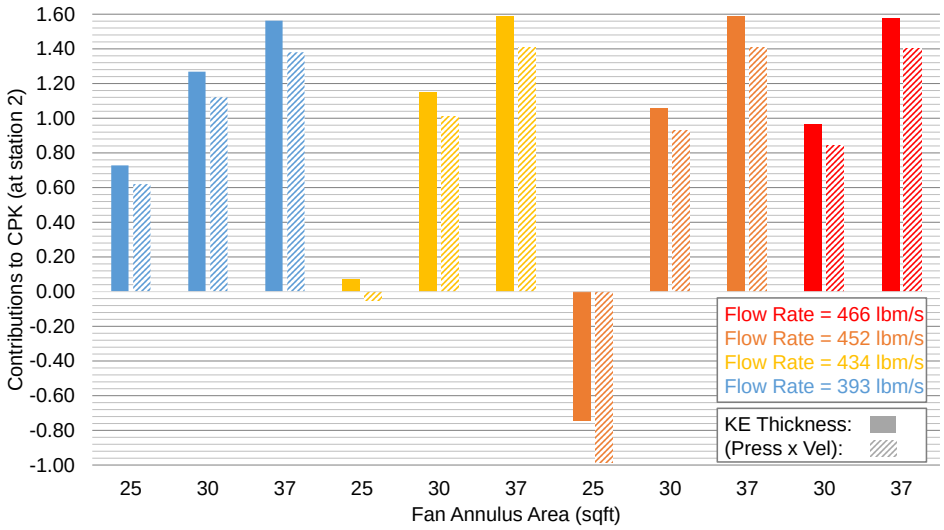

(a) Kinetic energy thickness and pressure-velocity contributions to $C_{P_{K_{\text{in}}}}$ varying with A_2 for different $\dot{m}_2$

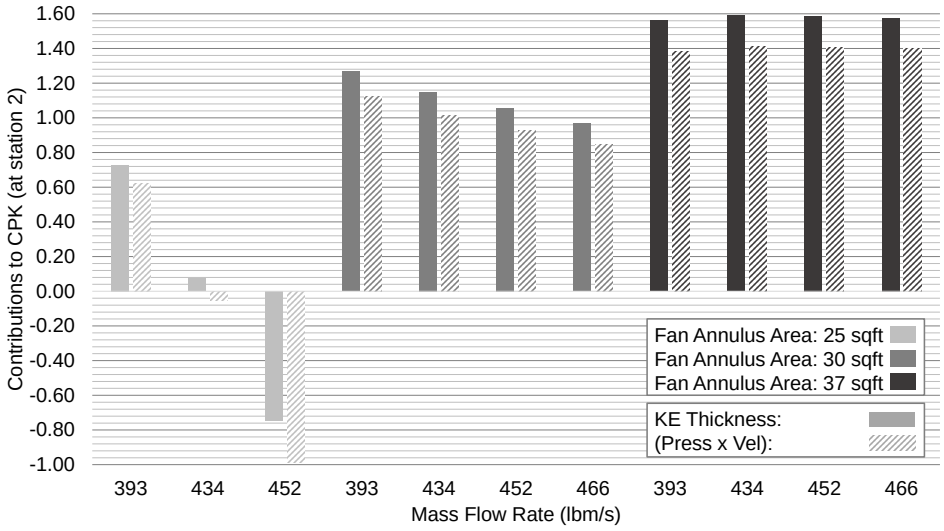

(b) Kinetic energy thickness and pressure-velocity contributions to $C_{P_{K_{\text{in}}}}$ varying with $\dot{m}_2$ for different A_2

Figure 6.8: Experiment 3.1 - variation of kinetic energy thickness and pressure-velocity contributions to $C_{P_{K_{\text{in}}}}$ as a function of A_2 and $\dot{m}_2$. The net result is a subtraction of the pressure velocity from the kinetic energy thickness component

Fig. 6.9 shows how the KE-thickness *integrand* in Eq. (5.1) varies as a function of *average* ingested velocity ratio $\frac{V_i}{V_\infty}$. Moving right on the x axis thus corresponds to an increase in $\dot{m}_2$ or a decrease in A_2. The average density ratio decreases with average velocity ratio (Fig. B.1 in Appendix B) and this trend is used to generate the curve

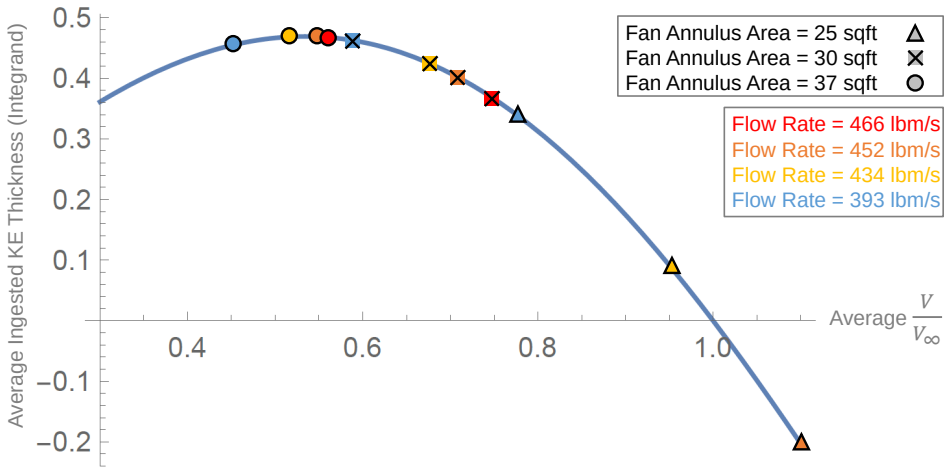

Figure 6.9: Experiment 3.1 - variation of average ingested kinetic energy thickness (integrand in Eq. (5.1)) with average ingested velocity ratio, measured at the fan face

shown in Fig. 6.9. The average velocity ratio is computed for each of the CFD cases at cruise and these points are overlaid on this curve. Note the three distinct clusters of points, corresponding to the three propulsor sizes investigated. The distribution of points within these clusters, based on the value of $\dot{m}_2$ they correspond to, and the relative location of these clusters to each other on the curve, matches the KE-thickness trends seen in Fig. 6.8, supporting the theoretical reasoning behind hypothesis 3.

However, the observation concerning the sensitivity of $C_{P_{K_{\text{in}}}}$ to $\dot{m}_2$ being dependent on the fan size, evident from Fig. 6.7, warrants further examination. This observation can be explained by comparing the streamtube captured by two propulsors of different sizes, shown in Fig. 6.10. In this top-view of the propulsor-airframe geometry, the outlines of the streamtubes captured by the 30ft^2 and 37ft^2 propulsors are traced for the smallest and largest mass flow rate tested. For a given inlet capture area, the streamtube capture area increases with $\dot{m}_2$. However, in the region in front of the inlet highlight, the streamtube captured by the larger propulsor is further away from the wall, than it is for the smaller one. Since the gradients in the ingested flow are larger closer to the wall, variations in streamtube capture area due to $\dot{m}_2$ have a

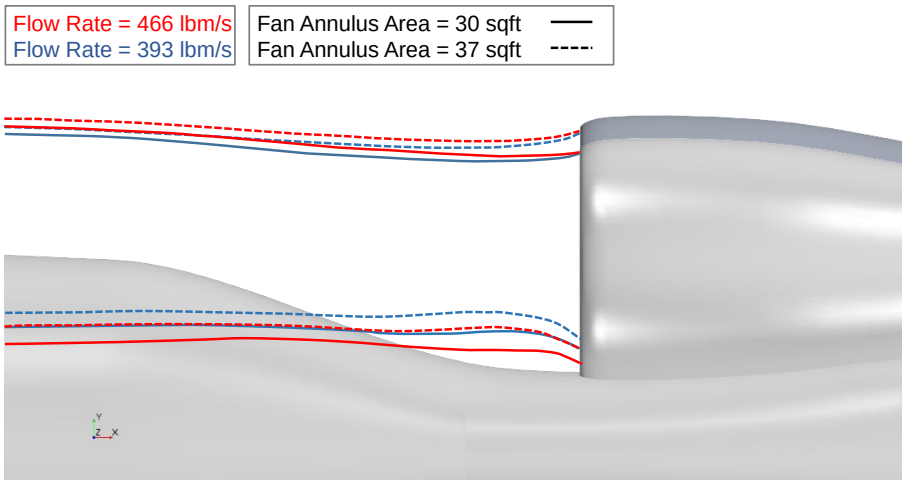

Figure 6.10: Experiment 3.1 - comparison of captured streamtubes for two propulsor sizes and mass flow rates (top view). This figure is a 2D view of the 3D ingested streamtube. The lower outline of the streamtubes shown vary in z direction

more pronounced impact on $C_{P_{K_{\text{in}}}}$ for the smaller propulsor. In the region between the ingested streamtube and the fuselage wall, there is a separation bubble. Though not present in all cases, the extent of this recirculating flow grows with propulsor size and with a decrease in $\dot{m}_2$, i.e, with a more adverse pressure gradient. This recirculating flow is not ingested by the fan for any of the cases tested, but rather, is spilled around the nacelle, as shown in Fig. 6.11.

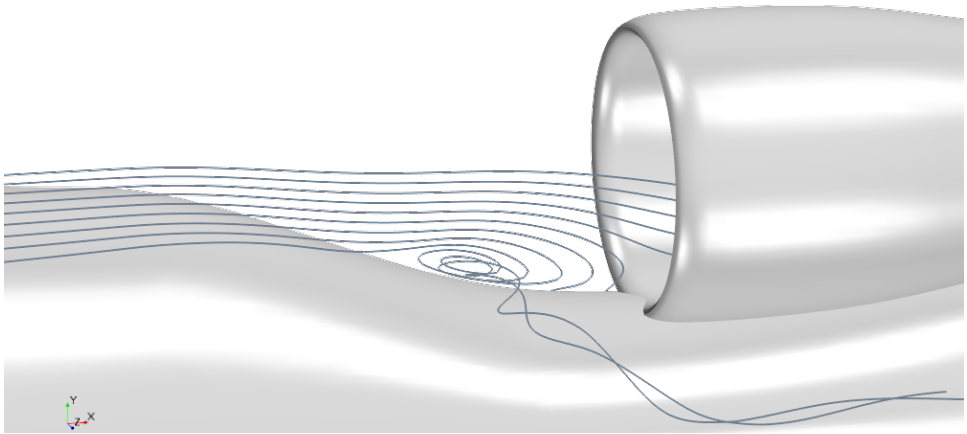

Figure 6.11: Experiment 3.1 - region of recirculating flow in front of inlet highlight, shown for $A_2 = 30\text{ft}^2$ and $\dot{m}_2 = 393\text{lbm/s}$

The two outliers to the trends discussed above are for the $A_2 = 25\text{ft}^2$ propulsor, with a required flow rate of $\dot{m}_2 = 452\text{lbm/s}$ and 434lbm/s. For these cases, the flow rate required is too high for the given propulsor size, nacelle geometry, and propulsor location. As a consequence of this small area, large flow rate requirement, large portions of the fan face experience high Mach number flow, as seen in the sub figures on the right in Fig. 6.12. For $\dot{m}_2 = 452\text{lbm/s}$, the average fan face Mach number is higher than freestream, while for $\dot{m}_2 = 434\text{lbm/s}$, it is just below freestream. The corresponding static pressures at the fan face are below freestream, unlike the other cases tested. In addition, high flow Mach number around the nacelle lip and throat results in a shock just aft of the throat, which is stronger for $\dot{m}_2 = 452\text{lbm/s}$. As a result, the nacelle wall boundary layer thickens behind this shock. The influence of these aspects can be seen through the $C_{P_{K_{\text{in}}}}$ contours at the fan face in the sub figures on the left in Fig. 6.12. As a result of the higher than freestream fan face velocity, the kinetic energy thickness component is negative for $\dot{m}_2 = 452\text{lbm/s}$. The same is true for the pressure-velocity component due to the lower than freestream

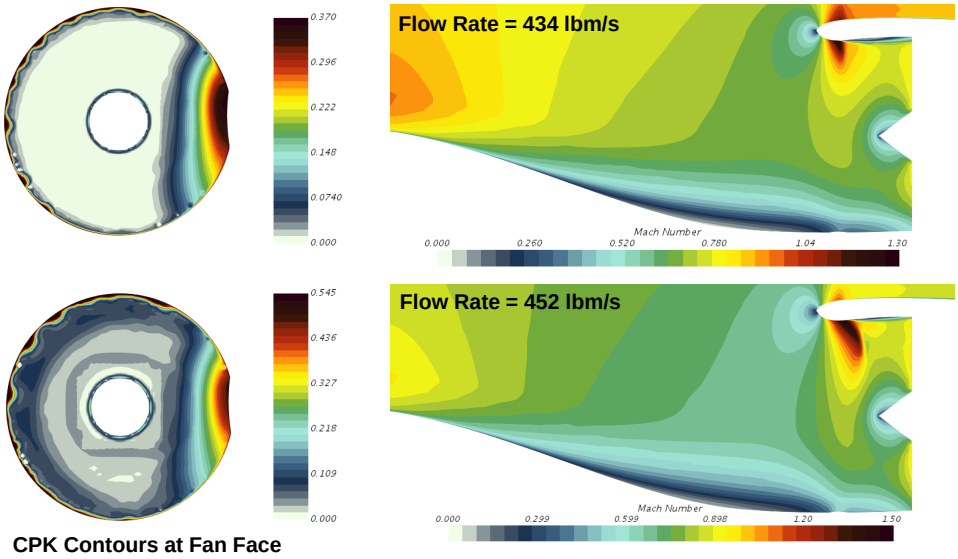

Figure 6.12: Comparison of fan face $C_{P_{K_{\text{in}}}}$ contours and Mach contours for $A_2 = 25\text{ft}^2$ at two different mass flow rates

static pressure. But the magnitude of the latter term is much larger than the former, as seen in Fig. 6.8a, which has a favorable impact on $C_{P_{K_{\text{in}}}}$. The thicker nacelle wall boundary layer after the shock also has a beneficial contribution to $C_{P_{K_{\text{in}}}}$. These two effects combined account for the sharp increase in $C_{P_{K_{\text{in}}}}$ seen for the smallest fan at $\dot{m}_2 = 452\text{lbm/s}$. For $\dot{m}_2 = 434\text{lbm/s}$, the impact on $C_{P_{K_{\text{in}}}}$ is less significant than $\dot{m}_2 = 452\text{lbm/s}$, but still larger than for $\dot{m}_2 = 393\text{lbm/s}$ for $A_2 = 25\text{ft}^2$, which is a shock free case. Note, the case $\dot{m}_2 = 466\text{lbm/s}$ diverged for $A_2 = 25\text{ft}^2$, which is why this point is not included.

To give an idea for how much $C_{P_{K_{\text{in}}}}$ varies with $\dot{m}_2$ and A_2, Table 6.2 shows the difference between the values of $C_{P_{K_{\text{in}}}}$ at the maximum and minimum flow rate tested. This range is calculated at the fan face, for a given propulsor size, expressed in counts, an equivalent force, and a change in equivalent force per unit flow rate. The difference in flow rate over which $\Delta C_{P_{K_{\text{in}}}}$ is evaluated is also included. Note that the $C_{P_{K_{\text{in}}}}$ trends are not strictly linear, especially for the smallest propulsor. Thus, the change in equivalent force per unit flow rate metric is only intended to be a ballpark estimate of the slope.

Recall from chapter 5 that 35lbf was considered as a minimum threshold for a significant *change* in thrust required at $M_\infty = 0.80$, Alt = 35,000ft, for a propulsor sized for a 150 pax aircraft. This change was approximately 0.55% of the design thrust required and corresponded to a 0.5% change in fuel flow rate. From the results shown

Table 6.2: Experiment 3.1 - Range of Variation in $C_{P_{K_{\text{in}}}}$ with $\dot{m}_2$ for Given A_2

A_2 (ft^2)	24.97[!]	30.32	36.94	36.94*
$\Delta C_{P_{K_{\text{in}}}}$ (counts)	1327	-236	-48	1945
$\Delta C_{P_{K_{\text{in}}}}$ Eqiv. Force (lbf)	319	-57	-12	467
$\Delta \dot{m}_2$ (lbm/s)	55	73	73	194
$\frac{\Delta C_{P_{K_{\text{in}}}}}{\Delta \dot{m}_2}$ ($\frac{\text{lbf}}{\text{lbm/s}}$)	5.8	-0.78	-0.16	0.83

*Conducted at $M_\infty = 0.25$ Alt = SL
[!]Case with inlet shock for high $\dot{m}_2$

in Table 6.2, excluding the smallest propulsor due to inlet shocks, $\Delta C_{P_{K_{\text{in}}}}$ exceeds this threshold only for the $A_2 = 30\text{ft}^2$ propulsor. For any propulsor smaller than this one, the slope $\frac{\Delta C_{P_{K_{\text{in}}}}}{\Delta \dot{m}_2}$ is expected to be larger.

Given the relative insensitivity of $C_{P_{K_{\text{in}}}}$ to $\dot{m}_2$ for the largest propulsor, the same propulsor is analyzed at takeoff conditions to assess whether $\frac{\Delta C_{P_{K_{\text{in}}}}}{\Delta \dot{m}_2}$ increases. At takeoff conditions, $C_{P_{K_{\text{in}}}} = 0.1434$ for $\dot{m}_2 = 828\text{lbm/s}$ and $C_{P_{K_{\text{in}}}} = 0.3379$ for $\dot{m}_2 = 1062\text{lbm/s}$. The slope $\frac{\Delta C_{P_{K_{\text{in}}}}}{\Delta \dot{m}_2}$ is larger than at the cruise condition and is comparable to that for the smaller propulsor at cruise. The total change in equivalent force is approximately 0.83% of the design thrust required at takeoff. These results suggest that the sensitivity of $C_{P_{K_{\text{in}}}}$ to $\dot{m}_2$ is larger at takeoff conditions. Qualitatively, the $C_{P_{K_{\text{in}}}}$ trend with $\frac{V_2}{V_\infty}$ at the specified takeoff conditions looks like that shown in Fig. 6.1. However, given the low Mach number, the density variation is minimal and $\frac{\rho_2}{\rho_\infty}$ is approximately 1. Additionally, the pressure coefficient is negative for both cases and thus C_p in this instance has a favorable impact on $C_{P_{K_{\text{in}}}}$, explaining the increase in $C_{P_{K_{\text{in}}}}$ with $\dot{m}_2$.

Variation of η_{PR} with A_2 and $\dot{m}_2$

Fig. 6.13a shows how η_{PR}, measured at the fan face, varies as a function of the fan annulus area A_2 for a constant $\dot{m}_2$ requirement. The same data are plotted in Fig. 6.13b to clearly illustrate how η_{PR} trends with $\dot{m}_2$ for a fixed A_2. Solid lines denote trends for η_{PR} measured at the fan face (P_{t_2}/P_{t_0}), while dashed lines represent trends of η_{PR} measured at a plane slightly offset from the inlet highlight (P_{t_1}/P_{t_0}), not shown in Fig. 6.13a). The latter results quantify the airframe contribution to η_{PR}. The difference between the solid and dashed curves indicates the effective contribution of the inlet to η_{PR}, shown in Fig. B.4 in Appendix B for completeness.

Like with $C_{P_{K_{\text{in}}}}$, pressure recovery shows a positive correlation with A_2 and negative with $\dot{m}_2$ as hypothesized. Consider the η_{PR} contours shown at the fan face in

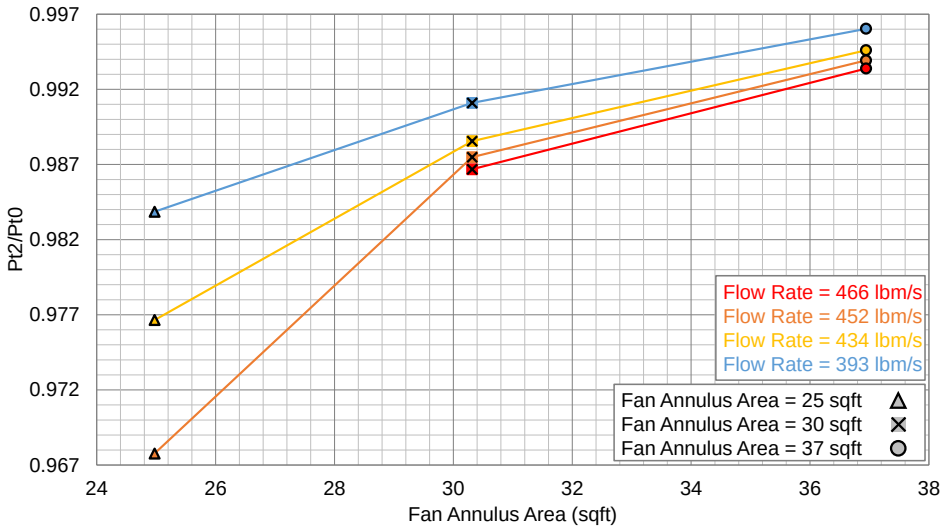

(a) η_{PR} variation with A_2 for different $\dot{m}_2$

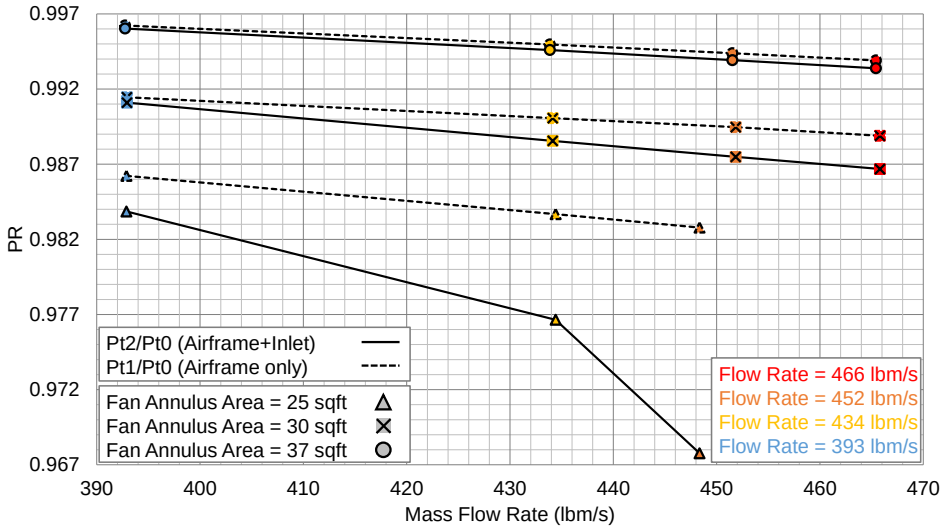

(b) η_{PR} variation with $\dot{m}_2$ for different A_2

Figure 6.13: Experiment 3.1 - variation of η_{PR} as a function of A_2 and $\dot{m}_2$

Fig. 6.14. Comparing Fig. 6.14a to c or Fig. 6.14b to d, it can be seen that the larger propulsor ingests more clean flow at a higher total pressure compared to the smaller propulsor. Additionally, while the extent of the ingested boundary layer is similar for both propulsor sizes, the total pressure variations in the boundary layer are not. For the larger propulsor, the ingested boundary layer has a higher η_{PR} compared to the smaller propulsor for the same $\dot{m}_2$. Differences in the captured streamtube, as discussed in relation to the $C_{P_{K_{\text{in}}}}$ trends, is one reason for this observation. The larger

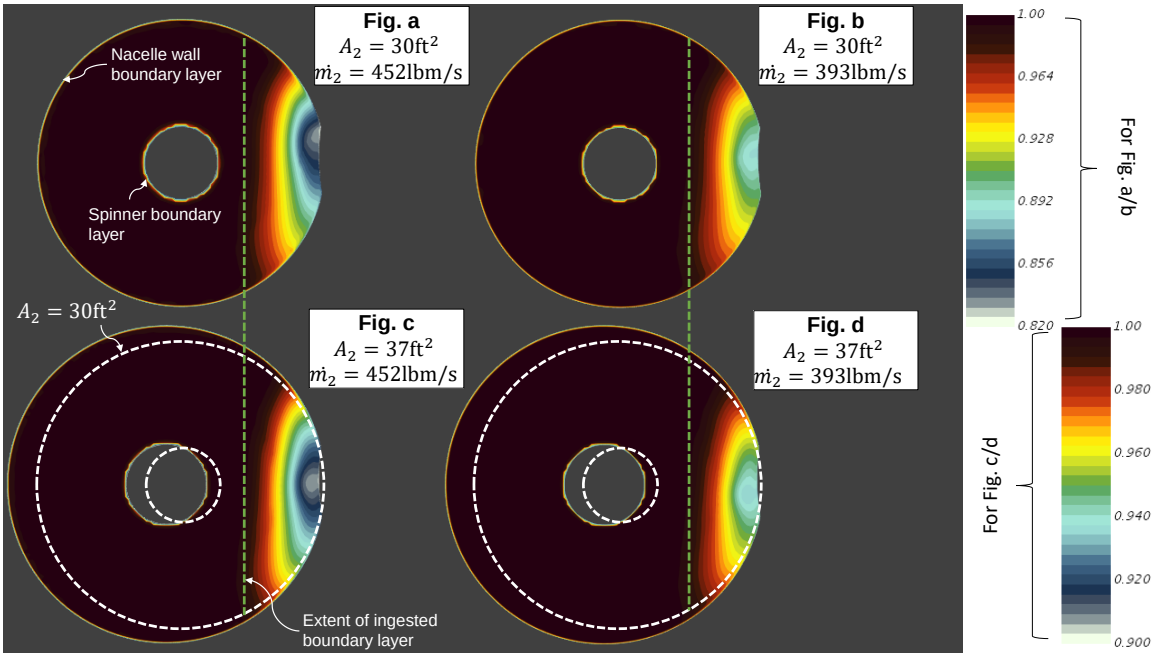

Figure 6.14: Experiment 3.1 - η_{PR} contours at the fan face

propulsor essentially ingests flow further away from the wall, from a region of higher total pressure, which in conjunction with ingesting more clean flow, has a favorable impact on η_{PR} and explains the positive correlation with A_2.

Impacts of the propulsor on the wall shear stress also explain the η_{PR} trends observed. Fig. B.6 in Appendix B compares the near wall velocity profiles for different flow rates. The velocity gradient at the wall, and thus shear stress, is larger for a higher flow rate. Similarly, for a fixed flow rate requirement, decreasing A_2 increases the inflow velocity and wall shear. This increase in viscous losses maps to a decrease in η_{PR} with $\dot{m}_2$. The presence of a shock in the inlet for $\dot{m}_2 = 434\text{lbm/s}$ and $\dot{m}_2 = 452\text{lbm/s}$ for the smallest propulsor has an detrimental impact on η_{PR}, unlike with $C_{P_{K_{\text{in}}}}$. Thus, $C_{P_{K_{\text{in}}}}$ in isolation is not an adequate metric to gage the BLI benefit and η_{PR} must also be considered to assess the net impact on propulsor performance.

Like with $C_{P_{K_{\text{in}}}}$, to give an idea for how much η_{PR} varies with $\dot{m}_2$ and A_2, Table 6.3 summarizes the range of variation in η_{PR}. This range is calculated at the fan face, for a given propulsor size, expressed in points (10^{-3}), a percentage difference,

Table 6.3: Experiment 3.1 - Range of Variation in η_{PR} with $\dot{m}_2$ for Given A_2

A_2 (ft^2)	24.97$^!$	30.32	36.94	36.94*
$\Delta\eta_{PR}$ (points)	-16.1	-4.4	-2.6	-0.6
$\Delta\eta_{PR}$ (%)	1.6	-0.44	-0.26	-0.06
$\Delta\dot{m}_2$ (lbm/s)	55	73	73	194
$\frac{\Delta\eta_{PR}}{\Delta\dot{m}_2}$ ($\frac{\%}{\text{lbm/s}}$)	-0.03	-0.006	-0.004	-0.0003

*Conducted at $M_\infty = 0.25$ Alt = SL
$^!$Case with inlet shock for high $\dot{m}_2$

and percentage difference per unit flow rate. Recall from chapter 5 that 0.35% was considered as a minimum threshold for a significant *change* in pressure recovery at $M_\infty = 0.80$, Alt = 35,000ft, for a propulsor sized for a 150 pax aircraft. Like with $C_{P_{K_{\text{in}}}}$, only propulsors sized between $A_2 = 25\text{ft}^2$ and $A_2 = 30\text{ft}^2$ show changes in η_{PR} that exceed the thresholds for the range of $\dot{m}_2$ tested. At takeoff conditions, $\eta_{PR} = 0.9983$ for $\dot{m}_2 = 828$lbm/s and $\eta_{PR} = 0.9977$ for $\dot{m}_2 = 1062$lbm/s. At these conditions the ratio of clean flow to boundary layer flow is much higher, relative to cruise, and thus η_{PR} is not as sensitive to changes in $\dot{m}_2$.

6.4 Experiment 3.2: Case B Boundary Layer Ingestion

6.4.1 Experimental Overview

The objective of this set of trials is to determine how the trends observed in the previous experiments translate to the case where more boundary layer is ingested. The propulsor in this experiment is placed at the fuselage trailing edge, like on the STARC-ABL, as shown in Fig. 6.15. The same propulsor areas are used as before,

Figure 6.15: Experiment 3.2 - engine location

but the range on $\dot{m}_2$ is adjusted. For $A_2 = 30\text{ft}^2$ and $A_2 = 37\text{ft}^2$, the upper bound is defined by when shocks appear in the inlet, while the lower bound is defined by the smallest mass flow that is possible without reversed flow at the fan face. The cases considered are shown in Table. 6.4. Given that there is only one common $\dot{m}_2$ point between the $A_2 = 30\text{ft}^2$ and $A_2 = 37\text{ft}^2$ propulsors, the trials for $A_2 = 25\text{ft}^2$ are conducted to augment data for A_2 trends.

Table 6.4: Experiment 3.2 - Overview of Cases

Experiment	d_2 (in)	A_2 (ft^2)	Target $\dot{m}_2$ (lbm/s)
3.2-1	69.9	24.97	348
3.2-2	69.9	24.97	321
3.2-3	77	30.32	422
3.2-4	77	30.32	374
3.2-5	77	30.32	348
3.2-6	77	30.32	321
3.2-7	85	36.94	537
3.2-8	85	36.94	502
3.2-9	85	36.94	422

6.4.2 Results and Discussion

Fig. 6.16 shows the $C_{P_{K_{\text{in}}}}$ and η_{PR} results as a function of $\dot{m}_2$. Unlike previously, $C_{P_{K_{\text{in}}}}$ now shows a positive correlation with $\dot{m}_2$ and negative with A_2. Additionally, the sensitivity of $C_{P_{K_{\text{in}}}}$ to changes in $\dot{m}_2$ is higher than before, as shown in Table

Table 6.5: Experiment 3.2 - Range of Variation in $C_{P_{K_{\text{in}}}}$ (at fan face) with $\dot{m}_2$

A_2 (ft^2)	24.97	30.32	36.94
$\Delta C_{P_{K_{\text{in}}}}$ (counts)	358	1062	975
$\Delta C_{P_{K_{\text{in}}}}$ Eqiv. Force (lbf)	86	255	234
$\Delta \dot{m}_2$ (lbm/s)	26	101	114
$\frac{\Delta C_{P_{K_{\text{in}}}}}{\Delta \dot{m}_2}$ ($\frac{\text{lbf}}{\text{lbm/s}}$)	3.3	2.5	2.1

6.5. Pressure recovery at the fan face still shows a positive correlation with A_2 and negative with $\dot{m}_2$, however, η_{PR} at the highlight trends differently with $\dot{m}_2$.

To understand these trends, one must understand the relation between $C_{P_{K_{\text{in}}}}$ and $\frac{V}{V_\infty}$. Fig. 6.17 compares the $C_{P_{K_{\text{in}}}}$ and $\frac{V}{V_\infty}$ contours at the fan face of the $A_2 = 30\text{ft}^2$ propulsor for different flow rates. One key observation from these contours is the 'bucket like' variation in both $C_{P_{K_{\text{in}}}}$ and $\frac{V}{V_\infty}$. The contours exhibit a 'lung' shaped

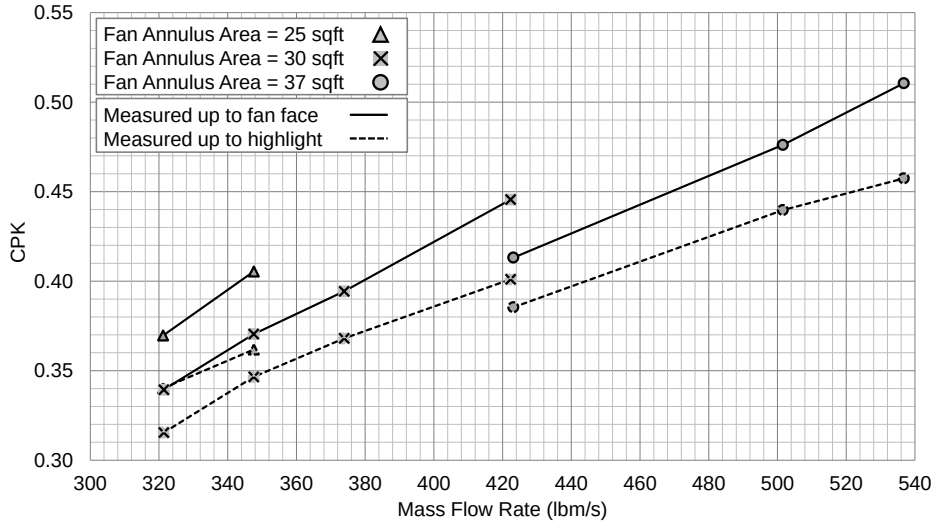

(a) $C_{P_{K_{\text{in}}}}$ variation with $\dot{m}_2$ for different A_2

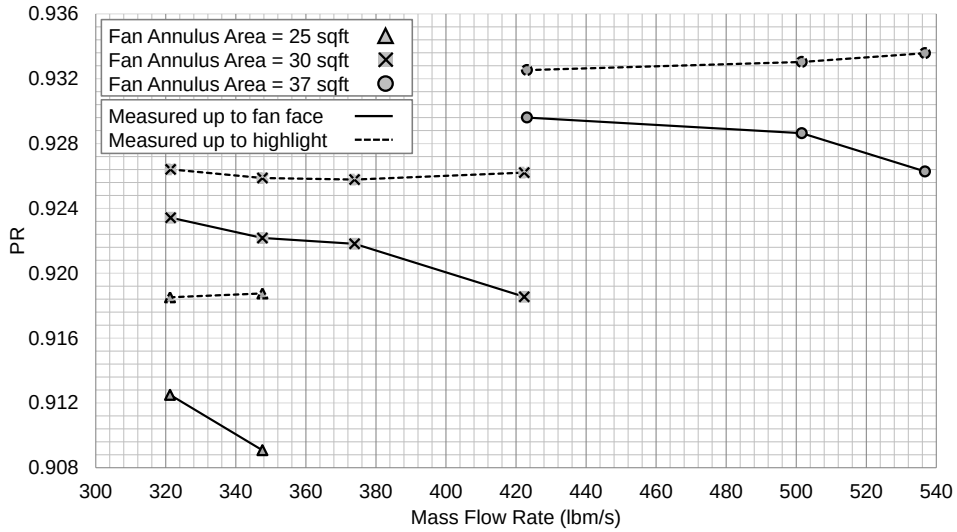

(b) η_{PR} variation with $\dot{m}_2$ for different A_2

Figure 6.16: Experiment 3.2 - variation of $C_{P_{K_{\text{in}}}}$ and η_{PR} with A_2 and $\dot{m}_2$

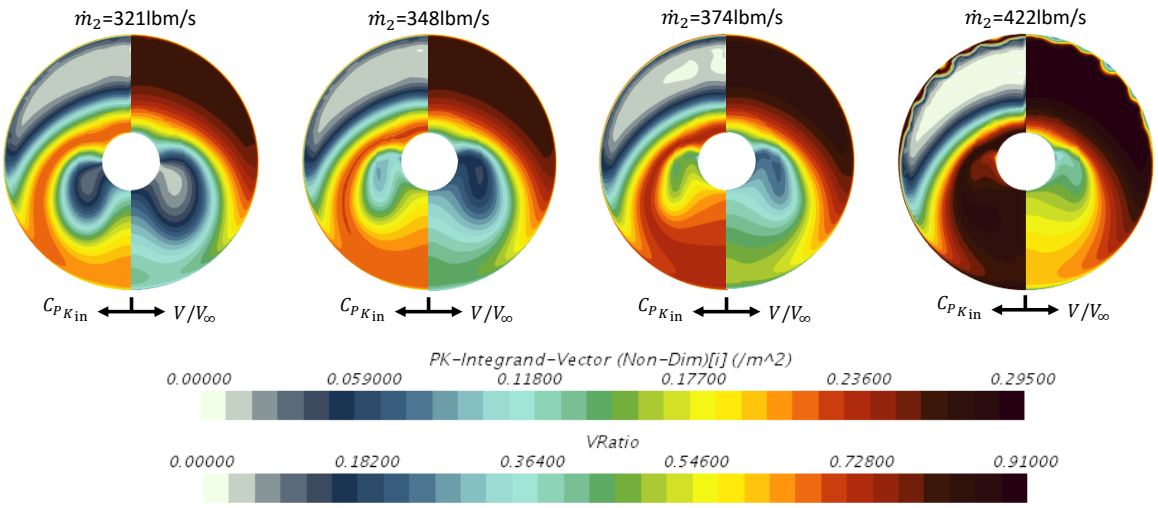

Figure 6.17: Experiment 3.2 - contour plots of $C_{P_{K_{\text{in}}}}$ and $\frac{V}{V_\infty}$ shown at the fan face for $A_2 = 30\text{ft}^2$ at different $\dot{m}_2$

pattern, not very dissimilar to the total pressure contours observed for the STARC-ABL at low angles of attack in [42]. Within this 'lung' shaped sector, the zone of low $\frac{V}{V_\infty}$ flow corresponds to a zone of low $C_{P_{K_{\text{in}}}}$. Outside this zone, there is a peak in $C_{P_{K_{\text{in}}}}$, after which it decreases radially upwards, while $\frac{V}{V_\infty}$ increases, transitioning from boundary layer flow to freestream. In other words, these contours highlight the non-monotonic behavior of $C_{P_{K_{\text{in}}}}$ with $\frac{V}{V_\infty}$, more clearly illustrated in Fig. 6.18.

In this figure, the integrand of $C_{P_{K_{\text{in}}}}$ in Eq. (5.1) is plotted as a function of $\frac{V}{V_\infty}$ at each of the $\dot{m}_2$ values tested for $A_2 = 30\text{ft}^2$. Unlike Fig. 6.9, the x axis should not be considered as the average fan face velocity for a given $\dot{m}_2$, but rather, a domain of possible velocity ratios that can be seen on the fan annulus for a given flow rate. To generate this figure, an estimate for how the mass flux ρV varies as a function of $\frac{V}{V_\infty}$ is obtained by fitting a surrogate to the average mass flux data obtained for all propulsors tested in experiment 3.2, shown in Fig. B.3 in Appendix B. Note that a given value of $\dot{m}_2$ corresponds to a fixed value of C_p given the uniform boundary condition imposed at the fan face. Fig. 6.18 essentially shows how the $C_{P_{K_{\text{in}}}}$ integrand varies at different points on the fan annulus where the flow is at different $\frac{V}{V_\infty}$. Initially, $C_{P_{K_{\text{in}}}}$ increases with velocity, but then the second order effects due to $1 - \frac{V^2}{V_\infty^2}$ result in

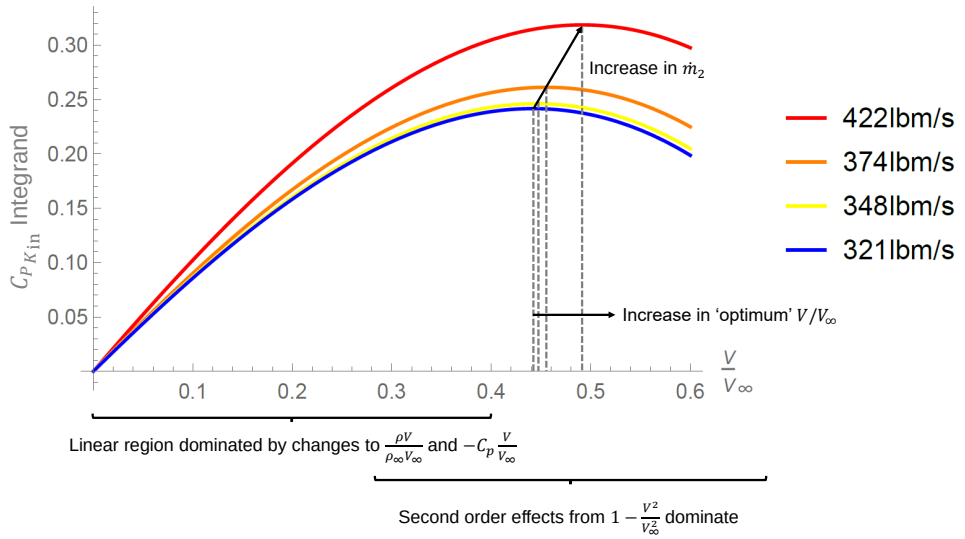

Figure 6.18: Experiment 3.2 - plot showing $C_{P_{K_{\text{in}}}}$ integrand varying as a function of $\frac{V}{V_\infty}$ at different required $\dot{m}_2$ for $A_2 = 30\text{ft}^2$

a decrease in $C_{P_{K_{\text{in}}}}$ with $\frac{V}{V_\infty}$. The optimum value of $\frac{V}{V_\infty}$, where the integrand peaks in value, increases with $\dot{m}_2$. The trends shown in Fig. 6.18 mirror the contours shown in Fig. 6.17. As required $\dot{m}_2$ increases, the value of the C_{p_2} boundary condition at the fan face decreases. In conjunction with the increase in mass flux in the linear region of the $C_{P_{K_{\text{in}}}}$ curve, the net result is an increase in $C_{P_{K_{\text{in}}}}$ with $\dot{m}_2$. Thus, as hypothesized, the amount of ingested boundary layer does play a role in influencing the sensitivity of $C_{P_{K_{\text{in}}}}$ to $\dot{m}_2$.

The fan face trends for η_{PR} are consistent with experiment 3.1, as expected, however, the inlet highlight values show inconsistent trends. This behavior is due to flow separation at the tail cone, as shown in Fig. 6.19. In this figure, streamlines are shown at the lowest and highest flow rate values for the $A_2 = 30\text{ft}^2$ propulsor. The velocity ratio scalar values are shown on the streamlines and at the fan face. For low flow rates, the adverse pressure gradient imposed by the fan and the tapering geometry results in flow separation on the bottom and side of the tail cone. This recirculating flow from both zones mixes into a vortical structure of low velocity and low total pressure, which extends partly into the nacelle, but not up to the fan face.

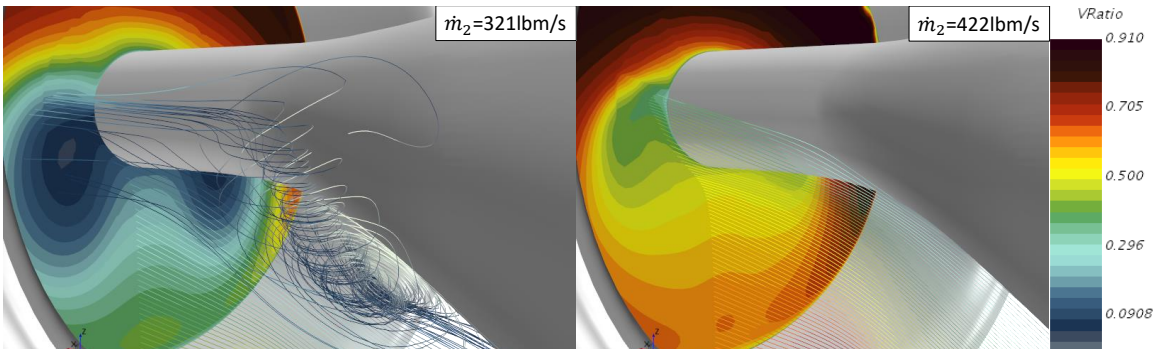

Figure 6.19: Experiment 3.2 - flow separation observed at the tail cone, in front of the inlet highlight, for $\dot{m}_2 = 321$lbm/s, which is virtually eliminated at $\dot{m}_2 = 422$lbm/s for $A_2 = 30\text{ft}^2$. Contours of $\frac{V}{V_\infty}$ are shown at the fan face and on the streamlines

As the flow rate increases, the extent of this recirculating flow region reduces, as seen in Fig. 6.19. The lung shaped patterns seen in Fig. 6.17 are due to this flow separation.

While the η_{PR} trends with A_2 are consistent with experiment 3.1 and hypothesis 3, $C_{P_{K_{\text{in}}}}$ trends are not. There are two reasons for this behavior. First, for the same mass flow rate, the smaller propulsor has a higher ρV. Since a large portion of the fan-face sees low velocity flow, evident in Fig. 6.17, this region is in the linear domain of the plot shown in Fig. 6.18. Thus, increases in ρV due to a decrease in A_2 for the same mass flow, for this specific configuration, result in an increase in $C_{P_{K_{\text{in}}}}$. Second, the differences also arise from the presence of shocks in the inlet for the highest flow rate. The shocks for the smaller propulsor are stronger than those in the larger propulsor, for the same flow rate. For the inlet highlight results, the larger propulsor tends to induce a larger extent of flow separation at the tail cone, for the same flow rate. Thus, for these three comparison points, $C_{P_{K_{\text{in}}}}$ is smaller for a larger A_2. However, when looking at two propulsors with the same specific flow rate, the larger propulsor does indeed have a higher value of $C_{P_{K_{\text{in}}}}$ at the fan face, as seen in Fig. B.9 in Appendix B.

6.5 Concluding Remarks

Table 6.6 summarizes the trends observed (evaluated at different propulsor stations) within the A_2 and $\dot{m}_2$ test bounds for experiments 3.1 and 3.2. If a given metric exhibits different behavior with a given propulsor variable, a tag is added to comment on when that correlation is observed. For example, $C_{P_{K_{\text{in}}}}$ evaluated at the fan face exhibits a negative correlation with $\dot{m}_2$ unless there is a shock in the inlet, at which point it becomes positive. If no description is provided in the 'Situation(s)' column, that correlation is expected to hold regardless of the flow characteristics.

It is apparent that the experimental results support hypothesis 3, with the exceptions arising in situations where shocks or flow separation have a direct impact on the measured quantity at a given propulsor station. While the geometries used

Table 6.6: Experiment 3 - Summary of Trends

Metric	**Variable**	**Case A BLI**		**Case B BLI**	
		Correlation	Situation(s)	Correlation	Situation(s)
$C_{P_{K_{\text{in}}}}$ (Station 1)	A_2	+		-	Separation
	$\dot{m}_2$	-		+	
$C_{P_{K_{\text{in}}}}$ (Station 2)	A_2	+	Shock Free OR Weak Inlet Shock Avg $V_2 < V_\infty$	-	Inlet Shock
		-	Strong Inlet Shock Avg $V_2 > V_\infty$		
	$\dot{m}_2$	-	Shock Free	+	
		+	Inlet Shock		
η_{PR} (p_{t_1}/p_{t_0})	A_2	+		+	
	$\dot{m}_2$	-		B/+	Separation
η_{PR} (p_{t_2}/p_{t_1})	A_2	+		+	
	$\dot{m}_2$	-		-	
η_{PR} (p_{t_2}/p_{t_0})	A_2	+		+	
	$\dot{m}_2$	-		-	

in these experiments are not optimized for a given flight condition, the presence of shocks or separation for some cases, but not for others, highlights the role played by the propulsor in affecting local flow characteristics. For example, in experiment 3.1, shocks were observed inside the inlet for the smallest propulsor at the highest flow rates, but not otherwise. This suggests that the nacelle contouring may not have been a big factor and that perhaps the fan diameter was too small for the required flow rates. Increasing the fan diameter for the same flow rates and nacelle design eliminated these shocks. However, if most of the cases in experiment 3.1 showed inlet shocks, then such a scenario would have been indicative of a poor inlet design, requiring more detailed design refinement. The underlying theme is the same as that behind hypothesis 2, i.e., there are macro parameters that are primarily responsible for major changes to the flow (A_2 and $\dot{m}_2$), and that the detailed parameters (inlet contouring) have a relatively smaller impact as long as these parameters are set to reasonable values that do not result in adverse flow for most cases. Similarly, the flow separation observed in experiments 3.1 and 3.2 for low flow rate cases can be mitigated by altering airframe macro parameters like the inlet ramp angle in experiment 3.1 and tail cone upsweep angle in experiment 3.2.

With respect to the aero-propulsive coupling methodology for BLI concepts, experiment 3 shows the need to include both A_2 and $\dot{m}_2$ as part of BLI effects surrogate model input space. While shocks and flow separation are likely at corner points within the design space, these points will be filtered out at the system level design if these features have a net negative impact on performance.

CHAPTER 7
CONCEPTUAL DESIGN WITH BLI EFFECTS

This chapter describes the implementation of the coupled aero-propulsive and parametric conceptual design methodology for BLI aircraft, presented in chapter 4. Given the nature of the BLI vehicle design process, the Environmental Design Space (EDS) [45] framework is an appropriate tool to implement the proposed methodology. The EDS framework was developed for the US Federal Aviation Administration to assess environmental impacts of aircraft. EDS integrates the aircraft sizing and mission analysis code FLOPS [64], engine cycle analysis code NPSS [60], engine weights and flowpath estimation code WATE++ [90], and other analysis modules for overall vehicle sizing and performance assessment. As discussed in chapter 2, these industry standard tools have been used for several BLI studies in literature.

A series of experiments were introduced in chapter 4 to quantify the consequences of ignoring aero-propulsive coupling when designing a BLI vehicle. These consequences are defined in terms of differences in fuel weight estimates and vehicle design characteristics. The experiments aim to show that the proposed methodology is more appropriate than existing decoupled methods where a point design estimate of the BLI effects are used. Lastly, these experiments also aim to establish that the differences between the decoupled and coupled approaches will be more significant in situations where the wing and engine exhibit stronger interaction. As such, two configurations with different engine locations (on top of the fuselage and on the side) are considered, as shown in Fig. 4.6. The following sections describe the different steps in the methodology, highlighting the considerations involved in the design of both BLI configurations. Results of the design parameter sweep experiments and optimizations are then discussed.

7.1 Pre-Vehicle Sizing Stage

7.1.1 High Level Requirements and Baseline Aircraft

The main objective is to develop a BLI equivalent of the current 737-8 aircraft, with lower block fuel burn requirements, and an E.I.S. between 2035 and 2040. As such, the current performance capability of the 737-8 is used to derive several requirements for the BLI version of this aircraft. The aircraft must carry up to 180 passengers, with a twin aisle layout. The twin aisle layout serves two main purposes. First, it enables faster boarding and unloading compared to a single aisle configuration [19, 101], which is an economic incentive for airlines. Second, the wider body enables easier integration of the BLI engines on the fuselage, especially for the top-mounted engine configuration. With a design payload carrying capability of 36,000 pounds, the aircraft must have a design range of 3450 nautical miles, derived from the payload-range capability of the 737-8 [14]. The design mission of the baseline non-BLI and the resulting BLI aircraft is shown in Fig. 7.1. The aircraft cruises at $M_\infty = 0.78$, starting at 35,000 ft. and ending at 39,000 ft. The maximum operating Mach number is 0.82. The aircraft must takeoff and land within 8000 ft at standard sea level conditions, assuming both engines are operational, and a dry runway. For context, at these conditions and at MTOW, the 737-8 has a takeoff field length of about 8200 ft. At maximum landing weight, the 737-8 is able to land in about 5800 ft. [14].

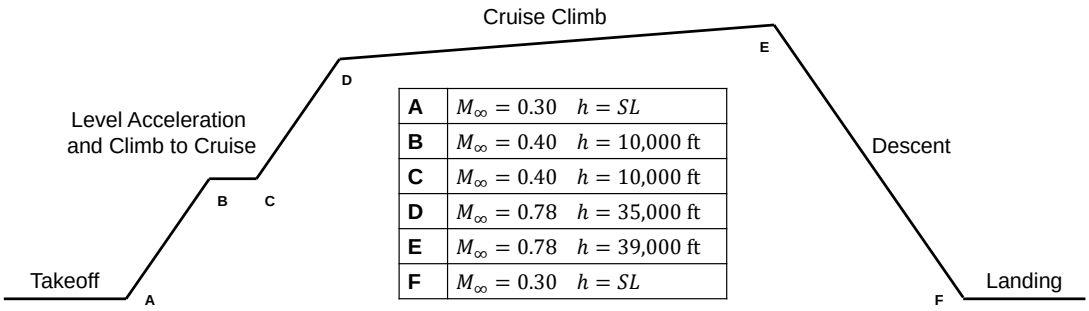

Figure 7.1: Design mission profile for the baseline non-BLI and BLI aircraft

A baseline non-BLI aircraft is created for each BLI configuration. Given differences in the engine location for the BLI configurations, the tail cone design for both is different. At the conceptual level, the only impact this difference has is on the fuselage wetted area calculations, and thus on the fuselage profile drag estimations in FLOPS. The baselines are sized in EDS using the conventional sizing process described in chapter 3. The baselines are designed to be similar to a notional 737-8, with key airframe and engine parameters obtained from publicly available data. Other engine and airframe design parameters are calibrated to produce performance and emissions results that are similar to available data. There are some differences however, due to the larger wetted area of the twin aisle fuselage.

Table 7.1: Key Characteristics of the Non-BLI Baselines

Parameter	Baseline (Top)	Baseline (Side)
S (ft^2)	1379	1377
AR	9.22	9.22
$\Lambda_{c/4}$ (°)	25.45	25.45
λ	0.303	0.303
Fuselage length (ft)	128.3	128.3
Max fuselage height (ft)	12.9	12.9
Max fuselage width (ft)	17.6	17.6
Fuselage wetted area (ft^2)	4926	4657
ADP FPR	1.539	1.539
ADP BPR	10.05	10.05
ADP LPCPR	1.55	1.55
ADP HPCPR	20.25	20.25
ADP OPR	47.6	47.6
SLS Thrust/Engine (lbf)	29315	29315
d_2 (in)	70.3	70.3
TOGW (lbf)	181,140	180,394
OEW (lbf)	98,618	98,414
Block Fuel (lbf)	38,967	38,502
TOFL All Engines (ft)	6686	6682
LDGFL (ft)	6535	6542

7.1.2 BLI Surrogates Generation Phase

In this sub-stage, surrogate models for $P_{K_{\text{in}}}$, η_{PR}, and $\Delta\Phi_{\text{wake}}$, are generated. In addition, corrections for the fuselage and nacelle wetted areas are also developed to account for $\Delta\Phi_{\text{surf}}$.

Define Input Variables and Bounds

Based on the studies presented in chapters 5 and 6, key airframe and propulsor variables affecting the BLI effects were identified. From that, a smaller subset of variables is picked to define the input variable space for the BLI surrogates, summarized in Table 7.2. The BLI effects directly impacted by a given variable are also listed in this table. The fuselage and nacelle wetted area corrections are only a function of the ramp angle (ϕ) and fan diameter. For engines located at the 90% axial station and aft on the fuselage, experiment 2.6 shows that the wing has a noticeable impact on the $\Delta\Phi_{\text{wake}}$ measurements. However, changes in the wing design have an insignificant influence on $\Delta\Phi_{\text{wake}}$ (Fig. A.6 in Appendix A). While the wing downwash affects the fuselage wake, changes to the wing design primarily impact the wing wake. Due to

Table 7.2: BLI Surrogate Model Input Variables

Input Variable	LB	UB	Type	BLI Effects
S (ft^2)	1076	1722	Airframe	$P_{K_{\text{in}}}$ and η_{PR}
AR	7	11	Airframe	$P_{K_{\text{in}}}$ and η_{PR}
Λ_{LE} (°)	20	40	Airframe	$P_{K_{\text{in}}}$ and η_{PR}
λ	0.2	0.4	Airframe	$P_{K_{\text{in}}}$ and η_{PR}
ϕ (°)	12	20	Airframe	All
d_2 (in)	68	78	Propulsor	All
SPW_{c_2} (lbm/ft^2-s)	$f(M_\infty)$	44	Propulsor	$P_{K_{\text{in}}}$ and η_{PR}
M_∞	0.25	0.85	Flight conditions	$P_{K_{\text{in}}}$ η_{PR} $\Delta\Phi_{\text{wake}}$
h (ft)	0	43000	Flight conditions	$P_{K_{\text{in}}}$ η_{PR} $\Delta\Phi_{\text{wake}}$
α (°)	0	4	Flight conditions	$P_{K_{\text{in}}}$ η_{PR} $\Delta\Phi_{\text{wake}}$

the relative location of the engine and wing, the engine mostly ingests the fuselage wake, and as a result, $\Delta\Phi_{\text{wake}}$ due to BLI by the engine is relatively insensitive to wing design changes. Thus, for the $\Delta\Phi_{\text{wake}}$ surrogates, the wing in the geometry model is fixed at the baseline non-BLI aircraft wing design.

Bounds on the wing design variables are the same as those discussed in experiment 2.6. These bounds represent a realistic design space for a 150-180 pax aircraft. FLOPS internal aerodynamics work with quarter chord sweep, and thus a mapping is used to translate between quarter chord and leading edge sweep as needed. The inlet ramp angle is changed by changing the cross sectional width (for the side mounted engine configuration) or the cross sectional height of the fuselage at a given station, as described in experiment 2.8. The upper bound is defined to avoid overly thin fuselage cross sections. The lower bound is defined somewhat arbitrarily to ensure a sufficiently high enough value of $P_{K_{\text{in}}}$ for BLI to have a propulsive power benefit. With regards to the propulsor variables, the upper bound on the fan diameter is constrained by the largest propulsor that can adequately fit on the fuselage for a top mounted engine configuration, assuming a two engines. The lower bound is about an inch smaller than the LEAP-1B fan. In experiment 3, mass flow rate was used as an independent variable. However, when considering multiple flight conditions and fan sizes, defining reasonable bounds on mass flow is problematic. Specific corrected flow, SPW_{c_2}, is better behaved over the operating envelope, as shown in Fig. 7.2.

This figure shows how SPW_{c_2} varies at different operating points in the mission for the baseline non-BLI aircraft. The upper bound on SPW_{c_2} represents max power and is determined by the design SPW_{c_2} assumed when sizing the fan, i.e., the fan blade technology assumption, as discussed in chapter 3. The smallest values correspond to flight idle conditions. The non-BLI configuration is designed with an assumption that the fan can handle a specific corrected flow of 48 lbm/sqft-s. However, due to blockage effects of the ingested boundary layer, the effective flow area available, for

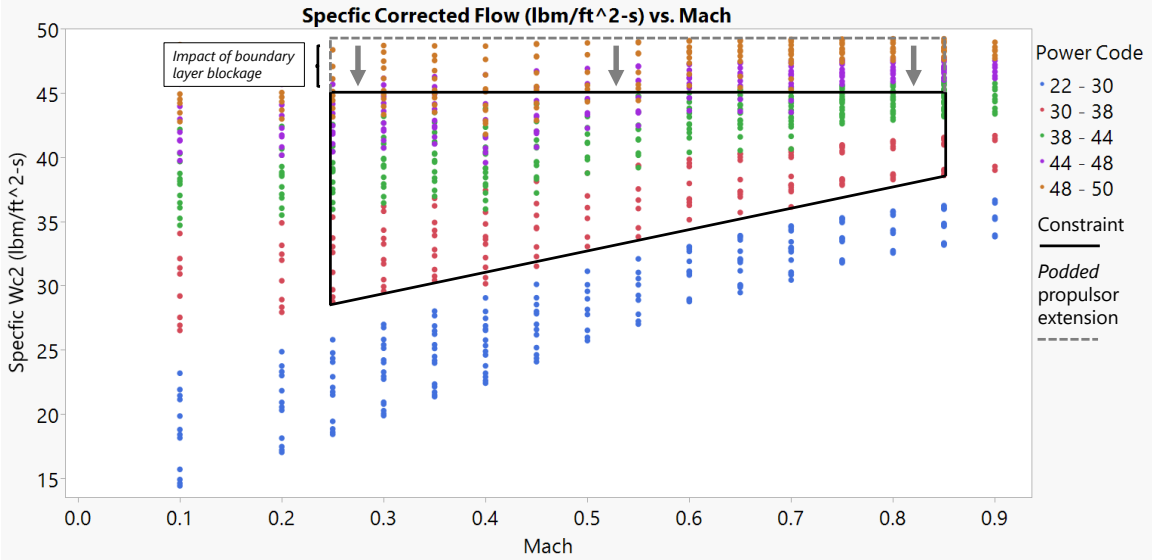

Figure 7.2: M_∞-SPW_{c_2} operating envelope for the baseline non-BLI aircraft. Black lines show constraints that restrict this space for the BLI surrogates

a given fan size, is much smaller. Thus, for the same desired mass flow rate, the effective Mach number of the ingested flow is much higher, which means that the flow is more likely to choke at a smaller mass flow for a BLI propulsor than for a podded propulsor. As such, a more realistic upper bound for the BLI propulsor SPW_{c_2} is 44 lbm/sqft-s. The lower bound for the surrogate model inputs, on the other hand, need not be as low as flight idle conditions. The aircraft lift and associated drag at different points in the mission will result in the engine operating at much higher power settings than idle. As such, one can define the lower bound at a higher specific power code, as shown by the black constraint line in Fig. 7.2. Below this constraint, one can assume no BLI effect for lower throttle settings, recognizing that the error in doing so is minimal. This constraint avoids wasting computational resources by sampling in regions that are unlikely to be encountered in a typical mission.

A similar strategy can be used to constrain the Mach-altitude operating zone, which is shown in Fig. 7.3 for the non-BLI baseline. This flight envelope is based on engineering judgment and existing aircraft operations. Black lines show the constrained operating envelope for the BLI surrogates. Lastly, as far as angle of attack

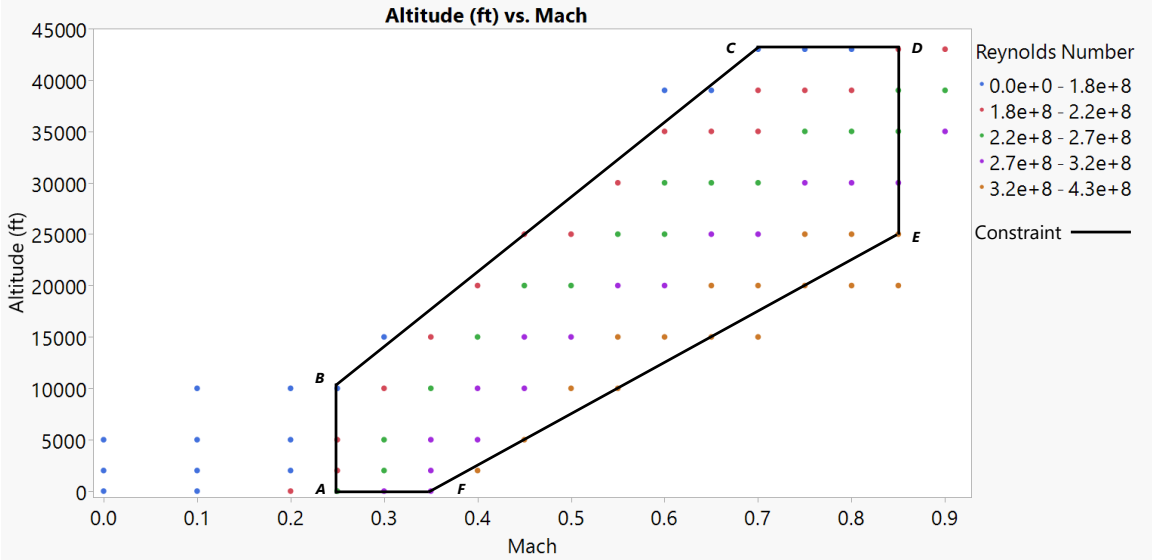

Figure 7.3: M_∞-h operating envelope for the baseline non-BLI aircraft. Black lines show constraints that restrict this space for the BLI surrogates

goes, the bounds represent a typical range that could be expected at most points in the mission. Since the wing sections are at a non-zero twist, the geometric angle of attack of the wing is different from the aircraft angle of attack specified in Table 7.2.

Define Design Space Sampling Strategy

A design of experiments is created to efficiently sample the design space for a globally accurate surrogate model. It is initially assumed that a standard second order response surface equation will be adequate. If regression analysis indicated a lack of fit, higher order terms or transformations would be considered. Traditionally, Central-Composite or Box-Behnken designs have been used for response surface modeling (RSM). For computer based experiments, space filling designs like the Latin Hypercube Sample (LHS) have been to used to avoid corner points in the design space where computer codes may crash. However, traditional DoEs assume a cubical design space. The irregular nature of the BLI surrogate input space stemming from constraints on the M_∞-h-SPW_{c_2} envelope warrants a computer generated custom design [69]. JMP is an ideal tool for generating such DoEs.

There are several optimality criteria that can be used to assess the quality of the design. One commonly used criterion is the D-optimal condition. D-optimal designs are typically used when the goal is to screen for active design variables [69]. These designs are tailored for precise estimation of the model coefficients. D-optimal designs may be efficient for screening, but since the goal is to generate a globally accurate surrogate, D-optimality is not an adequate criterion to gage the quality of the DoE. In contrast, I-optimal designs are a much better choice. In creating a DoE that maximizes the I-optimality criterion, one is creating a design that minimizes the prediction variance over the entire design space, thereby improving the precision of the predictions made by the surrogate model [69].

Once the optimality criterion is decided, the number of cases must be determined. The smallest number of cases that one can pick for a full second order RSE equals the number of terms in that model. For N design variables, the number of model terms and thus the minimum number of cases to run is given by the equation:

$$\text{Min. Number of Cases} = (N+1)(N+2)/2 \tag{7.1}$$

However, models generated from such saturated designs typically do not have adequate prediction capabilities. Thus, more samples are needed. However, given the computational cost of each case, an arbitrary number of cases cannot be picked. To determine an adequate number of samples required in the DoE, one can look at the relative prediction variance as a metric. The prediction variance at a design point $\mathbf{x}$, is given by the product of the mean square error (MSE) of the fitted RSM and the relative prediction variance as

$$\sigma^2(\mathbf{x}) = MSE\left[\mathbf{x}^T\left(\mathbf{X}^T\mathbf{X}\right)^{-1}\mathbf{x}\right] \tag{7.2}$$

where $\mathbf{X}$ is the matrix of basis functions evaluated at all points in the DoE. The

mean square error is dependent on the actual values of the function, $\mathbf{f}$, and the model prediction $\hat{\mathbf{f}}$, and is calculated as follows:

$$MSE = ||\mathbf{f} - \hat{\mathbf{f}}||^2/N \tag{7.3}$$

Evident from Eq. (7.2), the relative prediction variance is solely dependent on the DoE. The objective is to pick the right number of cases such that the relative prediction variance is reduced. The surrogates for $P_{K_{\text{in}}}$ and η_{PR} are a function of 10 design variables. From Eq. (7.1), one sees that these surrogates require a minimum of 66 samples. For the $\Delta\Phi_{\text{wake}}$ surrogates, there are a total of 5 variables. However, since d_2 can be changed easily without requiring an additional CFD run, this variable can be dropped from the DoE size calculations. Thus, the minimum number of cases required is 15. Fig. 7.4 shows the fraction of design space plot for the two DoEs. These plots compare the relative prediction variance over the design space for the smallest possible DoE, against larger DoEs with more cases. The best design is one that minimizes the relative prediction variance over a larger fraction of the design space, while minimizing the number of cases needed. Diminishing returns are evident in Fig. 7.4, where the reduction in relative prediction variance over the design space,

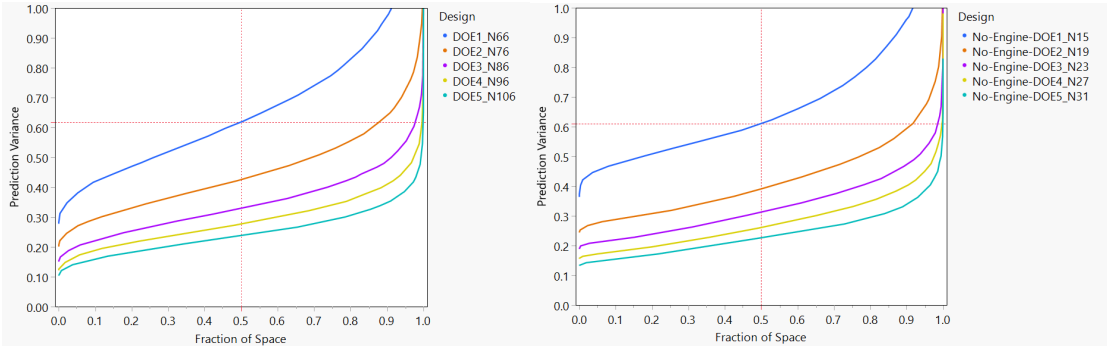

(a) For $P_{K_{\text{in}}}$ and η_{PR} **(b)** For $\Delta\Phi_{\text{wake}}$

Figure 7.4: Fraction of design space plot comparison of the five DoEs considered for the three BLI effects. The yellow curve shows the relative prediction variance for the chosen DoE

per 10 additional cases, decreases. Thus, for $P_{K_{\text{in}}}$ and η_{PR} surrogates, 96 cases appears to be adequate, while for $\Delta\Phi_{\text{wake}}$, 27 cases are sufficient. Note that for $\Delta\Phi_{\text{wake}}$, d_2 will be changed thrice per CFD run. So while the total CFD runs required is 27, the number of samples in the DoE will be 81. Scatterplot matrices showing the DoE structure for the training sets can be found in Fig. C.1 in Appendix C. An additional 20 cases for $P_{K_{\text{in}}}$ and η_{PR} and 9 CFD runs for $\Delta\Phi_{\text{wake}}$ are conducted for validating the surrogate models. The validation DoE scatterplot matrices are shown in Fig. C.2.

The fuselage and nacelle wetted areas calculated by FLOPS, for an input set of fuselage and engine dimensions, can be overwritten by user specified values for SWETF and SWETN respectively. If either quantity is less than 5, then the term is treated as a multiplier, otherwise, it is considered as a dimensional quantity for wetted area. Wetted and theoretical area calculations for each component can be obtained from OpenVSP. There are 9 unique combinations of d_2 and ϕ in the training DoE for $P_{K_{\text{in}}}$ and η_{PR}. These 9 points are used for training the SWETF and SWETN surrogates. For SWETF and SWETN validation, the first 9 points in the validation DoE for $P_{K_{\text{in}}}$ and η_{PR} are used. SWETF is specified as a dimensional quantity. SWETN on the other hand is calculated as a ratio of the wetted area to theoretical surface area of the nacelle. This quantity captures the reduction in surface area due to partial embedding of the nacelle in the fuselage. SWETN then corrects FLOPS's estimation of the nacelle wetted area, which is based on engine dimensions calculated by WATE++.

Prepare Geometry and CFD Models to Evaluate BLI Effects

The next step in generating the BLI surrogates is defining appropriate geometry models for the aircraft. OpenVSP is used to create a template for each configuration, as shown in Fig. 7.5. These templates are then modified for each case in the DoE. As seen in experiment 2.5, the fuselage length and cross sectional area are key parameters

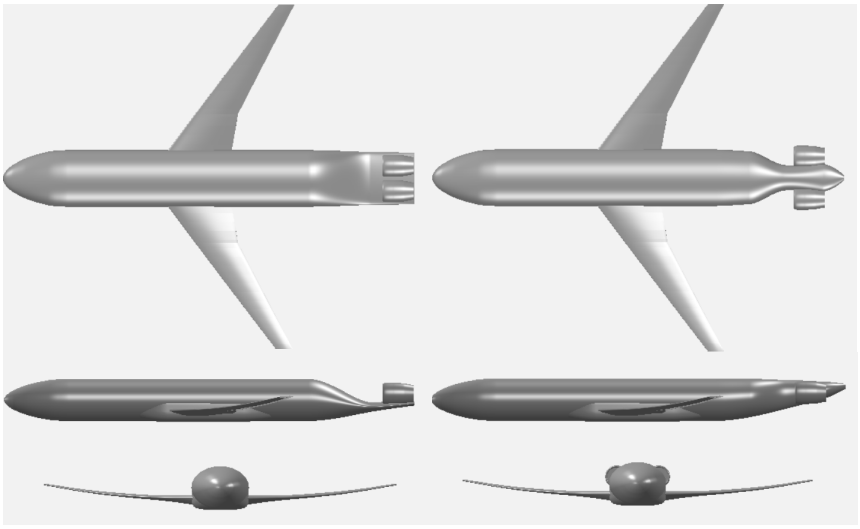

Figure 7.5: 3-views of the templates that are used for generating the geometry models for each DoE case

affecting the BLI effects. The length of the fuselage is fixed at the value chosen in experiment 2, which was based off a notional 737-8. The fuselage cross sectional design was driven by the need to fit two BLI engines on top of the fuselage. As such, this cross section is based off a notional D8, where the cross sectional area of the fore section is matched to values available in literature, and the shape is approximated by a 'sideways ellipse', which from experiment 2.5 is an adequate representation. Both configurations share the same cross section up until the tail cone region, which is modified to integrate the engines.

A simplified representation of the fuselage nose is used since experiment 2.2 shows that this simplification, for shock free cases, has a negligible impact on the BLI effects. A belly fairing is included to minimize the impact of flow separation, at the wing root-fuselage junction, on the BLI effects, as shown in experiment 2.6. Both templates share the same wing design, which is the scaled CRM wing that was used as a reference in experiment 2.6-1. No empennage is included in the templates since the impact of the tails is mostly on the fuselage trailing edge mounted propulsor, which is not considered in this study. However, the y location of the engine and the maximum diameter are constrained for the top mounted engine configuration

to integrate a vertical tail on the sides, like on the D8 concept. Experiment 2.8 highlighted the relative significance of the ramp angle over the skinning angles, as long as the skinning angle settings do not produce a local separation bubble. As such, the skinning angles are somewhat arbitrarily set to smoothen the transition between the fuselage and the ramp, but are not part of the design space.

Following the geometry model definition, the CFD cases have to be set up. The CFD solver settings are kept the same as previously defined in experiments 2 and 3. However, the "expert driver" option in STAR-CCM+ is activated for a small number of cases that struggle to converge. This option basically adjusts the CFL number at each iteration through a relaxation factor for improved convergence, but at the cost of a significantly longer run time. A grid refinement study is conducted for the top-mounted engine configuration to find an appropriately sized mesh that balances accuracy and computational expense. This study is conducted at $M_\infty = 0.8$, $h = 35,000$ft and $\alpha = 2.0$. The wing design parameters and fan diameter are set at the non-BLI baseline values. The results of the grid refinement study are shown in Fig. 7.6. The final mesh chosen is shown with a filled marker. The maximum variation in $C_{P_{K_{\text{in}}}}$ for finer meshes relative to the chosen mesh, when dimensionalized to a force, is approximately 1 lbf. For η_{PR}, this variation is approximately 0.01% and for $\dot{m}$ it is about 0.04%. These variations are quite small and do not warrant the use of a finer mesh.

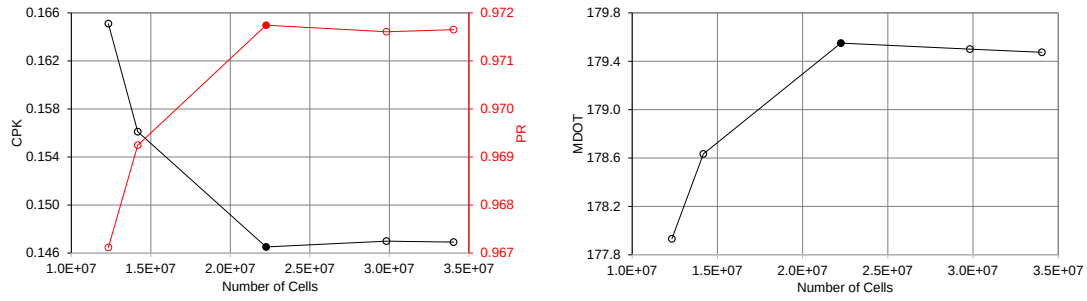

(a) $C_{P_{K_{\text{in}}}}$ and η_{PR} **(b)** $\dot{m}$

Figure 7.6: Summary of results from mesh sensitivity trials

Generate Surrogate Models and Evaluate Quality of Fits

Once the CFD cases are run for each point in the DoE, surrogate models can be fit to the responses. There are certain qualitative and quantitative diagnostic measures to evaluate the validity of generated surrogate models. These are listed as below. Each metric in isolation provides useful information about a surrogate model, but, a holistic view is required to determine the validity of this model.

- R^2 metrics
- Average error as a fraction of the mean response
- Actual vs. predicted trends
- Residual vs. predicted trends
- Model fit error (MFE) distribution
- Model representation error (MRE) distribution
- Evaluate predicted trends against expected results obtained from previous experiments or physics based reasoning

The R^2 metric is a commonly used quantitative measure of how well the assumed model measures variability of the input data. This metric can be evaluated for both the data used to fit the surrogate model and that used to validate it. A surrogate model that perfectly interpolates the input data, which occurs when the number of terms in the model equals the number of data points, has $R^2 = 1$. In general, when there are more data points than model terms, as is the case with the BLI surrogates, $R^2 < 1$. Low values of R^2, such as say $R^2 < 0.6$-0.7 is indicative that the assumed model form for a given response is lacking in accuracy. As a general rule of thumb, high values of R^2, typically above 0.9, are desirable. However, it should be emphasized that when looking at R^2, one must consider the training and validation data separately.

A surrogate model that has low error in fitting the training data will have a high R^2-Training result, but, may suffer from over fitting. In this scenario, the model predictions at data points not used for training the surrogate may be completely inaccurate due to the model overshooting the actual value. As such, R^2-Validation is severely penalized. Thus, when training the surrogate model, one must also track how well the model predicts previously unseen data, and thus, both R^2-Training and R^2-Validation greater than 0.9 are recommended. Typically, R^2-Training is higher than R^2-Validation. Table 7.3 shows the R^2-Training and R^2-Validation values for the BLI surrogates, calculated automatically by JMP. Most values are around 0.98 and above, except R^2-Validation for $\Delta\Phi_{\text{wake}}$ at 0.967, thus satisfying the R^2 criterion.

R^2 by itself, however, is not sufficient to indicate model accuracy. One must also look at other metrics. Another quick diagnostic is to check the root average square

Table 7.3: BLI Surrogate Models R^2 and RASE Metrics

Engine	Metric	$P_{K_{\text{in}}}$*	P_{t_2}	$\Delta\Phi_{\text{wake}}$*	SWETF	SWETN
Top	R^2 Training	0.9987	0.9999	0.9973	1	1
	R^2 Validation	0.9899	0.9995	0.9670	1	1
	RASE Training	0.038	180	0.034	0.002	1×10^{-5}
	RASE Validation	0.076	574	0.074	0.057	2×10^{-5}
	Mean Response	6.45	64354	3.39	4927	0.846
	RASE-Train %Mean	0.59	0.28	1.00	4×10^{-5}	1×10^{-3}
	RASE-Val %Mean	1.18	0.89	2.18	1×10^{-3}	2×10^{-3}
Side	R^2 Training	0.9937	0.9999	0.9964	1	1
	R^2 Validation	0.9840	0.9996	0.9893	1	1
	RASE Training	0.087	172	0.038	0.010	2×10^{-6}
	RASE Validation	0.094	480	0.049	0.036	2×10^{-5}
	Mean Response	6.06	63654	3.67	4656	0.904
	RASE-Train %Mean	1.43	0.27	1.04	2×10^{-4}	2×10^{-4}
	RASE-Val %Mean	1.55	0.75	1.33	8×10^{-4}	2×10^{-3}

*These responses are transformed to an equivalent force and then the natural log of the result is used as a response

error (RASE) as a percentage of the mean response for both the training and validation data. RASE is calculated as the square root of the sum of squared prediction errors divided by the number of observations. A more accurate model minimizes this percentage error. RASE-Training is typically lower than RASE-Validation. An error of less than 2% is desirable, with values closer to 0 being ideal. Table 7.3 shows the RASE and mean response values calculated by JMP for each BLI surrogate. Barring RASE-Validation for the top-engine configuration $\Delta\Phi_{\text{wake}}$ model, all errors as a fraction of the mean response are well below 2%.

The next two diagnostics are more qualitative measures of goodness of fit. The actual vs. predicted plot, as the name suggests, shows the distribution of the actual or true response plotted against the predicted response from the surrogate model. The ideal line of fit is a 45 degree line where the actual and predicted responses are identical. The distribution of points along this ideal fit line is a qualitative indicator of model adequacy. A surrogate model with low prediction error has a tighter fit of points around this ideal fit line, and is evenly distributed along this diagonal without obvious clumping of data points. The residual vs predicted plot on the other hand provides a different perspective on the same data by plotting the residual value (error between the predicted and actual value) against the predicted response. An ideal plot shows random scattering of points that have a residual that is at least an order of magnitude lower than the predicted response. These two plots combined can also indicate the need for higher order terms in the model, or transformations to the response, based on how well the distribution of points agrees with the ideal scenario. An example of poor and acceptable fits can be seen in Fig. 7.7 generated by JMP.

In Fig.7.7, the second order response surface fit is shown for $C_{P_{K_{\text{in}}}}$ on the left and the transformed response on the right. The actual vs. predicted plot for $C_{P_{K_{\text{in}}}}$ shows a clumping of points at the bottom corner, a few outliers, and a wide confidence interval around the ideal fit line, indicating poor statistical significance of the assumed

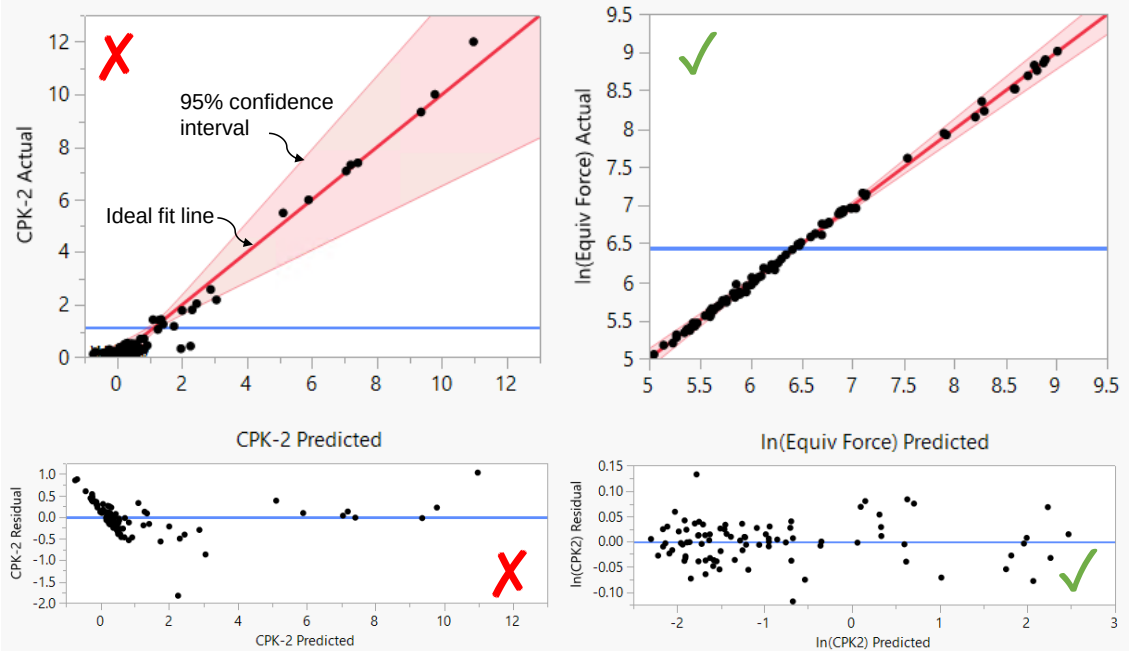

$C_{P_{K_{\text{in}}}}$ $\ln\left(C_{P_{K_{\text{in}}}} q_\infty S_{\text{ref}}\right)$

Figure 7.7: Actual vs. predicted and residual vs. predicted plots for the top mounted engine $P_{K_{\text{in}}}$ surrogate comparing a poor vs. acceptable fit

model for this response. The residual vs. predicted plot shows a distinctive clumping pattern, and the residuals are also on the same order as the predicted response. Both these plots indicate a poor fit for $C_{P_{K_{\text{in}}}}$, suggesting the need for a transformation. By converting the non-dimensional BLI effect to an equivalent force, and then taking the natural log of this metric, the second order response surface equation is now a much better model for this transformed response. The actual vs. predicted and residual vs. predicted plots are acceptable based on the diagnostics discussed above. The confidence interval is much smaller and the residuals are one to two orders of magnitude smaller than the predicted response. Similar transformations are required for $\Delta\Phi_{\text{wake}}$ to improve the fit. For η_{PR}, it is found that P_{t_2} is a better metric to fit a standard second order RSM. Fig. C.3 in Appendix C shows the actual vs. predicted and residual vs. predicted plots for the transformed responses. In general, the plots indicate adequate fits, with the $P_{K_{\text{in}}}$ response for the side engine case showing the

largest spread in the residuals. The residual pattern showing clusters of three points in Fig. C.3 for the $\Delta\Phi_{\text{wake}}$ responses is driven by the sampling plan described previously, where the fan diameter is changed independently three times per CFD run. There also appear to be clusters in the P_{t_2} residuals, but given that the errors are a much smaller percentage of the response, these are not concerning.

The last statistical diagnostic measures are the MFE and MRE distributions. The MFE distribution shows the relative error of the model with respect to the actual values, for the points used to train the surrogate. The MRE distribution on the other hand shows the same information, but for the points used to validate the model. These two distributions basically provide a quantitative perspective of the data in the actual vs. predicted and residual vs. predicted plots, categorized by training and validation samples. A good second order RSM is one that has an MFE histogram resembling a standard normal distribution, with a mean of zero, a standard deviation of 1%, and a range of ±3%. These criteria imply that the error in neglecting higher order terms in a second order RSM is acceptable. The MRE distributions on the other hand typically show a larger variation. Outliers will affect the standard deviation and range of these distributions. These should be investigated to determine whether they can be ignored or not. Fig. C.3 in Appendix C shows the MFE plots for the three main BLI effects, while Fig. C.4 shows the MRE distributions. The mean percentage error is close to zero for all responses. The standard deviations for the training data for all responses is either less than 1%, or marginally over 1%, with the $P_{K_{\text{in}}}$ surrogate for the side engine showing the largest standard deviation at 1.4%. The upper bound on percentage error for this response is around 3.4%, while the lower bound for this response is 2.97%. All remaining responses have an error range well within ±2-3%. The MRE plots show larger variations, as expected. However, the error range is still within 3%, the mean errors are still close to zero, and the standard deviations, though larger than those for the MFE, are in most instances below 1.5%.

Lastly, in addition to the statistical measures of goodness of fit, it is also helpful to see if the predicted trends make sense from a physics perspective. Fig. 7.8 presents profiler plots generated by JMP that show a snapshot of the BLI effects trends against the input variables, at a user specified design and operating point. These profilers are generated from the fitted surrogate models for the side-engine configuration. The chosen point can be interactively varied, and the observed trends change depending on the non-linearity of the response and interaction effects between the variables. The design and operating point shown in Fig. 7.8 is chosen to match the conditions at which experiments 2 and 3 were conducted. This way, trends from these experiments can help shed light on the reasonableness of the predicted response. While the profiler plots show dimensional forces and pressure, for a fixed Mach and altitude these dimensional values carry the same information as their non-dimensional counterparts investigated in experiments 2 and 3.

Directionality of the BLI effects trends with wing design changes agree with those seen in experiment 2.6, summarized in Fig. A.6 and Fig. 5.36. The reference engine location for comparison purposes in these figures would be at either A0.90C0 or A0.95C0. In addition, the opposite correlations of $P_{K_{\text{in}}}$ and pressure recovery with

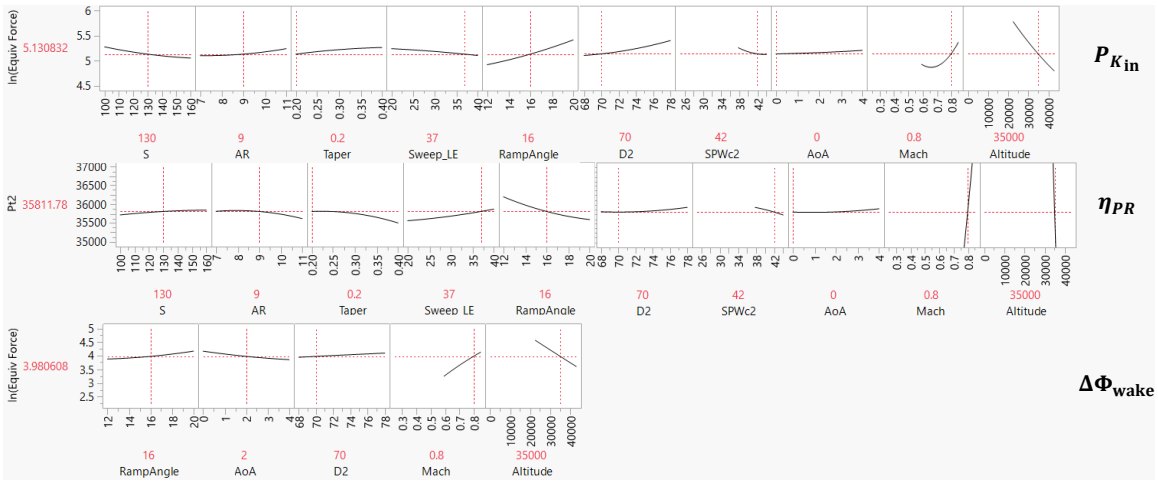

Figure 7.8: Profiler plots showing trends of the three main BLI effects for the side-engine configuration, at a given design and operating point

wing design changes, as expected and observed in experiment 2.6, is captured by the surrogate models. Trends with ramp angle, for all three BLI effects, also agree with findings from experiment 2.8. The decrease in $P_{K_{\text{in}}}$ and pressure recovery, with an increase in flow rate or a decrease in fan diameter, agrees with results from experiment 3.1, which considered a vehicle with the same engine location and extent of ingested boundary layer. Mach and altitude trends observed are also consistent with physics. One expects a reduction in the equivalent force benefit going up in altitude for a fixed Mach number, or lowering Mach number at the same altitude, due to dependency of dimensional force on freestream dynamic pressure. Mach and Reynolds number effects on the boundary layer also explain P_{t_2} trends with flight conditions. These trends, in conjunction with the statistical diagnostic information discussed above, show strong support for the validity of the developed BLI effects surrogate models.

7.2 Vehicle Sizing Loop

This section describes how the BLI coupled and decoupled methodologies are implemented for aircraft sizing in the EDS framework. The focus is on how the BLI surrogates are integrated and used within this design environment. Fig. 7.9 compares the XDSM of the coupled BLI vehicle sizing methodology, first introduced in Fig. 3.3 in chapter 3, to the decoupled approach. The order of the processes is indicated by the

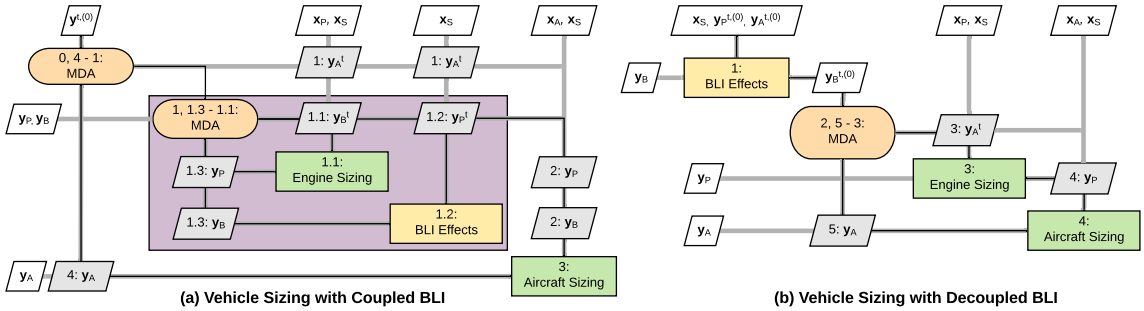

Figure 7.9: XDSMs comparing the coupled and decoupled BLI effects accounting approaches in conceptual design vehicle sizing

numbering, as is standard XDSM convention. The reader is also encouraged to refer to chapter 4, and in particular Fig. 4.5, for a general overview of the sizing process. The processes depicted in the diagrams are described in the following sub-sections.

7.2.1 Coupled BLI Sizing

The BLI aircraft sizing loop begins with a specification of airframe parameters, $\mathbf{x}_{\mathrm{A}}$, engine parameters, $\mathbf{x}_{\mathrm{P}}$, and parameters shared by the engine, airframe, and BLI effects models, $\mathbf{x}_{\mathrm{S}}$, in a csv file. Initial guesses for the coupling variables related to each discipline $\mathbf{y}^{t,(0)}$ are also specified in this file. These parameters are used as inputs for NPSS, FLOPS, WATE++, the BLI surrogates, and other disciplinary analysis tools in EDS. In addition to the csv input file, there are files defining the engine architecture for NPSS and a baseline aircraft model file for FLOPS. Table 7.4 highlights what kind of variables each of the above vectors represent. Note that the list of airframe and propulsor design variables shown in Table 7.4 is not exhaustive. The shared and coupling variable lists, however, are complete.

Table 7.4: Examples of Design Parameters and Coupling Variables

Parameter	Examples
$\mathbf{x}_{\mathrm{A}}$	Empennage volume coefficients, empennage: AR, λ, $\Lambda_{c/4}$, wing dihedral, component weight factor estimations: avionics, APUs, etc., component lengths, wing loading, thrust to weight ratio, etc.
$\mathbf{x}_{\mathrm{P}}$	FPR, BPR, HPCPR, LPCPR, maximum fan specific flow, compressor and turbine hub to tip ratios, component efficiencies, assumed turbomachinery design characteristics like number of blades, aspect ratio, etc. for weight calculations, assumed duct losses, $T_4^{\max}$, etc.
$\mathbf{x}_{\mathrm{S}}$	Wing: AR, Λ_{LE}, λ, ramp angle ϕ, flight conditions
$\mathbf{y}_{\mathrm{A}}$	Wing planform area and thrust scaling factor (or thrust requirements at engine design points)
$\mathbf{y}_{\mathrm{P}}$	Fan diameter, max nacelle diameter, engine length, engine weight, engine deck
$\mathbf{y}_{\mathrm{B}}$	$P_{K_{\mathrm{in}}}$, η_{PR}, $\Delta\Phi_{\mathrm{wake}}$, fuselage wetted area (SWETF), nacelle wetted area (SWETN)

Initial values for $\mathbf{x} \equiv \{\mathbf{x}_\mathrm{A}, \mathbf{x}_\mathrm{P}, \mathbf{x}_\mathrm{S}\}$ are provided by the non-BLI baseline obtained in the pre-vehicle sizing stage. These values are fixed for the sizing process. The first process in Fig. 7.9a is the engine design loop (process 1), which involves a feedback between engine sizing and the evaluation of BLI effects. The engine is sized using a multi-design point approach, as stated previously. The design points are: 1) Aerodynamic Design Point (ADP) 2) Top of Climb (TOC) 3) Takeoff (TKO) 4) Sea Level Static (SLS). Each design point requires a specification of the flight Mach number, altitude, deviation from standard atmosphere temperature (which is set to zero for these cases) and a design thrust required. ADP is set at $M_\infty = 0.8$ and $h = 35,000$ ft, which is where most of the experiments in this thesis have been conducted. TOC is also set at the same flight conditions, but involves operating the fan at a higher speed. TKO and SLS are set at sea level, but TKO is defined at $M_\infty = 0.25$, while SLS is by definition at static conditions. The initial thrust requirements at these points, contained in $\mathbf{y}_\mathrm{A}^t$, are meant to represent expectations of the vehicle performance at these flight conditions. A more accurate initial guess results in fewer iterations between NPSS and FLOPS.

For a given set of $\mathbf{x}_\mathrm{P}$ and $\mathbf{y}_\mathrm{A}^t$, NPSS designs an engine that meets the design requirements. The BLI effects, contained in the vector $\mathbf{y}_\mathrm{B}$, are integrated in different ways. The mapping between thrust-drag and power balance, derived in chapter 4, allows for the BLI effects P_{K_in} and $\Delta\Phi_\mathrm{wake}$ to be accounted for as an equivalent force benefit. This effective force is tacked on to the gross thrust calculations for the engine. The η_{PR} losses from the BLI surrogates are used to overwrite default inlet performance curves. The BLI surrogates are part of the engine model and are evaluated simultaneously with the cycle analysis in this iterative process. There is a set of surrogates per configuration, and if-statements are used to select the appropriate models based on the engine location. While the surrogate input bounds were set previously to capture a reasonable design and operation space, checks are imposed

within the environment to make sure there is no extrapolation from the BLI surrogate models. In particular, for flow rates below the surrogate lower bounds, the BLI gross thrust correction is set to zero, and the pressure recovery values are calculated from the built in inlet performance curves. Additionally, since the fan is oversped at TOC, the specific flow at that condition is marginally higher than the specified design value. To prevent extrapolation beyond the upper limit of 44 lbm/ft^2-s, the maximum design SPW_{c_2} is set to 43 lbm/ft^2-s such that even at overspeed conditions, the maximum SPW_{c_2} is within the BLI surrogate bounds. Note that these SPW_{c_2} values are based on standard atmosphere conditions. The 'Ambient' element in NPSS allows for specification of the flight Mach number and altitude, and can map these conditions to standard atmosphere properties.

While the BLI effects surrogates are a function of angle of attack, this variable is not recognized by any of the disciplinary analysis codes in EDS. All drag polars in FLOPS are specified in terms of C_D and C_L. Thus, one must provide an estimate for the operating angle of attack at any given point in the mission for the BLI surrogates. One way of doing so is to specify an h-α schedule. Within the range of 0°-4°, higher aircraft angles of attack are likely to be found at low altitudes during takeoff and climb. As the aircraft approaches cruising altitude, the angle of attack is expected to decrease. As such, a step function approach is adopted where for any operating point below 10,000 ft., α is assumed to be 4°. Between 10,000 and 30,000 ft. α is assumed to be 2° and for higher altitudes where the aircraft will cruise, α is set to 0°. Given the sensitivity of the BLI effects to α, seen in experiment 2.1, changes to this schedule will impact the fuel burn estimate of the BLI vehicle relative to the non-BLI counterpart. However, for the purposes of testing hypothesis 1, this sensitivity is not critical. Since the same schedule is used for all experiments, coupled and decoupled, the impact of α on the conclusions drawn with regards to hypothesis 1 are unaffected. This claim is supported with an α sensitivity study in experiment 1.1.

After the engine has been sized for an initial set of thrust requirements and BLI corrections, off design analysis generates the engine decks to be used by FLOPS. In addition, WATE++ provides estimates for the engine weight and critical dimensions. The pylon weight for a non-BLI configuration is calculated based on a fixed fraction of the total engine weight. For the BLI configurations without a python, this weight is set to zero. The engine dimensions provided by WATE++ are used by FLOPS to calculate the nacelle drag, however, the SWETN surrogate developed previously corrects the nacelle wetted area based on the sized fan diameter and inlet ramp angle. The fuselage wetted area is provided from the SWETF surrogate. FLOPS sizes the airframe for the specified wing loading, thrust to weight ratio, mission, range constraint, and other airframe design parameters. Based on the gross weight converged on by FLOPS and the user specified wing loading, the wing is resized from the initial guess. This new value is passed back to the surrogates in the subsequent iteration. In addition, the engines are rescaled if they produce more thrust than required for the mission, or are unable to meet the thrust requirements. This scaling factor is applied to the thrust requirements at the engine design points for the next sizing iteration. The sizing iteration converges when Eq. (4.34) is satisfied. For the wing area, the convergence tolerance is set to 5ft^2.

The only inputs to the BLI effects surrogates that change in the sizing process are d_2, and S. The fan diameter changes within both process 1 (as part of engine on-design) and as part of process 0 (when the engines are scaled based on airframe performance). The planform area only changes in the outer MDA loop (process 0). For the *coupled BLI sizing, both d_2, and S inputs to the surrogate models are updated with each iteration.* The fan diameter updates affect all 5 BLI effects surrogates in $\mathbf{y}_\text{B}$ while the planform area updates affect P_{K_in}, η_{PR}, and $\Delta\Phi_\text{wake}$.

7.2.2 Decoupled BLI Sizing

The decoupled approach shown in Fig. 7.9b is intended to be reflective of the decoupled methods described in literature for BLI modeling. In particular, the system level study for the BWB by Hardin [35] and the STARC-ABL vehicle design study by Welstead [98] are prime examples of this decoupled approach, as discussed in chapter 2. Both these studies relied on an handful of CFD solutions for the boundary layer, from a fixed aircraft geometry, thereby ignoring the aero-propulsive coupling. To mimic these approaches with the BLI surrogate models, the disciplinary coupling variable inputs to the surrogates: d_2 (in $\mathbf{y}_P^{t,(0)}$) and S (in $\mathbf{y}_A^{t,(0)}$), are fixed at their initial guessed values. These quantities are not updated over the course of the sizing loop. The operating condition inputs are allowed to vary for the surrogates, since the decoupled approaches in literature did account for these conditions in some manner. *It should be emphasized that the decoupled approach here solely refers to the treatment of the BLI effects on the aircraft design, and not the entire sizing process.* The engine size is still scaled with the aircraft in an iterative manner as before. It is just that the BLI effects are not corrected for the changing aircraft size.

The differences in aircraft design and performance between the decoupled and coupled approaches ultimately depend on the initial guess provided for d_2 and S. If these are close to the values that are obtained from the coupled approach, then naturally, the differences will be smaller. However, it is not always easy to estimate what the coupled design would look like without actually accounting for the BLI aero-propulsive coupling. A reduction in wetted area, engine pylon weight, along with $P_{K_{\text{in}}}$ and $\Delta\Phi_{\text{wake}}$ reduce engine thrust requirements, allowing for a smaller engine. However, boundary layer blockage effects need to be accounted for, and the drop in engine performance due to a loss in pressure recovery both tend to result in a larger fan diameter. The larger engine is heavier, has more wetted area, which tends to increase the thrust requirements, counteracting some of the aforementioned benefits.

While a larger area implies more BLI, this is not necessarily optimal for performance. Additionally, changes in fuel and engine weight also affect the wing size, which in turn has a direct impact on both aircraft drag and the BLI effects. Given all these competing interactions, a justifiable initial guess for d_2 and S would be that obtained from an equivalent non-BLI baseline. This strategy would be consistent with the decoupled approaches in literature, where the CFD profiles were obtained from a representative non-BLI aircraft. If BLI related aero-propulsive coupling is weak, then the final d_2 and S for the BLI aircraft (with a decoupled or coupled approach) will be close to the non-BLI baseline. If the coupling is stronger, more significant differences are expected, justifying the need for the methodology proposed in this thesis.

7.2.3 Experiment 1.1: MDA Sweeps

In these experiments, first, design FPR is varied between 1.48 and 1.60 for a constant value of wing loading (WSR) at 131.4 lbf/ft^2, for the non-BLI and BLI versions of both aircraft configurations. The ranges for FPR are determined based on expected variations in d_2. The fan diameter cannot be outside the 68-78 in. range for the BLI configuration. Then, WSR is varied between 115 to 145 at a fixed FPR of 1.54. The non-BLI configurations are analyzed first. The sized d_2 and S for each case are used as inputs for the decoupled-BLI runs. The metric of interest, design block fuel, accounts for fuel burn during the design mission and during taxi in, but not reserves. Different people make different assumptions regarding the reserve mission with respect to the distance to the nearest airport, maximum cruising altitude, speed, etc. While a 200 nautical mile reserve mission is specified when sizing both the BLI and non-BLI aircraft, the fuel burn for this mission is not considered for the experiments.

Fig. 7.10 shows the block fuel requirements for the top-engine configuration for the non-BLI, BLI-decoupled, and BLI-coupled variants, while Fig. 7.11 shows the same for the side-engine configuration. A few comments on the general fuel burn trends

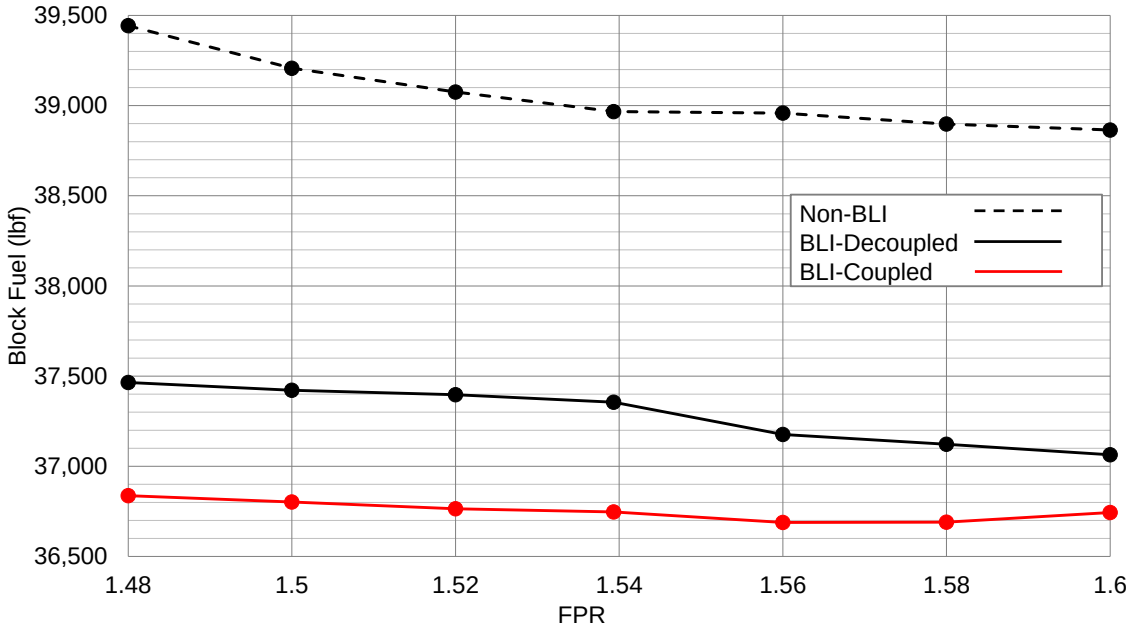

(a) FPR sweep for WSR=131 lbf/ft^2

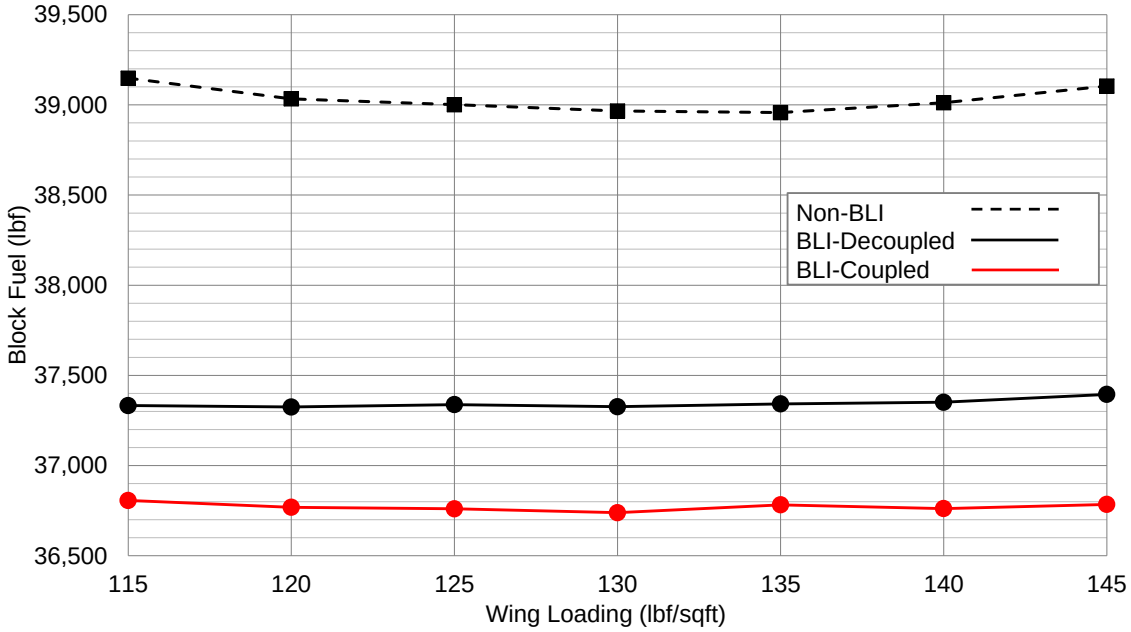

(b) WSR sweep for FPR = 1.54

Figure 7.10: Experiment 1.1 - Block fuel requirements for the non-BLI, BLI-decoupled, and BLI-coupled variants of the top engine configuration as a function of design FPR and WSR

with FPR and WSR can be made first, before focusing on how the results support hypothesis 1. In all cases, fuel burn savings going from the non-BLI to the BLI variant

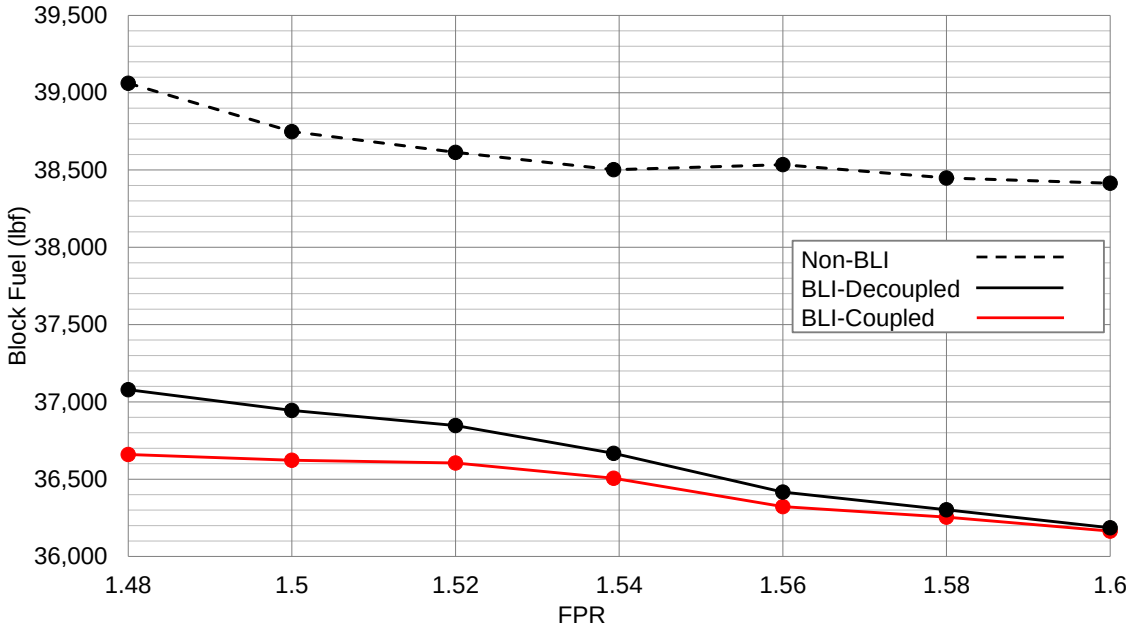

(a) FPR sweep for WSR=131 lbf/ft^2

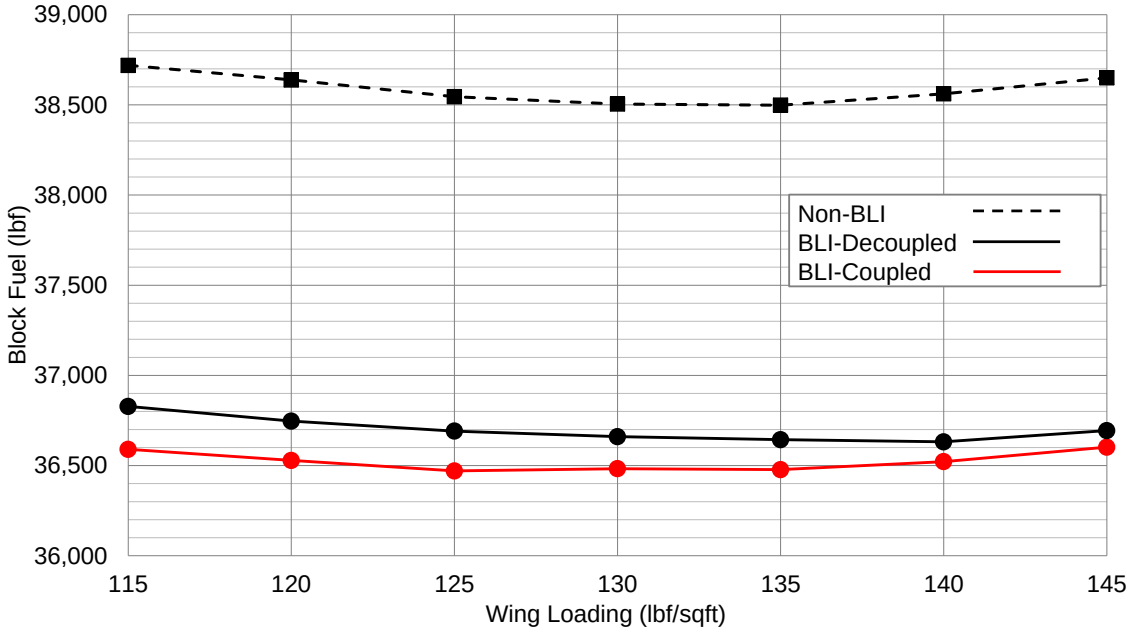

(b) WSR sweep for FPR = 1.54

Figure 7.11: Experiment 1.1 - Block fuel requirements for the non-BLI, BLI-decoupled, and BLI-coupled variants of the side engine configuration as a function of design FPR and WSR

is observed, as expected. With regards to FPR, both the BLI and non-BLI variants exhibit similar trends. Typically, for a large variation in FPR, a fuel burn bucket is

observed, where the fuel burn is minimized at some FPR value. Moving away from that point in either direction results in an increase in fuel burn. The aerodynamic penalties of large nacelles for low FPR engines outweigh the propulsive efficiency benefits, resulting in an increase in fuel burn with a decrease in FPR. This trend is observed in both Fig. 7.10 and Fig. 7.11. The BLI vehicle fuel burn increase with a decrease in FPR is much flatter for lower FPR values, compared to the non-BLI vehicle. This behavior is explained by the BLI benefit from larger fans offsetting the aerodynamic penalty to a certain extent, which is obviously not a factor for the non-BLI variant. On the other end, the lower propulsive efficiency of high FPR engines eventually outweighs the aerodynamic benefits of smaller engines, resulting in an increase in block fuel with an increase in FPR. This behavior is not observed in the results because the upper bound of FPR considered, based on the fan diameter constraint, is not high enough for the propulsive efficiency penalties to dominate.

Fuel burn trends with wing loading are again similar for both BLI and non-BLI variants and exhibit a bucket, which suggests an optimal wing size and aircraft weight combination. The fuel burn increase in either direction of the optimal is due to a combined effect of changes in aircraft weight due to sizing effects, which affects the required C_L, changes in wing size and weight, and the corresponding airframe drag resulting from the aerodynamic efficiency of the wing to produce the required C_L. BLI trends, in particular for the top-engine configuration, are flatter. Given that the wing has a more significant impact on the ingested boundary layer for the top-engine aircraft, as opposed to the side-engine vehicle, the differences in fuel burn vs. WSR slope for the BLI variants is not unexpected.

Now, with regards to the results in context of hypothesis 1, there are three main takeaways from Fig. 7.10 and 7.11:

(i) There are significant differences in block fuel burn for a fixed range constraint if one uses a decoupled approach instead of a coupled

(ii) These differences are more pronounced for the top-mounted engine, given the wing influence on the ingested inflow, as shown in experiment 2.6.

The decoupled approach consistently over-predicts the block fuel requirements for these cases, compared to the coupled method. The initial guesses for d_2 and S that are provided to the decoupled approach, from the non-BLI variants, result in an under-estimation of the BLI effects. As a consequence, the aircraft is over sized, as hypothesized. The converged d_2 and S for the decoupled BLI aircraft are larger than those predicted by the coupled approach, as seen in Fig. 7.12 for the top-engine configuration. Conversely, if the d_2 and S inputs to the BLI surrogates for the decoupled approach were higher than the converged results from the coupled approach, the BLI benefit would be over-predicted. Consequently, the final converged values of d_2 and S for the decoupled approach would be lower than the coupled results.

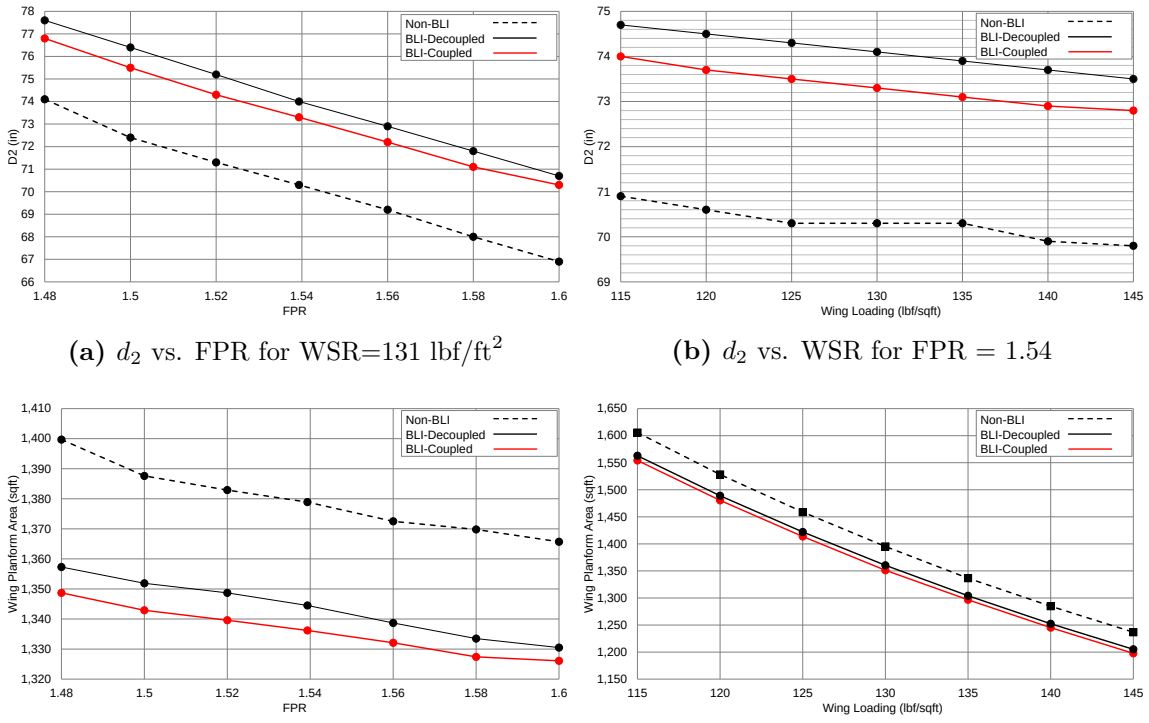

(a) d_2 vs. FPR for WSR=131 lbf/ft^2

(b) d_2 vs. WSR for FPR = 1.54

(c) S vs. FPR for WSR=131 lbf/ft^2

(d) S vs. WSR for FPR = 1.54

Figure 7.12: Experiment 1.1 - Variations in d_2 and S vs. FPR and WSR for the top engine non-BLI, decoupled-BLI, and coupled-BLI configurations

The discrepancy between the decoupled and coupled approaches is the smallest when either the initial d_2 and S inputs for the BLI surrogates are close to the converged coupled values, or, when the BLI related aero-propulsive coupling is weaker, as evident in the side engine block fuel results in Fig. 7.11, and the comparison of the final d_2 and S values for the aircraft in Fig. 7.13.

The results in Fig. 7.13 suggest that while BLI does have an impact on the sized vehicle, based on the difference between the BLI and non-BLI curves, the aero-propulsive coupling due to BLI is a lot weaker than observed for the top-engine configuration. As a result, even though the non-BLI values of d_2 and S, which are used as inputs for the decoupled approach BLI surrogates, are considerably different from the converged BLI results, variations in d_2 and S as part of the sizing process have a smaller impact on the BLI effects for this engine location. Thus, the coupled approach

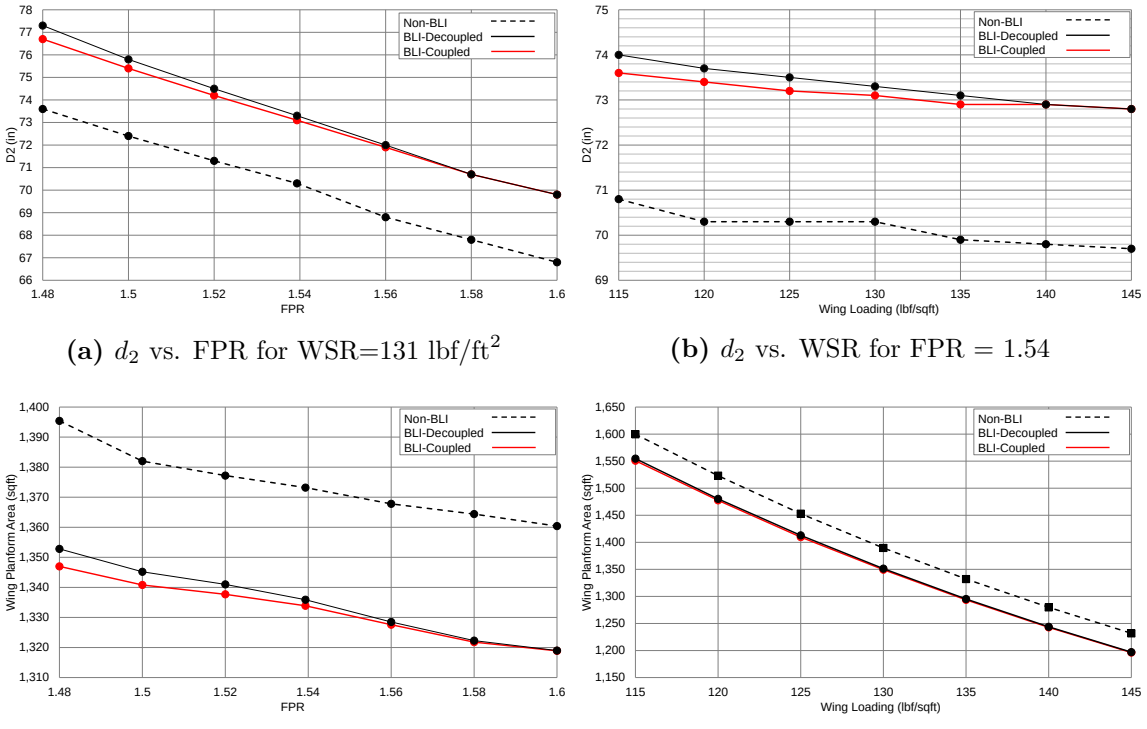

(a) d_2 vs. FPR for WSR=131 lbf/ft^2

(b) d_2 vs. WSR for FPR = 1.54

(c) S vs. FPR for WSR=131 lbf/ft^2

(d) S vs. WSR for FPR = 1.54

Figure 7.13: Experiment 1.1 - Variations in d_2 and S vs. FPR and WSR for the side engine non-BLI, decoupled-BLI, and coupled-BLI configurations

results are not much different from the decoupled approach. Another interesting observation is that the discrepancy between the coupled and decoupled approaches reduces with an increase in FPR and WSR (a decrease in d_2 and S). For larger fans, there is more BLI. Thus, the d_2 and S inputs based off the non-BLI configuration, are further away from the 'true' converged solutions from the coupled approach. For smaller fans with less BLI, relative variations in the BLI effects due to aero-propulsive coupling are less significant when compared to the net BLI effect over a non-BLI vehicle. Thus, while the MDA process is still able to converge to a BLI configuration with a relatively consistent difference in d_2, S, and block fuel, to the equivalent non-BLI configuration, the differences between the coupled and decoupled approaches decreases.

Fig. 7.14 shows the percentage difference in the block fuel burn estimate between the decoupled (D) and coupled (C) approaches ($100 \times \frac{D-C}{C}$), comparing it between the top and side engine configurations for each case in the FPR and WSR sweeps. The trends observed support the above discussion and hypothesis 1. The largest difference in the predicted fuel burn between the decoupled and coupled approaches is about 1.7% (628 lbf) for the top-engine configuration at FPR=1.48 for WSR=131.4lbf/ft^2. The fuel burn reduction benefit, comparing the coupled result to the same non-BLI design point is 6.6% (2606 lbf). Thus, the fuel burn discrepancy based on using a decoupled approach instead of a coupled, as a percentage of the fuel burn savings going from non-BLI to BLI ($100 \times \frac{D-C}{\text{No-BLI}-C}$), is about 24% for this design. This difference is a substantial portion of the predicted BLI-benefit and highlights how not modeling the aero-propulsive coupling can be a significant source of uncertainty in the fuel burn savings numbers quoted in literature.

There is some noise in these trends, primarily arising from the wiggle room offered by the convergence tolerances specified for the multitude of iteration loops involved in this sizing process. There are convergence loops in the MDP engine sizing with

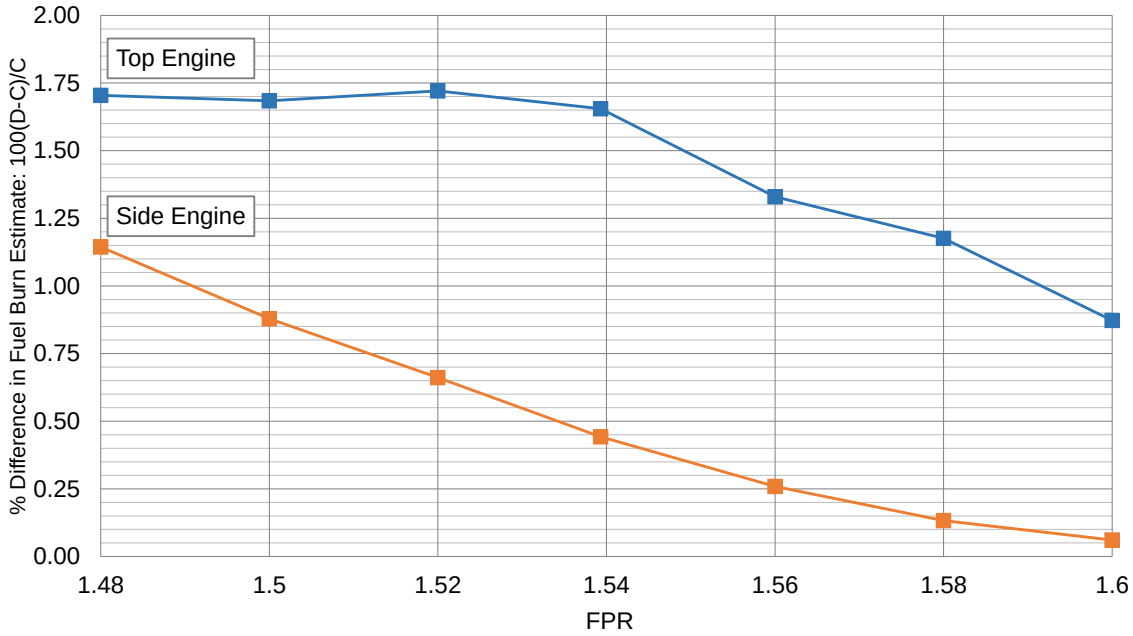

(a) FPR sweep for WSR=131 lbf/ft^2

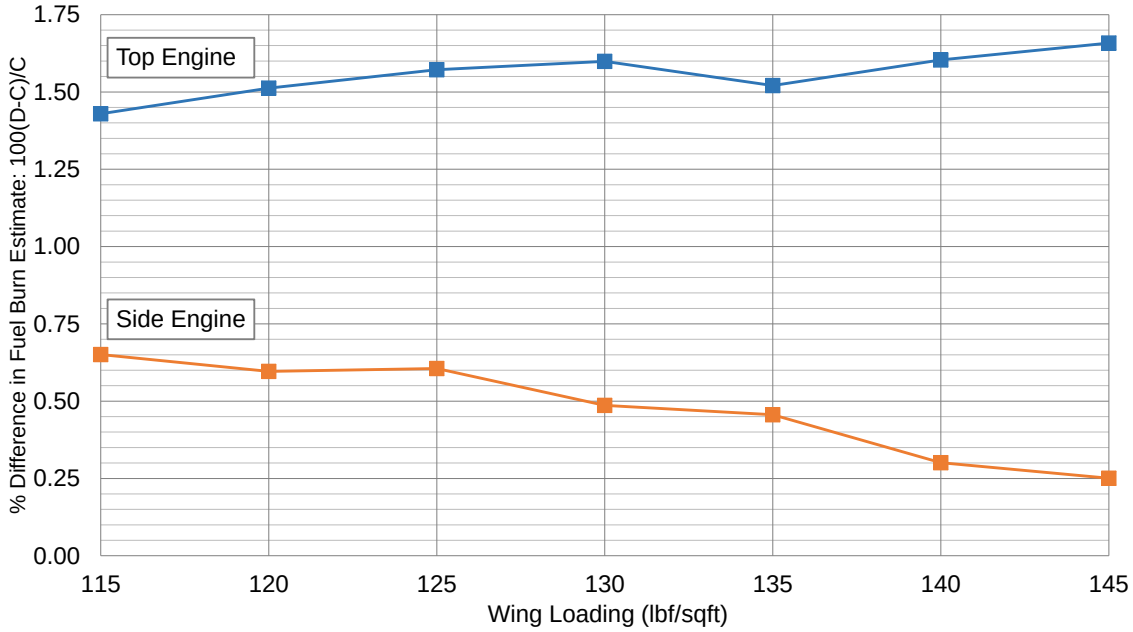

(b) WSR sweep for FPR = 1.54

Figure 7.14: Experiment 1.1 - Percentage difference in the block fuel burn estimate between the decoupled and coupled approaches for the top-engine configuration, compared to the side-engine configuration

the BLI effects, a convergence loop in the aircraft gross weight-wing scaling, and the main vehicle convergence involving scaling of the engine based on the airframe design.

While tightening the specified tolerances may flatten some of the observed 'bumps', it increases the risk of solver divergence. Minor perturbations to the initial D' values at the engine sizing points helped smoothen out the trends a little, which have been presented in the figures above.

A few comments need to be made to provide some support to the BLI benefit observed relative to the non-BLI configuration. For the top-engine vehicle, in the FPR sweep, there is a fuel burn reduction for the *coupled*-BLI configuration in the range of 5.5% to 6.6% and for the WSR sweep, between 5.6% to 6% relative to the non-BLI aircraft. For the side-engine configuration, the *coupled*-BLI fuel burn reduction varies between 5.2% and 6.1% for the FPR sweep and between 5.2% to 5.5% for the WSR sweep. *These differences in fuel burn are solely due to BLI and not due to the addition of technologies on the BLI configuration that are not on the non-BLI variants.* While quantifying the BLI benefit relative to a non-BLI configuration is not the primary purpose of this experiment, it should be noted that the fuel burn reductions calculated here are still within expectations. Context can be obtained by looking at some system level BLI studies in literature that have quoted fuel burn reduction numbers. Hardin [35] showed a 3-5% BLI fuel burn benefit for the N+2 BWB concept relative to an appropriate BWB baseline with podded engines. This benefit increased to around 10% for the N+3 BWB concept. Yutko [104] showed a 26-27% block fuel reduction for the D8 compared to the 737-800, though of course, the 737-800 is no longer state of the art. Welstead [98] showed a 12% reduction in design block fuel burn for the STARC-ABL, compared to a N3CC non-BLI reference with TRL 6 technologies. In context of the above results, the predicted system level fuel burn savings of 5-7%, using current state of the art technologies for both the BLI and non-BLI variants, is not unrealistic. Sources of uncertainty, in particular the BLI effects prediction errors from the surrogates, can affect these values. This point is discussed further in context of experiment 1.2 and in chapter 8.

Sensitivity of Hypothesis 1 to Operational Uncertainty in α

To determine whether the assumed h-α schedule affects the conclusions drawn above, α is changed and the FPR sweep is rerun for both the top and side-engine aircraft. The following h-α schedules are investigated:

(i) Fixed $\alpha = 3°$ over the entire flight envelope

(ii) Fixed $\alpha = 1°$ over the entire flight envelope

(iii) Varied $\alpha = 4°$ for $h < 10,000$ft., $\alpha = 3°$ for $10,000 \leq h < 30,000$ft. and $\alpha = 2°$ for $h \geq 30,000$ft.

Like in Fig. 7.14a, the percentage difference in block fuel burn benefit between the decoupled and coupled approaches is tracked and compared between engine locations, for the different schedules. Fig. 7.15 presents these trends. Trends from Fig. 7.14a are also included for reference. As expected, there are variations in the trends, high-

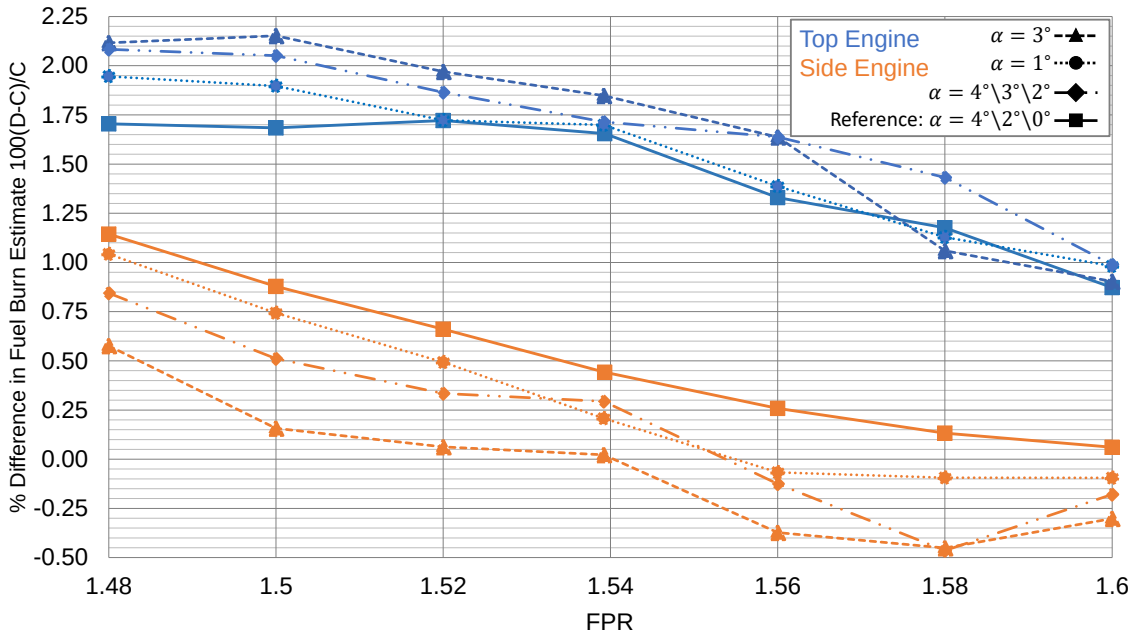

Figure 7.15: Experiment 1.1 - Percentage difference in the block fuel burn estimate between the decoupled and coupled approaches for the top-engine configuration, compared to the side-engine configuration, for varying h-α maps

lighting an additional source of uncertainty in fuel burn savings from BLI. However, the top-engine configuration consistently shows appreciable differences between the two approaches, and these differences are larger than those for the side-engine configuration. Thus, hypothesis 1 is still valid regardless of the h-α schedule assumed. For experiment 1.2, the original h-α map is used.

7.3 Vehicle Optimization

The results of experiment 1.1 clearly support hypothesis 1. Now, an extended design space exploration study is conducted and the optimum vehicle designs are chosen, first based on lowest block fuel burn, and then smallest TOGW. The design space exploration and optimization serve two purposes:

(i) Extend experiment 1.1 by looking at more airframe and cycle design parameters to investigate differences in trends of key metrics when comparing the decoupled approach to the coupled approach for both engine locations

(ii) Determine whether the optimized designs differ between the two approaches and how these differences compare between the top and side engine aircraft

Differences in the trends and optimized designs lend further support to hypothesis 1 and the need for a coupled and parametric aero-propulsive methodology for BLI concept design. The methodology described in chapter 4 leveraged the MDF architecture for MDAO. As discussed before, this architecture treats the MDA problem as a black-box function. Thus, while an optimizer can be directly linked to the EDS environment in which the vehicle sizing MDA takes place, this serial approach towards obtaining an optimum is not very informative. Given that the vehicle sizing loop in EDS takes only a few minutes to run, several hundreds of cases can be run *in parallel* for different design combinations in a design space exploration study. Main design and performance metrics for each case can be recored and surrogate models can be

generated for each response. With the surrogates, one gets a visual comparison of the trends, and one can also optimize on these surrogates. The design space exploration and optimization process is described in the following sub-section.

7.3.1 Experiment 1.2: Design Space Exploration and Optimization

The design space exploration and optimization are conducted for both the non-BLI and BLI variants of the top-engine and side-engine configurations. For the BLI versions, two separate studies are conducted: one with BLI-coupling, and the other decoupled. The design variables considered are shown in Table 7.5. An OPR constraint in the range of 45-55 (assuming duct losses) is imposed based on expected values for a direct drive fan in the 2035 time frame. This constraint filters out infeasible combinations of FPR, LPCPR, and HPCPR within the specified bounds. A leading edge sweep constraint between 20°-40° is also imposed. FLOPS internal aerodynamics are based on quarter chord sweep. The BLI surrogates, however, were modeled using leading edge sweep. Since the mapping between quarter chord and leading edge sweep is based on taper ratio and aspect ratio, the leading edge sweep constraint filters out disallowed combinations of AR, λ, and $\Lambda_{c/4}$. The inlet ramp angle variable does not feature in the non-BLI design space exploration.

Table 7.5: Experiment 1.2 - Design Variables for Design Space Exploration

Input Variable	LB	UB	Type	Comments
FPR	1.48	1.60	Propulsor	OPR Constraint 45-55
LPCPR	1.25	2.25	Propulsor	OPR Constraint 45-55
HPCPR	15	35	Propulsor	OPR Constraint 45-55
AR	7	11	Airframe	
λ	0.2	0.4	Airframe	
$\Lambda_{c/4}$ (°)	20	40	Airframe	Λ_{LE} constraint 20°-40°
ϕ (°)	12	20	Airframe	Only for BLI variants
WSR	115	145	Airframe	

Two space filling DoEs are created in JMP for the non-BLI and BLI studies. Each DoE has 2000 cases that are split 75%-25% for training and validation. There are enough cases within each DoE to account for significant non-linearity in the responses and failed cases due to convergence issues. Scatterplot matrices showing these DoEs for the BLI cases are presented in Fig. C.5 in Appendix C. The metrics of interest are design block fuel, d_2, S, TOFL, LDGFL, TOGW, and SLS thrust per engine. An artificial neural network model is used to fit these reposes, with the final architecture shown in Fig. 7.16. The number of neurons per layer and number of hidden layers are determined based on the surrogate model diagnostic measures for each response, introduced in context of the BLI effects models in section 7.1.2. The final surrogate model quality metrics calculated automatically by JMP for the non-BLI, BLI-coupled, and BLI-decoupled variants are included in Appendix C. Failed cases and some outliers are excluded. Based on the diagnostic information in Appendix C, one can clearly see that the surrogates of the system level metrics are excellent. Responses have an R^2 value above 0.99 for both training and validation.

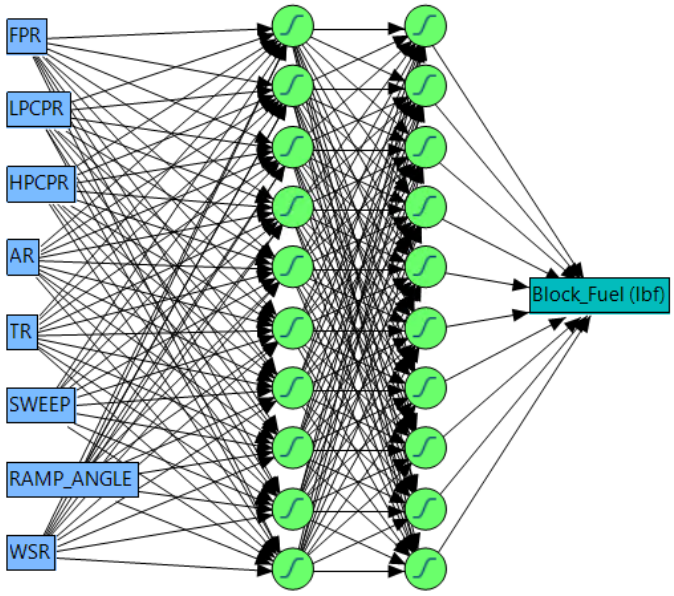

Figure 7.16: Example of ANN architecture used to fit a surrogate model to EDS responses, in this case block fuel. The ramp angle input is omitted for non-BLI cases

The actual vs. predicted and residual vs. predicted plots are indicative of good fits, based on criteria described previously. The MFE and MRE distributions have a mean error close to 0% along with a standard deviation and max error range well within 1%. The exception is TOFL, which compared to the other responses, shows the weakest fit. The prediction errors do not always satisfy the same error tolerances as the other responses. This relatively poorer fit is not a major concern given that TOFL is merely used as a constraint within the optimization problem. The optimized design performance is verified with EDS to ensure that all constraints are satisfied.

The design space can be viewed through a series of profiler plots generated by JMP. These profilers show snapshots of the responses as a function of the design variables. The neural network models behind these trends form a fully parametric environment, where the user can interactively change the design point and observe corresponding changes to the system level responses. These profilers are shown at the baseline design point in Table 7.1, for the non-BLI top-engine configuration in Fig. 7.17 and for the side-engine configuration in Fig. 7.18. It should be noted that the trends observed in these figures can change depending on the design value picked, based on interactions between variables. As such, the plots are merely meant to provide a general overview of the design space at a given design point. The trends for both the top and side-engine aircraft are similar, as expected. To minimize fuel burn, the trends suggest higher pressure ratios and aspect ratio as expected. A lower taper ratio is desirable to maintain an elliptical lift distribution, while interestingly, smaller sweep angles also appear to minimize fuel burn. For a transonic aircraft, increasing sweep decreases drag, but also lowers lift. Depending on the operating weight of the vehicle and the required lift at a given flight condition, increasing sweep may not be optimal. In addition, for a given wing span, increasing sweep increases the length of the wing spars and their required stiffness must also increase. Consequently, wing weight increases with sweep, which has an adverse impact on required block fuel.

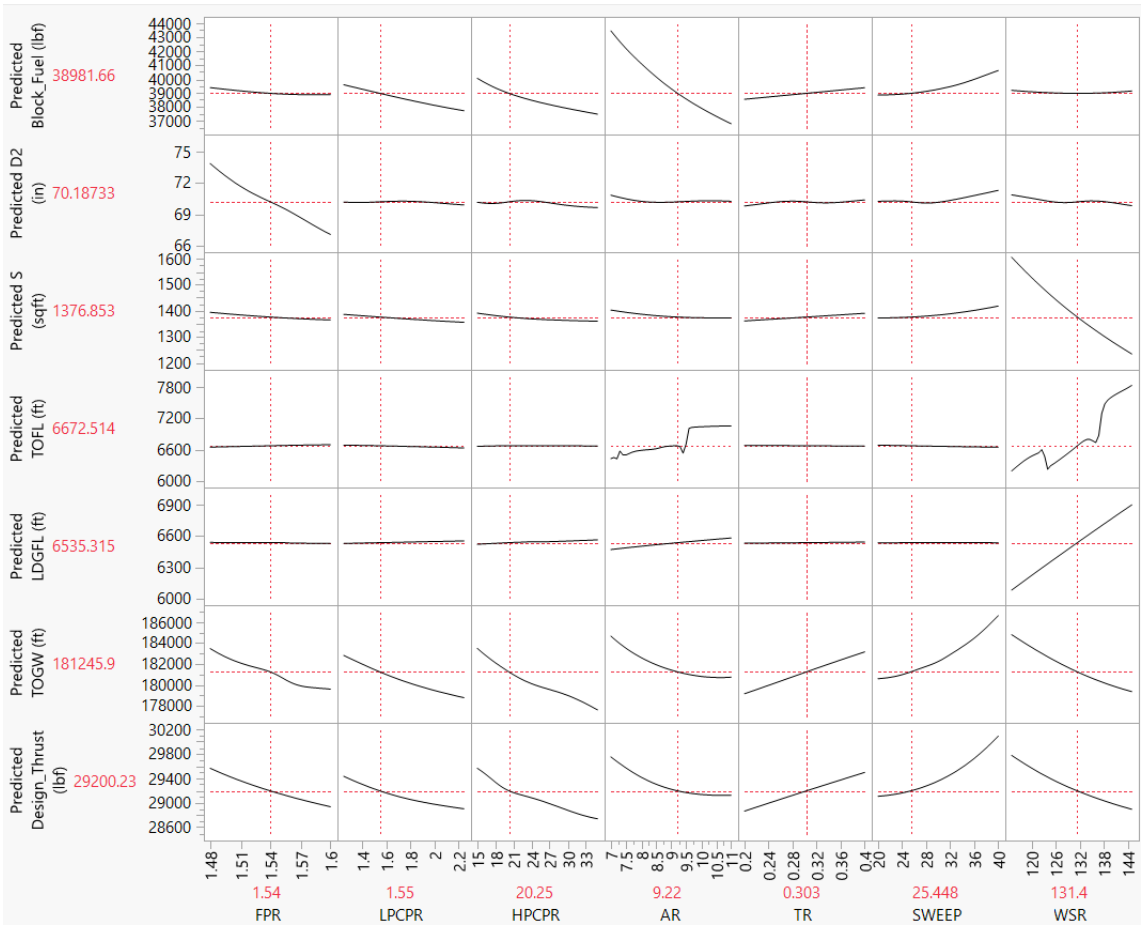

Figure 7.17: Experiment 1.2 - Top-Engine Non-BLI profiler plots showing trends of key metrics with the design variables at the design point shown in Table 7.1

Lastly, the wing loading trend shows a bucket, implying an optimum somewhere in the middle of the specified range. The block fuel, d_2 and S variations with FPR and WSR are consistent with the trends shown in experiment 1.1 for the non-BLI aircraft.

TOGW trends are also expected, with a reduction in TOGW observed with FPR, LPCPR and HPCPR, which is mostly driven by the fuel burn benefits of a higher OPR. While higher aspect ratio wings are expected to be heavier, it would appear that the aerodynamic benefit of such wings and their subsequent impact on fuel burn savings is the dominant factor. TOGW trends with taper and wing sweep are driven by both the aerodynamic impacts of these variables on fuel burn, discussed previously, and by the wing weight penalties incurred by increasing these values.

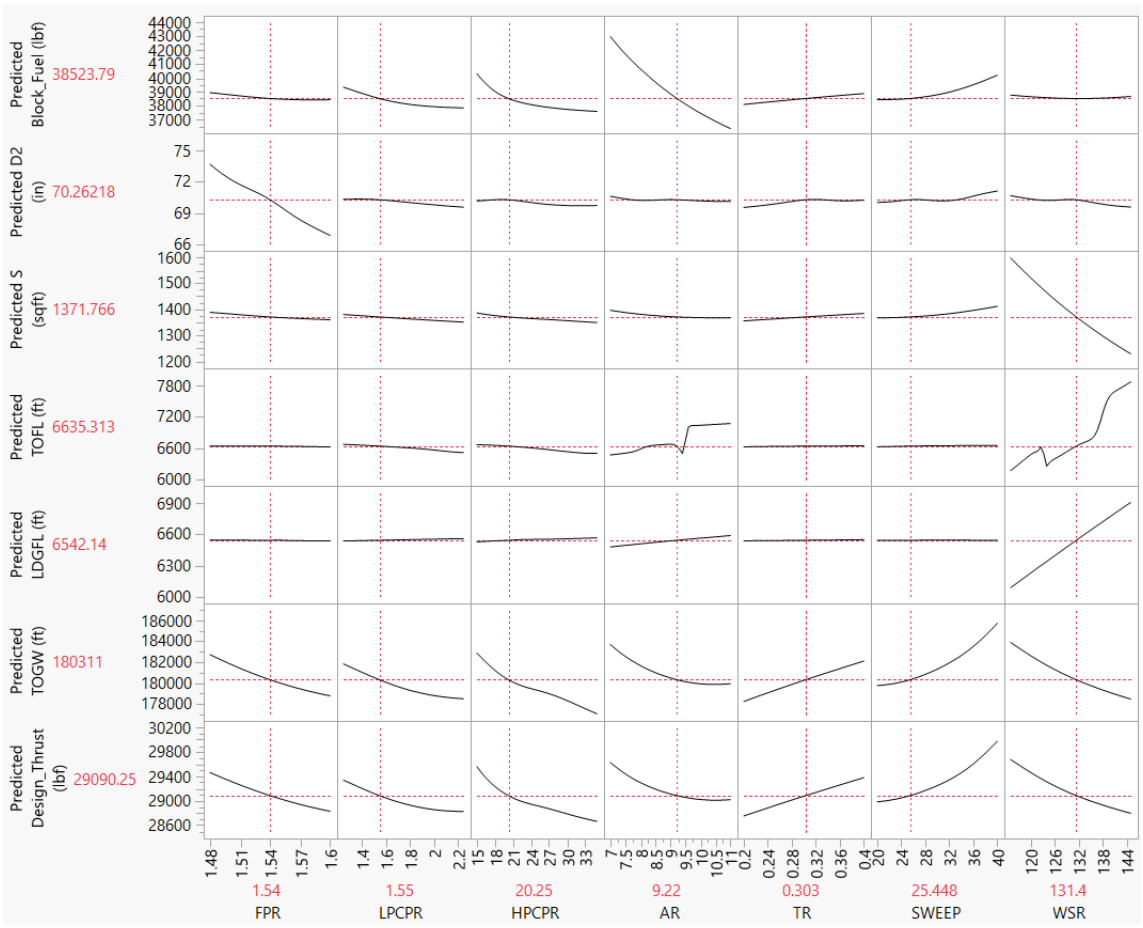

Figure 7.18: Experiment 1.2 - Side-Engine Non-BLI profiler plots showing trends of key metrics with the design variables at the design point shown in Table 7.1

The reader may also notice a strange trend of TOFL with aspect ratio and wing loading for both configurations. Focusing on the general direction of the trends first, at the design point shown in the figures above, an increase in TOFL with an increase in aspect ratio and wing loading is observed. TOFL also shows greater sensitivity to WSR. The smaller wing, as a consequence of higher wing loading, severely penalizes its lifting capability, explaining the increase in TOFL. For a given wing loading, an increase in AR has a favorable impact on fuel burn and thus results in a decrease in TOGW. To maintain the same WSR, the wing planform area must decrease. As such, takeoff performance is penalized, albeit not to the same degree as that from an increase in WSR. The neural network models also pick up an interaction effect

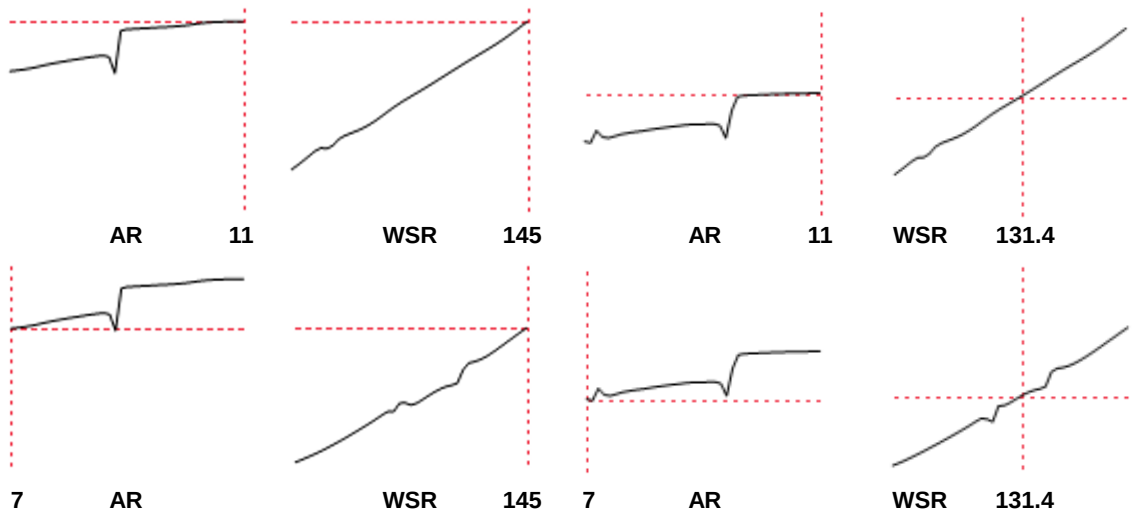

Figure 7.19: Experiment 1.2 - Top-Engine non-BLI TOFL trends with AR and WSR showing interaction effects between the variables

between these two variables that alters the shape of these trends, as shown for the top-engine non-BLI configuration in Fig. 7.19 for example. Notice how the TOFL trends vs. wing loading are now linear with a positive slope, as one would expect.

The non-smooth trends of TOFL vs. AR and WSR suggests numerical issues, rather than physics based phenomena. Possible explanations include noise in the responses used to train the surrogate, impact of outliers, and model over fitting to noisy data. As evident from the actual vs. predicted, residual vs. predicted, MFE and MRE plots in Appendix C, there are several points that show up as outliers for the TOFL responses that are not so for any of the other metrics. These issues, however, are ultimately not a major concern for experiment 1.2. As stated before, TOFL is used as a constraint in the optimization problem. The optimized designs are run through EDS to obtain the final performance values and check how good the surrogate predictions are compared to the actual results. As a preview, for the optimized designs shown in Table 7.6, the final TOFL values are far away from the specified constraint for the model to bias the outcome. For the optimized designs in Table 7.7, the EDS predictions and surrogate predictions for TOFL agree well.

The non-BLI responses are only intended to provide a reference to the observed BLI-results and a set of inputs to the BLI surrogates for the decoupled approach. The main focus is on the differences in the BLI responses, for a given engine location, between the decoupled and coupled approaches. Fig. 7.20 compares the decoupled and coupled trends for the top-engine configuration, while Fig. 7.21 does the same for the side-engine vehicle. Both the decoupled and coupled trends in general are similar to the non-BLI counterparts. The 'anomalies' in TOFL trends with AR and WSR also persist for the BLI concepts, despite the remaining responses showing smooth behavior. Recall, the decoupled approaches in literature use a fixed aircraft geometry to obtain estimates of the BLI effects. For these decoupled trends, inputs to the BLI effects surrogates are fixed at the non-BLI optimized values, summarized in Table 7.6.

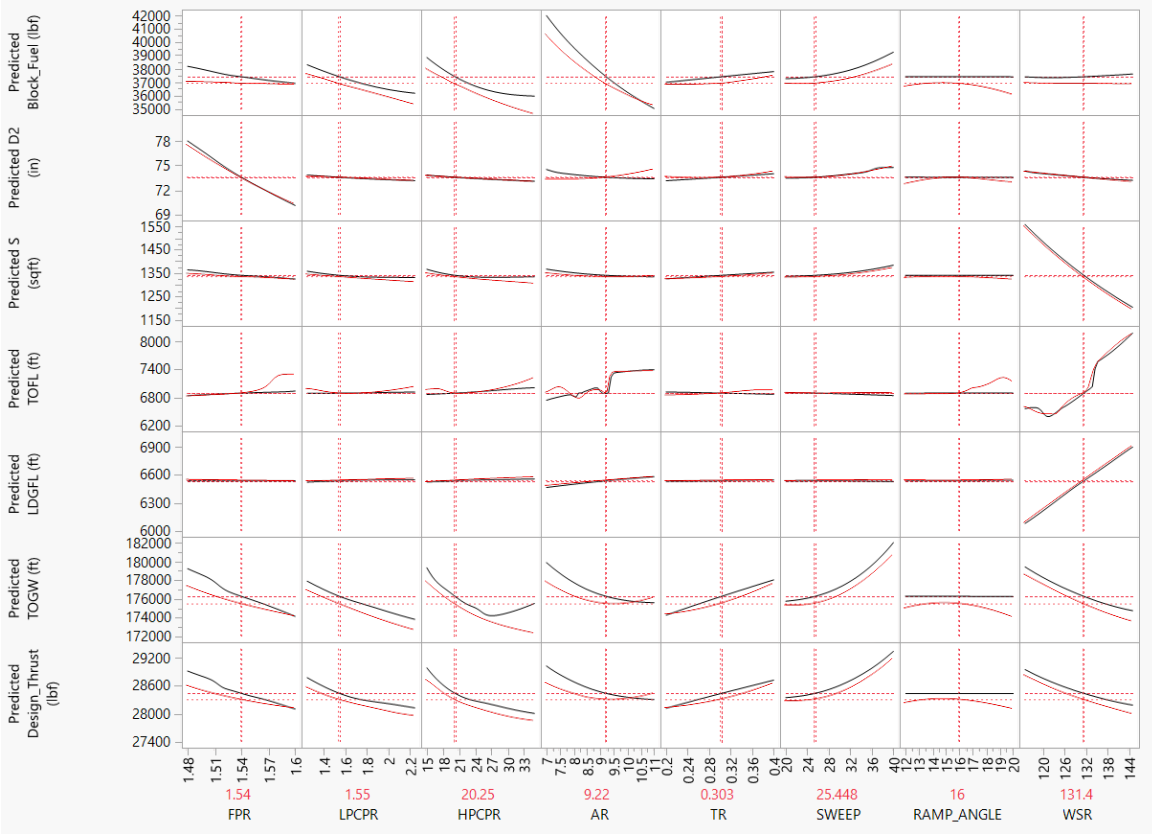

Figure 7.20: Experiment 1.2 - Top-Engine BLI profiler plots showing trends of key metrics with the design variables at the design point shown in Table 7.1. The coupled approach trends are shown in red and the decoupled in black

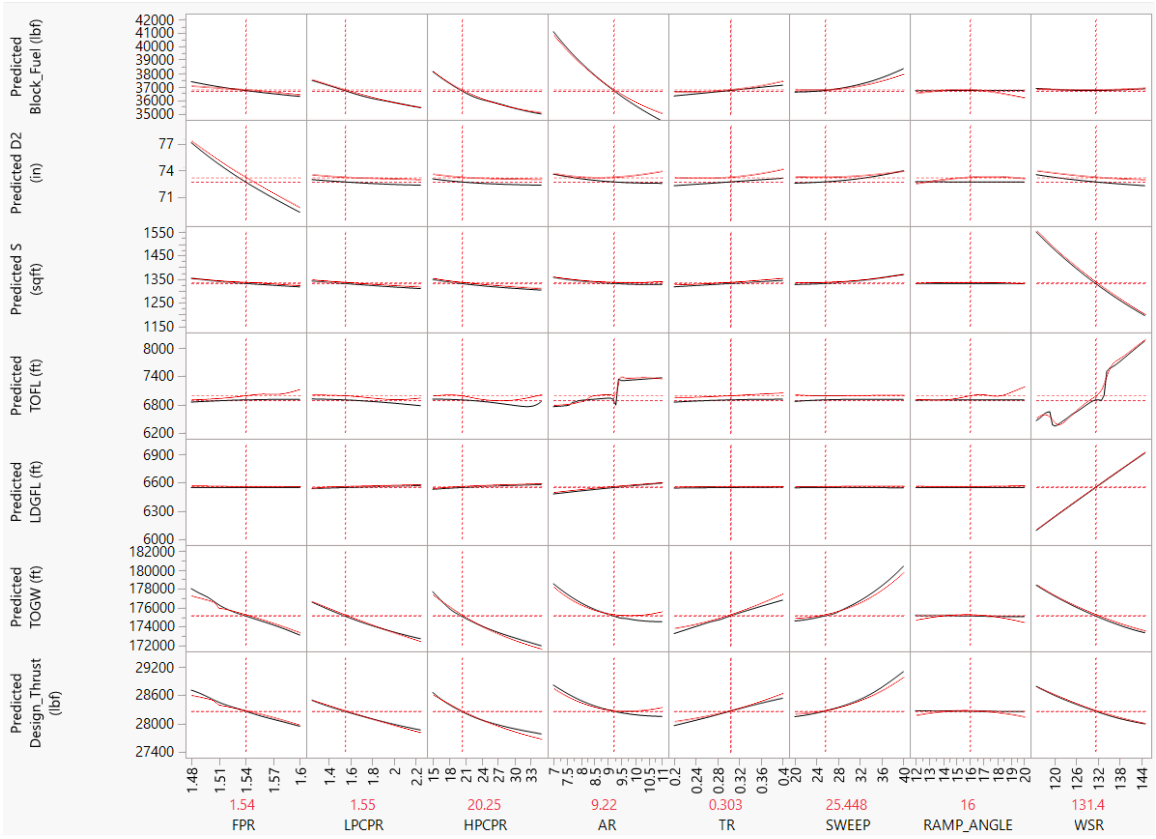

Figure 7.21: Experiment 1.2 - Side-Engine BLI profiler plots showing trends of key metrics with the design variables at the design point shown in Table 7.1. The coupled approach trends are shown in red and the decoupled in black

Consistent with experiment 1.1, there are noticeable differences between the decoupled and coupled trends for the top-engine configuration, which are much smaller for the side-engine aircraft. There is also agreement between the surrogate model trends for block fuel, d_2, and S with FPR and WSR, and the EDS results in experiment 1.1. Despite variations in the decoupled and coupled trends, expected optimum design variable values for minimum fuel burn do not appear to be significantly different at first glance.

Optimization of the BLI and non-BLI aircraft is conducted in JMP with the help of desirability functions [17]. The design block fuel is defined as the objective function. The following constraints are imposed on the optimization problem, implemented using disallowed combinations and desirability functions in JMP:

(i) $45 \leq \text{OPR} \leq 55$ with assumed pressure ratio multiplier of 0.985 to account for duct losses between the compressors

(ii) $20^\circ \leq \Lambda_{LE} \leq 40^\circ$ since inputs for FLOPS require quarter chord sweep and inputs to the BLI surrogates are based on leading edge sweep

(iii) $68\text{in} \leq d_2 \leq 78\text{in}$

(iv) TOFL (All Engine Operational) ≤ 8000ft

(v) LDGFL ≤ 8000ft

The objective function is optimized ten times with different initial values and the resulting designs that meet the constraints with the lowest fuel burn are recorded. Each of these designs are then run through EDS to verify the results predicted by the surrogates, and then the best designs are chosen. The final designs are compared in Table 7.6. The predicted BLI fuel burn reduction, comparing the coupled-BLI to the non-BLI optimum is 6.2% for the top-engine and 6.5% for the side-engine vehicles. The two modeling approaches show different optimum values of HPCPR, LPCPR, and quarter chord sweep. Other variables are the same. All optimized BLI vehicles favor smaller engines, based on the optimum FPR of 1.6. It would appear that the aerodynamic penalty on D' due to larger fans is more substantial than the propulsive efficiency benefit, even for BLI, hence the trend towards higher FPR fans. The higher FPR fan for BLI variants, compared to non-BLI, suggests that the propulsive efficiency loss going to a smaller fan is offset by the BLI benefit. Optimum values for OPR, AR, and λ are all expected, the latter two primarily driven by the aerodynamic impacts on D'. The optimum value of inlet ramp angle being at the lower bound is indicative of the competing effects of η_{PR} and $P_{K_{\text{in}}}$, $\Delta\Phi_{\text{wake}}$. Experiment 2.8 showed that both $P_{K_{\text{in}}}$ and $\Delta\Phi_{\text{wake}}$ increased with ramp angle, but η_{PR} decreased. In Fig. 7.20 for example, $\phi = 12^\circ$ and $\phi = 20^\circ$ show the lowest fuel burn for the selected

Table 7.6: Experiment 1.2 - Comparison of Block Fuel Optimized Designs

	Top-Engine			Side-Engine		
Design Var.	Non-BLI	BLI-C	BLI-D	Non-BLI	BLI-C	BLI-D
FPR	1.566	1.6	1.6	1.553	1.6	1.6
LPCPR	2.007	1.659	1.263	1.841	1.341	1.482
HPCPR	17.748	21.028	27.628	19.525	26.018	23.537
AR	11	11	11	11	11	11
λ	0.2	0.2	0.2	0.2	0.2	0.2
$\Lambda_{c/4}$ (°)	24	27.62	24	24	28.41	24
WSR	130	130	130	133.5	130	130
ϕ (°)	NA	12	12	NA	12	12
Key Outputs						
Des. Block Fuel (lbf)	35824	33619	33663	35491	33198	33272
S (ft^2)	1357	1313	1314	1319	1312	1308
d_2 (in)	68	69.3	69.5	68.4	68.8	68.8
OPR	55	55	55	55	55	55
TOGW (lbf)	176429	170726	170801	176082	170513	170023
AEO TOFL (ft)	6988	7393	7403	7208	7374	7386
LDGFL (ft)	6535	6550	6553	6641	6562	6556

design point, with the latter being the global optimum. Increasing block fuel burn with an increase in the ramp angle from 12° suggests that the η_{PR} losses are more dominant, but after a certain value, the $P_{K_{\text{in}}}$ and $\Delta\Phi_{\text{wake}}$ benefits overcome the η_{PR} losses. Due to interactions with the wing, at the optimum design, this trend changes and the smallest ramp angle results in lower fuel burn.

The same exercise is repeated with TOGW as the objective function instead. A comparison of the optimum designs is presented in Table 7.7. In this design space, lower TOGW is primarily achieved through a reduction in the wing weight. This is possible with a smaller wing planform and a lower quarter chord sweep. The smaller wing, however, comes at the cost of an increase in block fuel burn, takeoff length, and landing field length. Differences between the coupled and decoupled designs are

Table 7.7: Experiment 1.2 - Comparison of TOGW Optimized Designs

	Top-Engine			Side-Engine		
Design Var.	Non-BLI	BLI-C	BLI-D	Non-BLI	BLI-C	BLI-D
FPR	1.558	1.599	1.6	1.546	1.592	1.6
LPCPR	1.354	1.396	1.282	1.841	1.616	1.849
HPCPR	26.469	25	27.215	19.619	21.524	18.876
AR	11	10.24	11	11	11	11
λ	0.2	0.2	0.2	0.2	0.2	0.2
$\Lambda_{c/4}$ (°)	20	24	20	20	24	20
WSR	145	137	136	145	136	136
ϕ (°)	NA	12	12	NA	12	12
Key Outputs						
Des. Block Fuel (lbf)	36029	34576	33742	35651	33266	33325
S (ft^2)	1206	1242	1253	1203	1246	1241
d_2 (in)	68.1	69.2	69.2	68.5	69	68.5
OPR	55	55	55	55	55	55
TOGW (lbf)	174856	170144	169814	174497	169113	168789
AEO TOFL (ft)	7972	7805	7732	7952	7734	7739
LDGFL (ft)	6942	6721	6699	6950	6712	6717

again primarily seen in HPCPR, LPCPR, and quarter chord sweep, along with a small difference in AR for the top-engine configuration. This difference in AR results in a larger block fuel and TOGW discrepancy between coupled and decoupled (-2.41% and -0.19% respectively) for the TOGW optimized top-engine configuration, when compared to the fuel optimized vehicle (0.13% for fuel and 0.04% for TOGW), where the optimum AR is the same for both decoupled and coupled. Also, since TOGW accounts for both OEW and fuel weight, by ignoring sizing impacts on the BLI effects, the error observed in both metrics can be exaggerated when one aims to minimize TOGW instead of just fuel weight.

7.3.2 Comments on BLI Effects Surrogate Model Prediction Error

All results generated so far depend on the accuracy of the BLI effects surrogate models in capturing the 'true' response, as would be predicted by CFD. However, each of the surrogates shows a certain distribution on prediction error, that is highlighted in the MFE and MRE distributions for a given response. While the main objective of this thesis was to quantify the uncertainty in the predicted BLI fuel burn savings as a result of ignoring aero-propulsive coupling, it is also worthwhile to estimate uncertainty in the predicted BLI fuel burn savings as a result of surrogate prediction error. Specifically, an estimate for the theoretical upper and lower bound on fuel burn, based on the largest prediction errors for each surrogate, will provide a perspective on the potential variability of the response. The TOGW optimized (coupled approach) top-engine configuration shown in Table 7.7 is used as a test case for this quick study.

For each BLI surrogate, prediction errors at the 2.5 and 97.5 percentiles are recored for the combined training and validation dataset. Thus, 95% of the data is covered with this range. Additionally, the test case geometry is run in CFD at the start and end cruise points, which are at $M_\infty = 0.78$ at 35,000 ft. and 39,000 ft. The BLI effects calculated in CFD are compared against the surrogate predictions. Thus, a CFD generated cruise point error estimate for each BLI effect is also obtained. To get the largest and smallest fuel burn estimate, the upper and lower percentile errors need to be combined in a logical manner, while accounting for the physics. In general, $P_{K_{\text{in}}}$ and $\Delta\Phi_{\text{wake}}$ correlate opposite to η_{PR}, as seen in the experiment 2. So for example, setting the percentage errors at the largest positive value for the first two BLI effects requires that the η_{PR} error be set to the largest magnitude negative value.

Another interesting finding is that within these error ranges, fuel burn is more sensitive to errors in η_{PR} than the combined effect of errors in $P_{K_{\text{in}}}$ and $\Delta\Phi_{\text{wake}}$. This observed dominance of η_{PR} was also noted above, in context of the discussion concerning the optimum ramp angle value favoring the lower bound of 12°. Thus,

to estimate the upper bound on fuel burn, the percentage error for η_{PR} should be set to the largest magnitude negative value. The three trials conducted to get the fuel burn error estimates are shown in Table 7.8. The cruise error point is defined by the average of the percentage error at the start and end points. It should be noted that the percentage errors shown for the three CFD measured BLI effects apply to the transformed metrics that were used as the surrogate responses. For each trial, the percentage error in the response is applied as a correction to the BLI effects surrogates within EDS, at every operating point, and the fuel burn from the resulting design is tracked. Note, this approach assumes that the same percentage error for a BLI response is valid across the entire mission. This assumption is not quite true, as evident in the percent error variation between the start and end of cruise. This assumption however does simplify the process and allow for a quick and dirty estimation of the fuel burn range, which is adequate for now.

Fig. 7.22 presents the results from this study. In Fig. 7.22a, ranges on block fuel are shown for the coupled TOGW optimized design in red. The value of fuel burn predicted by EDS (as shown in Table 7.7) without any error correction on the BLI surrogates is shown as a red circle. The fuel burn prediction upon applying the errors calculated through the CFD spot check at cruise is shown with a red cross. The fuel burn ranges for the corresponding decoupled TOGW optimized top-engine design are also shown for reference purposes. Since the CFD cruise error point was obtained

Table 7.8: Summary of Model Prediction Percentage Errors

Condition	$P_{K_{\text{in}}}$	η_{PR}	$\Delta\Phi_{\text{wake}}$	SWETF	SWETN
1) Fuel Burn Upper Bound	1.81	-1.51	2.89	0.0013	0.0028
2) Fuel Burn Lower Bound	-1.54	1.32	-3.29	-0.0020	-0.0050
Start of Cruise	1.37	-0.62	0.61	0	0
End of Cruise	1.31	-0.20	0.32	0	0
3) Cruise Average	1.34	-0.41	0.46	0	0

from the coupled optimum geometry, it cannot be applied to the decoupled design results and is thus not shown for this case. The TOGW optimized non-BLI design

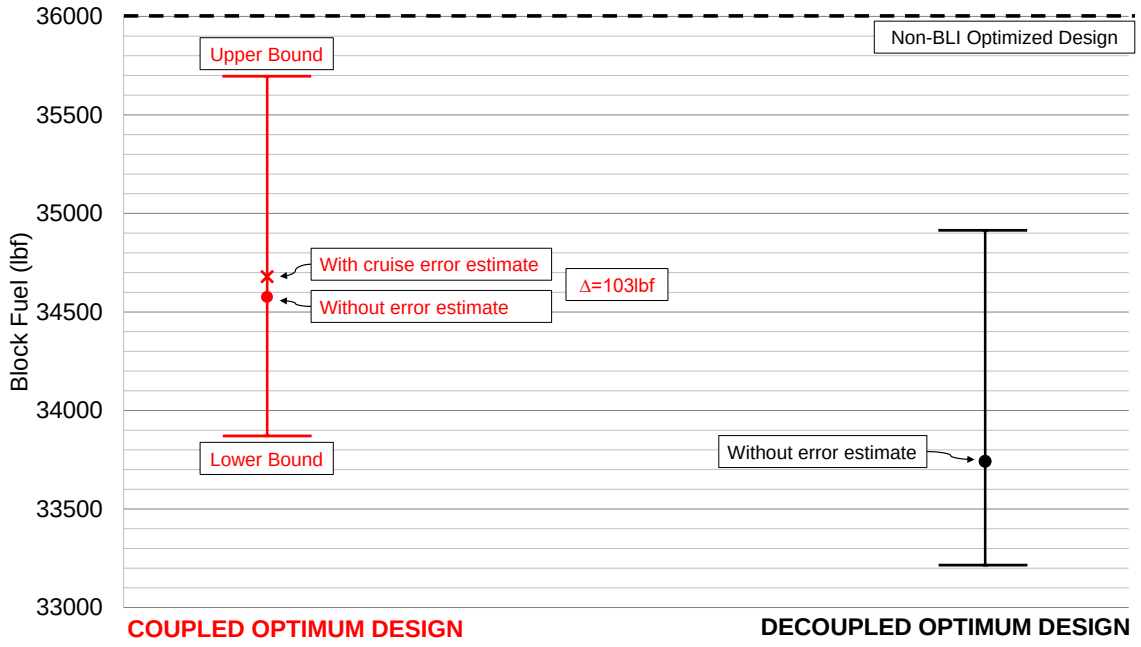

(a) Block fuel burn (lbf)

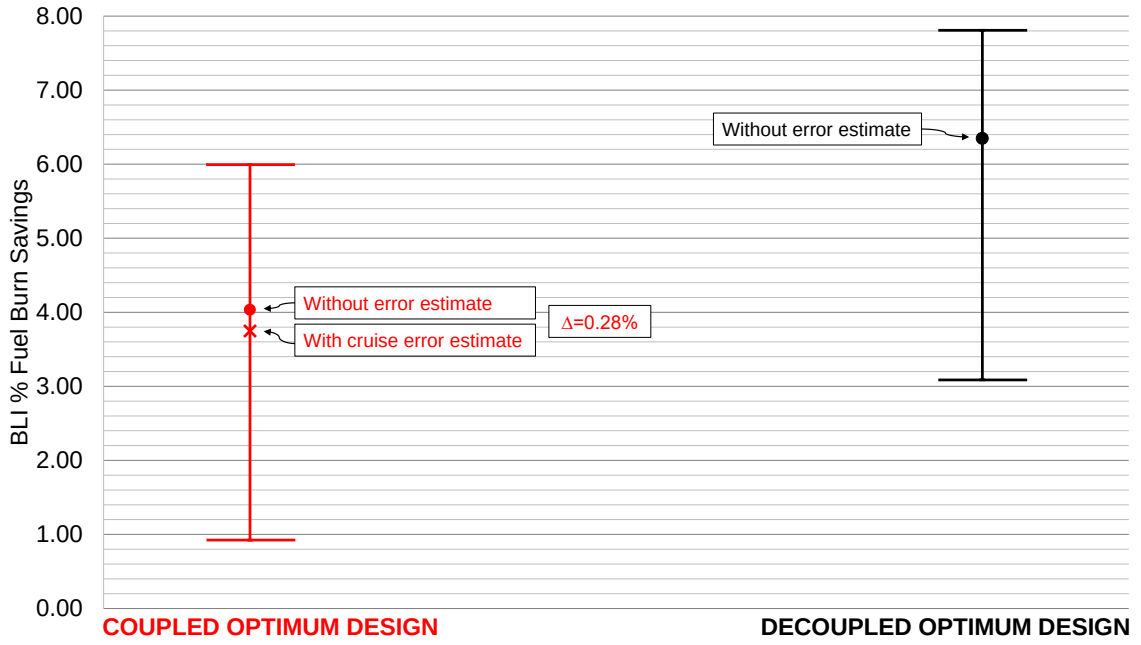

(b) BLI fuel burn percent savings

Figure 7.22: Error ranges in block fuel and BLI fuel savings for the top-engine TOGW optimized configurations, relative to the top-engine non-BLI optimized design

fuel burn (also shown in Table 7.7), is included for comparison. Ranges on the BLI fuel burn percent savings going from the optimized non-BLI to the optimized BLI designs are presented in a similar format in Fig. 7.22b. The following conclusions can be drawn from these figures:

(i) The upper and lower error bound in the BLI fuel burn savings is on the same order of magnitude as the predicted BLI fuel burn savings

(ii) This discrepancy, however, is one order of magnitude smaller than the predicted BLI fuel burn savings, using the more realistic cruise point surrogate error

(iii) Differences in fuel burn between the decoupled and coupled designs is maintained at the upper and lower error bounds as well

The large range in fuel burn error and thus the predicted BLI fuel burn savings clearly motivates the need for a formal uncertainty quantification study, discussed in chapter 8. This study will help paint a more realistic picture by providing a distribution of fuel burn, based on assumed surrogate error distributions, rather than just the worst case upper and lower bounds. From this distribution, one can determine the probability of encountering a given fuel burn value within the ranges shown in Fig. 7.22, thereby providing better context concerning the accuracy of the BLI effects surrogates. With respect to the cruise error spot check, given that this regime constitutes a major part of the mission, surrogate prediction errors calculated here through CFD provide a more representative estimate of the actual fuel burn error for a given design. The small magnitude of fuel burn discrepancy, resulting from the CFD spot check of surrogate error, is thus quite encouraging. This result lends confidence to the optimized designs and the conclusions drawn in this chapter.

7.4 Concluding Remarks

Experiments 1.1 and 1.2 clearly show the scope of potential uncertainty in BLI aircraft design and performance by using a decoupled approach instead of a coupled, thereby answering the primary research question. As observed in experiment 1.1 for example, the discrepancy in fuel burn introduced by using a fixed point design estimate (decoupled approach) for the BLI effects, instead of a parametric and coupled estimation, can be anywhere in the range of 0.06% to 1.7%, depending on the aircraft design and engine location, as hypothesized. For the designs considered in experiment 1.1, the fuel burn savings relative to the non-BLI configuration is between 5-7%. As a fraction of the predicted BLI fuel burn savings relative to the non-BLI configuration, the error due to ignoring aero-propulsive coupling can be as high as 24%. Experiment 1.2 showed noticeable differences in optimized engine cycle and airframe design as a result of ignoring aero-propulsive coupling.

A caveat to the results in this chapter concerns the role of uncertainty in the value of the BLI effects. For example, the operational uncertainty study in experiment 1.1 (Fig. 7.15) regarding the assumed angle of attack variations over the mission showed how the fuel burn predictions changed based on the angle of attack assumptions. A consequence of this uncertainty is the discrepancy between the decoupled and coupled fuel burn predictions, which in general was higher than the numbers stated above. The impact of surrogate prediction error on the BLI fuel burn savings was also highlighted in a quick study discussed in section 7.3.2. The 5-7% fuel burn savings stated above is thus subject to a certain degree of variation, depending on the significance of the surrogate prediction errors. However, while the numbers may be 'fuzzy' due to different sources of uncertainty, in general, the results show strong support for use of coupled and parametric methodologies for BLI concept design.

CHAPTER 8
CONCLUSIONS AND RECOMMENDATIONS

This chapter condenses the research effort described in this dissertation. It starts with a summary of the problem formulation, followed by a listing of the main conclusions from the experiments, key contributions of this work, and recommendations for future studies. Fig. 8.1 shows a road map highlighting the journey from literature review to the experiments. Elements in this figure are expanded in the following sections.

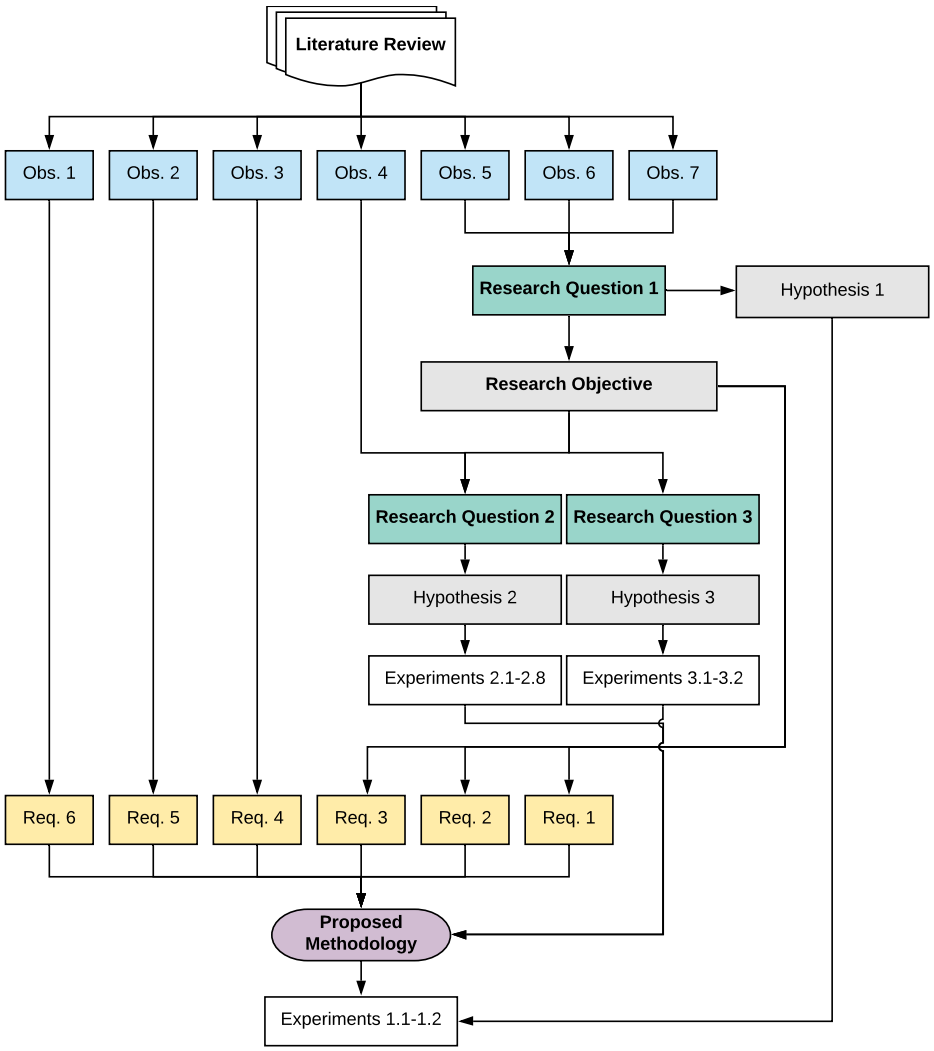

Figure 8.1: Research formulation road map

8.1 Summary of Research Formulation

8.1.1 Motivation

As described in chapter 1, boundary layer ingestion is proposed as one of many solutions to improve the fuel efficiency of aircraft. Given the highly integrated nature of the propulsion system with the airframe, a claim was made that the aero-propulsive interactions need to be accounted for in the design and analysis of BLI concepts. Error in the fuel burn estimation, and other performance and design characteristics as a result of ignoring this coupling can be significant. A coupled and parametric conceptual design methodology is thus required. The question then arises regarding the validity of this claim and the consequences of ignoring this aero-propulsive coupling resulting from BLI on vehicle sizing, engine cycle design, and vehicle performance? This was the overarching research question that motivated this thesis.

8.1.2 Literature Review and Observations

A literature review into different BLI concept related studies was conducted to search for some answers. This review was described in chapter 2, which highlighted key terminology associated with modeling approaches and model fidelity, and the different ways in which the aerodynamics and propulsion disciplines were accounted for in the BLI problem. This reviewed literature was then categorized in Fig. 3.1 in chapter 3, from which a series of observations could be derived, which were presented in section 3.1. Observation 1 commented on the prevalence of 1D thermodynamic cycle propulsor models in literature, while observations 2-4 discussed the use of CFD in conceptual design of BLI aircraft. Observations 5-7 highlighted the largely decoupled nature of BLI studies, and established the advantages and limitations of existing coupled BLI analyses. A gap in the literature was identified concerning the absence of a parametric and coupled aero-propulsive design and analysis methodology that

was appropriate for conceptual design BLI vehicle sizing and corresponding trade studies. The research objective, thus, was to develop such a method and answer the primary motivating question. Minimum requirements concerning model fidelity, the need for parametric analyses, and capturing aero-propulsive coupling were derived from the observations, as shown in yellow in Fig. 8.1 and described in section 3.2. These requirements formed the basis for the proposed methodology.

8.1.3 Research Questions and Hypotheses

A series of research questions were formulated based on previously identified gaps in the literature, that are described in section 3.3. The primary research question derived from observations 5-7 is stated as follows:

> **Research Question 1:** What are the consequences of ignoring the aero-propulsive coupling resulting from BLI on vehicle sizing, engine cycle design, and vehicle performance?

A secondary problem, arising from research question 1 and the research objective, concerned assessing the sensitivity of the BLI performance impacts ('BLI effects') to the airframe and propulsor design, and operation. This problem was posed as research questions 2 and 3. These questions, in particular question 2, also stemmed from observation 4, which highlighted how several studies in literature used CFD generated profiles of the boundary layer from a fixed airframe. None of these studies commented on the sensitivity of the ingested boundary layer properties to the airframe design from which they were obtained. A study by Kenway and Kiris for the STARC-ABL, discussed in chapter 2, showed wing downwash impacts on the distortion pattern. Research question 2 expanded the scope to consider the impacts of other tube and wing airframe design features on the BLI effects, for different engine locations, and is stated as follows:

Research Question 2: What features of the airframe OML and external layout need to be considered when generating a parametric representation of the BLI effects using CFD in conceptual design, and what features can be defaulted?

The high level objectives of research question 2 were to identify the critical airframe design space that had the most significant impact on the BLI effects, how the engine location played a role, and to establish rule of thumb guidelines that defined how these parameters should be handled in BLI conceptual design. Answers to this question would help make the problem more tractable in the early conceptual stage, where there is not enough design knowledge to reduce degrees of freedom. Along similar lines, research question 3 looked at the propulsor on-design and off-design impacts on the BLI effects, with the objective of highlighting the engine's contribution to the aero-propulsive coupling:

Research Question 3: In CFD modeling of the ingested boundary layer for a BLI propulsor, what aspects of its on-design and off-design characteristics need to be considered?

For each of the above research questions, a hypothesis was formulated in chapter 3. These hypotheses were based on logic and physics based reasoning grounded in boundary layer theory and fundamental conservation laws of fluid mechanics. For research question 1, hypothesis 1 commented on expected impacts of ignoring aero-propulsive coupling:

Hypothesis 1: If aero-propulsive coupling is ignored at the vehicle sizing stage, then the error introduced by neglecting throttle dependent physics and variations in airframe and engine size on the BLI effects will result in an under-sized and infeasible vehicle if the BLI benefits are overestimated. In contrast, the vehicle

is over-sized if the BLI benefits are underestimated. Significance of the aero-propulsive interaction is determined by the effective contribution of the wing to the BLI effects, which is driven by the engine location. Vehicle design and performance differences between the decoupled and coupled approaches will be more severe in configurations where the wing has a more significant impact on engine inflow.

Hypothesis 2 commented on how the BLI effects are expected to show greater sensitivity to certain airframe design variables typically associated with vehicle sizing (macro parameters) over more detailed parameters commonly associated with outer mold line refinement. The more significant variables were termed the 'active variables', while those that could be set to fixed reasonable values for conceptual design purposes were termed 'inactive variables'.

Hypothesis 2: Parameters present in the active and inactive variable sets are determined by the axial and circumferential location of the engine on the airframe. The axial location defines the distance over which the boundary layer grows, as well as the impact of small perturbations in the zone of dependence. The circumferential location determines how much the wing contributes to the ingested boundary layer properties. Within the active set, if perturbations in detailed parameters do not result in shocks or flow separation in the ingested streamtube, then these parameters can be defaulted for conceptual design purposes since the BLI effects in this instance are more sensitive to changes in macro parameters.

Hypothesis 3 commented on how two main BLI effects, defined formally in chapter 4, are expected to vary with changes in fan size and flow rate:

Hypothesis 3: Fan size and mass flow rate requirements are the main engine on-design and off-design factors that influence the BLI effects. Due to expected changes in inflow velocity, wall shear, and ingested boundary layer fraction with

a change in A_2 or $\dot{m}$, η_{PR} will exhibit a negative correlation with $\dot{m}$, and with $C_{P_{K_{\text{in}}}}$, will positively correlate with A_2. If the ingested boundary layer fraction is small, $C_{P_{K_{\text{in}}}}$ will correlate negatively with $\dot{m}$, otherwise, a positive correlation is expected. These differences are due to non-linear dependence of $C_{P_{K_{\text{in}}}}$ on velocity.

8.1.4 Methodology

Following the problem definition in chapter 3, chapter 4 began with presenting a method for defining the BLI effects, specifically identified in section 4.3.2. The thrust-drag bookkeeping ambiguity for BLI concepts was noted and Drela's power balance formulation was used instead. However, given the widespread adoption of thrust-drag in current industry standard codes, a mapping was needed between the two bookkeeping schemes. A key aspect of this mapping was to recognize that the power balance formulation applied to both BLI and non-BLI aircraft. Thus, the power balance approach must be equivalent in some manner to the thrust-drag bookkeeping for non-BLI aircraft. With some simple and justifiable assumptions, this mapping was derived in section 4.3 for a non-BLI vehicle, from the functional forms of the terms in the power balance equation. Moving from the BLI form of the power balance to the non-BLI version results in the identification of certain terms that are non-zero for the former, but zero for the latter. These additional terms were called the BLI effects as they captured changes in the propulsive power requirements due to the engine ingesting the boundary layer. Thus, one was able to use conventional thrust-drag for sizing a non-BLI vehicle, but account for the impacts of BLI using the power balance definitions.

The main methodology described in section 4.5 was a product of the requirements stipulated in section 3.2. This process leveraged CFD generated semi-empirical models capturing the impacts of BLI on vehicle performance. These correlations were embedded within a vehicle sizing environment. This framework consisted of cycle

analysis, engine weights and flowpath estimation, and aircraft sizing and mission analysis codes. The overall methodology was broken down into three distinct phases: i) Pre-Vehicle Sizing ii) Vehicle Sizing iii) Vehicle Optimization. The first stage spanned activities like the requirements definition, the BLI effects sensitivity studies, and the BLI effects correlation generation. The BLI effects sensitivity studies were experiments 2 and 3, relating to research questions 2 and 3. The second stage was the core component of the methodology, where the BLI concept was designed for a fixed set of airframe and propulsor design parameters, with the BLI corrections. The final stage involved a design space exploration and optimization, where certain design parameters could be varied to improve performance.

8.2 Conclusions from Experiments

The experiments conducted in this study were designed to answer the three research questions. Specifically, the hypotheses laid out a set of requirements that the experiments needed to test. Experiments 2 and 3, capturing the sensitivity of the BLI effects to the airframe and propulsor, answered research questions 2 and 3 respectively. These experiments were an integral part of the proposed concept design methodology as stated above. Experiment 1 on the other hand answered the primary research question. The sections below outline the experimental objectives, procedure, and high level conclusions.

8.2.1 Sensitivity of BLI Effects to Airframe

Experiment 2 tested the following aspects of hypothesis 2:

(i) The BLI effects are more sensitive to larger scale macro parameters, typically associated with vehicle sizing, than detailed parameters, which are finer features of the geometry that add definition to the airframe shape

(ii) Engine axial and circumferential location on the fuselage determines which variables are important (active) and which ones are relatively insignificant (inactive)

These points were tested through eight trials (Experiment 2.1-2.8), as described in chapter 5, that covered the fuselage nose, tail cone, fairing, overall shape and size, wing, vertical tail, and inlet ramp angle regions of the airframe. The BLI effects were measured at 10 stations along the length of the fuselage, at three circumferential engine locations per station. These circumferential locations were at 0° (engine on fuselage side), 45°, and 90° (engine on top of fuselage). Section 5.10 presents detailed concluding remarks for experiment 2, with the high level conclusions outlined below. In general, the conclusions support hypothesis 2, with exceptions noted below.

(i) Engine axial location determines active and inactive variables, with small geometry perturbations having a local impact on the flow

- Supported by the nose (E2.2), tail cone (E2.3), fairing (E2.4), wing (E2.6), and vertical tail (E2.7) trials
- Exceptions noted for a) nose geometry change trial that produced a shock and thus affected measurements at all downstream stations (E2.2-2 in section 5.3.2) b) fairing impacts at the fuselage trailing edge engine station for a 2° angle of attack (E2.4-2 in section 5.5.2)

(ii) Engine circumferential location determines the effective contribution of the wing to the BLI effects, as seen in wing geometry trials (E2.6 in section 5.7.2) described in section 5.7. Differences in the BLI effects due to the presence of a wing, relative to a no-wing baseline, vary in magnitude based on engine location as follows:

- Largest at the 90° stations, where the engine is on the top of the fuselage, and exceed the significant difference minimum thresholds defined in section 5.1.5, followed by

- Differences at the 45° stations, which also exceed the thresholds, and then
- Those at the 0° stations, where the engine is on the side, and the differences are below the thresholds

These trends are driven by the wing downwash impacts on the ingested boundary layer. Trends suggest that the wing must be part of the geometry model used for generating correlations of the BLI effects for concepts with engine locations similar to the STARC-ABL and the D8.

(iii) BLI effects are in general more sensitive to the macro parameters than detailed

- Supported by the nose, tail cone, fuselage shape and size (E2.5), wing, vertical tail, and inlet ramp angle (E2.8) experiments
- Conditional to detailed parameter settings that do not produce shocks and/or separation (large flow perturbations) in the ingested streamtube

This point does not imply that the detailed parameters are irrelevant. Merely, that these variables are not as important early on and can be optimized in preliminary design, as is typically done in literature

8.2.2 Sensitivity of BLI Effects to Propulsor

Experiment 3 tested the trends predicted in hypothesis 3 for two different engine locations. In experiment 3.1, the engine was on the side of the fuselage, like on the NOVA-BLI. For experiment 3.2, the engine was mounted on the aft end, like on the STARC-ABL. These two locations experience different circumferential and radial extents of ingested boundary layer. For each location, a small set of trials was conducted where the fan annuals area was changed for a fixed flow rate requirement, followed by a change in the flow rate, for a fixed fan size. Detailed concluding remarks can be found in section 6.5, with high level conclusions listed below. In general, the conclusions support hypothesis 3, with exceptions also listed below

(i) The metric $C_{P_{K_{\text{in}}}}$ shows a positive correlation with fan size and negative with flow rate, for a low ingested boundary layer extent and in the absence of inlet shocks, as expected

(ii) The same response shows opposite correlations with fan size and flow rate when the extent of the ingested boundary layer is much higher, as hypothesized

(iii) The BLI effect η_{PR} shows a positive correlation with fan size and a negative correlation with flow rate, assuming no flow separation, as predicted

(iv) Presence of inlet shocks have a favorable impact on $C_{P_{K_{\text{in}}}}$, with small propulsors showing a positive correlation with flow rate if shocks exist

(v) Flow separation at the measurement plane on which η_{PR} is being calculated results in η_{PR} showing a positive correlation with flow rate, as long as separation is present and its extent reduces with an increase in flow

8.2.3 Consequences of Ignoring Aero-Propulsive Coupling

The primary goal of experiment 1 was to see if the claim made in chapter 1 regarding the necessity of coupled and parametric methodologies for BLI aircraft concept design was justified. Using the method proposed in this thesis, the following points from hypothesis 1 were tested:

(i) Decoupled and coupled methodologies show differences in vehicle design and performance

(ii) These differences depend on the relative location of the engine to the wing, which determines the contribution of the wing to the ingested boundary layer properties

Experiment 1.1 compared block fuel burn differences between the proposed methodology and a decoupled approach for a fan pressure ratio and wing loading sweep.

This exercise was conducted for two BLI configurations, one with an engine location like that on the D8 and the other similar to the NOVA-BLI. Experiment 1.2 conducted a larger scale design space exploration and optimization study for the same two configurations and compared design and performance differences between the two approaches. Detailed conclusions can be found in section 7.4. The high level conclusions stated below strongly support hypothesis 1 and the need for coupled and parametric methodologies for BLI aircraft

(i) Experiment 1.1: There are substantial differences in the block fuel burn estimate comparing the coupled approach to a decoupled method (section 7.2.3)

- Error in the block fuel burn estimate from a decoupled approach, compared to that from the coupled approach, as a percentage of the coupled results, ranges anywhere from 0.06% to 1.7% depending on the value of fan pressure ratio, wing loading, and engine location
- For context, at the design point corresponding to the 1.7% error value, the predicted BLI fuel burn savings going from the non-BLI configuration to the BLI vehicle sized using the proposed method is around 6.6%. As a fraction of this fuel burn savings, the error in ignoring aero-propulsive coupling is about 24%
- The fuel burn error between the coupled and decoupled approaches is consistently much larger for the engine located on top of the fuselage, than that for the configuration where the engine is on the side. Note that the wing has a stronger influence on the BLI effects in the top-engine case, as discussed in context of experiment 2.6

(ii) Experiment 1.2: Trends in key system level responses as a function of some airframe and engine cycle parameters also show significant differences between coupled and decoupled approaches (section 7.3.1)

- Differences in fuel burn, takeoff gross weight, and sea level static thrust in particular are much larger between the two approaches
- The side-engine configurations again show smaller differences between the coupled and decoupled approaches, relative to the top-engine case
- Optimized designs also show differences as a consequence of the aero-propulsive coupling
  - Engine high and low pressure compressor pressure ratios, wing quarter chord sweep, and in one instance wing aspect ratio show the largest differences between the coupled and decoupled approaches
  - In terms of performance, the top-engine configuration optimized for takeoff gross weight, for example, showed a 2.4% error in fuel burn and 0.19% error in weight between the coupled and decoupled approaches

(iii) Factors like assumed angle of attack variations in the mission and surrogate prediction errors add a degree of uncertainty in the predicted fuel burn estimates, though the main conclusions are unaffected

8.3 Contributions to Literature

The research effort described in this thesis, from the main methodology to the key findings from experiments 1 to 3, provide novel insight into the conceptual design problem for BLI aircraft. The contributions of this dissertation are highlighted below:

(i) Development of a parametric, aero-propulsive coupled methodology for conceptual BLI aircraft sizing and cycle design selection, an improvement over decoupled approaches typically adopted in literature

(ii) Accounting of BLI impacts as a parametric function of airframe geometry, engine cycle design and operation, and flight conditions, unlike the point design treatment common in literature

(iii) Identification of critical airframe and propulsor design space that most significantly impacts the BLI effects, augmenting findings in literature with a systematic experimental approach

(iv) Quantification of the consequences of ignoring aero-propulsive coupling at the vehicle sizing stage, in terms of design and performance, to establish the necessity of the proposed method

(v) Simultaneous optimization of the airframe and cycle with BLI effects allowing for overall improved performance estimates over decoupled approaches where the airframe and engine are optimized in isolation

8.4 Recommendations for Future Work

The work in this thesis can be extended in several directions. Outlined below are some recommendations for future work that builds on the foundation developed in this dissertation.

8.4.1 Determining Coupling Characteristics for Other Concepts

The most obvious path would be to investigate the aero-propulsive coupling characteristics of vehicles like the STARC-ABL, with fuselage trailing edge mounted propulsors. This concept features more BLI, significant contributions to the BLI effects from the vertical tail in addition to the wing, and dependency of the under-wing engine design to the BLI propulsor efficiency. These factors would suggest that the aero-propulsive coupling for such concepts would be the strongest.

The proposed BLI concept design method is general enough to even handle non-tube and wing configurations, like the blended-wing-body. While some trials from experiment 2 do not apply to such unconventional configurations, the high level conclusions from the trials should still hold. Thus, one can also potentially investigate the

design and performance characteristics of such concepts using the proposed method. Of course, this point assumes that the aircraft sizing code that is used to implement this method can accurately model the non-BLI aspects of unconventional airframes, such as structural weight estimations and airframe drag predictions for example.

8.4.2 Incorporating Distortion Effects

Another natural extension would be to include distortion analysis. In particular, research question 2 needs to be revisited to determine whether the relative contribution of macro and detailed parameters to the BLI effects, seen in experiment 2, still holds when considering distortion metrics. Several studies have been proposed in literature to account for distortion impacts on turbomachinery performance. If surrogates of the distortion metrics can be formulated, then the BLI concept design methodology in this thesis can be augmented with distortion effects. It will be interesting to see if and how distortion affects the conclusions made with respect to hypotheses 1 and 2, and how the resulting aircraft design and performance estimates change with this added BLI penalty.

8.4.3 Improving Efficiency of Method

While this thesis shows the need for a coupled and parametric methodology, the method proposed in this thesis is just a starting point. It would be worthwhile to investigate different ways into further improving the efficiency of this method, in particular, reducing the CFD burden while still retaining the high-fidelity physics estimates of the BLI effects. One avenue is to investigate the use of active subspaces to reduce the dimensionality of the problem. However, such an approach requires gradients with respect to the input variables, which itself can be costly without an adjoint capability. At that point, gradient free dimensionality reduction techniques should be considered. Another possibility is investigating whether a universal set of

correlations can be developed. For this thesis, one set of surrogates was developed per configuration. While every effort was made to maximize the information gained from the smallest possible set of CFD runs, the proposed method is not very efficient if multiple aircraft with different engine locations need to be considered. A potential first step in this direction would be to see how the surrogate model trends look if all data were normalized with respect to a baseline design. Would the correlations mapping the changes in the BLI effects, with respect to the baseline, be universal across configurations? If so, then one merely needs to run a handful of CFD cases for a baseline design/engine location, and then apply the universal set of correlations to investigate how the performance changes with changes to the design. If not universally applicable, can a physics or statistical approach be formulated to map these correlations from a set of reference data to any new data set?

8.4.4 Uncertainty Impacts of Power Balance Implementation

While the BLI effects modeled in this thesis are defined based on Drela's power balance, which in turn is derived from the conservation laws, calculation of these quantities in CFD is an exercise that requires a certain degree of engineering judgment, as alluded to in chapters 4-7. As a consequence, there is some uncertainty in the BLI effects estimates due to implementation differences. Common to both $P_{K_{\text{in}}}$ and $\Delta\Phi_{\text{wake}}$ is the problem of defining the control volume boundaries on which these terms are to be integrated. The term $P_{K_{\text{in}}}$ can be calculated at the inlet highlight or at the fan-face. The highlight plane ignores contributions from the inlet, which is justifiable for early conceptual design since the inlet geometry is still fuzzy. Pressure recovery must then also be calculated at the same plane, otherwise there is an inconsistency if the inlet losses are accounted for in η_{PR}, as is convention, but not in in $P_{K_{\text{in}}}$. However, experiment 3 in this thesis showed a non-negligible contribution from the inlet to both $P_{K_{\text{in}}}$ and η_{PR}, which is why the fan-face was chosen as the integration plane

for the surrogates used in experiment 1. Both approaches are justifiable, but yield dissimilar results. Which one then is more appropriate? For $\Delta\Phi_{\text{wake}}$, the uncertainty relates to the question of whether a through-flow nacelle should be included as part of the un-powered vehicle control volume or not. If not, the alternative is to define a simple integration disc without the nacelle and calculate $\Delta\Phi_{\text{wake}}$ on that. The other source of uncertainty arises from the physical model used to estimate the wake dissipation change due to BLI. Both the integration plane and physics model options were discussed in chapter 4.

The conclusions drawn in this thesis are based on differences in performance and design between coupled and decoupled approaches. These conclusions should be valid regardless of the implementation uncertainty, since the same modeling technique is used for all experiments. However, since the BLI effects, and thus the fuel burn estimate for the BLI configuration, are subject to this uncertainty, it is worthwhile to look into the following aspects: i) whether this implementation uncertainty matters? and ii) if so, is there a basis to strongly favor one approach over the other? The first question can be addressed by repeating the experiments 1.1 and 1.2 in this thesis, using different combinations of the above modeling approaches when generating the surrogates Sensitivity of the performance and design of the BLI vehicle to these implementation differences determines the need to address question (ii). This question can potentially be answered by comparing the fuel burn estimates from power balance to a study that calculates fuel burn from the net axial force F_X on the aircraft.

Recall, F_X is one level above power balance and thrust-drag as it does not separate out contributions from the airframe and propulsor. Studies in literature have varied the propulsor boundary conditions in CFD to meet a target net axial force. These boundary conditions have then been mapped to an engine operating point using a cycle analysis code, and the resulting fuel flow rate for that point was calculated. At a high level, the idea is to take a BLI configuration in CFD, calculate the net axial force

for a specified set of engine boundary conditions, and back out the fuel flow rate at that engine operating point. Then, for same geometry, the BLI effects are calculated using all possible approaches, and accounted for in the same manner as described in this thesis. The resulting change in fuel flow rate at the reference point can thus be compared to the F_X approach. The relative closeness of the power-balance fuel burn estimates to the F_X result can be a criterion to favor a set of implementation choices.

This comparison, however, is not as straightforward as it sounds. First, the level of fidelity used to calculate D' for the power balance approaches needs to be the same as that used for F_X. If CFD is used to calculate F_X for a powered engine-aircraft model, a low fidelity estimate of D' from FLOPS is not appropriate. Thus, for purposes of this comparison, D' ought to be calculated from CFD for an un-powered configuration that is very similar to the powered configuration used to obtain F_X, except for the engine location. Next, it is important to maintain the same C_L between configurations to eliminate discrepancies related to operating conditions. Both D' and F_X calculated in CFD are very sensitive to all design details, as discussed in relation to observation 4 from literature. If certain components, like the empennage for example, are not part of the CFD model, these need to be accounted for somehow in F_X and D' to set realistic power requirements for the propulsor. Another source of concern is matching the inlet and outlet momentum fluxes for the powered CFD engine model to that obtained from the cycle analysis code. This matching is needed to accurately map the fuel flow rate calculated by the cycle code to the operating point modeled in CFD. This places requirements on the inlet and nozzle designs for the CFD geometry model, in addition to the boundary conditions. The choice of engine model, i.e., 1D powered boundary conditions, actuator disc, or body force, also have a significant influence on F_X. If one wishes to address the implementation uncertainty associated with power balance, all these aspects should be carefully considered to ensure a fair and justifiable comparison between power balance and F_X.

8.4.5 Uncertainty Quantification

The section above commented on one specific source of uncertainty in the BLI effects. There are other sources of uncertainty in the BLI responses like surrogate model prediction error, mesh refinement error, CFD solver convergence error, etc. Section 7.3.2 provided preliminary estimates quantifying the impacts of surrogate prediction error on the BLI fuel burn savings, highlighting the need for further studies. Future work could quantify the consequences of all these sources uncertainty on the system level responses of interest. A straightforward, but brute force approach to do so involves the use of Monte Carlo Simulations. First, based on any empirical evidence, an error distribution on each of the five BLI effects is defined. Typically, this error distribution is assumed to be Gaussian. Following this, Monte Carlo Sampling is done on these distributions, using a statistically significant number of samples, which is typically on the order of a thousand. Every sample corresponds to a random draw of percentage error from each of the five BLI effects error distributions. For a fixed vehicle design, these percentage errors in a given sample are then applied to the surrogate models integrated in the vehicle design environment. The system level responses for that sample are recorded, and the process repeats for the remaining samples. From these samples, a probability distribution function is obtained for all system level responses that are tracked for a given design. This function shows the uncertainty in the system response (most likely value, standard deviation, range, etc.) as a result of all the sources of uncertainty in the BLI effects. This probability function can then be integrated to generate a cumulative distribution function. This function, ranging from 0 to 1, shows the probability of a given system level response being equal to or less than a specified value.

For a probabilistic design space exploration study, the process above must be repeated for every design combination in the DoE. The end result is a cumulative distribution function for each system level response of interest, for every design. Then,

each of these cumulative distributions can be discretized to obtain the value of the system level response that corresponds to a given confidence level (probability). So for example, the value of the system level responses at the 10% probability level, followed by those at the 50% and 90% probability levels can be tracked at a minimum. Then, for each set of responses corresponding to a given confidence level, surrogate models can be generated as a function of the variables considered in the design space exploration study. Fig. 7.20 showed a snapshot of the results from a deterministic design space exploration study. The end result of this probabilistic study is a series of design spaces, each corresponding to a given level of probability, that account for the impacts of uncertainty in the BLI effects. The amount of computational effort expended to achieve these results is significant, owing to the number of cases needed to generate probabilistic trends. More efficient uncertainty quantification approaches could be considered to minimize this expense.

8.5 Final Comments

In conclusion, this thesis shows that aero-propulsive interactions due to BLI can substantially affect the performance and design of the vehicle. Decoupled approaches that rely on a point design estimate of the BLI effects are inadequate. The proposed method thus serves as a foundation for future BLI concept design studies.

Appendices

APPENDIX A
ADDITIONAL FIGURES FROM EXP. 2

In this appendix, the reader will find additional plots that pertain to experiment 2, which is described in chapter 5. These plots show the raw non-dimensional BLI effects measurements and are only included for completeness. The main results derived from the raw data and observations from this processed data have been covered in chapter 5. In this appendix, cross references to the figures in the main body are included as part of the figure captions.

Figures A.1 to A.5

These figures show the non-dimensional BLI effects $C_{P_{K_{\text{in}}}}$, $C_{\dot{E}}$, and η_{PR} at every axial and circumferential measurement station location on the fuselage. All trials from experiments 2.2, 2.3, 2.4 and 2.5 are covered in this plots. Red, blue, and green markers are used to denote measurements of the BLI effects at the 0°, 45°, and 90° circumferential stations respectively. Each of these figures compares two sets of raw measurements using different marker shapes, from which the differences in the BLI effects were calculated for a particular trial, as shown in chapter 5. The legends within each plot and the figure captions describe the two data sets being compared. Experiment number formatting follows the main body.

Figure A.6

Fig. A.6 shows the individual BLI effects $C_{P_{K_{\text{in}}}}$ and $C_{\dot{E}}$ and how they vary as a function of wing design changes. The trends shown in Fig. 5.35 and Fig. 5.36 in chapter 5 are a summation of the individual effects shown in the appendix. Fig. A.6 follows formatting rules of Fig. 5.35.

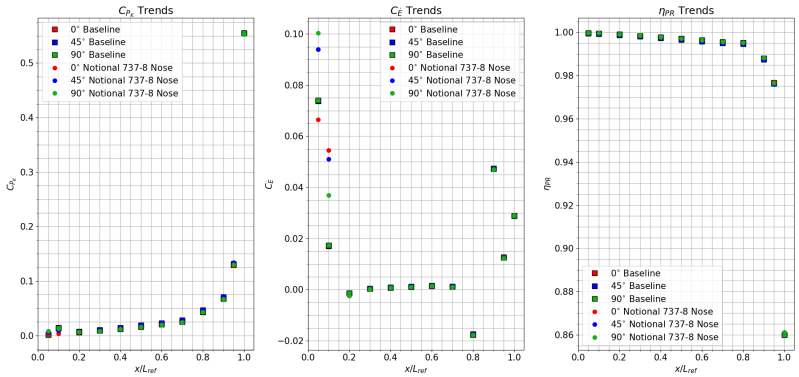

(a) E2.2-1 vs. E2.1-1 (Baseline)

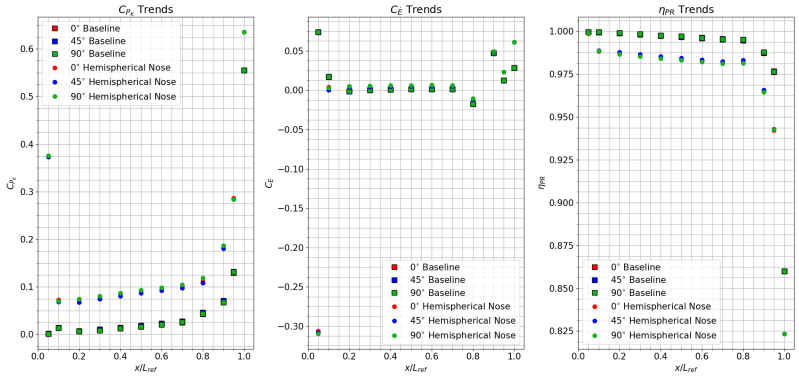

(b) E2.2-2 vs. E2.1-1 (Baseline)

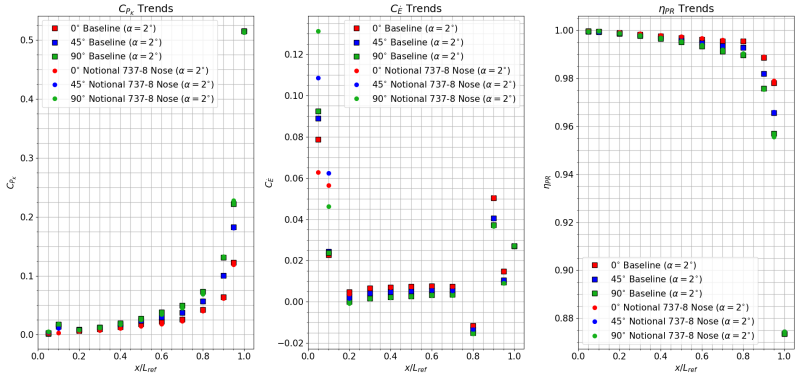

(c) E2.2-3 vs. E2.1-5 ($\alpha = 2°$ Baseline)

Figure A.1: Experiment 2.2 - axial and circumferential trends in the BLI effects, relative to the baseline, due to changes in fuselage nose shape (cross-ref. Fig. 5.16)

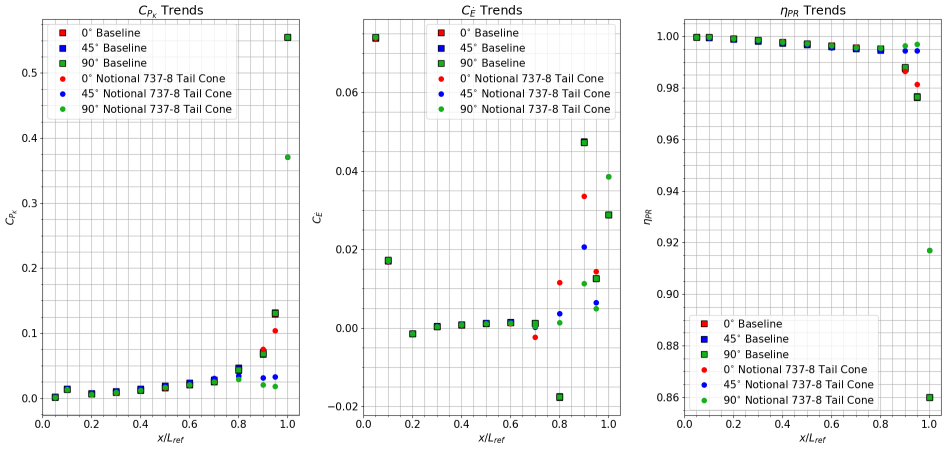

(a) E2.3-1 vs. E2.1-1 (Baseline)

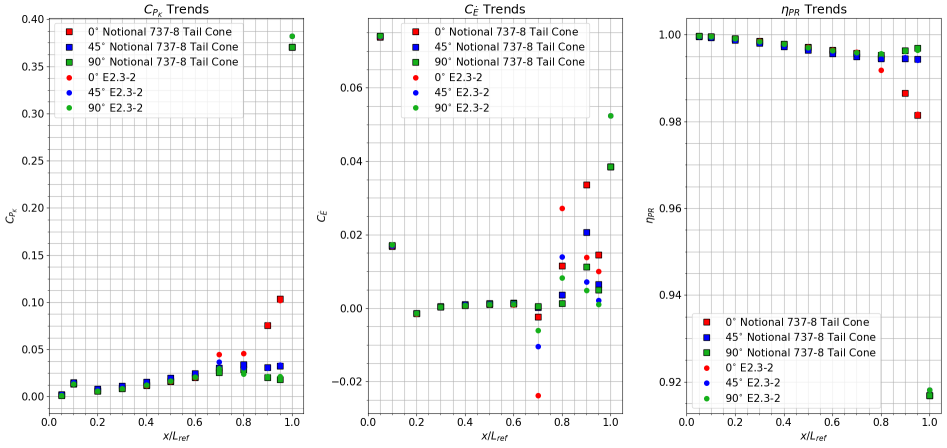

(b) E2.3-2 vs. E2.3-1

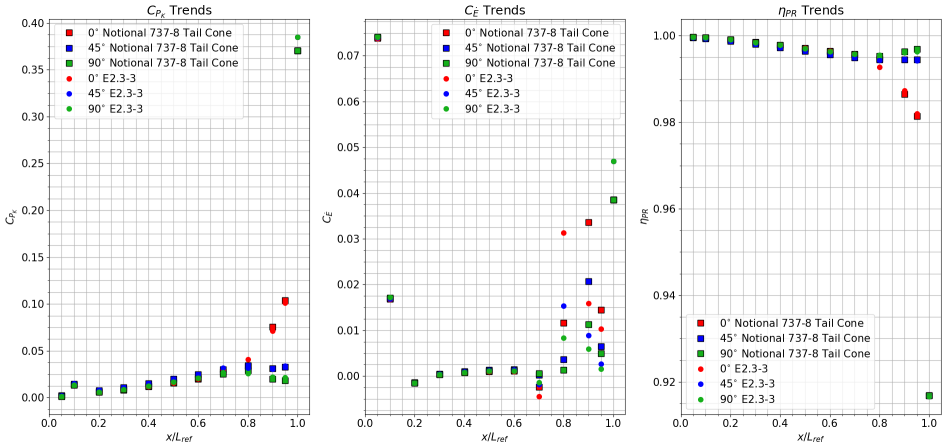

(c) E2.3-3 vs. E2.3-1

Figure A.2: Experiment 2.3 - axial and circumferential trends in the BLI effects due to changes in fuselage aft section shape (cross-ref. Fig. 5.19)

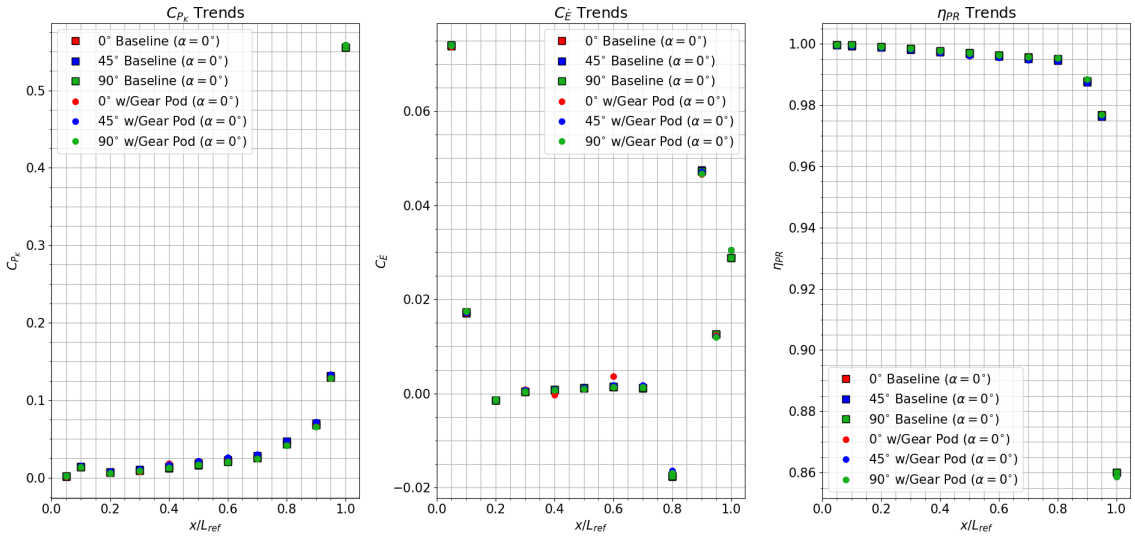

(a) E2.4-1 vs. E2.1-1 ($\alpha = 0°$ Baseline)

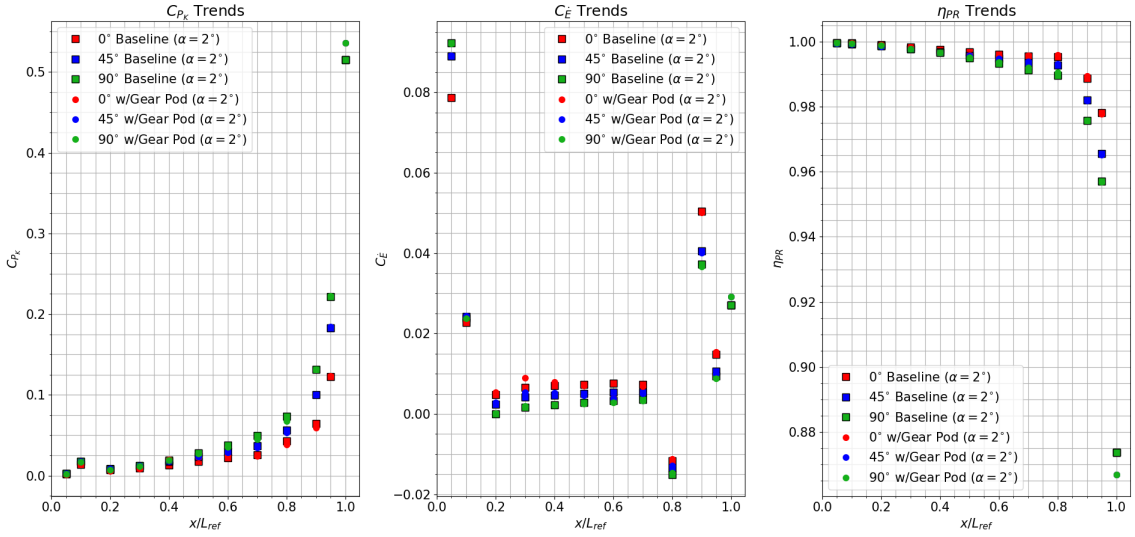

(b) E2.4-2 vs. E2.1-5 ($\alpha = 2°$ Baseline)

Figure A.3: Experiment 2.4 - axial and circumferential trends in the BLI effects, relative to the baseline, due to addition of gear pod housing (cross-ref. Fig. 5.24)

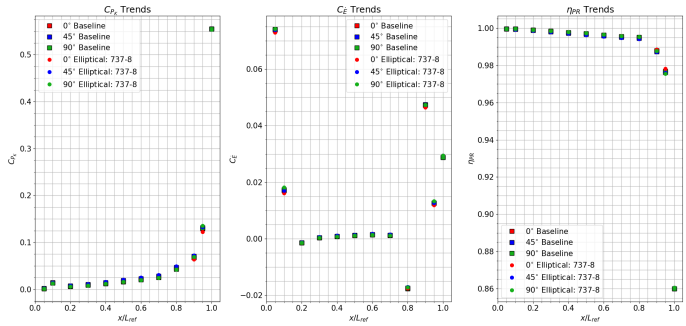

(a) Comparison 1: E2.5-1 vs. E2.1-1 (Baseline)

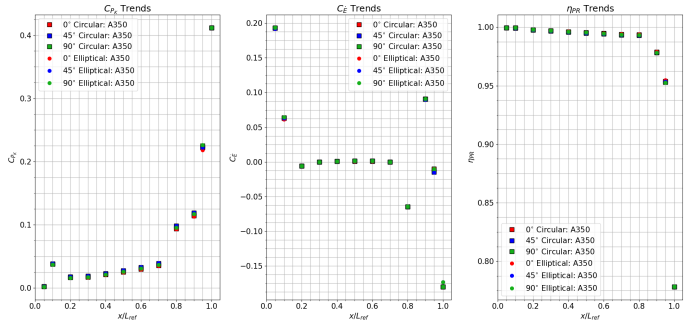

(b) Comparison 2: E2.5-2 vs. E2.5-3

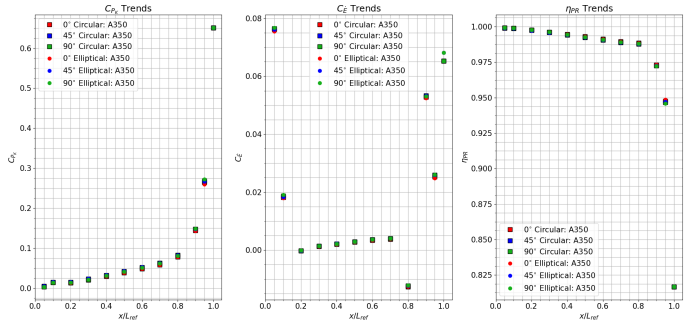

(c) Comparison 3: E2.5-4 vs. E2.5-5

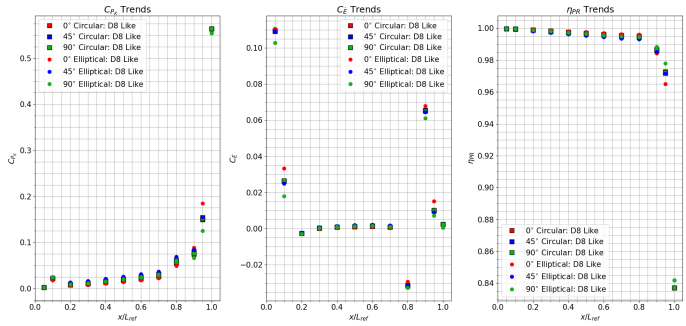

(d) Comparison 4: E2.5-7 vs. E2.5-8

Figure A.4: Experiment 2.5 - axial and circumferential trends in the BLI effects due to changes in fuselage cross sectional shape representation (elliptical vs circular). Cross-ref Fig. 5.27

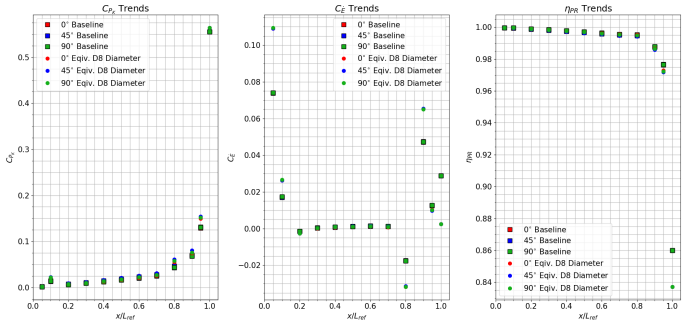

(a) Comparison 5: E2.5-8 vs. E2.1-1 (Baseline)

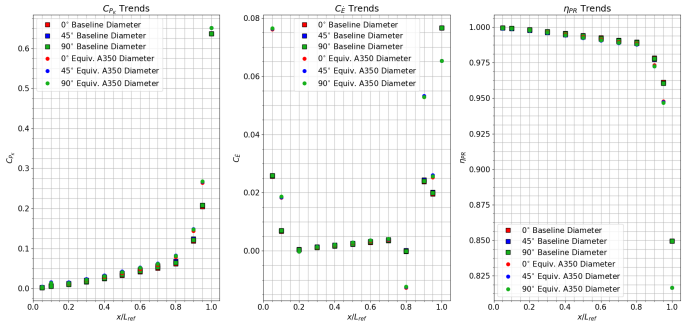

(b) Comparison 6: E2.5-6 vs. E2.5-5

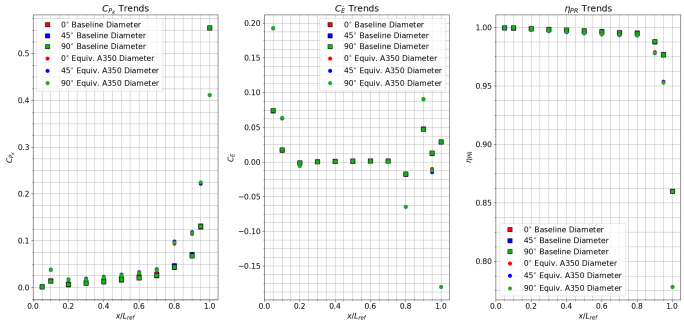

(c) Comparison 7: E2.5-3 vs. E2.1-1 (Baseline)

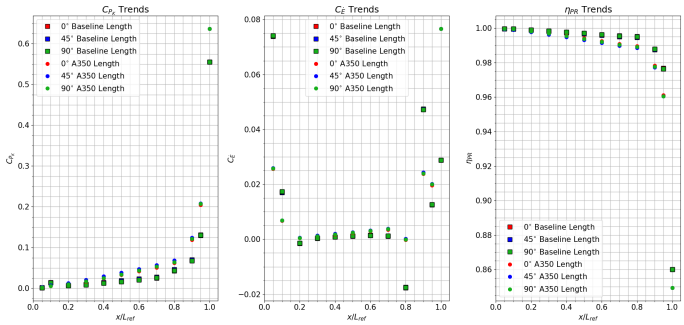

(d) Comparison 8: E2.5-6 vs. E2.1-1 (Baseline)

Figure A.5: Experiment 2.5 - axial and circumferential trends in the BLI effects due to changes in fuselage cross sectional area and length (cross-ref. Fig. 5.29)

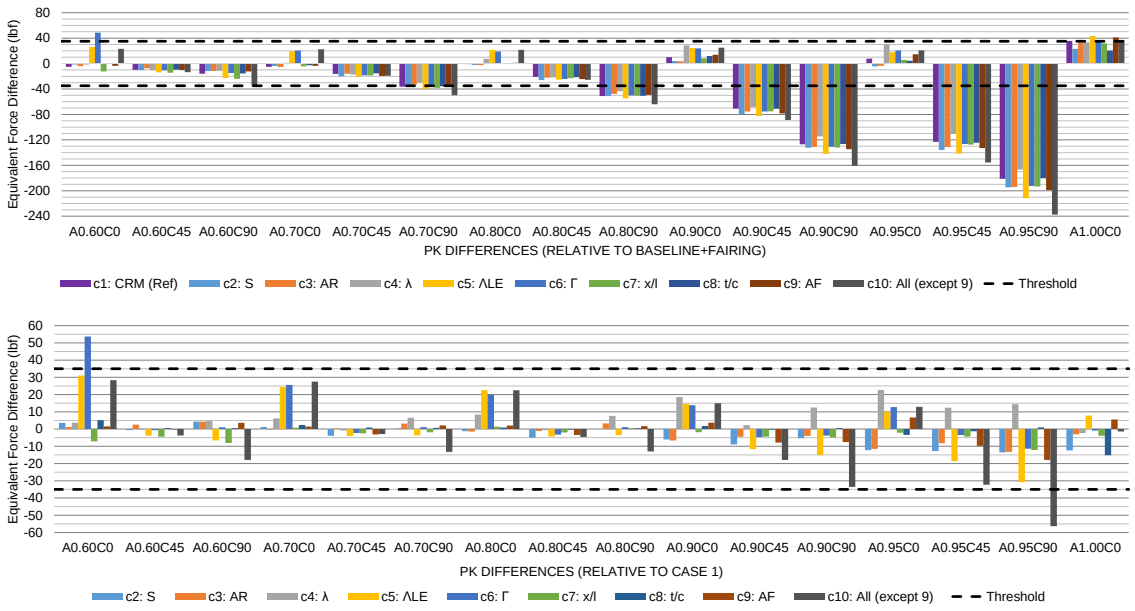

(a) $C_{P_{K_{\text{in}}}}$

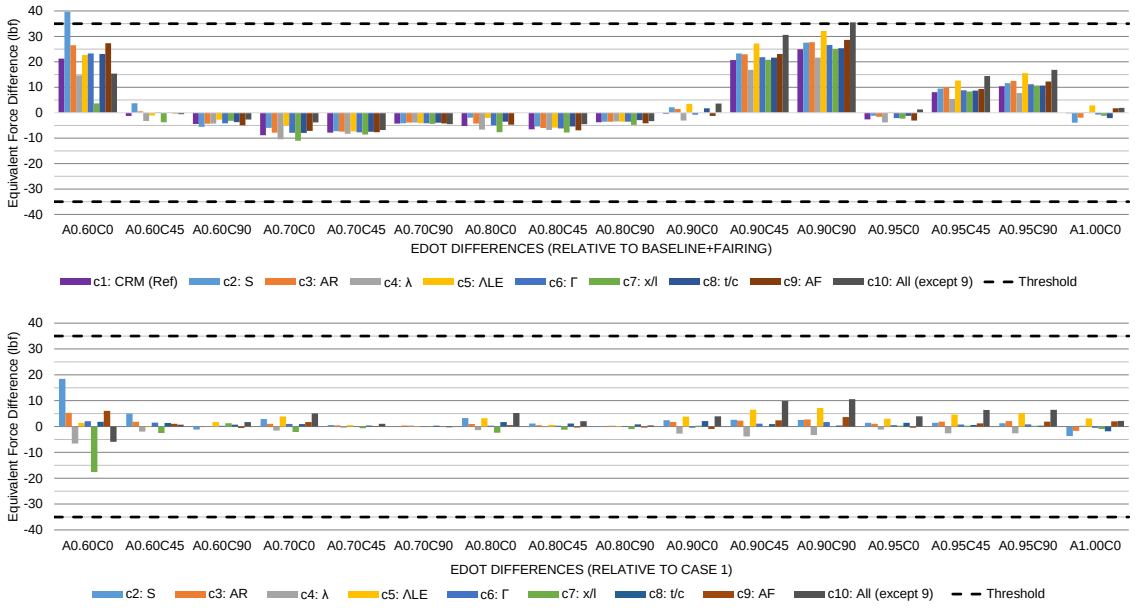

(b) $C_{\dot{E}}$

Figure A.6: Experiment 2.6 - influence of the wing on $C_{P_{K_{\text{in}}}}$ and $C_{\dot{E}}$ at measurement stations aft of the wing at $\alpha = 2°$ (cross-ref. Fig. 5.35 and Fig. 5.36)

APPENDIX B
ADDITIONAL FIGURES FROM EXP. 3

In this appendix, the reader will find additional plots that pertain to experiment 3, which is described in chapter 6. These plots show supporting evidence for the discussion in chapter 6 regarding the variation in the BLI effects to propulsor design and operation. Like before, these figures in the Appendix are referenced within the main text, where appropriate, and cross references to the relevant sections within the main body are included in the introductory paragraphs for a given set of figures, and in the figure captions themselves.

Evidence Supporting $P_{K_{\text{in}}}$ Trends

In section 6.1.2, the theoretical non-linear behavior of $C_{P_{K_{\text{in}}}}$ to velocity ratio $\frac{V}{V_\infty}$ was discussed as a means to predict variations in $C_{P_{K_{\text{in}}}}$ with flow rate and fan size. Fig. B.1 and B.2 show how the density $\frac{\rho}{\rho_\infty}$ and pressure coefficient terms of $C_{P_{K_{\text{in}}}}$, highlighted in Eqs. (5.1) and (6.1), vary with velocity ratio, using experiment 3.1 raw CFD data, as a means to explain the trends shown in Figs. 6.8 and 6.9. These trends were discussed in section 6.3.2. The curve fit equation shown in Fig. B.1 was used in the generation of Fig. 6.9. Similarly, Fig. B.3 shows the variation of mass flux with velocity ratio at the fan face, using CFD data from all experiment 3.2 trials, as a means to explain the trends shown in Fig. 6.18 for experiment 3.2, discussed in section 6.4.2. The equation of the polynomial fit was used in the generation of Fig. 6.18. Formatting of the plots in terms of marker shapes and colors is consistent with the figures in chapter 6 for experiments 3.1 and 3.2.

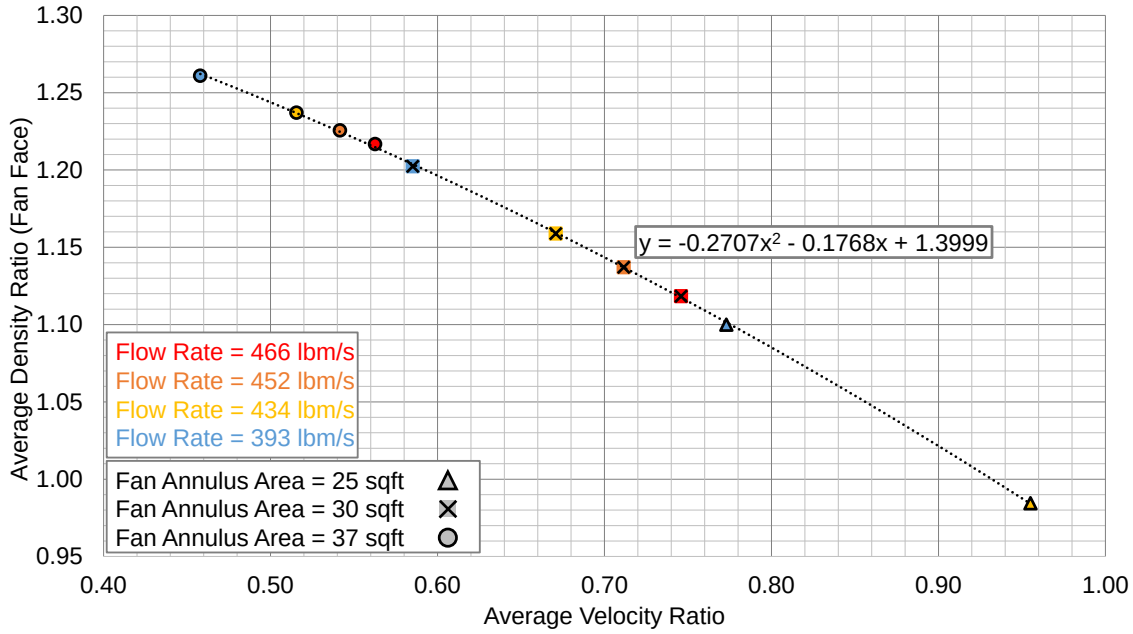

Figure B.1: Experiment 3.1 - variation of average density ratio with average velocity ratio, at the fan face, with the polynomial fit to the CFD data (cross-ref. Fig. 6.9)

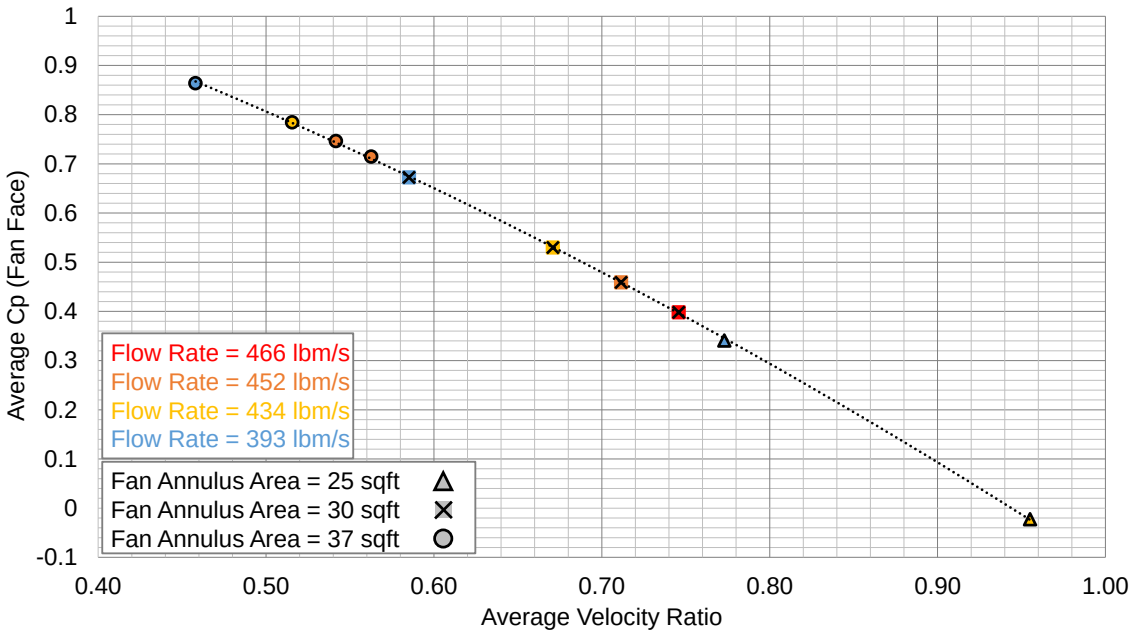

Figure B.2: Experiment 3.1 - variation of average pressure coefficient with average velocity ratio, measured at the fan face (cross-ref. section 6.1.2)

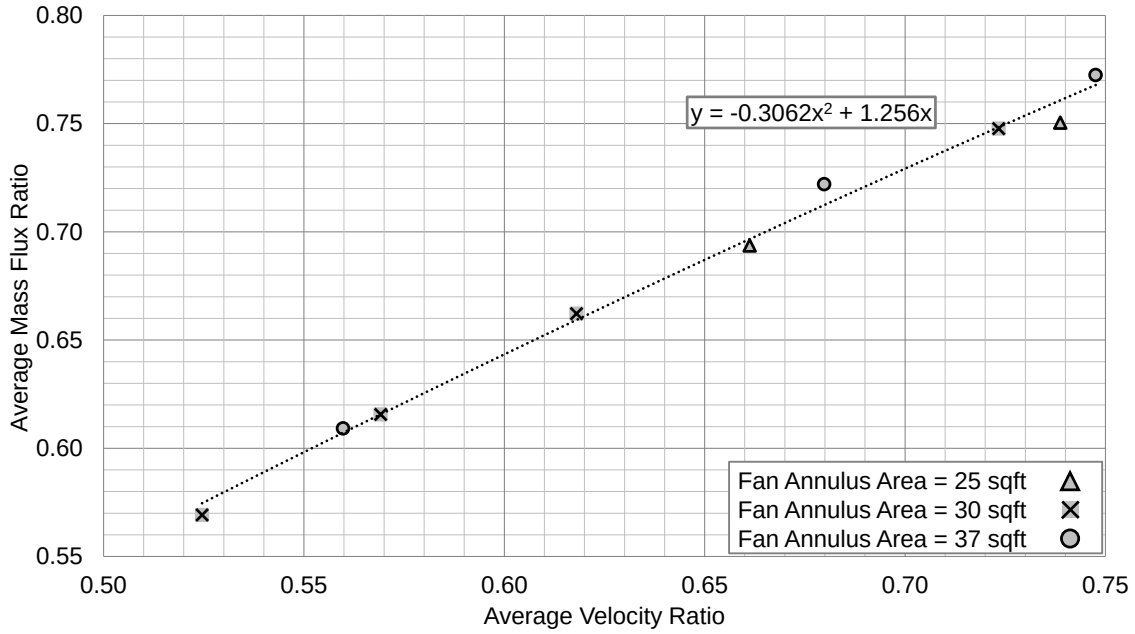

Figure B.3: Experiment 3.2 - variation of average mass flux ratio $\frac{\rho V}{\rho_\infty V_\infty}$ with average velocity ratio, measured at the fan face, with the functional form of the polynomial fit to the CFD data (cross-ref. Fig. 6.18)

Pressure Recovery Trends and Supporting Evidence

Figs. B.4 and B.5 show how the inlet pressure recovery $\left(\eta_{PR} = \frac{p_{t_2}}{p_{t_1}}\right)$ varies as a function of flow rate and fan size for experiment 3.1 and 3.2 respectively. These figures essentially show the nacelle's contribution to the pressure losses in the ingested flow. These trends are consistent with those observed at the fan face and agree with hypothesis 3. The sharp drops in pressure recovery are indicative of shocks in the nacelle, which are discussed in chapter 6. Fig. B.4 is associated with Fig. 6.13b and Fig. B.5 is linked to Fig. 6.16b. Fig. B.6 shows the near wall velocity profiles, for a fixed propulsor size, at four different flow rates to highlight how wall shear, which is a function of the wall velocity gradient, increases with flow rate, thereby explaining the decrease in pressure recovery with flow. This plot is linked with Fig. 6.13b. Discussion of the pressure recovery trends for experiments 3.1 and 3.2 can be found in sections 6.3.2 and 6.4.2 respectively.

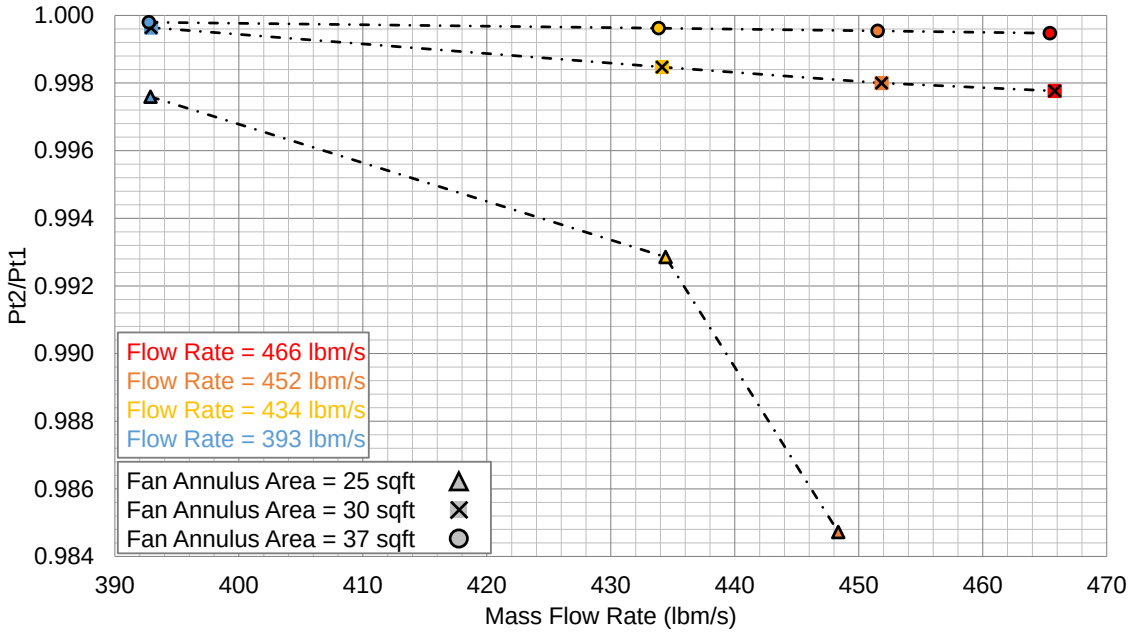

Figure B.4: Experiment 3.1 - variation of inlet $\eta_{PR} = \frac{p_{t_2}}{p_{t_1}}$ as a function of $\dot{m}_2$ (cross-ref. Fig. 6.13b)

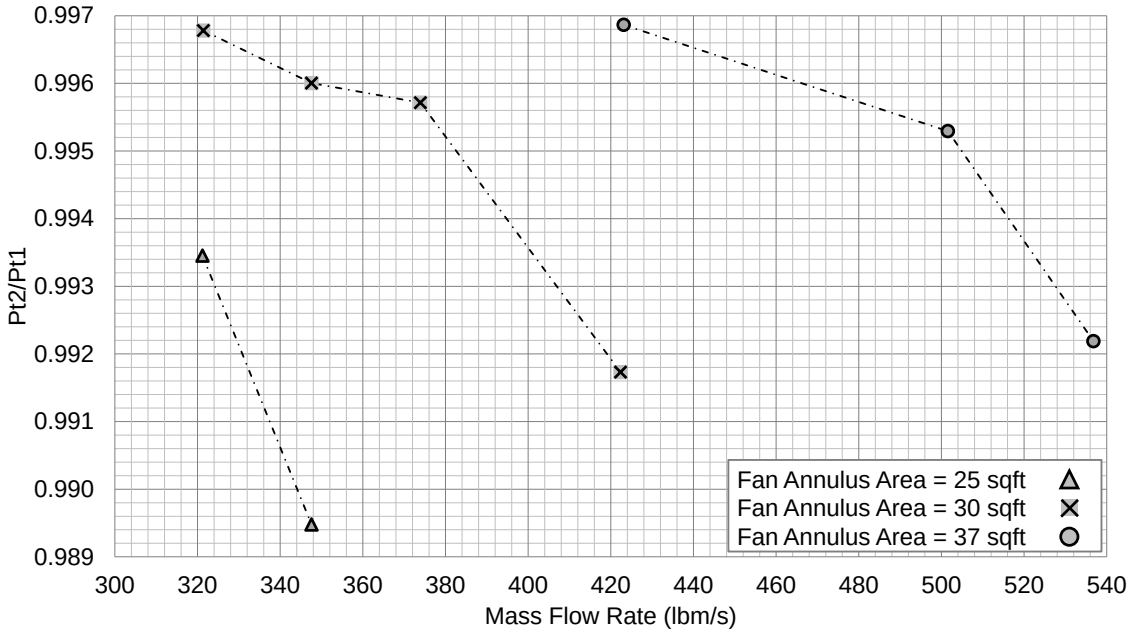

Figure B.5: Experiment 3.2 - variation of inlet $\eta_{PR} = \frac{p_{t_2}}{p_{t_1}}$ as a function of $\dot{m}_2$ (cross-ref. Fig. 6.16b)

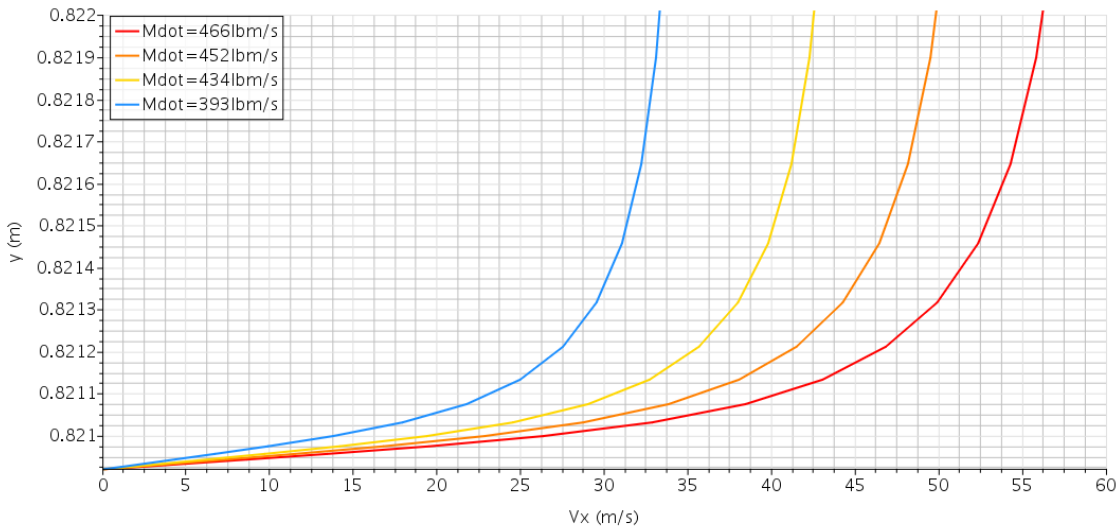

Figure B.6: Experiment 3.1 - Velocity profiles near the wall for $A_2 = 30\text{ft}^2$, for varying $\dot{m}_2$, measured in the inlet (cross-ref. Fig. 6.13b)

Trends with Specific Flow

Figs. B.7 to B.10 show how the BLI effects vary with specific flow, i.e., flow rate per unit area, for experiments 3.1 and 3.2. These plots are derived from the raw flow rate and fan area trends, collapsing both variables into one quantity, and thus only represent a different perspective on existing data. Formatting of these plots is again consistent with that used in chapter 6. An initially inconsistent finding is observed for the $C_{P_{K_{\text{in}}}}$ trends with specific flow for experiment 3.2 in Fig. B.9. While Fig. 6.16a showed a decrease in $C_{P_{K_{\text{in}}}}$ with area for a fixed flow rate, we see that in the specific flow domain, $C_{P_{K_{\text{in}}}}$ increases with area for a fixed specific flow. While this trend may seem inconsistent, one must realize that a reduction in area must also correspond to a decrease in flow rate to maintain the same specific flow. Since $C_{P_{K_{\text{in}}}}$ decreases with a reduction in flow for this particular configuration, these trends are actually consistent with the physics discussed in chapter 6.

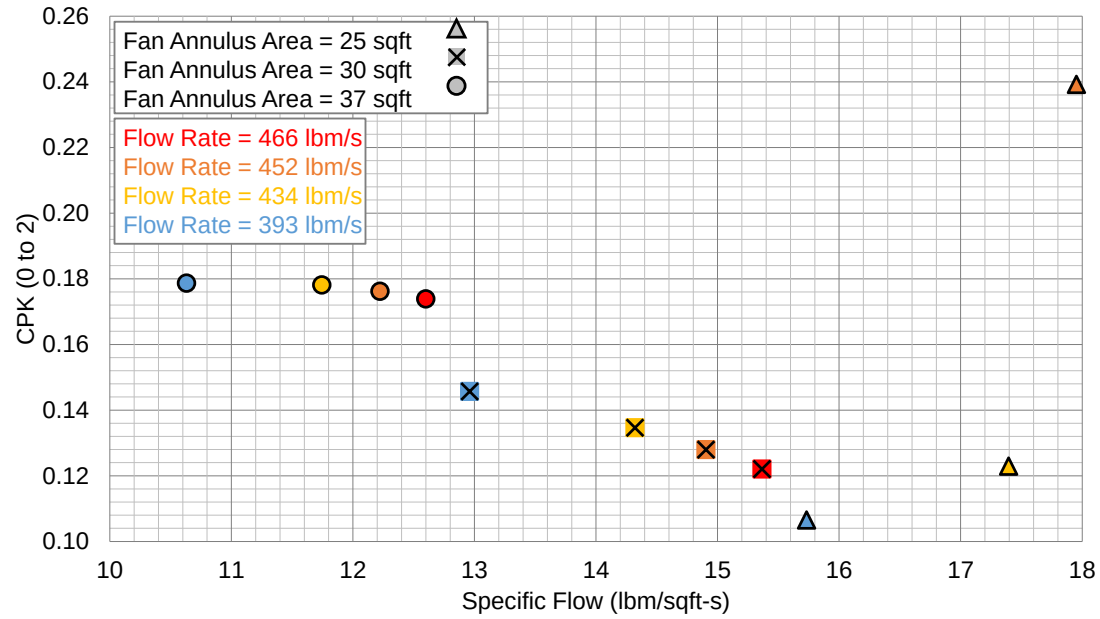

Figure B.7: Experiment 3.1 - variation of $C_{P_{K_{\text{in}}}}$ at fan face as a function of $\frac{\dot{m}_2}{A_2}$ (cross-ref. Fig. 6.7)

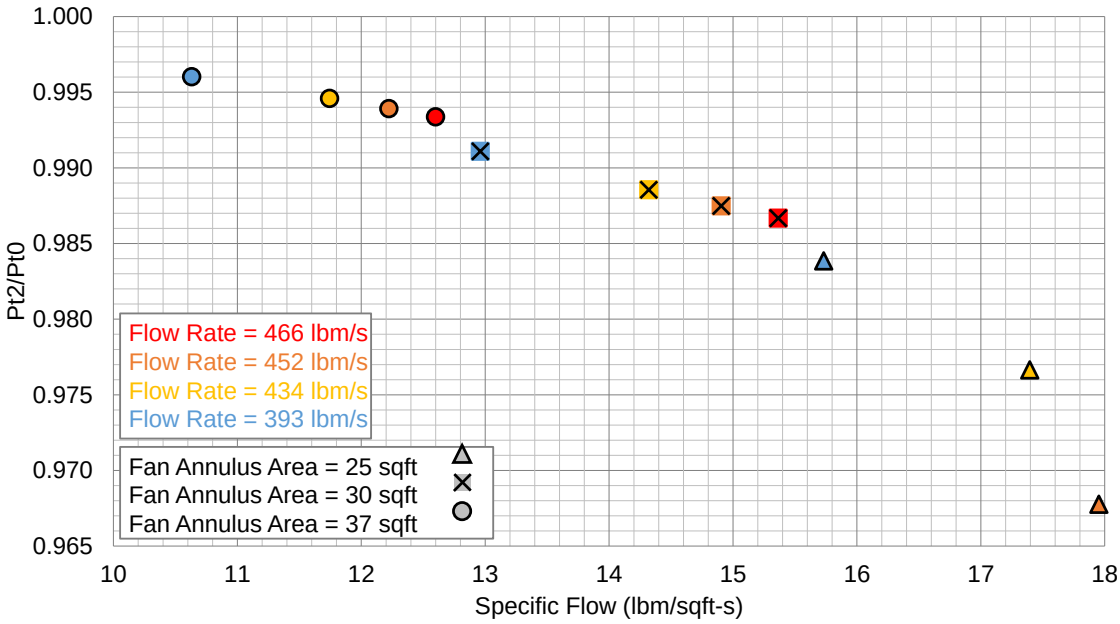

Figure B.8: Experiment 3.1 - variation of $\eta_{PR} = \frac{p_{t_2}}{p_{t_0}}$ as a function of $\frac{\dot{m}_2}{A_2}$ (cross-ref. Fig. 6.13)

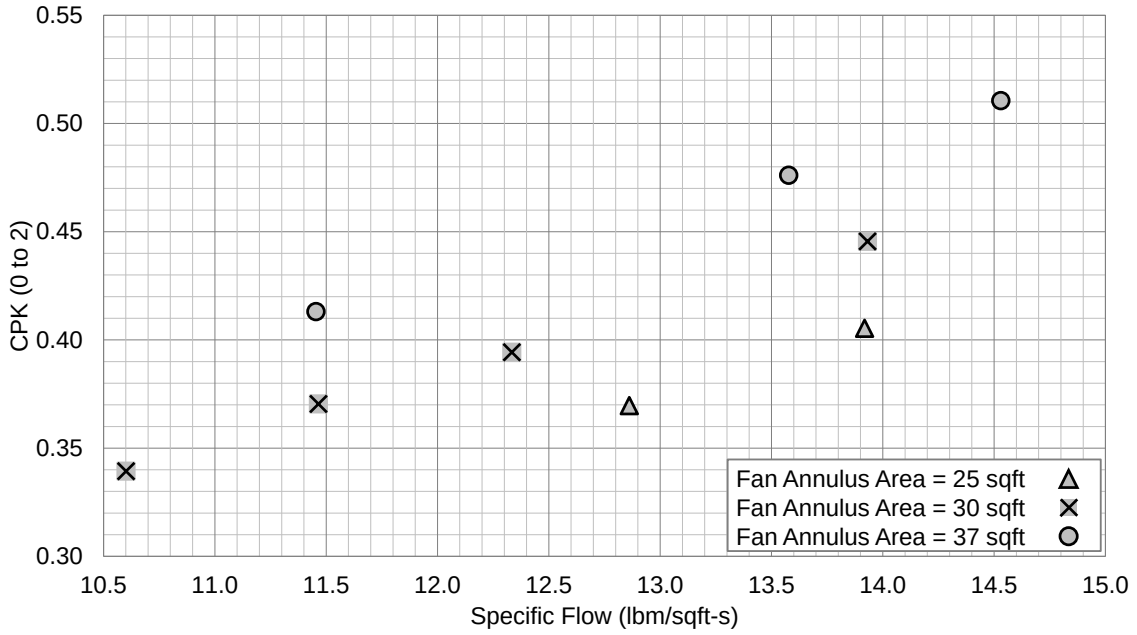

Figure B.9: Experiment 3.2 - variation of $C_{P_{K_{\text{in}}}}$ at fan face as a function of $\frac{\dot{m}_2}{A_2}$ (cross-ref. Fig. 6.16)

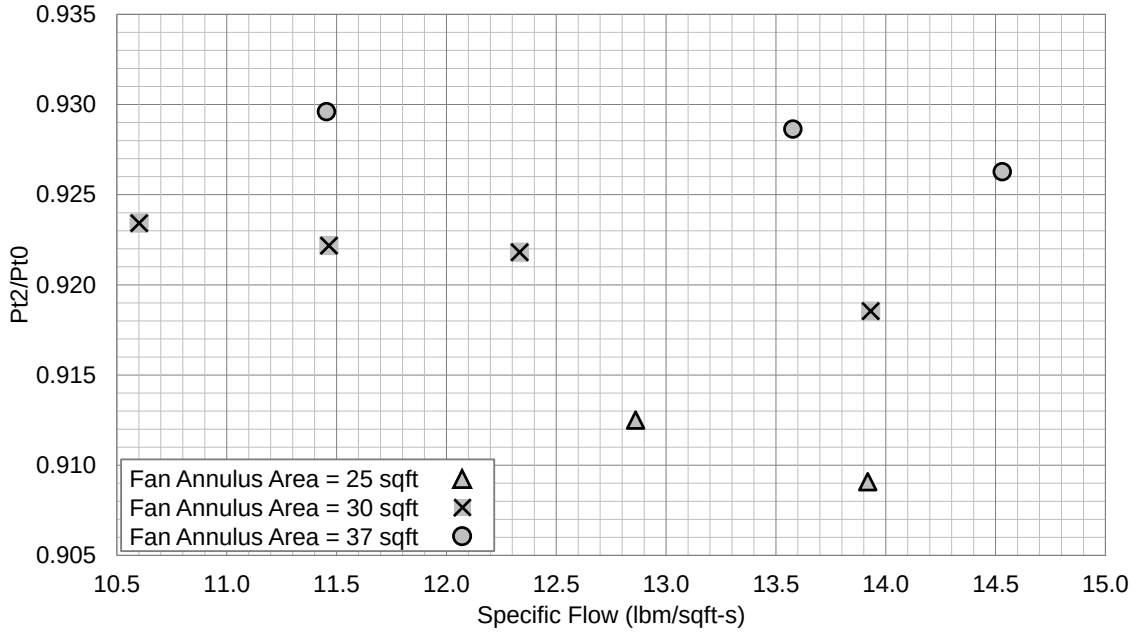

Figure B.10: Experiment 3.2 - variation of $\eta_{PR} = \frac{p_{t_2}}{p_{t_0}}$ as a function of $\frac{\dot{m}_2}{A_2}$ (cross-ref. Fig. 6.16)

APPENDIX C
ADDITIONAL FIGURES FROM EXP. 1

This appendix provides data supporting the validity of the two sets of surrogate models developed in this thesis. The first set applies to the BLI effects surrogates that are used within the vehicle design framework as part of the proposed coupled and parametric methodology. In particular, data for the main BLI effects $P_{K_{\text{in}}}$, η_{PR} and $\Delta\Phi_{\text{wake}}$ are presented. The second set of surrogates model key system level responses generated from this design framework, which are then used for vehicle design optimization.

Figures C.1 and C.2

These figures show how the sampled points are distributed for training (Fig. C.1) and validating (Fig. C.2) the main BLI effects surrogate models as a series of 2-D snapshots of the design space. As discussed in section 7.1.2, I-optimal DoEs are used for training the BLI effects models. To validate these models, a space filling design is used. Note that every sample point within the training and validation DoEs satisfies the constraints described in section 7.1.2.

Figures C.3 and C.4

Figures C.3 presents the BLI effects surrogates diagnostic information. The actual vs. predicted, residual vs. predicted, and model fit error distribution plots are presented. Fig. C.4 presents the model representation error. In the error distribution plots, the main metrics of interest are the mean, standard deviation, and bounds. Outliers are identified as points on the outside of the box plot bounds. Discussion about the quality of fits based on this diagnostic information can be found in chapter 7.

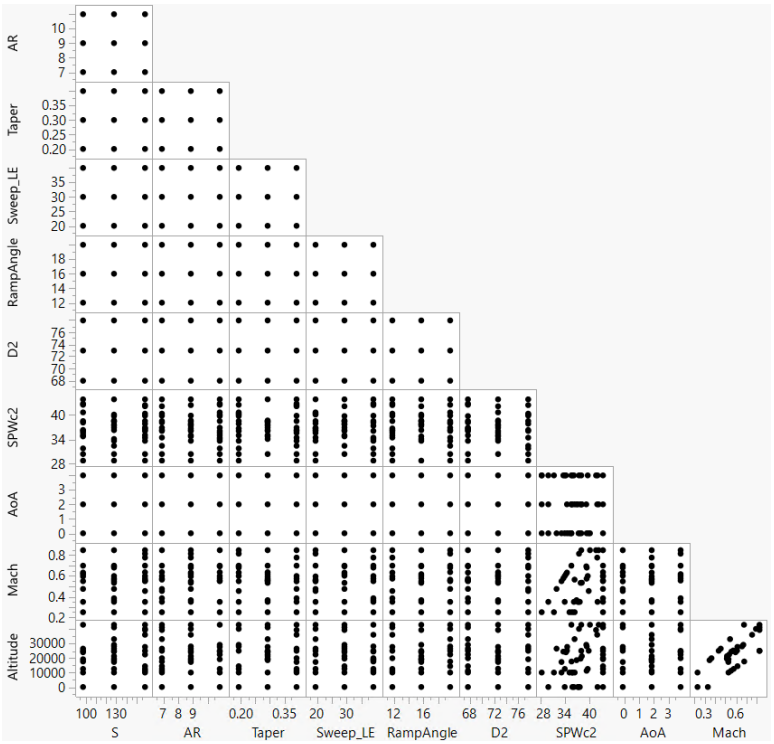

(a) DoE for $P_{K_{\text{in}}}$ and η_{PR}

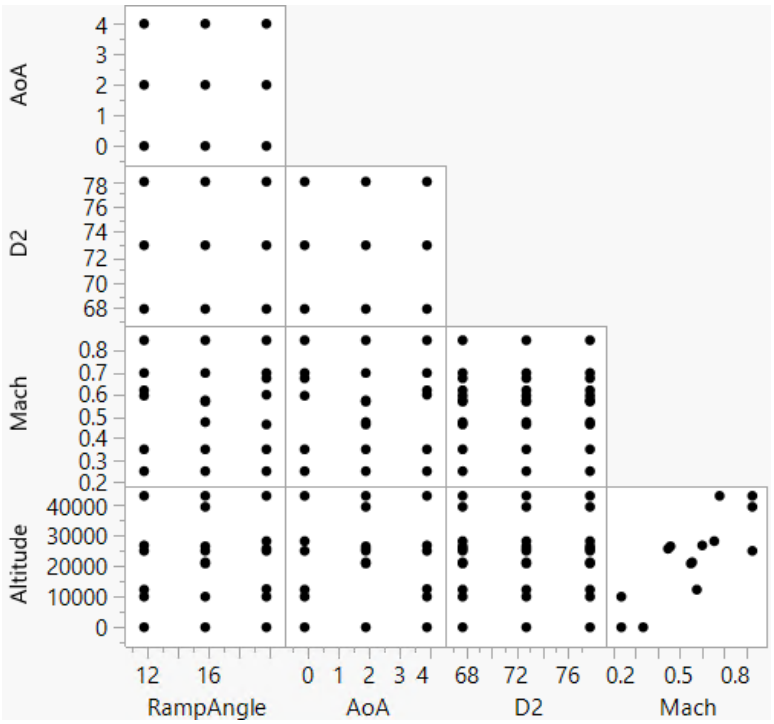

(b) DoE for $\Delta\Phi_{\text{wake}}$

Figure C.1: Scatterplot matrices showing the I-optimal DoEs used for training the BLI effects surrogate models

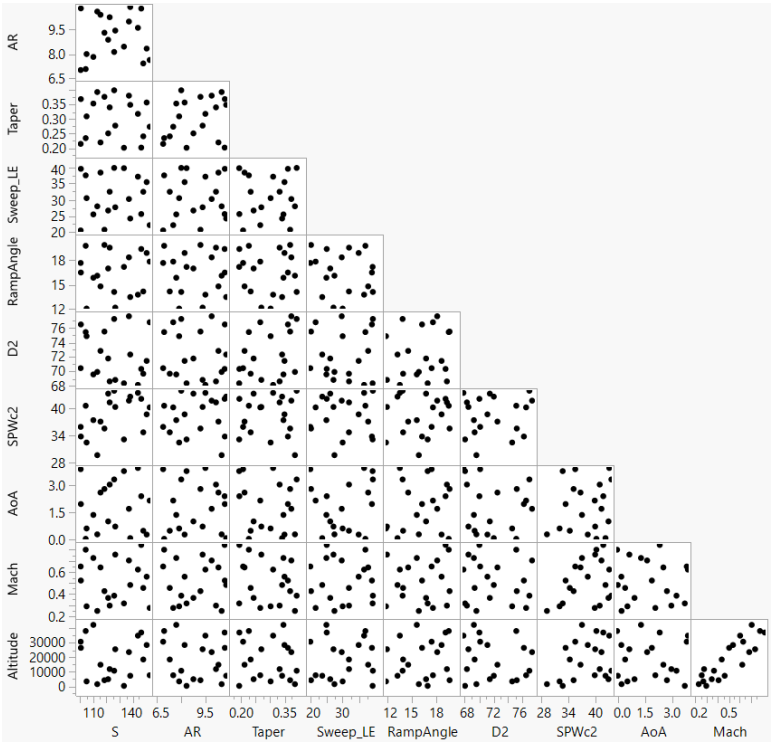

(a) DoE for $P_{K_{\text{in}}}$ and η_{PR}

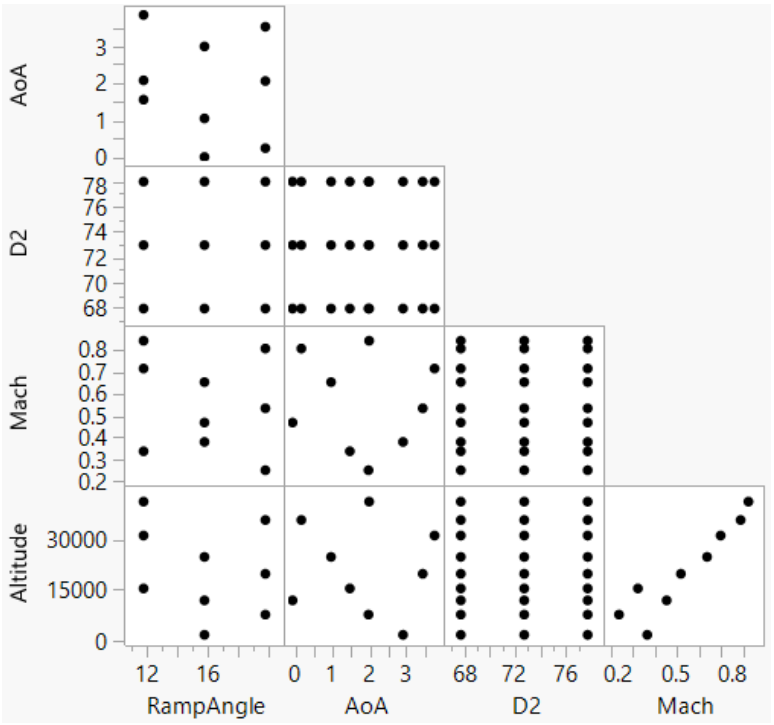

(b) DoE for $\Delta\Phi_{\text{wake}}$

Figure C.2: Scatterplot matrices showing the space filling DoEs used for validating the BLI effects surrogate models

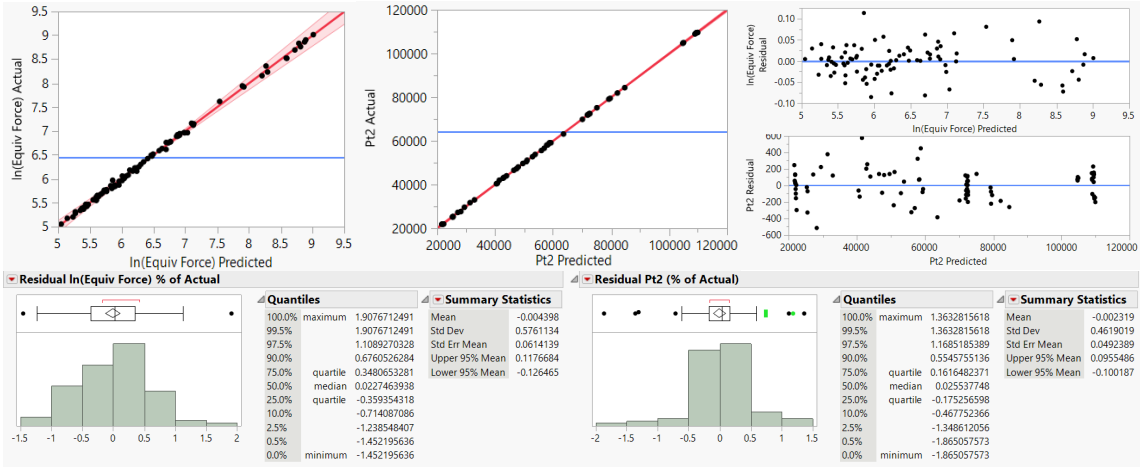

(a) $ln\left(C_{P_{K_{\text{in}}}} \frac{1}{2}\rho_\infty V_\infty^2 S_{\text{ref}}\right)$ and P_{t_2} for top-engine configuration

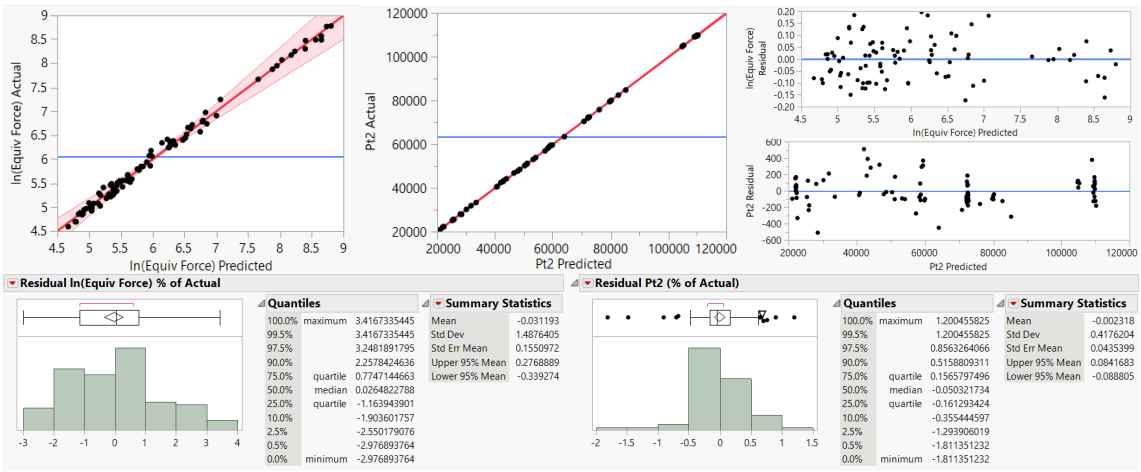

(b) $ln\left(C_{P_{K_{\text{in}}}} \frac{1}{2}\rho_\infty V_\infty^2 S_{\text{ref}}\right)$ and P_{t_2} for side-engine configuration

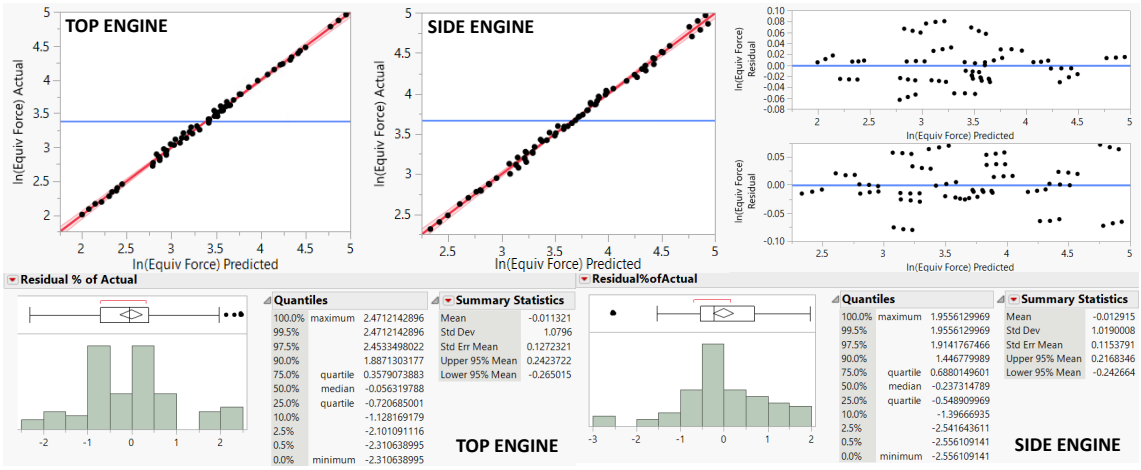

(c) $ln\left(C_{\dot{E}} \frac{1}{2}\rho_\infty V_\infty^2 S_{\text{ref}}\right)$ for both the top and side-engine configuration

Figure C.3: Actual vs. predicted, residual vs. predicted, and model fit error plots

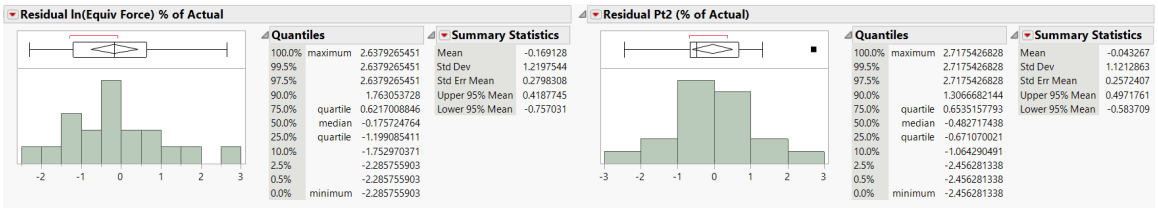

(a) $ln\left(C_{P_{K_{\text{in}}}}\frac{1}{2}\rho_\infty V_\infty^2 S_{\text{ref}}\right)$ and P_{t_2} for top-engine configuration

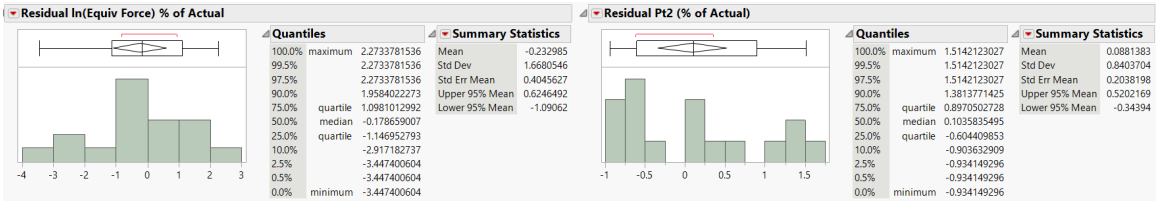

(b) $ln\left(C_{P_{K_{\text{in}}}}\frac{1}{2}\rho_\infty V_\infty^2 S_{\text{ref}}\right)$ and P_{t_2} for side-engine configuration

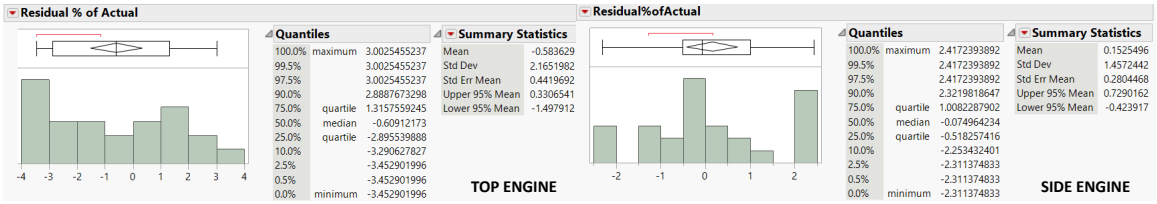

(c) $ln\left(C_{\dot{E}}\frac{1}{2}\rho_\infty V_\infty^2 S_{\text{ref}}\right)$ for both the top and side-engine configuration

Figure C.4: Model representation error distributions for BLI surrogates

Figures C.5 to C.11

These figures show the same diagnostic information as above for the surrogates of design block fuel, sea level static thrust, wing planform area, takeoff gross weight, takeoff field length, landing field length, and fan diameter. These response are obtained from EDS, as discussed in section 7.3. Fig. C.5 shows the 2-D snapshots of the training and validation points. The same DoE is used for both the top and side engine configurations. Figs. C.6 to C.11 show quality of fit diagnostics for the top engine configuration, followed by the side engine aircraft, in the given order: non-BLI variant, BLI-decoupled version, and then the BLI-coupled models. Again, the quality of these fits based on the diagnostic information is discussed in chapter 7.

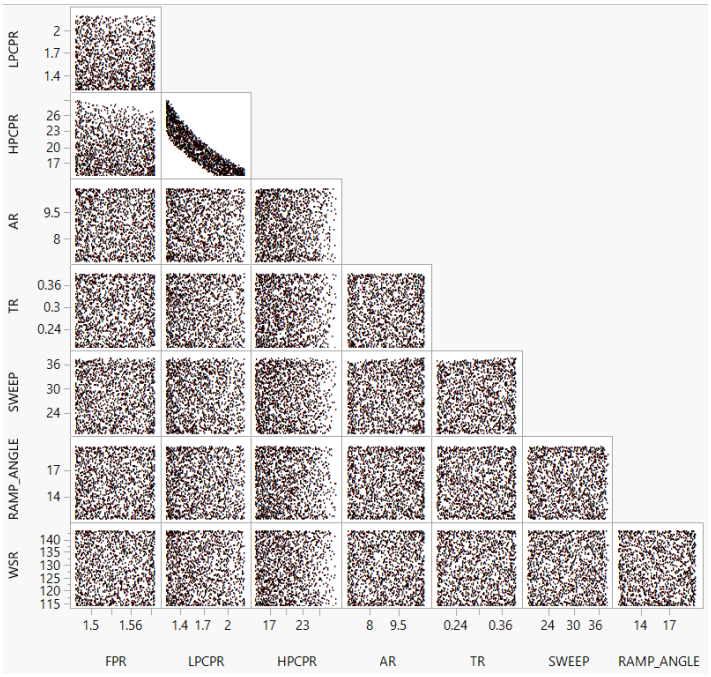

(a) Training DoE

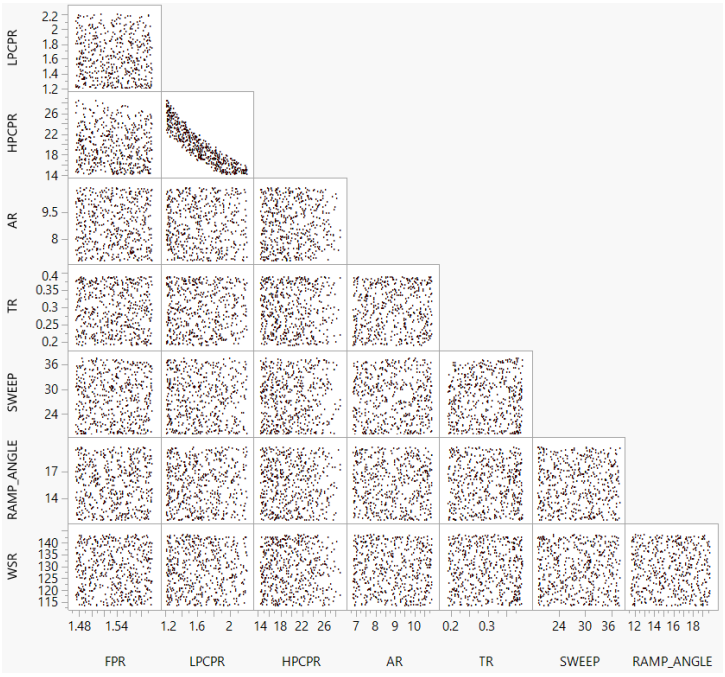

(b) Validation DoE

Figure C.5: Scatterplot matrices showing the space filling DoEs used for the design space exploration of the BLI top and side-engine configurations. The same DoEs are used to train and validate surrogate models of key design and performance metrics

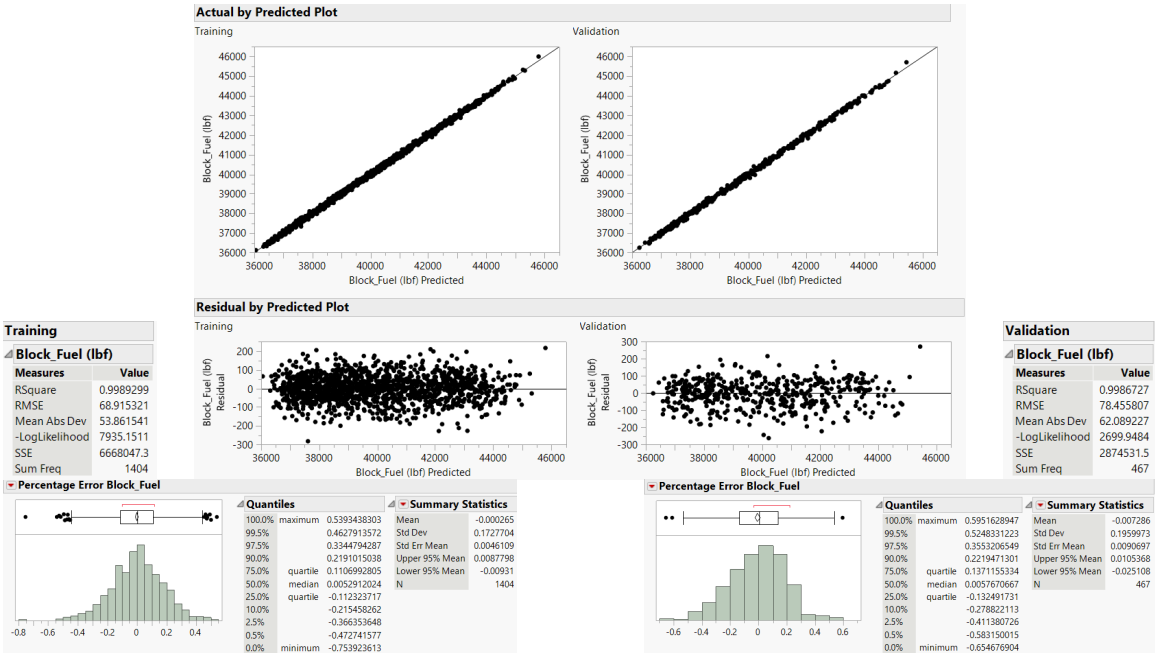

(a) Design block fuel

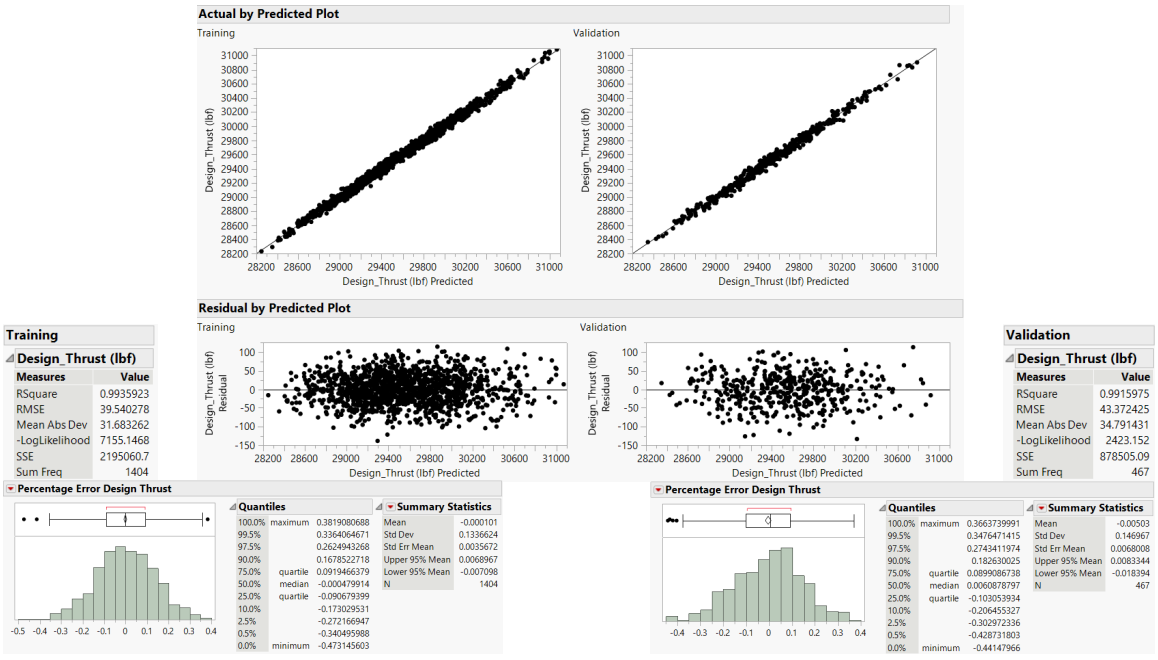

(b) SLS thrust per engine

Figure C.6: Top-engine non-BLI actual vs. predicted, residual vs. predicted, model fit and model representation error plots for surrogates

(c) Wing planform area

(d) Takeoff gross weight

Figure C.6: Top-engine non-BLI actual vs. predicted, residual vs. predicted, model fit and model representation error plots for surrogates (contd.)

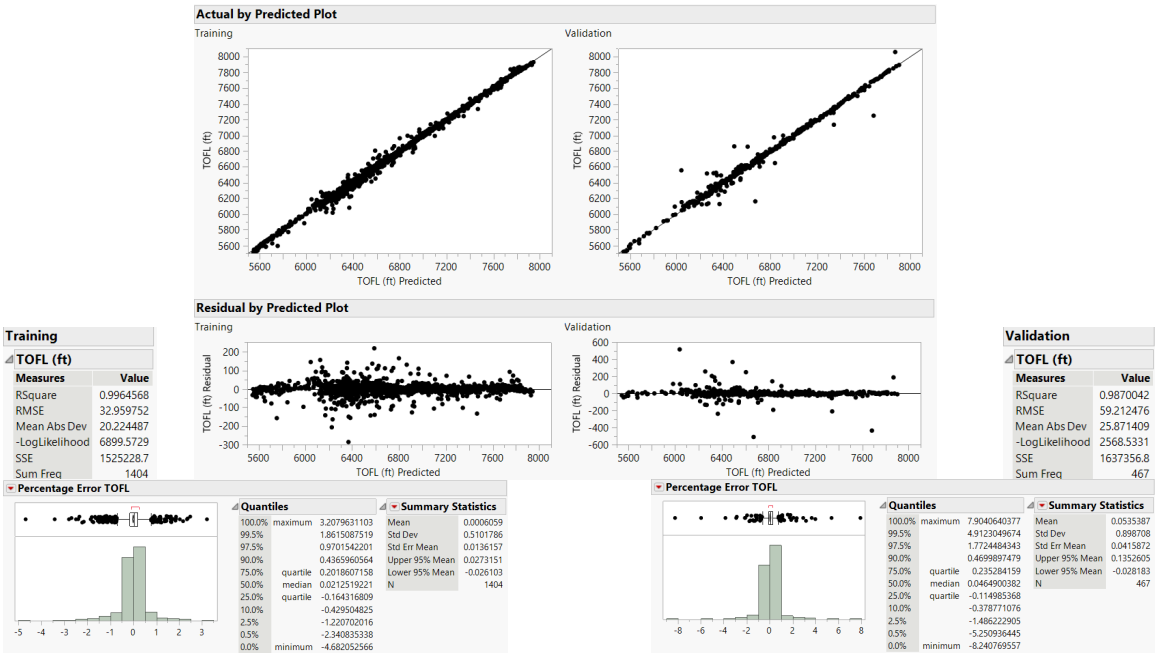

(e) Takeoff field length

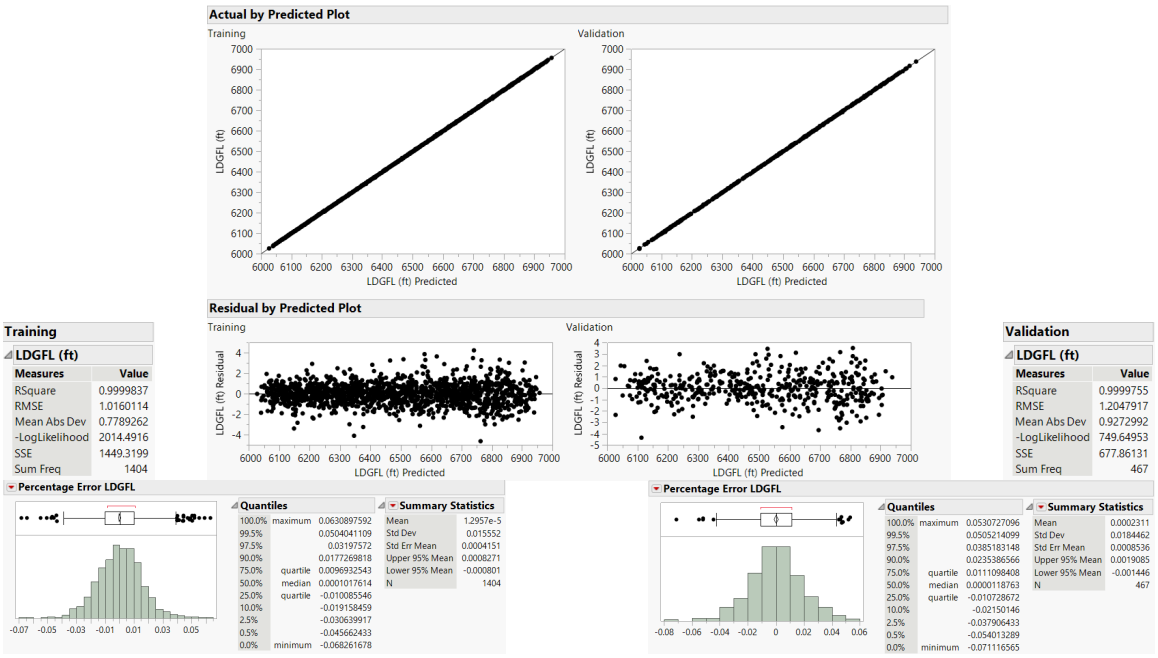

(f) Landing field length

Figure C.6: Top-engine non-BLI actual vs. predicted, residual vs. predicted, model fit and model representation error plots for surrogates (contd.)

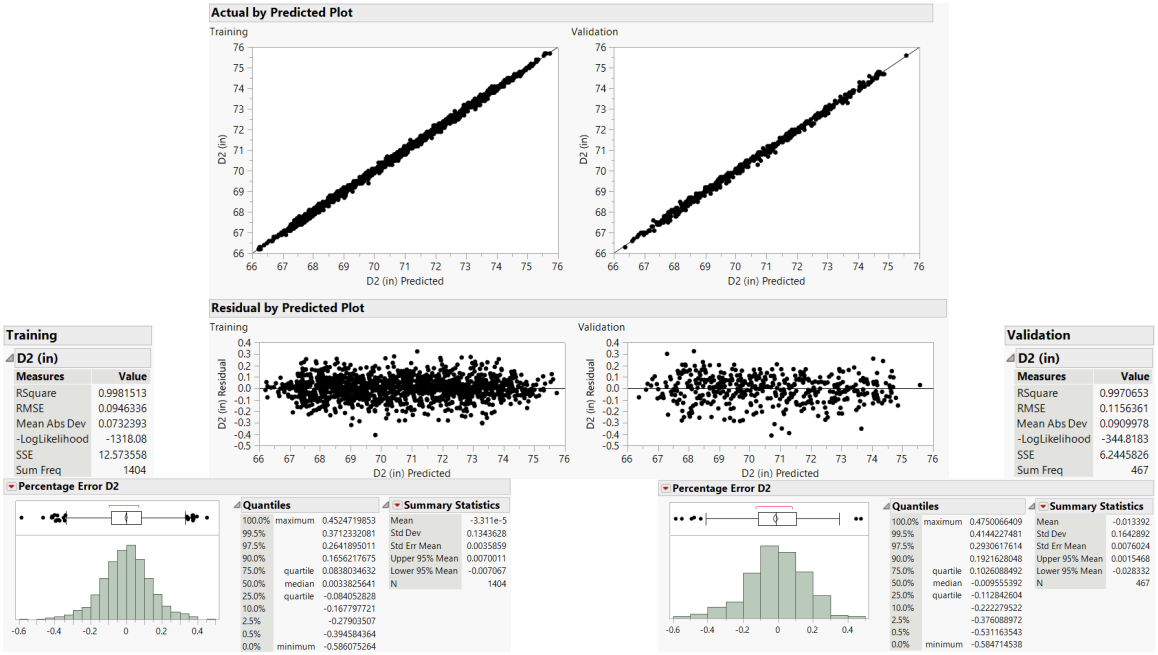

(g) Fan diameter

Figure C.6: Top-engine non-BLI actual vs. predicted, residual vs. predicted, model fit and model representation error plots for surrogates (contd.)

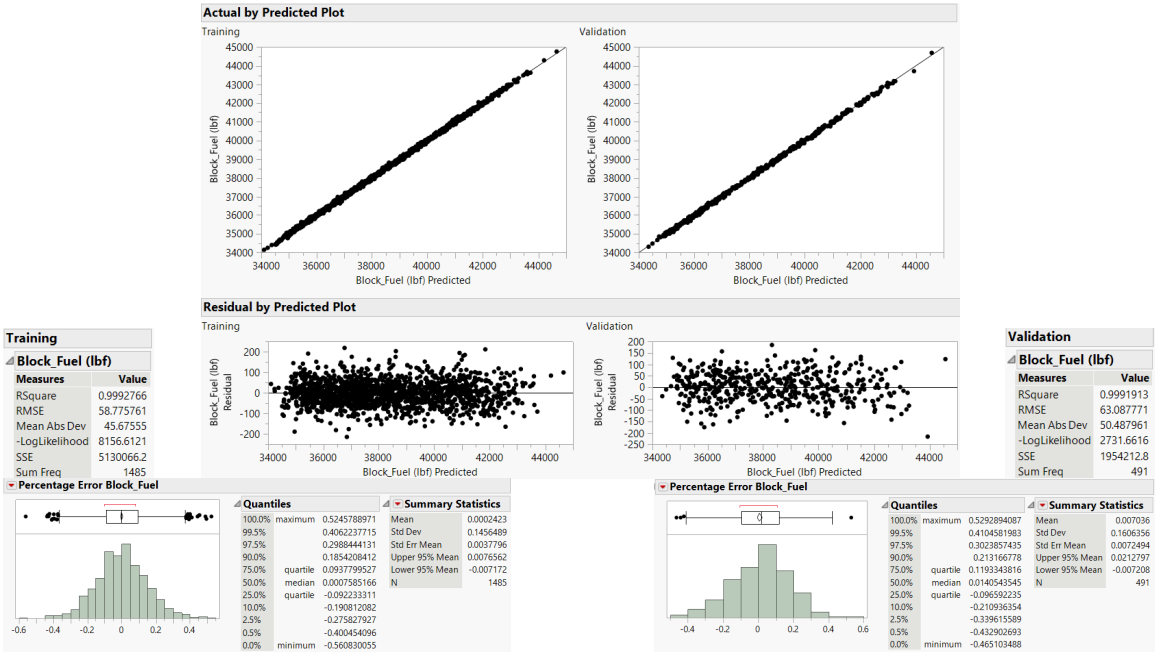

(a) Design block fuel

Figure C.7: Top-engine BLI-decoupled configuration actual vs. predicted, residual vs. predicted, model fit and model representation error plots for surrogate models

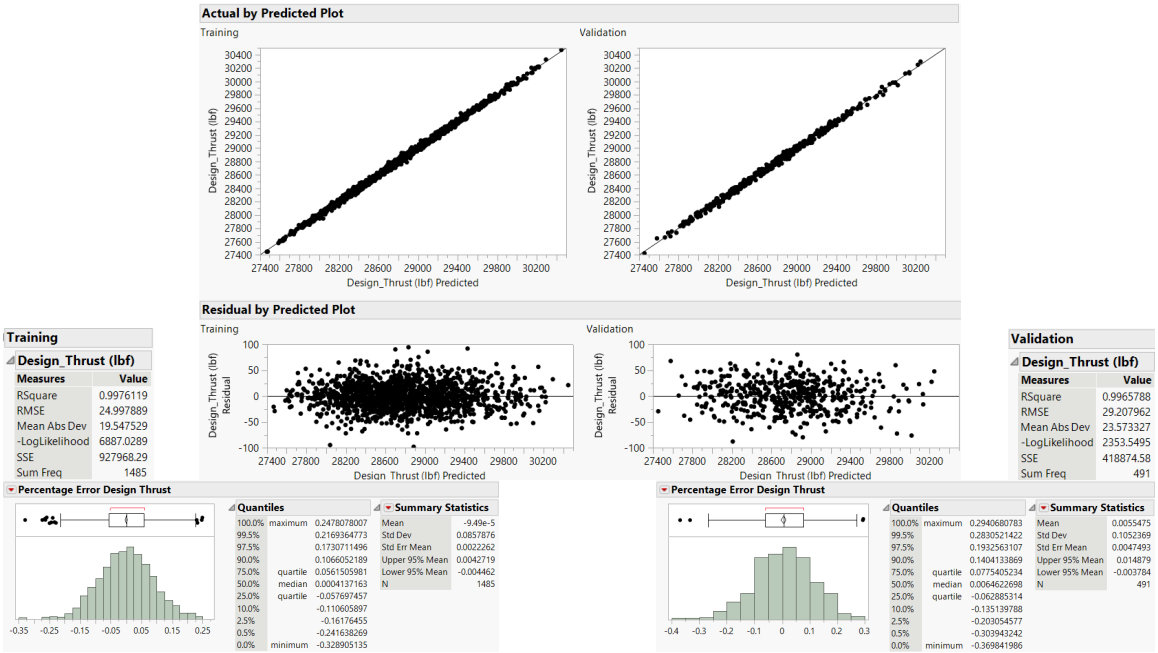

(b) SLS thrust per engine

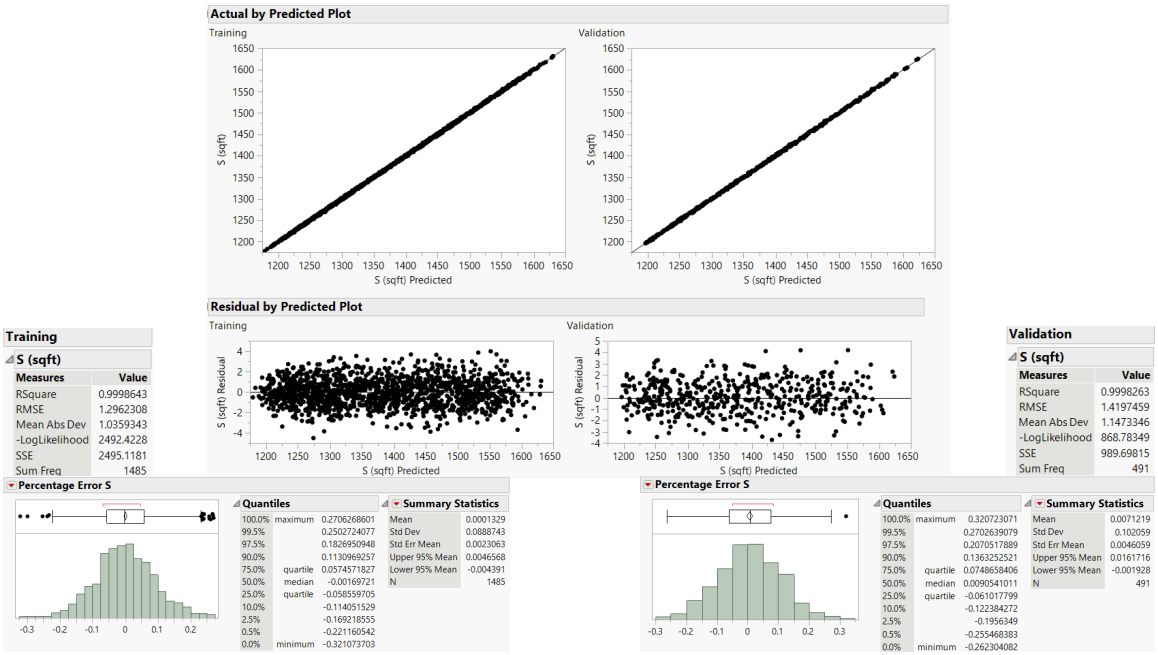

(c) Wing planform area

Figure C.7: Top-engine BLI-decoupled configuration actual vs. predicted, residual vs. predicted, model fit and model representation error plots for surrogate models (contd.)

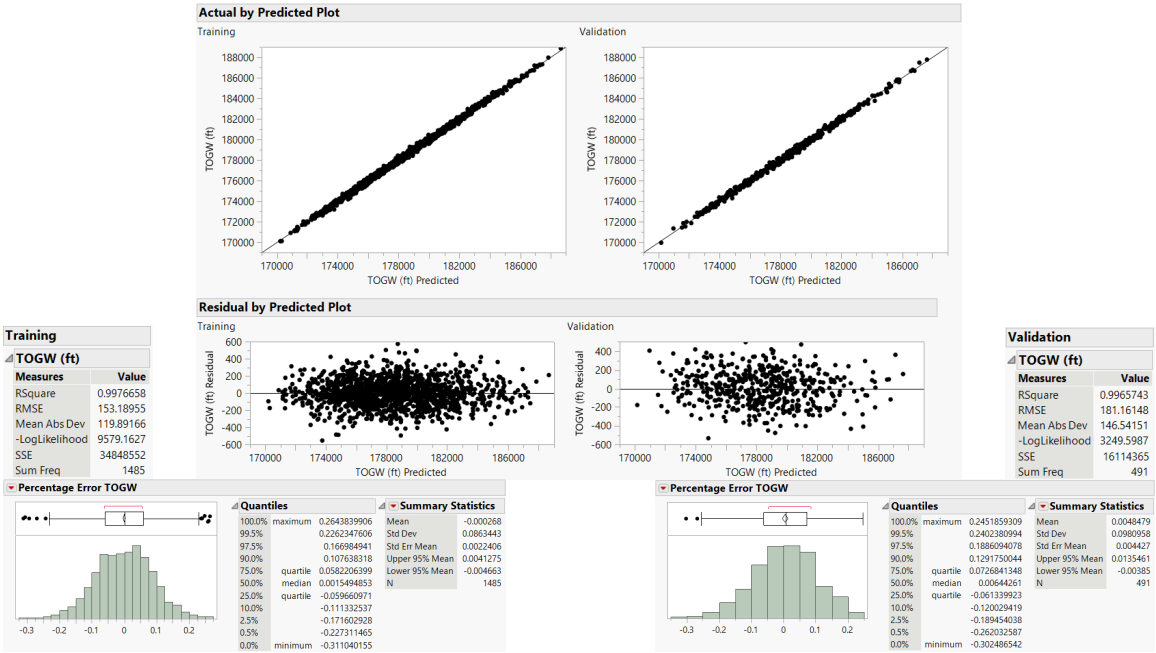

(d) Takeoff gross weight

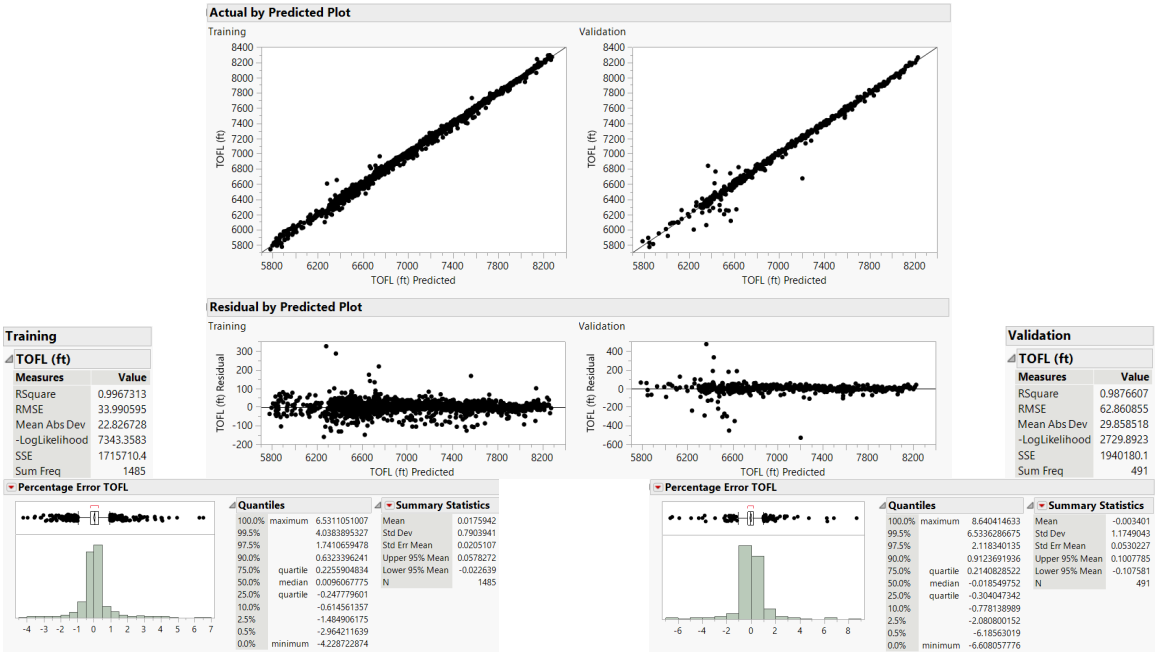

(e) Takeoff field length

Figure C.7: Top-engine BLI-decoupled configuration actual vs. predicted, residual vs. predicted, model fit and model representation error plots for surrogate models (contd.)

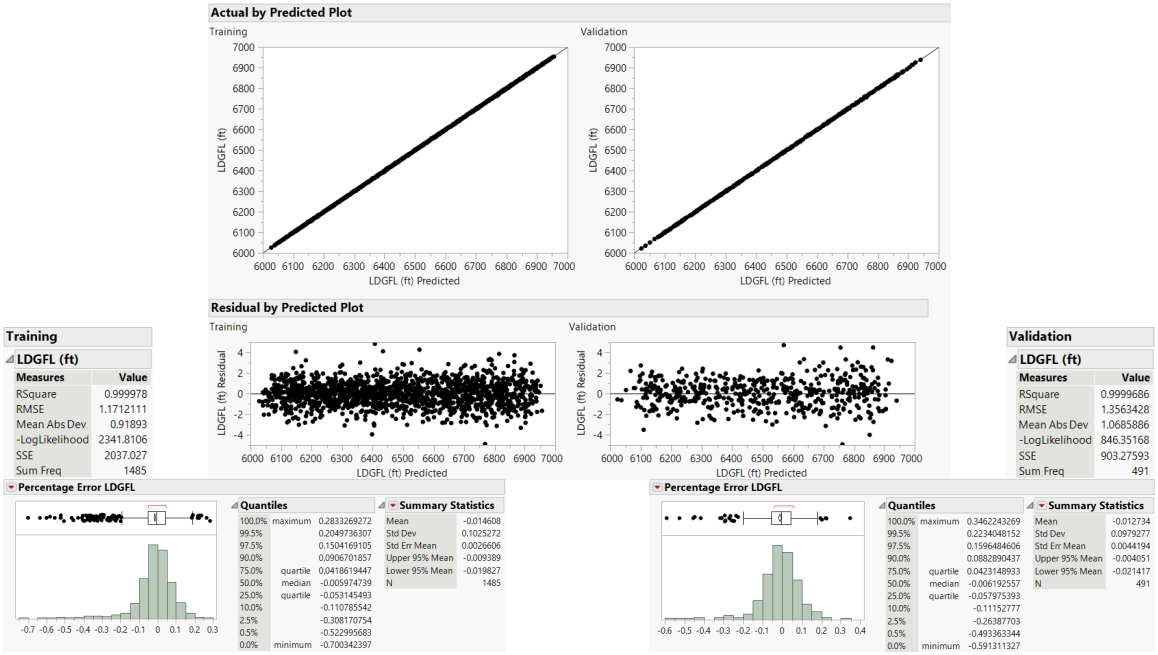

(f) Landing field length

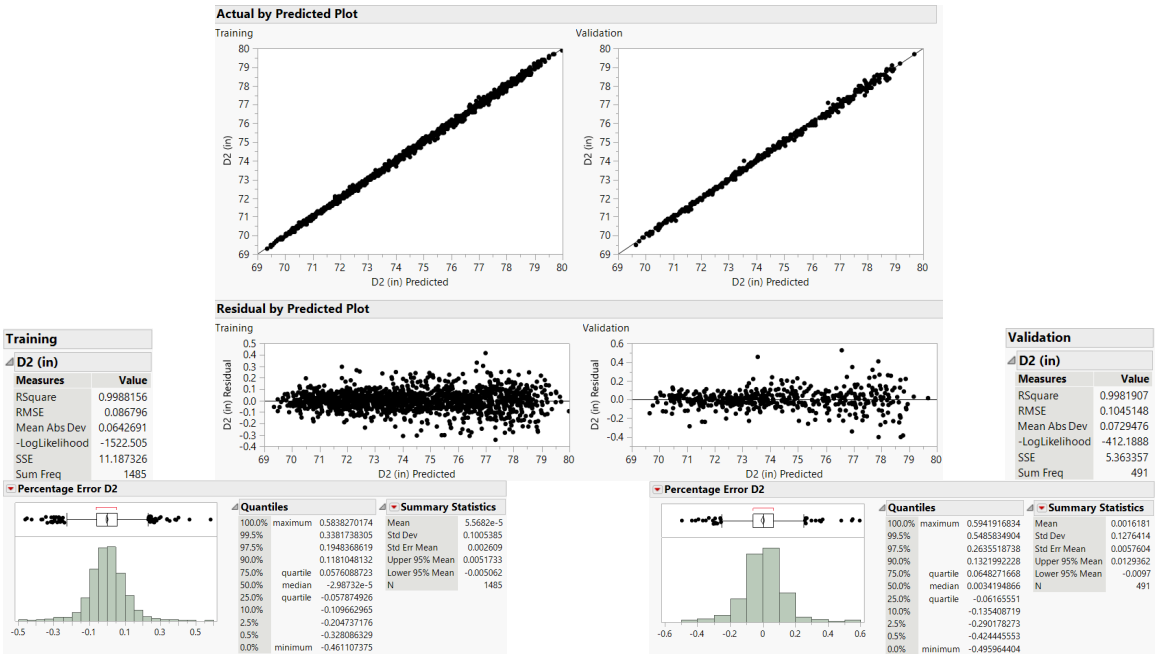

(g) Fan diameter

Figure C.7: Top-engine BLI-decoupled configuration actual vs. predicted, residual vs. predicted, model fit and model representation error plots for surrogate models (contd.)

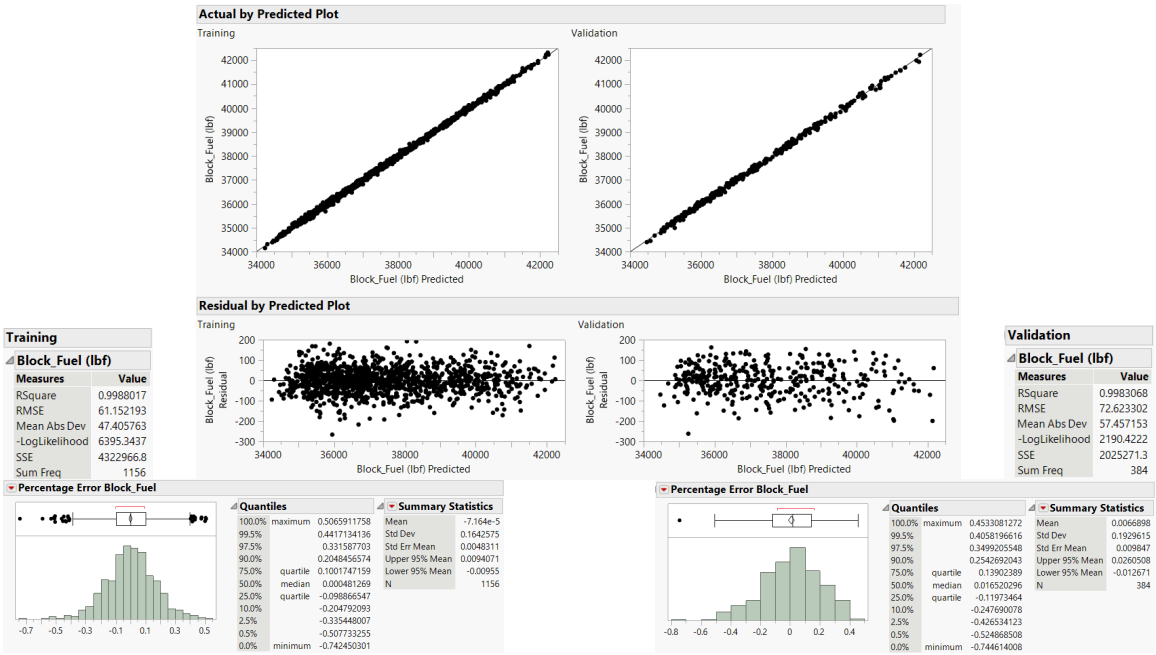

(a) Design block fuel

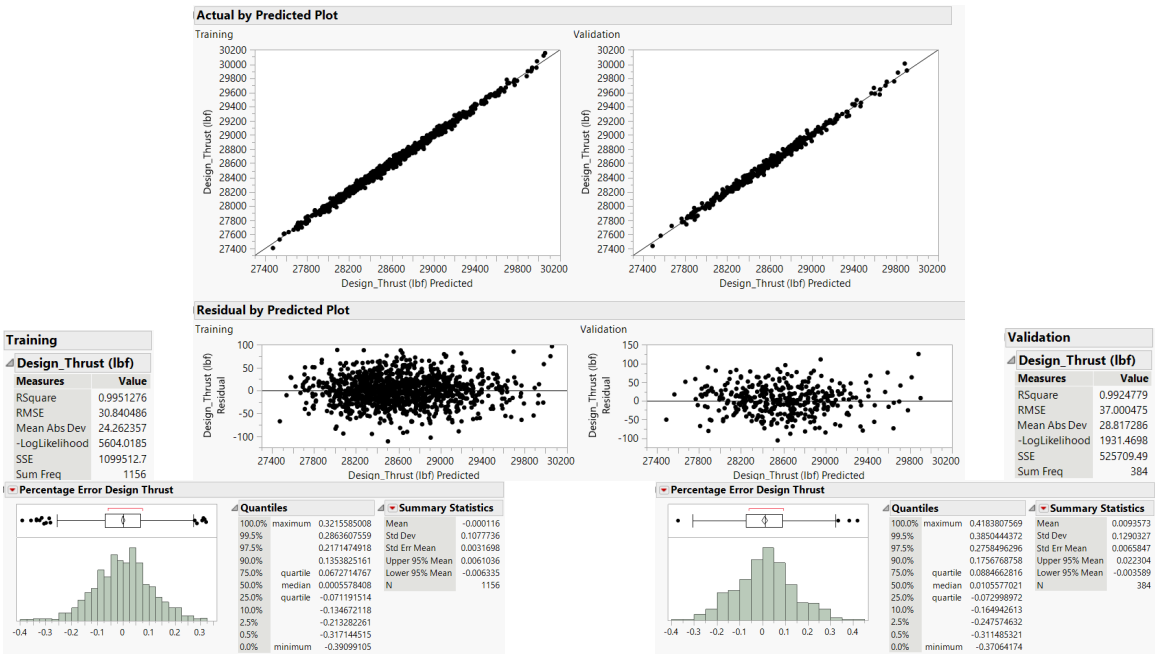

(b) SLS thrust per engine

Figure C.8: Top-engine BLI-coupled configuration actual vs. predicted, residual vs. predicted, model fit and model representation error plots for surrogate models

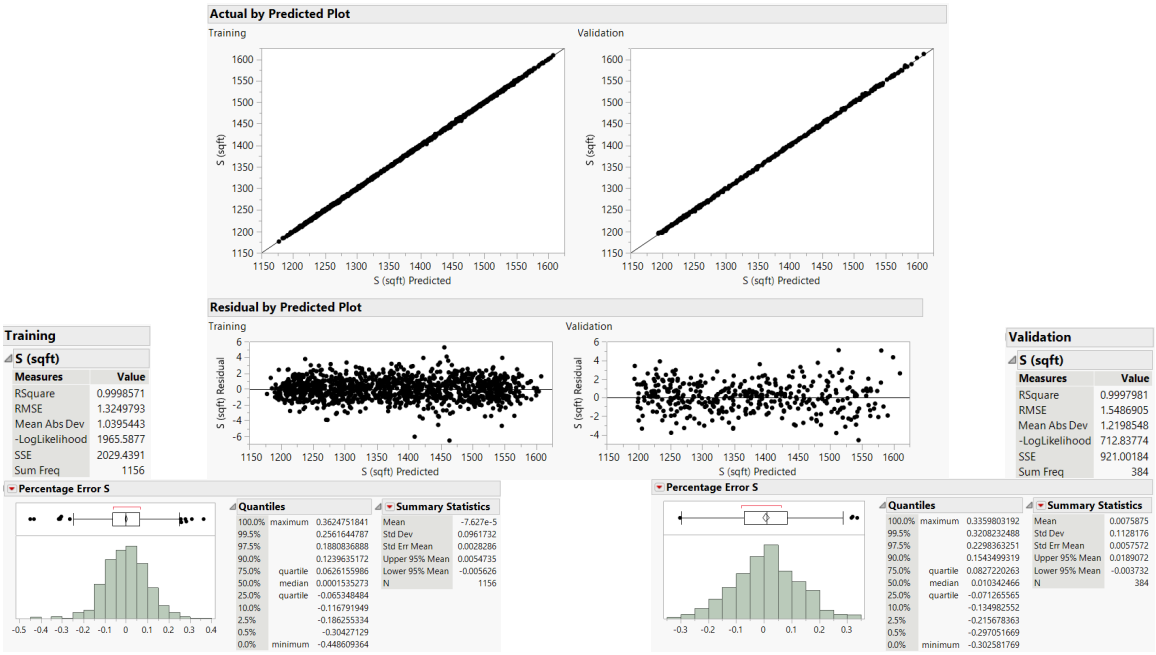

(c) Wing planform area

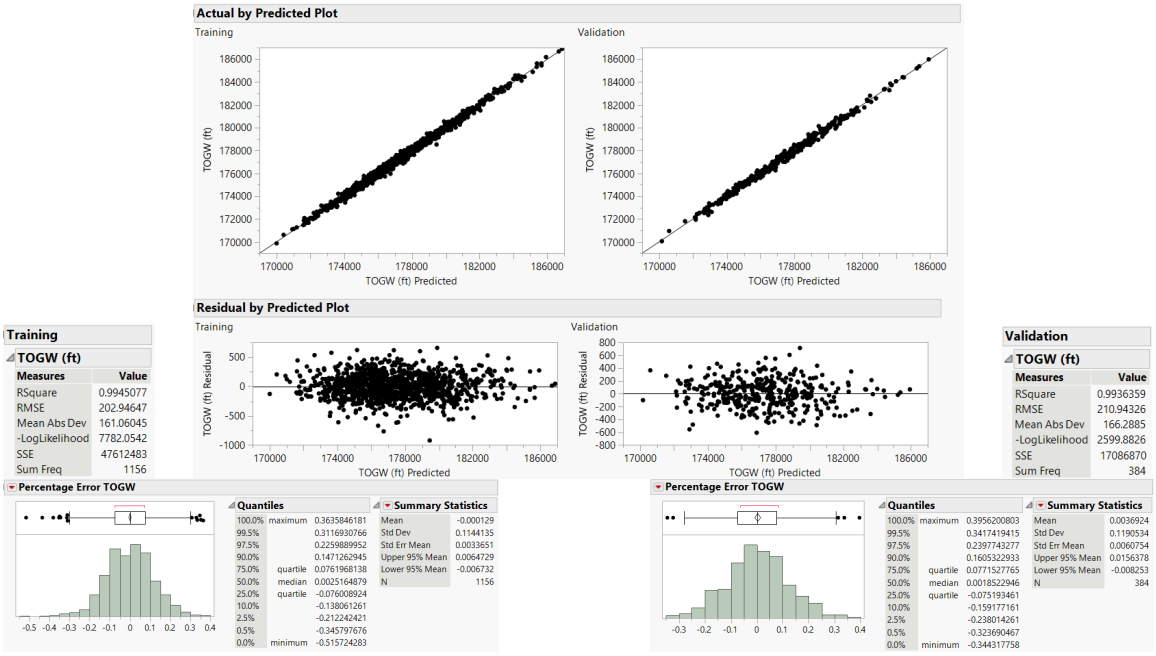

(d) Takeoff gross weight

Figure C.8: Top-engine BLI-coupled configuration actual vs. predicted, residual vs. predicted, model fit and model representation error plots for surrogate models (contd.)

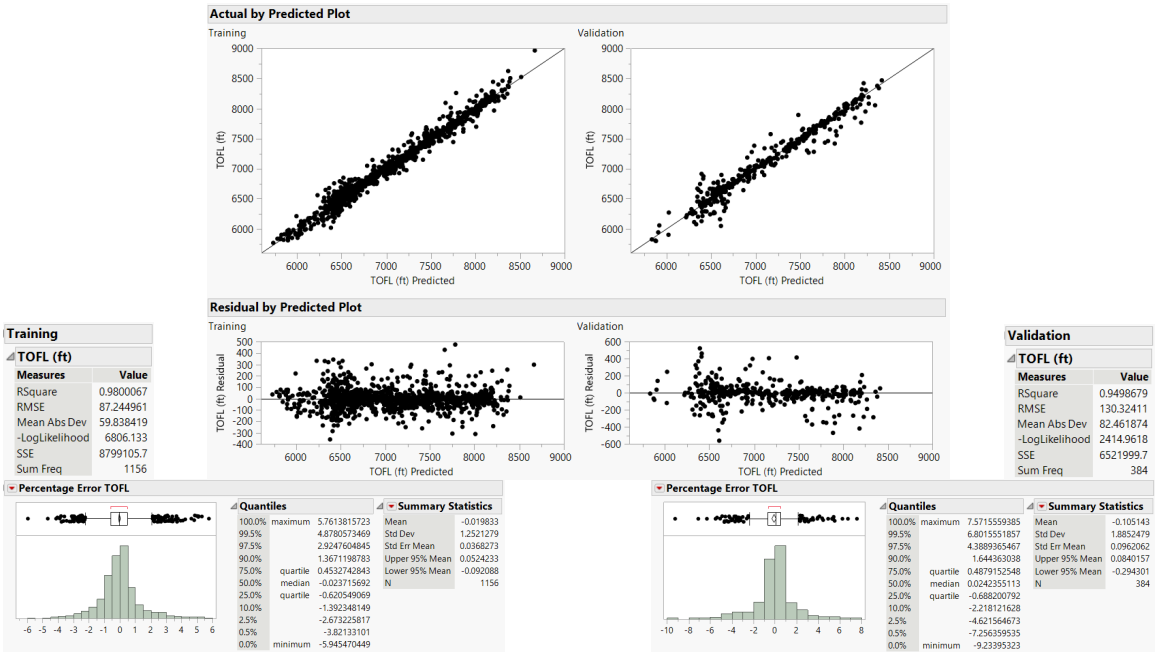

(e) Takeoff field length

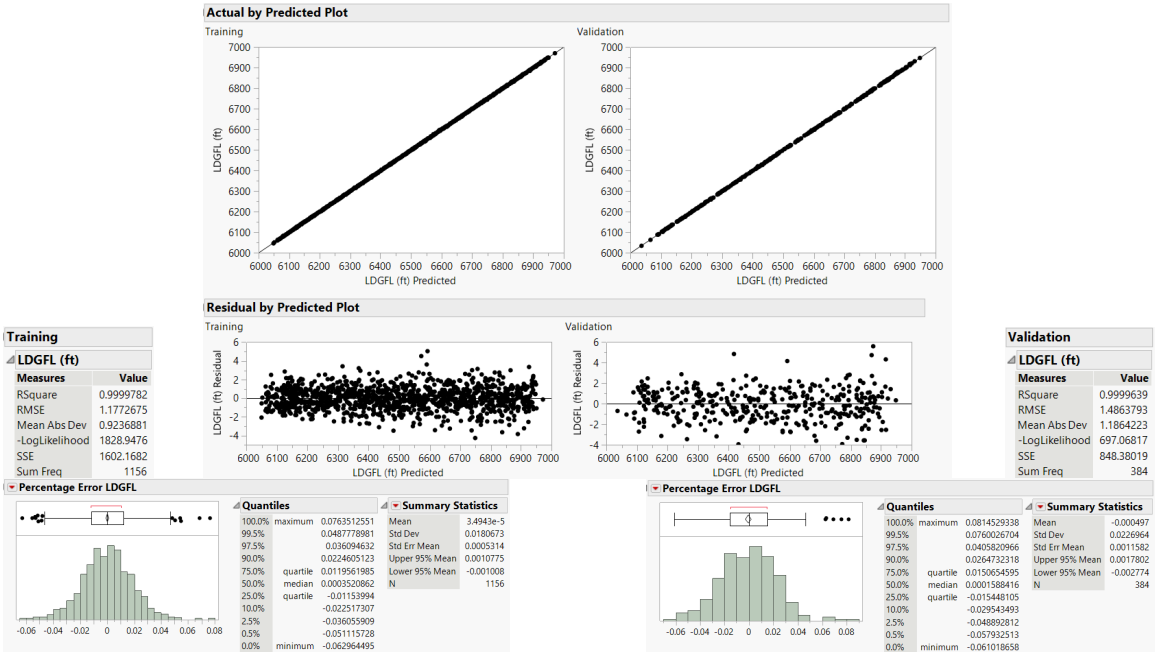

(f) Landing field length

Figure C.8: Top-engine BLI-coupled configuration actual vs. predicted, residual vs. predicted, model fit and model representation error plots for surrogate models (contd.)

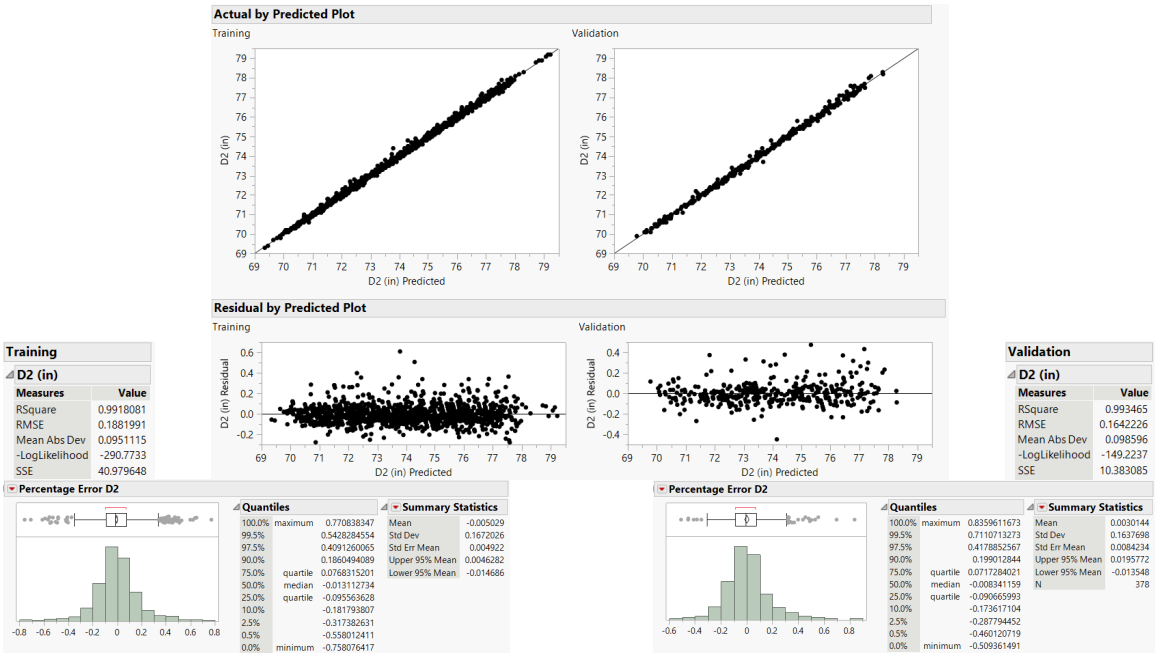

(g) Fan diameter

Figure C.8: Top-engine BLI-coupled configuration actual vs. predicted, residual vs. predicted, model fit and model representation error plots for surrogate models (contd.)

(a) Design block fuel

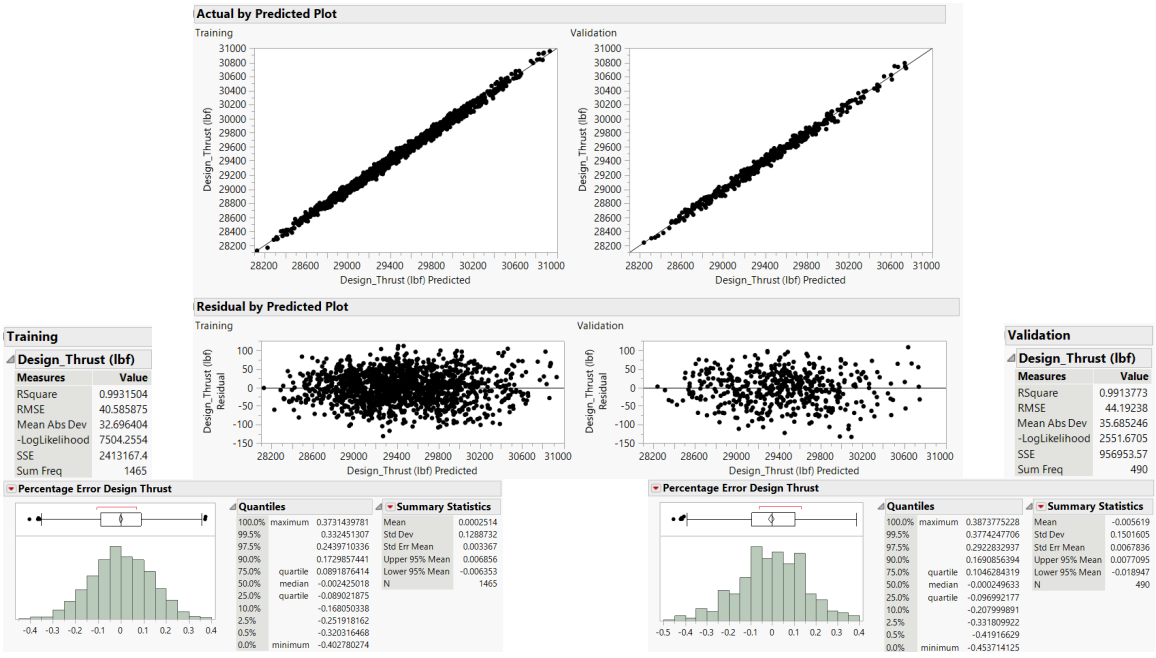

(b) SLS thrust per engine

Figure C.9: Side-engine non-BLI actual vs. predicted, residual vs. predicted, model fit and model representation error plots for surrogates

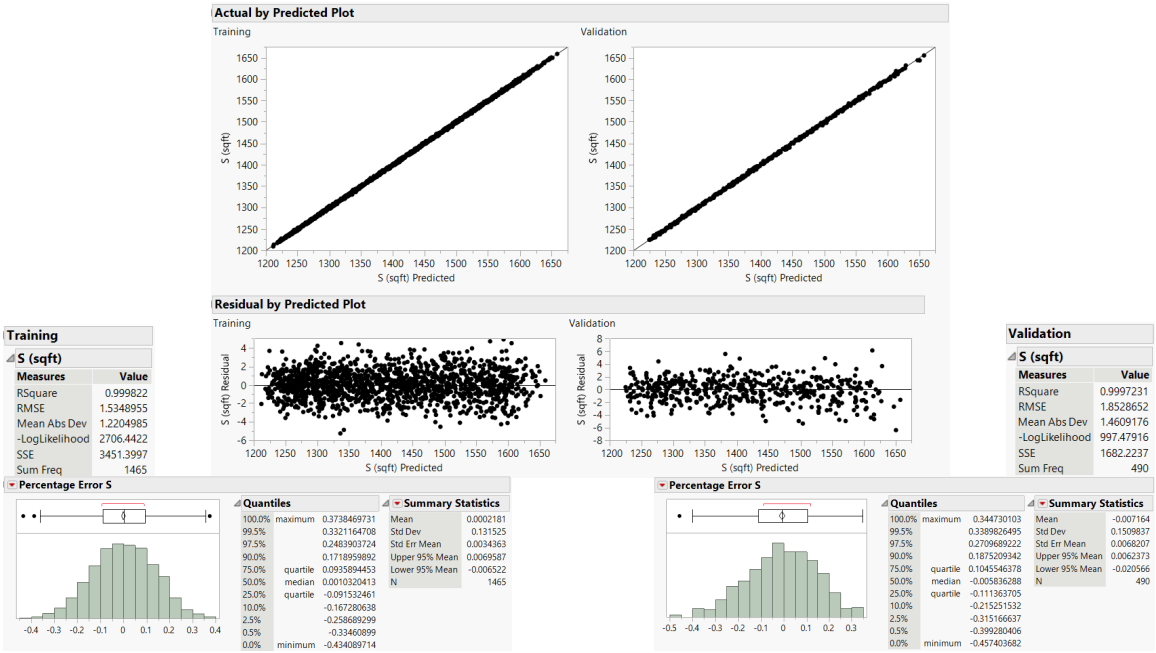

(c) Wing planform area

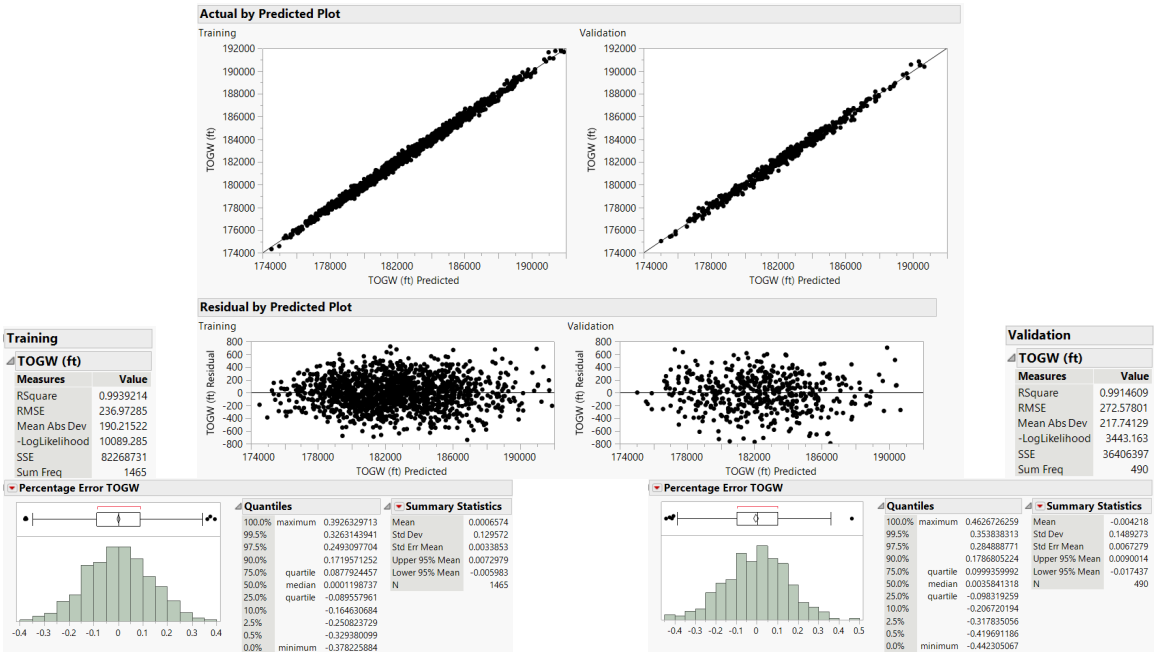

(d) Takeoff gross weight

Figure C.9: Side-engine non-BLI actual vs. predicted, residual vs. predicted, model fit and model representation error plots for surrogates (contd.)

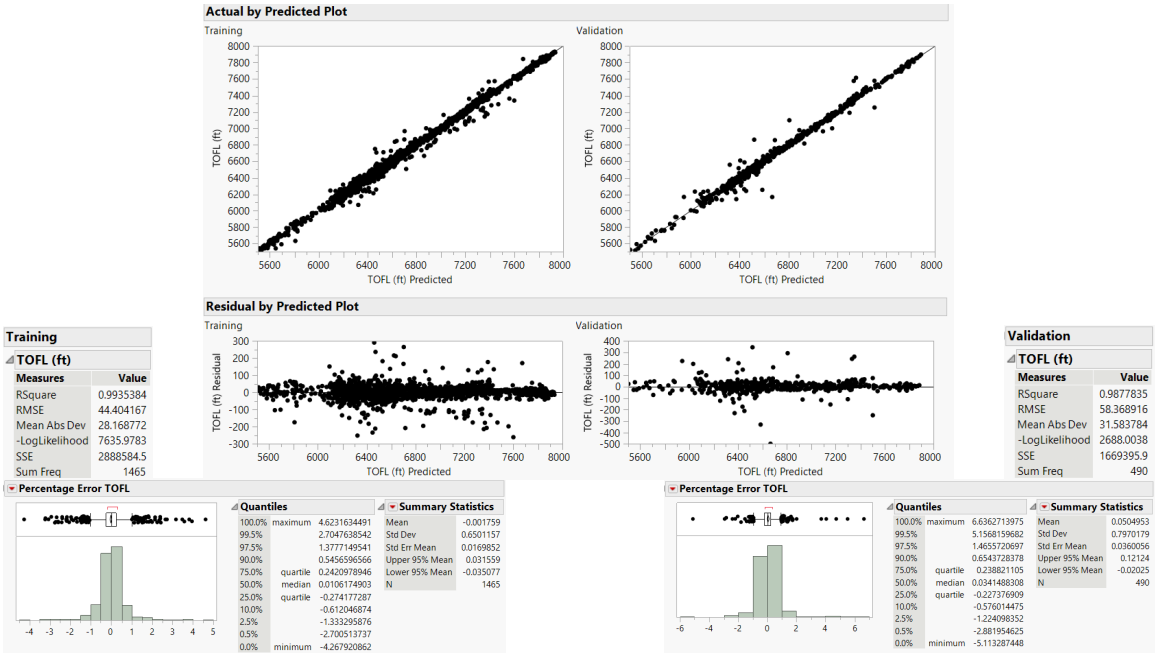

(e) Takeoff field length

(f) Landing field length

Figure C.9: Side-engine non-BLI actual vs. predicted, residual vs. predicted, model fit and model representation error plots for surrogates (contd.)

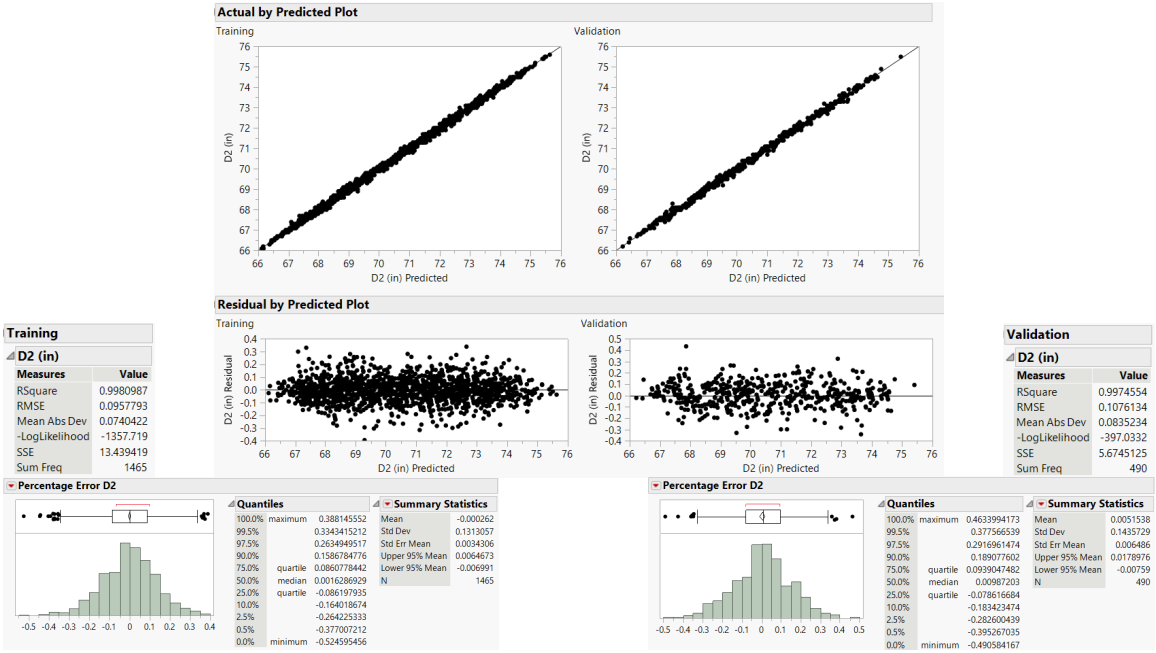

(g) Fan diameter

Figure C.9: Side-engine non-BLI actual vs. predicted, residual vs. predicted, model fit and model representation error plots for surrogates (contd.)

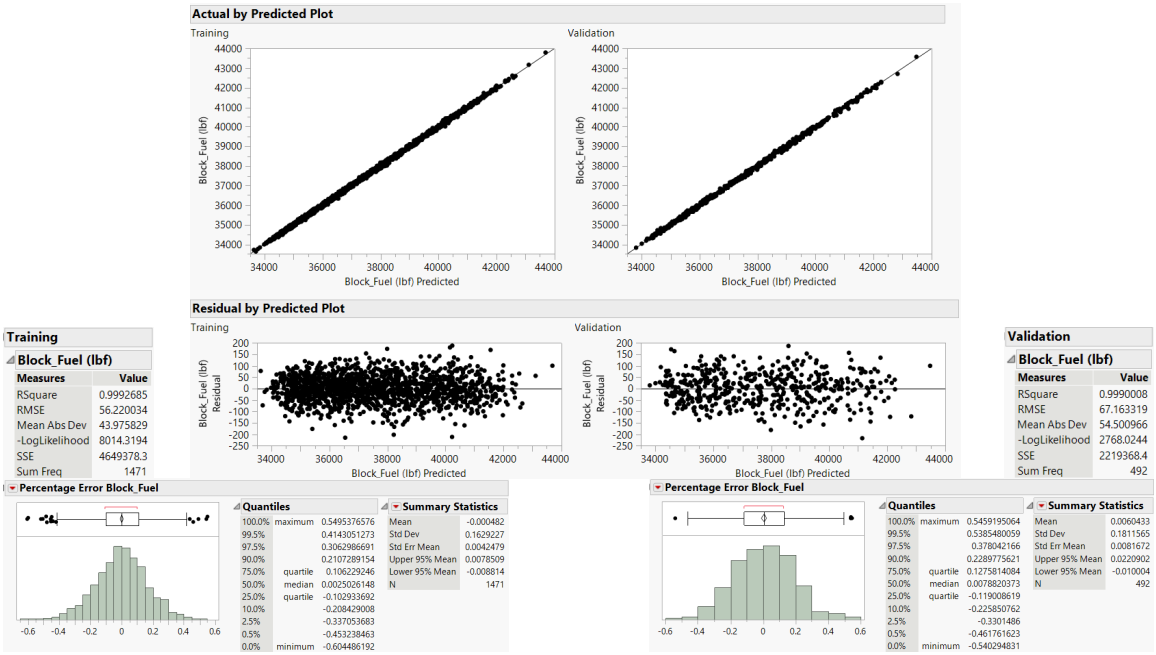

(a) Design block fuel

Figure C.10: Side-engine BLI-decoupled configuration actual vs. predicted, residual vs. predicted, model fit and model representation error plots for surrogate models

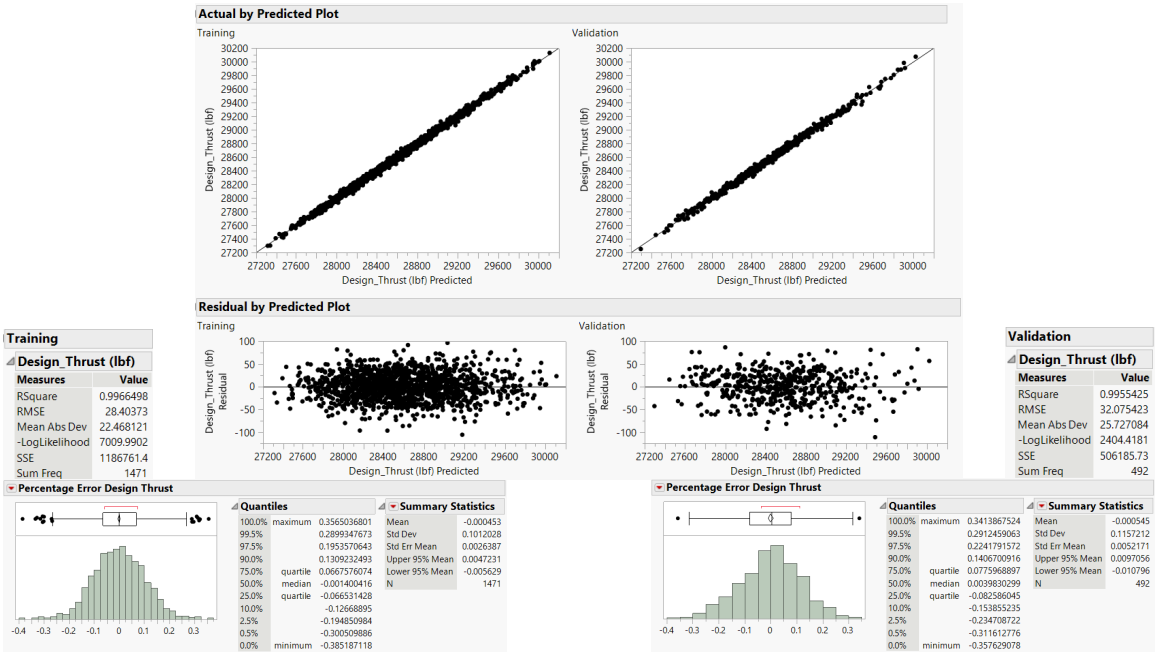

(b) SLS thrust per engine

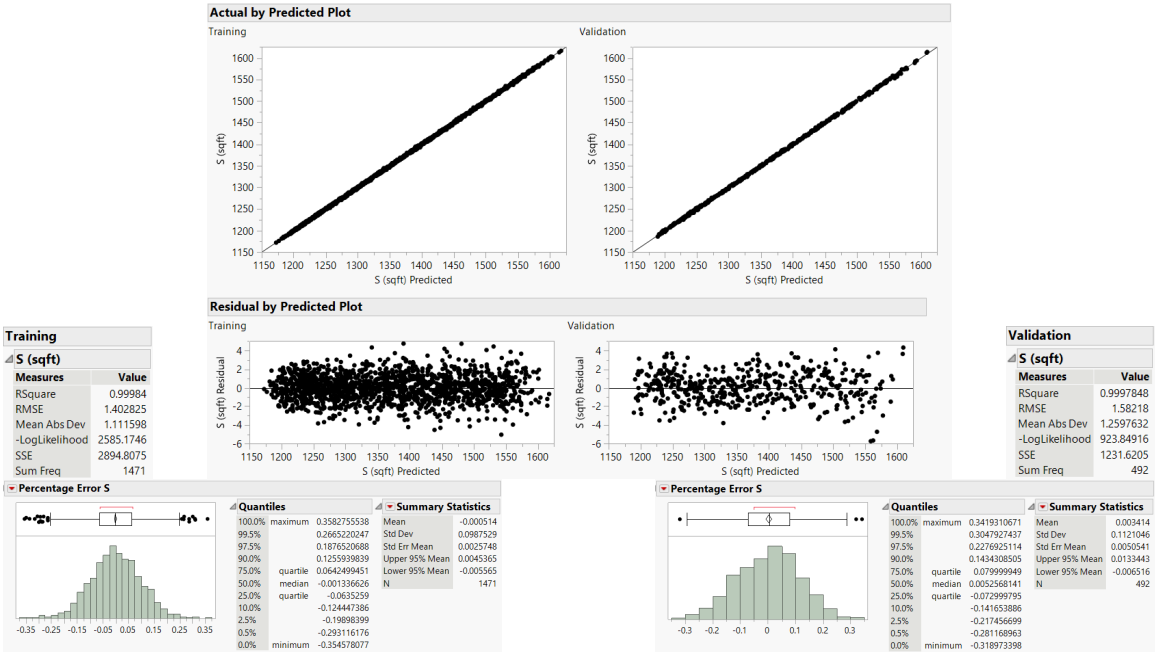

(c) Wing planform area

Figure C.10: Side-engine BLI-decoupled configuration actual vs. predicted, residual vs. predicted, model fit and model representation error plots for surrogate models (contd.)

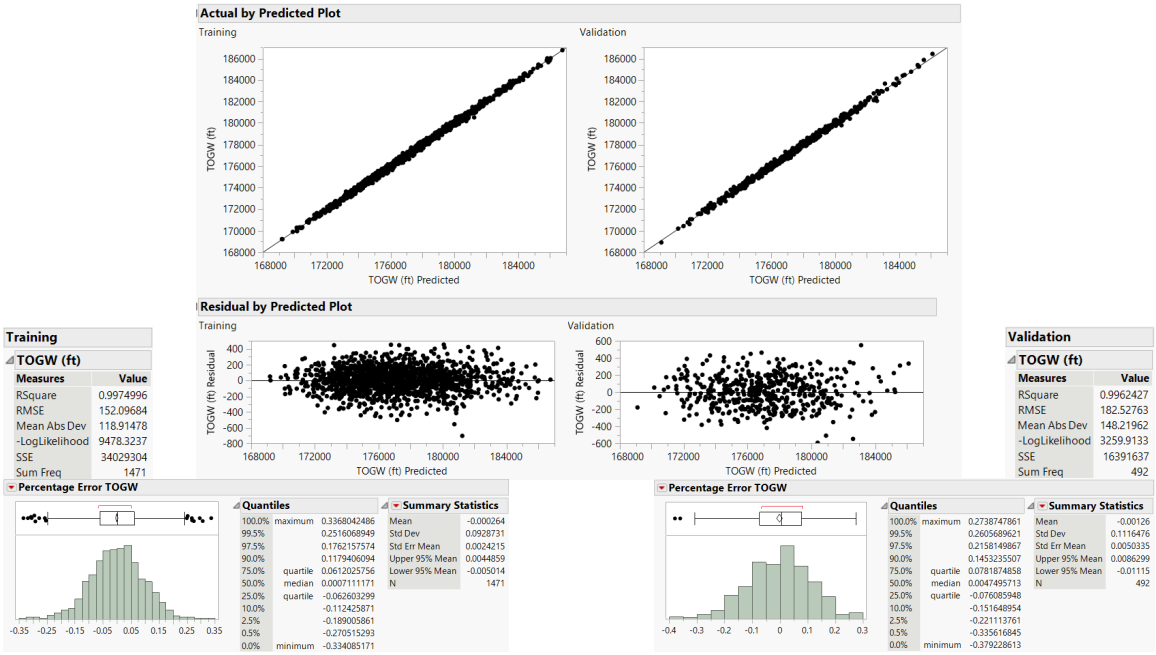

(d) Takeoff gross weight

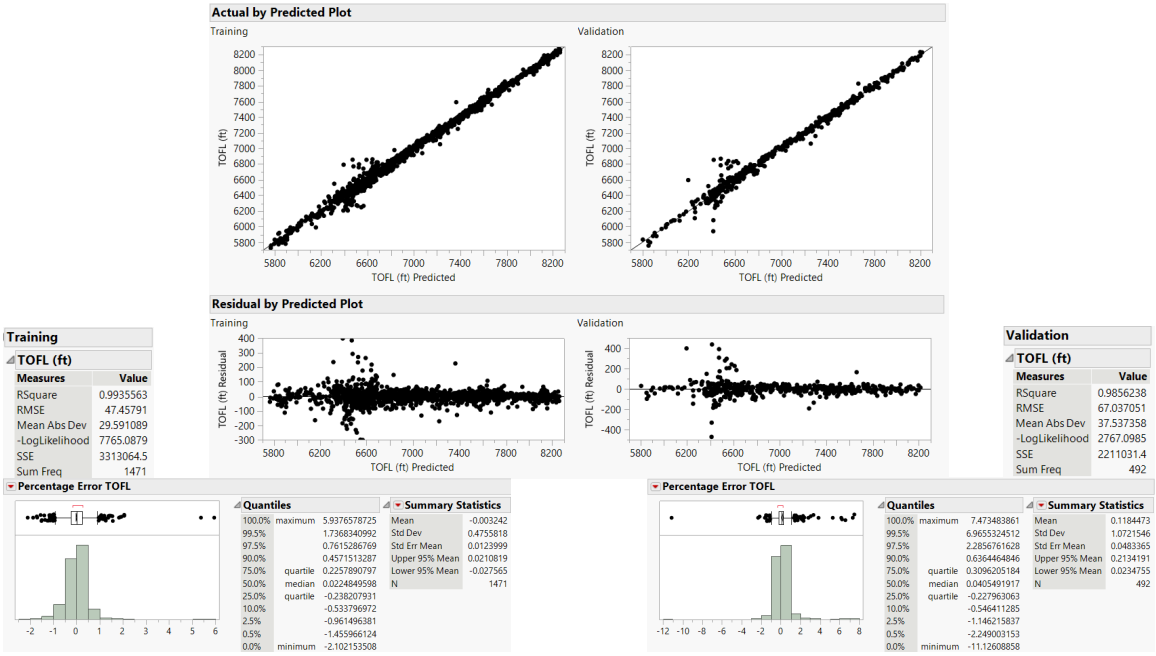

(e) Takeoff field length

Figure C.10: Side-engine BLI-decoupled configuration actual vs. predicted, residual vs. predicted, model fit and model representation error plots for surrogate models (contd.)

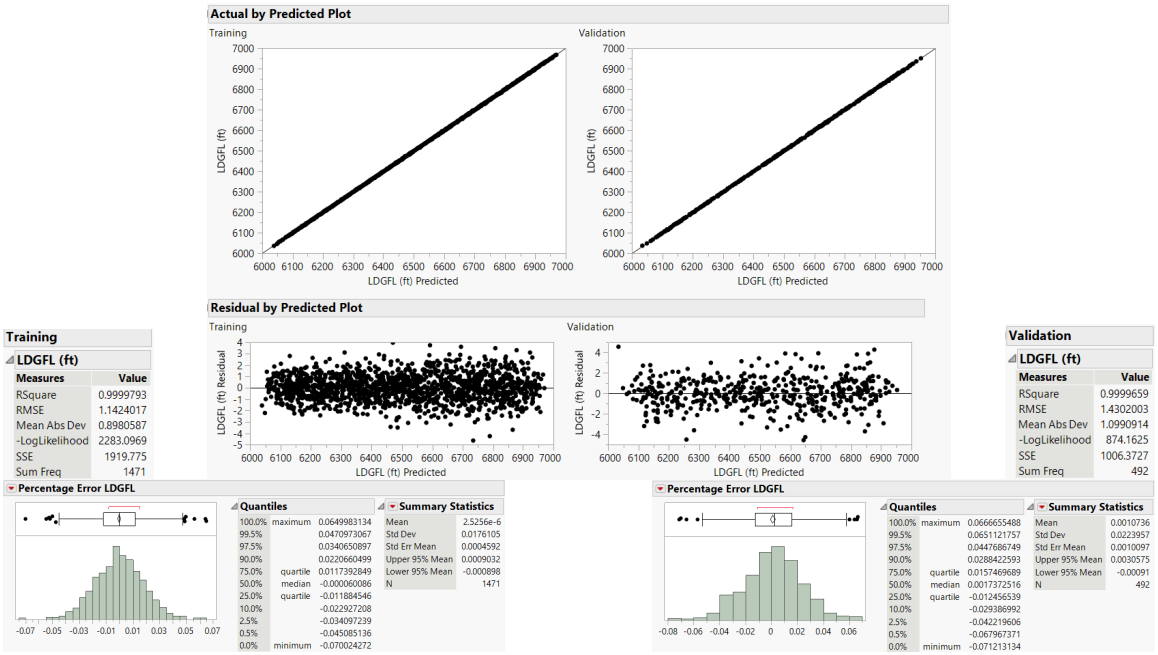

(f) Landing field length

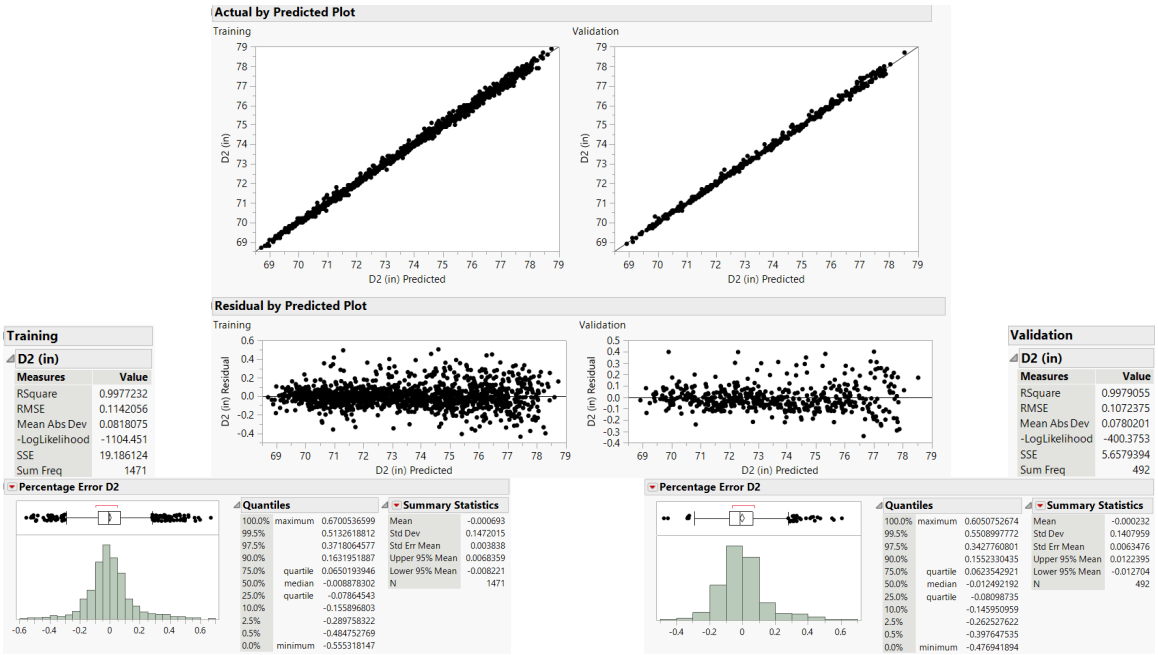

(g) Fan diameter

Figure C.10: Side-engine BLI-decoupled configuration actual vs. predicted, residual vs. predicted, model fit and model representation error plots for surrogate models (contd.)

(a) Design block fuel

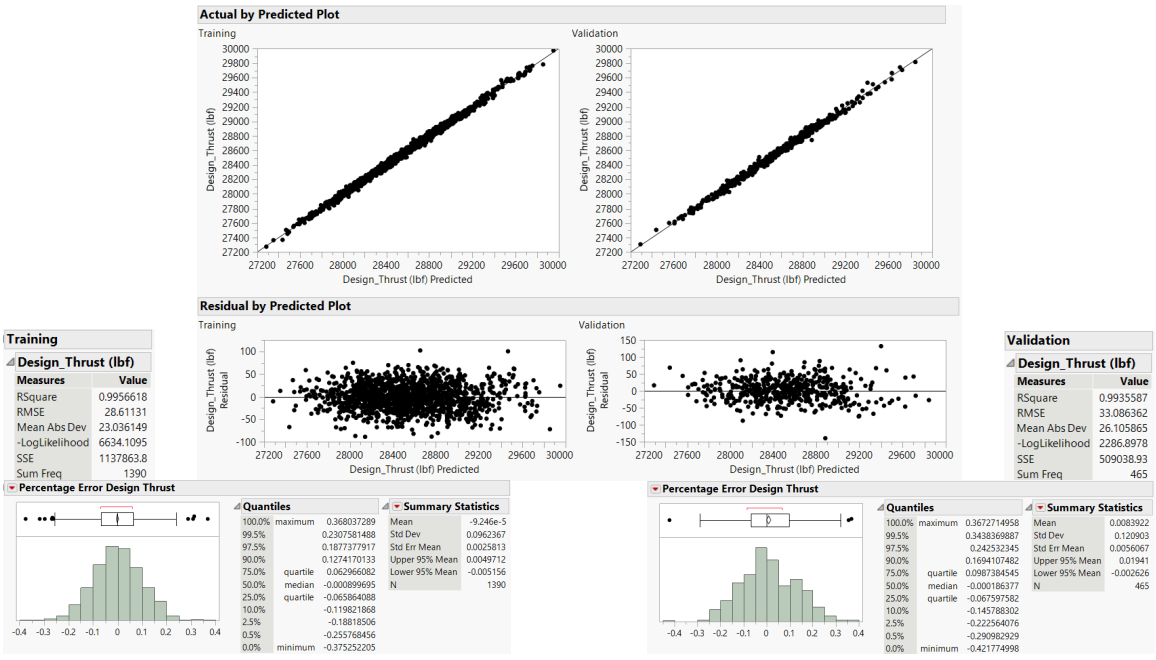

(b) SLS thrust per engine

Figure C.11: Side-engine BLI-coupled configuration actual vs. predicted, residual vs. predicted, model fit and model representation error plots for surrogate models

(c) Wing planform area

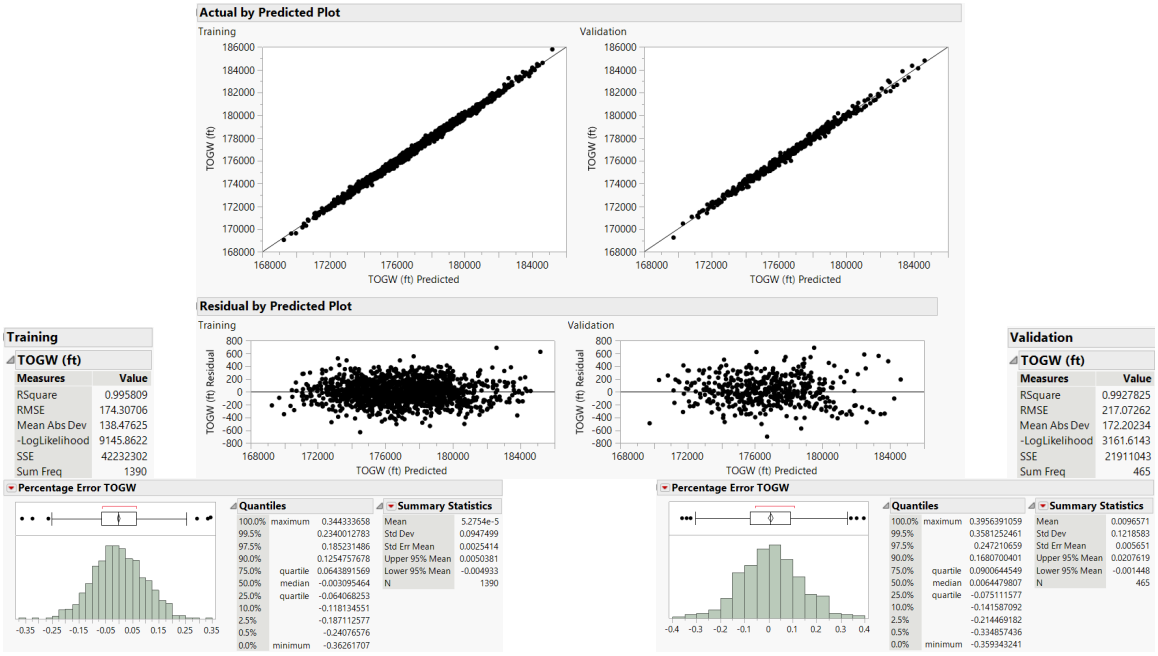

(d) Takeoff gross weight

Figure C.11: Side-engine BLI-coupled configuration actual vs. predicted, residual vs. predicted, model fit and model representation error plots for surrogate models (contd.)

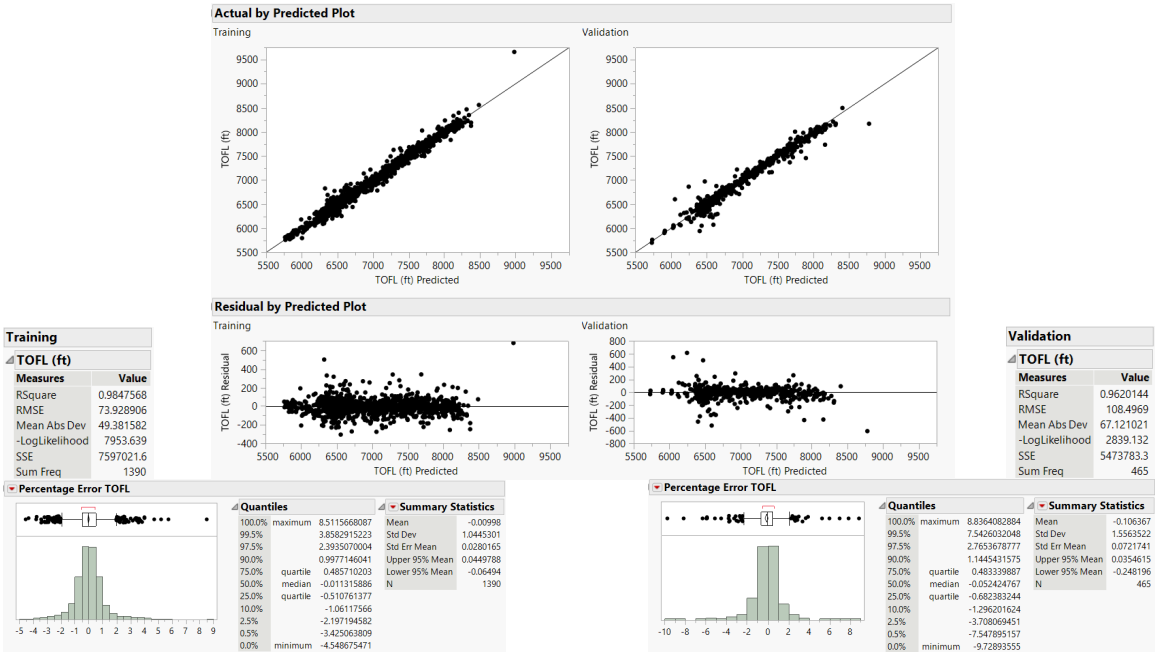

(e) Takeoff field length

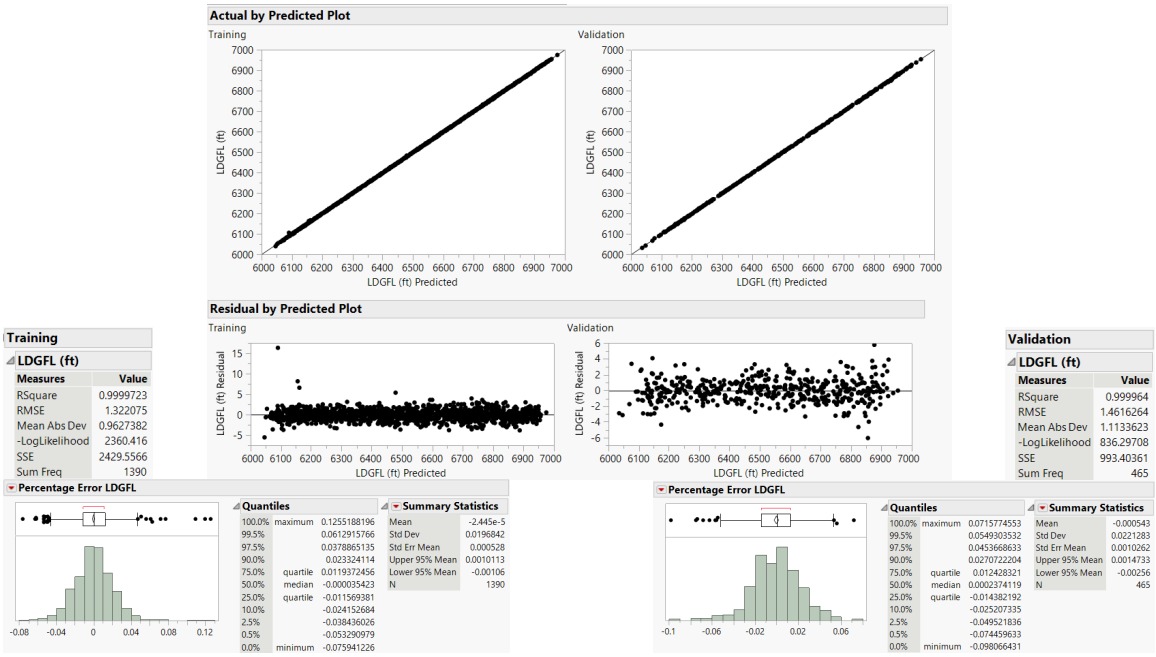

(f) Landing field length

Figure C.11: Side-engine BLI-coupled configuration actual vs. predicted, residual vs. predicted, model fit and model representation error plots for surrogate models (contd.)

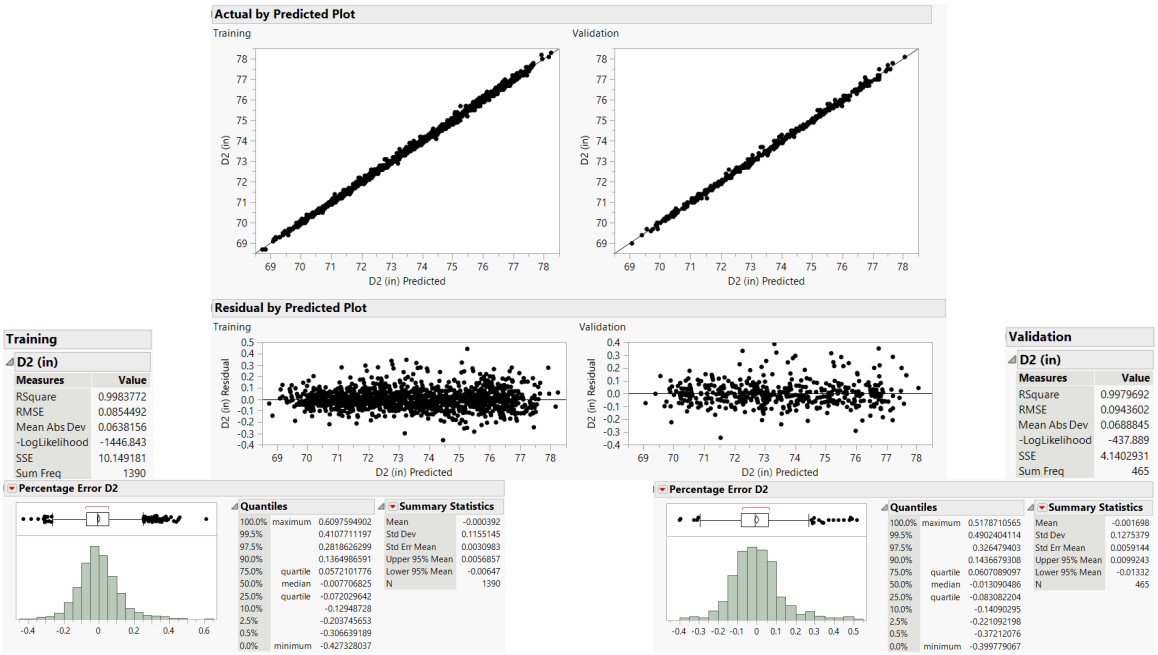

(g) Fan diameter

Figure C.11: Side-engine BLI-coupled configuration actual vs. predicted, residual vs. predicted, model fit and model representation error plots for surrogate models (contd.)

REFERENCES

[1] *A4A Passenger Airline Cost Index (PACI)*. Web Page. 2017.

[2] AHUJA, J. and MAVRIS, D. N. "A Method for Modeling the Aero-Propulsive Coupling Characteristics of BLI Aircraft in Conceptual Design". In: *AIAA SciTech Forum*. AIAA, 2021.

[3] AHUJA, J. and MAVRIS, D. N. "Assessment of Propulsor On-Design and Off-Design Impacts on BLI Effects". In: *AIAA SciTech Forum*. AIAA, 2021.

[4] AHUJA, J. and MAVRIS, D. N. "Sensitivity of Boundary Layer Ingestion Effects to Tube and Wing Airframe Design Features". In: *AIAA SciTech Forum*. AIAA, 2020.

[5] AIRBUS. *A350 Aircraft Characteristics Airport and Maintenence Planning*. Report. Airbus SAS, 2019.

[6] AKAYDIN, H. D. and PANDYA, S. A. "Implementation of a Body Force Model in OVERFLOW for Propulsor Simulations". In: *AIAA Aviation Forum*. AIAA, 2017.

[7] ARNTZ, A. "Civil Aircraft Aero-thermo-propulsive Performance Assessment by an Exergy Analysis of High-fidelity CFD-RANS Flow Solutions". Thesis. 2014.

[8] ATINAULT, O. and HUE, D. *Design of a Vertical Tail for the CRM Configuration*. Report. Onera, 2014.

[9] BALLING, R. J. and SOBIESZCZANSKI-SOBIESKI, J. "Optimization of Coupled Systems: A Critical Overview of Approaches". In: *AIAA Journal* 34.1 (1996).

[10] BERGUIN, S. H. et al. *CFD Study of an Over-Wing Nacelle Configuration*. Report. Georgia Institute of Technology, 2018.

[11] BERGUIN, S. H. et al. "Sensitivity Analysis of Aero-Propulsive Coupling for Over-Wing-Nacelle Concepts". In: *AIAA SciTech Forum*. AIAA, 2018.

[12] BETZ, A. *Introduction to the Theory of Flow Mechanics*. 1st ed. Karlsruhe, Germany: Pergamon Press, 1966.

[13] BLUMENTHAL, B. T. et al. "Computational Investigation of a Boundary-Layer Ingesting Propulsion System for the Common Research Model". In: *46th AIAA Fluid Dynamics Conference*. AIAA, 2016.

[14] BOEING. *737 MAX Airplane Characteristics for Airport Planning (Rev. B)*. Report. Boeing Commercial Airplanes, 2018.

[15] CRAMER, E. J. et al. "Problem Formulation for Multidisciplinary Optimization". In: *SIAM Journal on Optimization* 4.4 (1994), pp. 754–776.

[16] CRESSIE, N. "The Origins of Kriging". In: *Mathematical Geosciences* 22.3 (1990), p. 14.

[17] DERRINGER, G. and SUICH, R. "Simultaneous Optimization of Several Response Variables". In: *Journal of Quality Technology* 12.4 (1980), pp. 214–219. eprint: `https://doi.org/10.1080/00224065.1980.11980968`.

[18] DIEDRICH, A. et al. "Multidisciplinary Design and Optimization of the Silent Aircraft". In: *AIAA Aerospace Sciences Meeting and Exhibit*. AIAA, 2006.

[19] DRELA, M. "Development of the D8 Transport Configuration". In: *AIAA Applied Aerodynamics Conference*. AIAA.

[20] DRELA, M. "Power Balance in Aerodynamic Flows". In: *AIAA Journal* 47.7 (2009).

[21] DRELA, M. "Simultaneous Optimization of the Airframe, Powerplant, and Operation of Transport Aircraft". In: *Proceedings of the 2nd Aircraft Structural Design Conference*. Royal Aeronautical Society.

[22] FELDER, J. L., KIM, H. D., and BROWN, G. V. "Turboelectric Distributed Propulsion Engine Cycle Analysis for Hybrid-Wing-Body Aircraft". In: *47th AIAA Aerospace Sciences Meeting including the New Horizons Forum and Aerospace Exposition*. AIAA, 2009.

[23] FELDER, J. L. et al. "An Examination of the Effect of Boundary Layer Ingestion on Turboelectric Distributed Propulsion Systems". In: *49th AIAA Aerospace Sciences Meeting including the New Horizons Forum and Aerospace Exposition*. AIAA, 2011.

[24] FLOREA, R. V. et al. "Parametric Analysis and Design for Embedded Engine Inlets". In: *48th AIAA/ASME/SAE/ASEE Joint Propulsion Conference & Exhibit*. AIAA, 2012.

[25] GOLDSCHMIED, F. R. "Integrated Hull Design, Boundary-layer Control and Propulsion of Submerged Bodies". In: *Journal of Hydronautics* 1.1 (1967), p. 9.

[26] GRAY, J. S. and MARTINS, J. R.R. A. "Coupled Aeropropulsive Design Optimization of a Boundary Layer Ingestion Propulsor". In: *The Aeronautical Journal* (2018), p. 19.

[27] GRAY, J. S. et al. "Aeropropulsive Design Optimization of a Turboelectric Boundary Layer Ingestion Propulsion System". In: *Aviation 2018*. AIAA, 2018.

[28] GRAY, J. S. et al. "Modeling Boundary Layer Ingestion Using a Coupled Aeropropulsive Analysis". In: *Journal of Aircraft* 55.3 (2018).

[29] GREITZER, E. M. and DRELA, M. *Volume 2: Appendices Design Methodologies for Aerodynamics, Structures, Weight, and Thermodynamic Cycles*. Report. Massachusetts Institute of Technology, 2010.

[30] GREITZER, E. M. et al. *N+3 Aircraft Concept Designs and Trade Studies, Final Report*. Report. NASA Glenn Research Centre, 2010.

[31] HAFTKA, R. T., SOBIESZCZANSKI-SOBIESKI, J., and PADULA, S. "On Options for Interdisciplinary Analysis and Design Optimization". In: *Structural and Multidisciplinary Optimization* 4.2 (1992), pp. 65–74.

[32] HALL, C. A. and CRICHTON, D. "Engine Design Studies for a Silent Aircraft". In: *Journal of Turbomachinery* 129.3 (2006), p. 9.

[33] HALL, D. K., LIEU, M. K., and DRELA, M. "Aerodynamic Performance Accounting for Ultra-Integrated Air Vehicle Configurations". In: *AIAA SciTech Forum*. AIAA, 2019.

[34] HALL, D. K. et al. "Boundary Layer Ingestion Propulsion Benefit for Transport Aircraft". In: *Journal of Propulsion and Power* 33.5 (2017).

[35] HARDIN, L. W. et al. "Aircraft System Study of Boundary Layer Ingesting Propulsion". In: *48th AIAA/ASME/SAE/ASEE Joint Propulsion Conference & Exhibit*. AIAA, 2012.

[36] HENDRICKS, E. *A Review of Boundary Layer Ingesting Modeling Approaches for use in Conceptual Design*. Report. NASA Glenn Research Center, 2018.

[37] HILEMAN, J. et al. "Aerodynamic and Aeroacoustic Three-Dimensional Design for a Silent Aircraft". In: *44th AIAA Aerospace Sciences Meeting and Exhibit*. AIAA, 2006.

[38] HILEMAN, J. I., SPAKOVSZKY, Z. S., and DRELA, M. "Airframe Design for Silent Aircraft"". In: *45th AIAA Aerospace Sciences Meeting and Exhibit*. AIAA, 2007.

[39] JONES, D. R., SCHONLAU, M., and WELCH, W. J. "Efficient Global Optimization of Expensive Black-Box Functions". In: *Journal of Global Optimization* 13 (1998), p. 37.

[40] JULES, K. and LIN, P. *Artificial Neural Networks Applications: From Aircraft Design Optimization to Orbiting Spacecraft On-Board Environment Monitoring*. Report. NASA Glenn Research Center, 2002.

[41] KENWAY, G. K., KENNEDY Graeme, J., and MARTINS, J. R.R. A. "A CAD-Free Approach to High-Fidelity Aerostructural Optimization". In: *13th AIAA/ISSMO Multidisciplinary Analysis Optimization Conference*. AIAA, 2010.

[42] KENWAY, G. K. and KIRIS, C. "Aerodynamic Shape Optimization of the STARC-ABL Concept for Minimal Inlet Distortion". In: *AIAA SciTech Forum*. AIAA.

[43] KIM, H. and LIOU, M.-S. "Optimal Inlet Shape Design of N2B Hybrid Wing Body Configuration". In: *48th AIAA/ASME/SAE/ASEE Joint Propulsion Conference & Exhibit*. AIAA, 2012.

[44] KIM, H. and LIOU, M.-S. "Optimal Shape Design of Mail-Slot Nacelle on N3X Hybrid Wing-Body Configuration". In: *31st AIAA Applied Aerodynamics Conference*. AIAA, 2013.

[45] KIRBY Michelle, R. and MAVRIS, D. N. "The Environmental Design Space". In: *28th International Congress of the Aeronautical Sciences*. ICAS, 2008.

[46] KO, Y.-Y. A. "The Multidisciplinary Design Optimization of a Distributed Propulsion Blended-Wing-Body Aircraft". Thesis. 2003.

[47] KULFAN, B. M. "Universal Parametric Geometry Representation Method". In: *Journal of Aircraft* 45.1 (2008).

[48] KUNTAWALA, N. B., HICKEN, J. E., and ZINGG, D. W. "Preliminary Aerodynamic Shape Optimization of a Blended-Wing-Body Aircraft Configuration". In: *49th AIAA Aerospace Sciences Meeting including the New Horizons Forum and Aerospace Exposition*. AIAA, 2011.

[49] KURZKE, J. "Effects of Inlet Flow Distortion on the Performance of Aircraft Gas Turbines". In: *Journal of Engineering for Gas Turbines and Power* 130.4 (2008).

[50] LAMBE, A. B. and MARTINS, J. R.R. A. "A Unified Description of MDO Architectures". In: *9th World Congress on Structural and Multidisciplinary Optimization*.

[51] LEE, B. J., LIOU, M. F., and LIOU, M.-S. "Conceptual Aerodynamic Design of a Tail Cone Thruster System Under Axi-symmetric Inlet Distortion". In: *ASME Turbo Expo*. ASME, 2018.

[52] LEE, B. J., LIOU, M.-S., and KIM, C. "Optimizing a Boundary-Layer-Ingestion Offset Inlet by Discrete Adjoint Approach". In: *AIAA Journal* 48.9 (2010).

[53] LEE, C. H. "Bayesian Collaborative Sampling: Adaptive Learning for Multidisciplinary Design". Thesis. 2011.

[54] LIEBECK, R. H. "Blended Wing Body Design Challenges". In: *AIAA International Air and Space Symposium and Exposition: The Next 100 Years*. AIAA, 2003.

[55] LIEBECK, R. H. "Design of the BlendedWing Body Subsonic Transport". In: *Journal of Aircraft* 41.1 (2004).

[56] LIEBECK, R. H., PAGE, M. A., and RAWDON, B. K. "Blended-Wing-Body Subsonic Commercial Transport". In: *36th AIAA Aerospace Sciences Meeting and Exhibit*. AIAA, 1998.

[57] LIU, C. et al. "Thermal cycle analysis of turboelectric distributed propulsion system with boundary layer ingestion". In: *Aerospace Science and Technology* 27.1 (2013), p. 8.

[58] LIU, Y. et al. "Exploring Vehicle Level Benefits of Revolutionary Technology Progress via Aircraft Design and Optimization". In: *Energies* 11.1 (2018).

[59] LORD, W. K. et al. "Engine Architecture for High Efficiency at Small Core Size". In: *AIAA SciTech Forum*. AIAA, 2015.

[60] LYTLE, J. K. "The Numerical Propulsion System Simulation: A Multidisciplinary Design System for Aerospace Vehicles". In: *14th International Symposium on Air Breathing Engines*. NASA, 1999.

[61] LYU, Z. and MARTINS, J. R.R. A. "Aerodynamic Design Optimization Studies of a Blended-Wing-Body Aircraft". In: *Journal of Aircraft* 51.5 (2014).

[62] MARIEN, T. V., WELSTEAD, J. R., and JONES, S. M. "Vehicle-Level System Impact of Boundary Layer Ingestion for the NASA D8 Concept Aircraft". In: *AIAA SciTech Forum*. AIAA.

[63] MARTINS, J. R.R. A. and LAMBE, A. B. "Multidisciplinary Design Optimization: A Survey of Architecture". In: *AIAA Journal* 51.9 (2013).

[64] MCCULLERS, L. A. "Aircraft Configuration Optimization Including Optimized Flight Profiles". In: *NASA Symposium on Recent Experiences in Multidisciplinary Analysis and Optimization*. NASA, 1984.

[65] MCKAY, M. D., J., B. R., and J., C. W. "A Comparison of Three Methods for Selecting Values of Input Variables in the Analysis of Output from a Computer Code". In: *Technometrics* 21.2 (1979), p. 7.

[66] MCLEAN, J. D. *Understanding Aerodynamics : Arguing from the Real Physics*. John Wiley Sons, Incorporated, 2012.

[67] MENTER, F. R. "Two-Equation Eddy-Viscosity Turbulence Models for Engineering Applications". In: *AIAA Journal* 32.8 (1994).

[68] MULLER, R. *ACARE Goals (AGAPE) Progress Evaluation, Project Final Report Publishable Summary*. Report. Advisory Council for Aeronautics Research in Europe, 2010.

[69] MYERS, R. H., MONTGOMERY, D. C., and ANDERSON-COOK, C. M. *Response Surface Methodology: Process and Product Optimization Using Designed Experiments*. Wiley Series in Probability and Statistics. Hoboken, Nj: John Wiley and Sons, 2009.

[70] ORDAZ, I. *Aero-Propulsion Analysis and Design Framework*. Report. NASA, 2018.

[71] ORDAZ, I. et al. "Mitigation of Engine Inlet Distortion through Adjoint-Based Design". In: *AIAA AVIATION Forum*. AIAA, 2017.

[72] PANDYA, S. A. *Preliminary Assessment of the Boundary Layer Ingestion Benefit for the D8 Aircraft*. Report. NASA Ames Research Center, 2014.

[73] PANDYA, S. A. et al. "Computational Assessment of the Boundary Layer Ingesting Nacelle Design of the D8 Aircraft". In: *AIAA SciTech Forum*. AIAA.

[74] PLAS, A. P. et al. "Performance of a Boundary Layer Ingesting (BLI) Propulsion System". In: *45th AIAA Aerospace Sciences Meeting and Exhibit*. AIAA, 2007.

[75] POKHREL, M. et al. "A Methodology for Quantifying Distortion Impacts Using a Modified Parallel Compressor Theory". In: *ASME Turbo Expo 2018*. ASME, 2018.

[76] RAYMER, D. P. *Aircraft Design: A Conceptual Approach*. Fifth. Reston, VA: AIAA, 2012.

[77] REIST, T. A. and ZINGG, D. W. "Aerodynamic Shape Optimization of a Blended-Wing-Body Regional Transport for a Short Range Mission". In: *31st AIAA Applied Aerodynamics Conference*. AIAA, 2013.

[78] RODRIGUEZ, D. L. "A Multidisciplinary Optimization Method for Desiging Boundary Layer Ingesting Inlets". Thesis. 2001.

[79] RODRIGUEZ, D. L. "Multidisciplinary Optimization Method for Designing Boundary-Layer-Ingesting Inlets". In: *Journal of Aircraft* 46.3 (2009).

[80] SAMAREH, J. A. "Aerodynamic Shape Optimization Based on Free-form Deformation". In: *10th AIAA/ISSMO Multidisciplinary Analysis and Optimization Conference*. AIAA, 2004.

[81] SATO, S. "The Power Balance Method for Aerodynamic Performance Assessment". Thesis. 2012.

[82] SCHUTTE, J. "Simultaneous Multi-Design Point Approach to Gas Turbine On-Design Cycle Analysis for Aircraft Engines". Thesis. 2009.

[83] SCHUTTE, J. et al. "Cycle Design Exploration Using Multi-Design Point Approach". In: *ASME Turbo Expo 2012: Turbine Technical Conference and Exposition*. ASME, 2012.

[84] SECCO, N. R. and MATTOS, B. Silva de. "Artificial Neural Networks Applied to Airplane Design". In: *AIAA SciTech Forum*. AIAA, 2015.

[85] SMITH, A. M. O and ROBERTS, H. E. "The Jet Airplane Utilizing Boundary Layer Air for Propulsion". In: *Journal of the Aeronautical Sciences* 14.2 (1947).

[86] SMITH, L. H. "Wake Ingestion Propulsion Benefit". In: *Journal of Propulsion and Power* 9.1 (1993).

[87] SUDER, K. "Overview of the NASA Environmentally Responsible Aviation Project's Propulsion Technology Portfolio". In: *48th AIAA/ASME/SAE/ASEE Joint Propulsion Conference & Exhibit, Joint Propulsion Conferences*. AIAA, 2012.

[88] SULEMAN, A. et al. "Non-Linear Aeroelastic Analysis in the Time Domain of High-Aspect-Ratio Wings: Effect of Chord and Taper-Ratio Variation". In: *The Aeronautical Journal* 121.1235 (2017), p. 33.

[89] TEAL, M. "New 737 MAX: Improved Fuel Efficiency and Performance". In: *Boeing AERO Magazine, Q1 2014* 53 (2014).

[90] TONG, M. T. and NAYLOR, B. A. *An Object-Oriented Computer Code for Aircraft Engine Weight Estimation*. Report. NASA Glenn Research Center, 2009.

[91] URANGA, A. et al. "Boundary Layer Ingestion Benefit of the D8 Transport Aircraft". In: *AIAA Journal* 55.11 (2017).

[92] URANGA, A. et al. "Preliminary Experimental Assessment of the Boundary Layer Ingestion Benet for the D8 Aircraft". In: *AIAA SciTech Forum*. AIAA.

[93] *U.S. Passenger Carrier Delay Costs*. Web Page. 2017.

[94] *US Standard Atmosphere 1976*. Report. National Aeronautics and Space Administration, 1976.

[95] VASSBERG, J. C. et al. "Development of a Common Research Model for Applied CFD Validation Studies". In: *Applied Aerodynamics Conference*. AIAA, 2008.

[96] WANG, K. C. "On the Determination of the Zones of Influence and Dependence for Three-Dimensional Boundary-Layer Equations". In: *Journal of Fluid Mechanics* 8.2 (1971), pp. 397–404.

[97] WELSTEAD, J. R. *D8 Independent Assessment Briefing*. Report. NASA Langley Research Centre, 2015.

[98] WELSTEAD, J. R. and FELDER, J. L. "Conceptual Design of a Single-Aisle Turboelectric Commercial Transport with Fuselage Boundary Layer Ingestion". In: *AIAA SciTech Forum*. AIAA, 2016.

[99] WHITE, F. M. *Viscous Fluid Flow*. Third. New York,NY: McGraw Hill, 2006.

[100] WIART, L. et al. "Aeropropulsive Performance Analysis of The Nova Configurations". In: *30th Congress of the International Council of the Aeronautical Sciences*. ICAS.

[101] WIART, L. et al. "Development of NOVA Aircraft Configurations for Large Engine Integration Studies". In: *33rd AIAA Applied Aerodynamics Conference*. AIAA.

[102] WISLICENUS, G. F. "Hydrodynamics and Propulsion of Submerged Bodies". In: *ARS Journal* 30.12 (1960).

[103] YI, S. I., SHIN, J. K., and PARK, G. J. "Comparison of MDO Methods with Mathematical Examples". In: *Structural and Multidisciplinary Optimization* 35 (2008), 391402.

[104] YUTKO, B. et al. "Conceptual Design of a D8 Commercial Aircraft". In: *AIAA Aviation Forum*. AIAA.

ACKNOWLEDGMENT OF PRIOR PUBLICATIONS

This section acknowledges that the research described in this thesis has been presented in following conference papers written by the author:

(i) Experiment 2 in chapter 5: Sensitivity of Boundary Layer Ingestion Effects to Tube and Wing Airframe Design Features [4]

(ii) Experiment 3 in chapter 6: Assessment of Propulsor On-Design and Off-Design Impacts on BLI Effects [3] (to be published in 2021)

(iii) Experiment 1 in chapter 7: A Method for Modeling the Aero-Propulsive Coupling Characteristics of BLI Aircraft in Conceptual Design [2] (to be published in 2021)